Experimental and simulation study of neutron-induced single event effects in accelerator environment and implications on qualification approach

Matteo Cecchetto

THÈSE POUR OBTENIR LE GRADE DE DOCTEUR DE L'UNIVERSITÉ DE MONTPELLIER

En Électronique

École doctorale I2S- Information Structures et Systèmes

IES – Institut d'Electronique et des Systèmes

Experimental and simulation study of neutron-induced Single Event Effects in accelerator environment and implications on qualification approach

Étude expérimentale et simulation des événements singuliers induits par des neutrons issus d'accélérateurs et impacts sur la qualification

Présentée par Matteo CECCHETTO

Le 13 Avril 2021

Sous la direction de Frédéric WROBEL et Rubén GARCÍA ALÍA

Devant le jury composé de

Jean-Luc AUTRAN, Professeur, Université d'Aix-Marseille	Rapporteur
Florent MILLER, Docteur, Nucletudes	Rapporteur
Jean-Luc LERAY, Docteur, International Thermonuclear Experimental Reactor (ITER)	Examinateur
Frédéric SAIGNÉ, Professeur, Université de Montpellier, IES	Examinateur
Rubén GARCÍA ALÍA, Docteur, European Organization for Nuclear Research (CERN)	Superviseur CERN
Frédéric WROBEL, Professeur, Université de Montpellier, IES	Directeur de thèse
Robert BAUMANN, Docteur, IEEE et Radiosity Solutions	Invité

UNIVERSITÉ DE MONTPELLIER

CERN

Abstract

(ENGLISH)

Electronic components and systems operating in the Large Hadron Collider (LHC) accelerator at CERN are subjected to a mixed-field radiation environment, mainly composed of neutrons with energies ranging from thermal up to a few GeV. This thesis aims at determining the impact of thermal and intermediate energy neutrons (0.2-20 MeV) with respect to highly energetic particles on the Single Event Upset (SEU) and Latch-up (SEL) rates induced in advanced Commercial-Off-The-Shelf (COTS) components, typically used in accelerator systems.

The radiation environments of several locations in the accelerator are described, characterized and compared to the ground level and atmospheric spectra at varying altitude. Inelastic and elastic nuclear processes through which neutrons of different energies induce Single Event Effects (SEEs) are extensively studied through Monte Carlo simulations, in terms of produced secondaries and their properties. Electronic components are experimentally characterized in monoenergetic and spallation facilities, and the SEE cross sections benchmarked with Monte Carlo simulations, where the energy deposition is associated with the SEE probability.

From these studies, the SEE rate is estimated for accelerator and atmospheric applications and put in the context of the qualification approaches at component and system level used in these environments. The qualification implications are derived from the combined simulation and experimental study, in order to determine the approach for quantifying the thermal and intermediate energy neutron contributions. Several solutions are proposed aiming towards a radiation hardness assurance (RHA) methodology based on mixed-field and monoenergetic experimental results, besides the consolidated knowledge of the operational environments and the associated effects.

Résumé

(FRANÇAIS)

Les composants et systèmes électroniques qui fonctionnent dans l'accélérateur Grand collisionneur de hadrons (LHC) au CERN sont soumis à un environnement radiatif à champ mixte, composé principalement de neutrons ayant des énergies allant des énergies thermiques jusqu'à quelques GeV. Cette thèse vise à déterminer l'impact des neutrons thermiques et d'énergie intermédiaire (0.2-20 MeV) par rapport aux particules hautement énergétiques sur les taux de Single Event Upset (SEU) et de Latch-up (SEL) induits dans des composants COTS (Commercial-Off-The-Shelf), généralement utilisés dans les systèmes d'accélérateurs.

Les environnements radiatifs dans l'accélérateur sont décrits en différents endroits. Ils sont caractérisés et comparés aux spectres au niveau du sol et de l'atmosphère à différentes altitudes. Les processus nucléaires inélastiques et élastiques par lesquels des neutrons de différentes énergies induisent des événements singuliers (SEE) sont largement étudiés par le biais de simulations Monte Carlo, en termes de particules secondaires produites et de leurs propriétés. Les composants électroniques sont caractérisés expérimentalement dans des installations mono-énergétiques et de spallation, et les sections efficaces aux SEE sont comparées avec les simulations Monte Carlo, pour lesquelles le dépôt d'énergie est associé à la probabilité de SEE.

À partir de ces études, le taux des SEE est estimé pour des applications d'accélérateur et atmosphérique et mis dans le contexte des approches de qualification au niveau des composants et des systèmes utilisés dans ces environnements. Les implications de qualification sont dérivées de la simulation et de l'étude expérimentale combinées. Cela permet de déterminer l'approche pour quantifier les contributions des neutrons thermiques et d'énergie intermédiaire. Au final, la méthodologie permet tenue des composants aux radiations (RHA) en se basant sur des résultats expérimentaux à champ mixte et mono-énergétiques et des connaissances consolidées de l'environnement opérationnel et des effets associés.

Contents

Chapter 1

Introduction

The European Organization for Nuclear Research (CERN), is the largest research centre for particle physics in the world, located in Switzerland and France. Since its foundation in 1954, CERN aims to answer those questions concerning the origin of the universe and what are the basic elements of which our world is made of. Over the years, CERN discovered how elementary particles combine together to form nuclei and atoms, the basic components that constitute more complex systems. The Higgs boson, in addition to the W and Z bosons, is one of the major discoveries of elementary particles, constituting the standard model. Nevertheless, some inventions we benefit from in everyday life owe their early foundation stages to CERN, such as the world wide web (www) or the Positron Emission Tomography (PET) in medicine. The basic concept to discover and study particles relies on colliding typically high energy protons (or electrons) against each other. Inside an accelerator, particles are accelerated with radio-frequency cavities, which apply an electric potential between two electrodes, and travel inside a vacuum pipe. Their trajectory, to form a circular path, and focus are maintained through magnets, controlled by a very precise current. The two main parameters of a collider are the energy of the particles and the luminosity, the latter linked to how many collisions the machine is designed to produce.

The Large Hadron Collider (LHC) at CERN is a 27 km long accelerator, located at about 100 m underground, providing two beams of protons both at 7 TeV of energy. These beams circulating in opposite directions are collided inside the so-called experiments, that are complex detectors that measure the particles generated from the collisions, such as ATLAS and CMS, which are the large-scale detectors that discovered the Higgs boson. Several accelerating stages are required to accelerate particles up to TeV of energies, and nowadays the complex is formed by a chain of five accelerators, ending with the LHC. A graphical representation of the accelerator complex and main facilities at CERN is depicted in Fig. 1.1.

As can be inferred, a large number of electronic devices and systems are needed to operate the accelerator and a great effort by engineers and physicists is required to ensure the reliability of the machine. For instance, a vast quantity of electronics is used for the following applications:

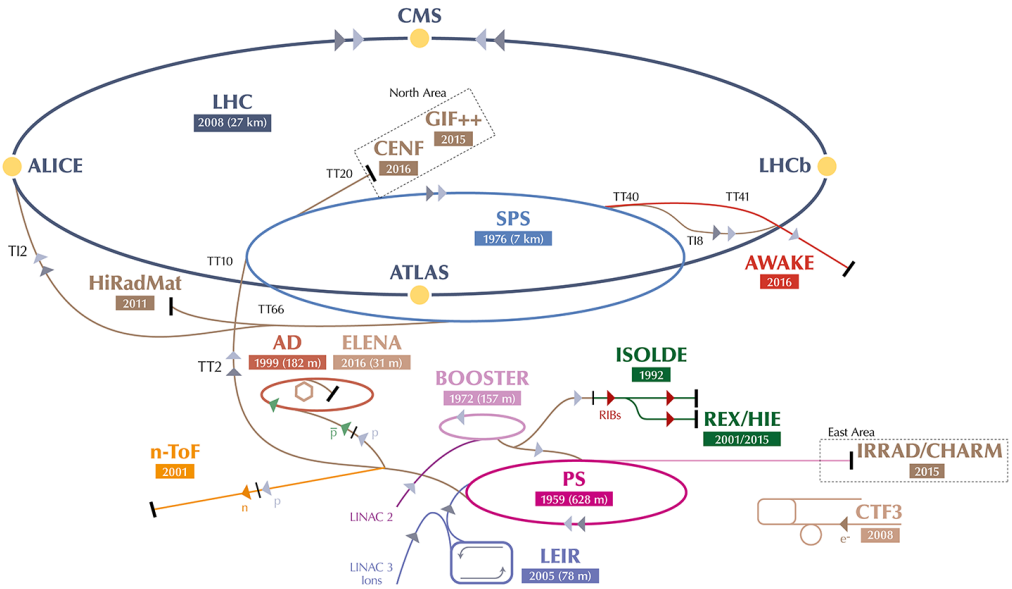

Figure 1.1: CERN accelerator complex: The LHC is the final stage of a chain composed of five accelerators [1].

- Power converters - The corrector magnets need to be feed with currents up to several kA in order to produce a magnetic field capable to bend the proton trajectory in a circular path.
- Vacuum - The proton beams travel inside two vacuum pipes (vacuum in the order of 10^{-11} mbar) to avoid interactions with air molecules.
- Cryogenics - Magnets are cooled down to $-270°C$ to act as superconductors in order to reduce as much as possible their power dissipation and dimensions.
- Quench protection systems - Prompt electronic systems are needed to protect the superconducting magnets from permanent damage in case of heat dissipation.
- Beam instrumentation - The beam has to be constantly monitored and corrected with complex instrumentation.
- Radio-frequency (RF) - The beam is accelerated through RF cavities.

Some of these electronic devices have to be installed underneath the magnets in the tunnel, while when the length of cabling is less restrictive they are placed inside partially shielded rooms called alcoves, which are parallel to the tunnel. In both cases, electronics are subjected to a very broad radiation environment mainly composed of neutrons, whose intensity and energies vary depending on the location. These radiation levels are mainly due to beam-beam collisions (at the interaction points) and to the interaction of the beam with collimators and with the residual gas molecules inside the vacuum pipe.

Electronics in the accelerator are mainly based on Commercial Off The Shelf (COTS) components, as opposed to radiation-hardened (rad-hard), for three main reasons: the performance and availability of COTS are not achievable when using rad-hard components, as well as their cost is limited and do not require a dedicated development. However, COTS need to be thoroughly tested to assess their correct operation under radiation environment.

Failures in electronics can lead to premature beam dumps, with the consequent downtime during which the entire machine cannot operate and the experiments cannot acquire data. After a failure, a few hours are needed to re-initialize the LHC and prepare the beams, and in more critical cases the intervention to replace the involved component is required. Moreover, as of 2025 with the High Luminosity (HL-LHC) upgrade, radiation levels in the accelerator will increase, hence electronics in the accelerator must be as reliable as possible.

In this context, the different radiation environments in the accelerator have to be assessed through measurements and simulations. Moreover, the radiation effects in electronics have to be studied to understand what triggers the events from the physical point of view. Finally, an efficient radiation qualification approach is needed with guidelines for testing components in dedicated facilities and evaluate their suitability for the accelerator. The Radiation to Electronic (R2E) project at CERN aims at studying these effects to minimize possible failures and to limit the impact of radiation on the LHC operation. Indeed, during the first years of the LHC operation, many failures occurred due to electronics which were mitigated and prevented over the years.

The work of this thesis is focused in studying the Single Event Effects (SEEs) induced by neutrons in electronics, from thermal ($\sim$25 meV) up to GeV of energies, with correlations to the current state of the art knowledge and qualification approach. The analysis is performed through Single Event Upset (SEU) and Single Event Latch-up (SEL) experimental measurements, which are benchmarked with Monte Carlo models. A particular focus is set on the contribution of thermal and intermediate energy (0.2-20 MeV) neutrons on the overall Soft Error Rate (SER) of electronic components, because they characterize a significant fraction of the radiation environment found in the LHC accelerator. The final objective is to outline some radiation hardness assurance (RHA) solutions to pave the way for a possible guideline for the qualification of accelerator electronic components against neutrons.

Moreover, the accelerator environment is compared to other fields that share similar issues with neutrons, such as the atmospheric and avionic ones. For instance, the SEE rate in avionic environment is estimated using standard test procedures for components with a strong SEE dependence with the energy, which were studied for accelerator applications. Nevertheless, results can be of interest for fusion, medical and automotive applications, as the involved neutron energies are a portion of those studied for the accelerator.

The thesis, whose work was carried out at CERN, develops through the following structure:

- Chapter 2 introduces the SEE response functions employed in the mixed-field radiation environment found in the LHC accelerator, defining the main quantities.
- Chapter 3 describes the sources of ionizing radiation, characterizing the accelerator and

atmospheric operational environments.

- Chapter 4 studies the nuclear interactions of neutrons in silicon through Monte Carlo simulations, analysing the energy distributions of produced secondaries which explain several aspects regarding the behaviour of the SEE cross sections.
- Chapter 5 describes the radiation test facilities and the calibration approach introduced to compare different facilities to the operational environments.
- Chapter 6 reports the SEE measurements of SRAMs performed in thermal, monoenergetic and spallation facilities.
- Chapter 7 is devoted to estimating the impact of thermal and intermediate energy neutrons on the overall SER for accelerator and atmospheric applications through measurements and Monte Carlo simulations, with consequent RHA implications.
- Chapter 8 summarizes the main results and achievements of the thesis.

Chapter 2

Radiation Effects in Electronics

The thesis is focused on the study of SEEs induced by neutrons that interacting with nuclei of atoms produce secondary ions. This chapter aims to define the main quantities of these particles, the mechanisms of SEEs of interest and the response function of electronics in the context of the accelerator.

2.1 Radiation Effects in Matter

A charged particle loses energy when passing through a certain material. The energy loss, for ionizing processes, is characterized through the **Linear Energy Transfer (LET)**, which is the energy deposited per unit of length by a single particle (ion). This quantity [MeV/cm] is generally normalized by the material density (ρ) to be independent on the state of the matter (solid, liquid, gas) and expressed in Eq. 2.1 in unit of $[MeV \cdot cm^2/mg]$. It is shown as a negative quantity because the particle loses energy (dE/dX<0) so that LET>0.

$$LET = -\frac{1}{\rho}\frac{dE}{dx} \tag{2.1}$$

The energy lost by the particle (ion) that produces ionization charge is also called electronic stopping power, and in silicon, an electron-hole pair is produced every 3.6 eV of energy lost by the ion (on average). The deposited energy can be easily converted into deposited charge, and considering that 1 eV is $1.6 \cdot 10^{-19}$ J, the energy to charge conversion in silicon is given by Eq. 2.2.

$$Q[pC] = \frac{E[MeV]}{22.5[MeV/pC]} \tag{2.2}$$

There is not a linear relation between LET and initial energy of the particle: LET and energy are correlated through an asymmetric function whose peak is referred to as the Bragg peak, as can be seen in Fig. 2.1 for an alpha particle impacting in silicon. These results are extracted trough the Stopping and Range of Ions in Matter (SRIM) tool [2], which is based on Monte

Carlo simulations. The cumulative effect of the LET is called Total Ionizing Dose (TID), defined as the total energy deposited through ionization per unit of mass, and given by the product of a constant (to convert eV in J, k=1.602·10^{-4} [Gy · mg/MeV]) by LET [MeV · cm^2/mg] and fluence [cm^2]: $TID = k \cdot LET \cdot \Phi$.

A similar quantity to describe the energy loss is the stopping power, which can be subdivided in the electronic and nuclear contributions (the radiative one is negligible for ions). The **electronic stopping power** regards energy loss due to ionization and it is the quantity considered as LET, while the **nuclear stopping power** involves non-ionizing processes of the nuclei, such as the displacement of the target nuclei by an ion [3]. The latter describes the Non Ionizing Energy Loss (NIEL) in electronics, whose cumulative effect is the Displacement Damage (DD) defined as the total energy deposited through non-ionizing processes per unit of mass. The total stopping power is the sum of the two contributions, where LET and NIEL are more significant at high and low energy, respectively. The **range** is another important parameter and is defined as the average length travelled by the ion before stopping owing to the dE/dx energy loss. Differently from the LET, the range is monotonically increasing as a function of the ion energy.

In addition, it has to be noted that LET and range are statistical in nature because identical ion events can have different paths and interactions with the target (multiple collisions, etc.). The variation in range is known as longitudinal and lateral straggling (with respect to the incidence of the ion).

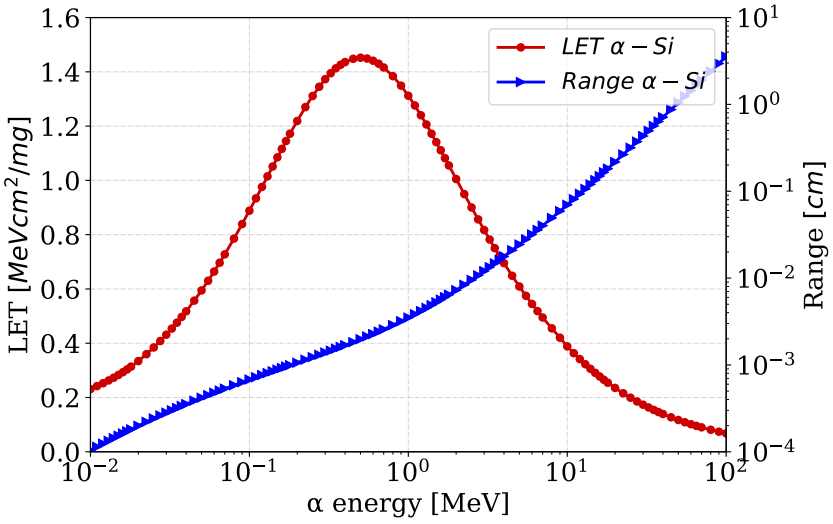

Figure 2.1: LET (or electronic stopping power) and range of an alpha particle (projectile) in silicon (target).

Coulomb barrier

The Coulomb barrier describes the minimum energy required by two nuclei so that a nuclear reaction can occur. The two nuclei need to get close enough to each other to overcome

the electrostatic Coulomb force. As neutrons are electrically neutral, they are not affected by the Coulomb barrier, and therefore can potentially initiate a nuclear reaction at lower energies with respect to protons. Fig. 2.2 shows this effect, considering the neutron $(n, x\alpha)$ and proton $(p, x\alpha)$ cross sections in ^{28}Si, extracted through the *TENDL* nuclear library [4] and compared to the total inelastic contributions. These nuclear cross sections, not to be confused with the SEE ones, describe the probability that a specific nuclear reaction can occur when neutrons or protons impact in silicon. They are measured in barn, which is an area corresponding to 10^{-24} cm^2. As can be seen, neutrons have a higher cross section compared to that of protons, especially below 20 MeV. The main contributions to the total inelastic cross sections are the (n, n') and (p, p') for neutrons and protons, respectively. Regarding the inelastic interactions with neutrons, the scattered cross sections below 8 MeV are due to resonance effects (see Fig. 2.2). However, secondary protons yield an ionization contribution that is small compared to that of alpha particles, and secondary neutrons have to indirectly interact again. Hence, the $(n, x\alpha)$ are the more effective reactions that can deposit a large quantity of charge triggering possible SEEs. As far as protons are regarded, below 50 MeV the Coulombic effect dominates over other reactions, while above 50 MeV protons have enough energy to overcome the repulsive force, and nuclear reactions similar to those induced by neutrons can occur [3]. The difference between neutrons and protons below 20 MeV is mainly because the $x\alpha$ reactions require higher incident energies for protons, due to the Coulomb barrier (this concept is associated to the Q reaction values described in Section 4.5). For instance, a minimum energy of 7.714 MeV (Q) has to be supplied for the (p, α) reactions, while only 2.654 MeV for the (n, α) reactions. As a consequence, the $(p, x\alpha)$ proton cross section decreases below 20 MeV [5], as seen in Fig. 2.2.

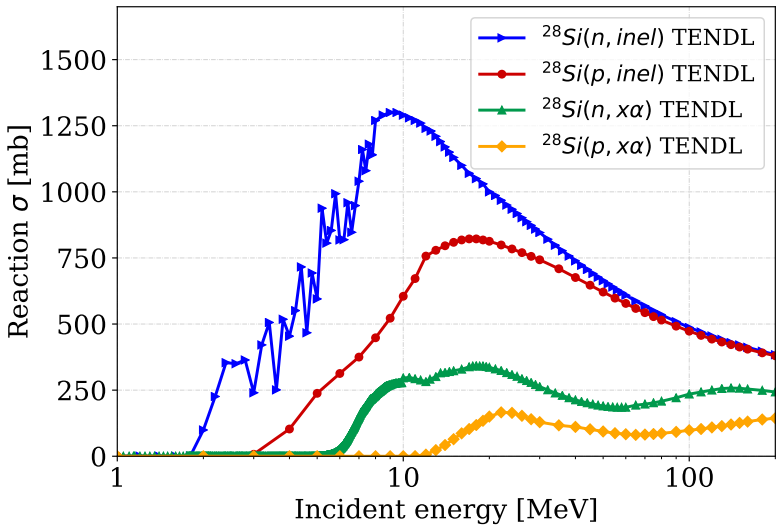

Figure 2.2: Neutron and proton $x\alpha$ cross sections and total inelastic interaction cross sections in ^{28}Si. Data extracted from the TENDL library [4].

2.2 Single Event Effects

A Single Event Effect (SEE) is a stochastic effect provoked by a single ionizing particle hitting the sensitive volume of a powered device. Differently from the TID, SEEs are not cumulative effects and just a single particle can induce an event. SEEs can be either non-destructive, called Soft Errors (SE), or destructive (hard errors) where permanent physical damage is produced, although in some cases the mechanism can be stopped if properly detected and circumvented. Table 2.1 briefly describes the different types of SEEs.

Table 2.1: Soft and hard SEEs notation and description. The SEEs treated in this thesis are highlighted in bold.

	SEE	Notation	Description
Soft Errors	**Single Event Upset**	**SEU**	Single bit flip in a memory cell, it can be restored by rewriting the correct bit information as no physical damage is produced. Error Correcting Code (ECC) algorithms are normally implemented to automatically correct the memory state for a limited amount of SEUs. It is also called Single Bit Upset (SBU) when a single bit flip occur in the same memory word.
	Multiple Cell Upset	**MCU**	Same mechanism as an SEU but with multiple bit flips in different memory cells (that can be located in different words and addresses of the memory).
	Multiple Bit Upset	MBU	Similar to the MCU but the multiple bit flips occur in the same word of the memory.
	Single Event Transient	SET	Voltage or current pulse occurring in a node of combinatorial logic, that can be propagated in digital devices.
	Single Event Functional Interruption	SEFI	Physically like an SEU or MCU but induced in an important register (microprocessor, FPGA), which leads an interruption of the proper operation of the circuit.
Hard Errors	**Single Event Latch-up**	**SEL**	The particle turns on a parasitic transistor, which current can destroy the device whether a protective circuit is not implemented to detect and stop the increase of current.
	Single Event Gate Rupture	SEGR	In power MOSFETs, the rupture of the gate oxide. No protective circuits can prevent this descructive event.
	Single Event Burnout	SEB	In power MOSFETs, the activation of a parasitic BJT which leads an abrupt increase of the current and the subsequent catastrophic failure of the device.

The basic physical phenomena of every SEE is that the incoming particle, or the secondary produced, succeeds in ionizing atoms of the device structure and the released charge is collected, for instance by an inverse-biased PN junction (SEU), or it contributes to activate a parasitic transistor structure (SEL). In general, the charge deposition process can originate from direct (charged particles) and indirect (neutrons) ionization, the latter due to energy deposition from the secondaries produced. In any case, as a result of the interaction of ionizing particles with matter is the generation of free electrons, which eventually induce a SEE

through a certain mechanism.

The SEE cross section (σ_{SEE}) is defined in Eq. 2.3 to quantify the sensitivity of an electronic device to a certain SEE.

$$\sigma_{SEE} = \frac{N_{SEE}}{\Phi} \tag{2.3}$$

Where N_{SEE} is the number of measured SEEs and Φ is the fluence of particles $[cm^{-2}]$ that invest the device. SRAM cross sections are normally indicated in units of $\left[\frac{cm^{-2}}{bit}\right]$ or $\left[\frac{cm^{-2}}{device}\right]$. This is a generic definition to introduce the concept of cross sections and more details are provided in Section 2.3.4.

As will be shown, neutrons are the main radiation source in the accelerator, avionic and ground level environments and therefore they are the major concern regarding reliability in electronics. The thesis focuses on SEU and SEL in SRAM devices, therefore a detailed description of these two effects and related mechanisms of activation are presented in the following.

2.2.1 Single Event Upset (SEU)

A Single Event Upset (SEU) consists of a bit flip of a memory cell, where a logic 1 flips a logic 0 or vice-versa, hence generating data corruption. It is a soft error because the proper operation of the device can be restored with a power cycle or re-writing the memory cell. An Error Correcting Code (ECC) algorithm is typically implemented to automatic restore the corrupted bits when SEUs are in a limited amount. However, SEUs can also be critical (for instance if happening in the configuration memory of an FPGA).

The basic phenomena to trigger an SEU develops in three steps. An impinging charged particle leaves an ionisation track composed of electron-hole pairs (ionization phase) in the silicon substrate (for instance in a reverse-biased p-n junction or around it, as shown in Fig. 2.3a). The volume in which the released charge can be collected by the electric field of the structure is typically called Sensitive Volume (SV) of the device. As anticipated, neutrons interact indirectly through nuclear reactions, with the production of charged particles as a result. However, neutrons can even collide with materials surrounding the p-n junction, such as the chip package, Back End Of Line (BEOL), etc., and the produced secondary ions can reach the SV depending on their range and direction.

The production of electron-hole pairs deforms the depletion region of the junction, and its corresponding electric field is extended downward in the substrate, creating the shape of a funnel (Fig. 2.3b). Owning to the presence of the high electric field, which does not allow the recombination of the generated e-h pairs, and since the collection volume increased due to the funnel, the charged particles are separated producing a drift current immediately collected (a few ps).

As the last process depletes the funnel, the residual e-h pairs in the substrate can move

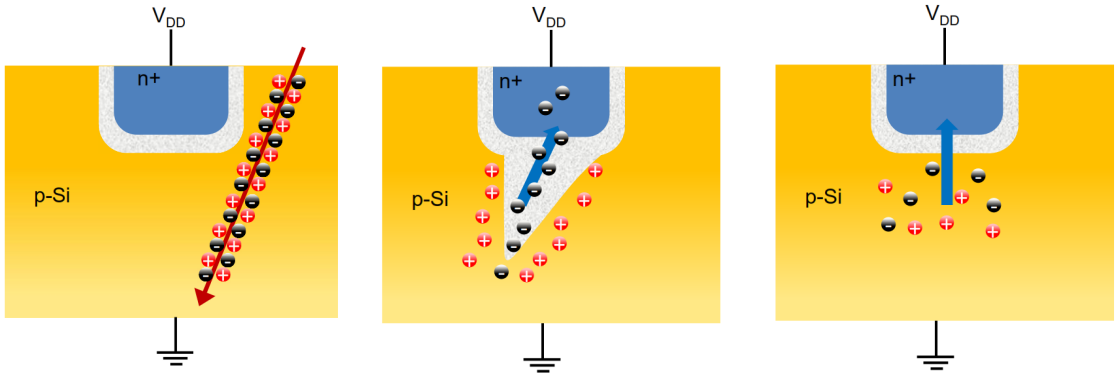

(a) *Onset*. **(b)** *Funnel*. **(c)** *Diffusion*.

Figure 2.3: Three steps SEU mechanism (from [6]).

by diffusion, as the electric field vanished in this area (Fig. 2.3c). This third phase is slower (order of ns): the excess of free charge density moves towards those areas with less concentration, and it is typically not as critical as the drift.

The charge collection mechanism exposed above with related repercussions can be applied for an SRAM. A typical SRAM memory cell is composed of 6 MOSFET (see Fig. 2.4a) of which the two couples in the middle form two CMOS inverters, while M5 and M6 are access transistors. In a first stage, the voltage on the drain of the rightmost MOSFETs (M3 and M4) is positive and indicated with the logic value of "1" in Fig. 2.4b. The M3 n-MOS is explored in its NPN physical structure. In this memory state, M3 is turned off as its gate has applied low voltage, and the bit information of the SRAM is retained in V_Q and V_{NQ}. When a neutron impacts the substrate charged particles are indirectly generated as described above, the electrons produced by the ionization are attracted to the positive voltage on the Q node and the negative charge collected from these electrons tends to pull down its voltage. However, the node capacitance slows down this voltage variation, and the transient can be stopped also because the respective p-MOS inverter starts to restore the lost charge on the node. In this case, when the voltage transient induced by the drift current is below the switching threshold, the cell does not flip (Fig. 2.4c). Otherwise, when the particle generates enough e-h pairs to overcome the critical charge (Qc) required for a bit flip, the cell changes status and this event is called SEU (Fig. 2.4d). The critical charge required to trigger an SEU varies from SRAM to SRAM according to the voltage, technology node, internal structure dimensions, internal materials, etc. This parameter, which is fundamental for SEU simulations, is not trivial to retrieve and has a general trend to decrease with technology scaling [7]. In particular, the higher the voltage applied to the SRAM, the higher the required critical charge, and consequently the SEU cross section decreases for a given memory. Noteworthy that the SEU cross section in general decreases for more integrated technologies because the sensitive area is smaller.

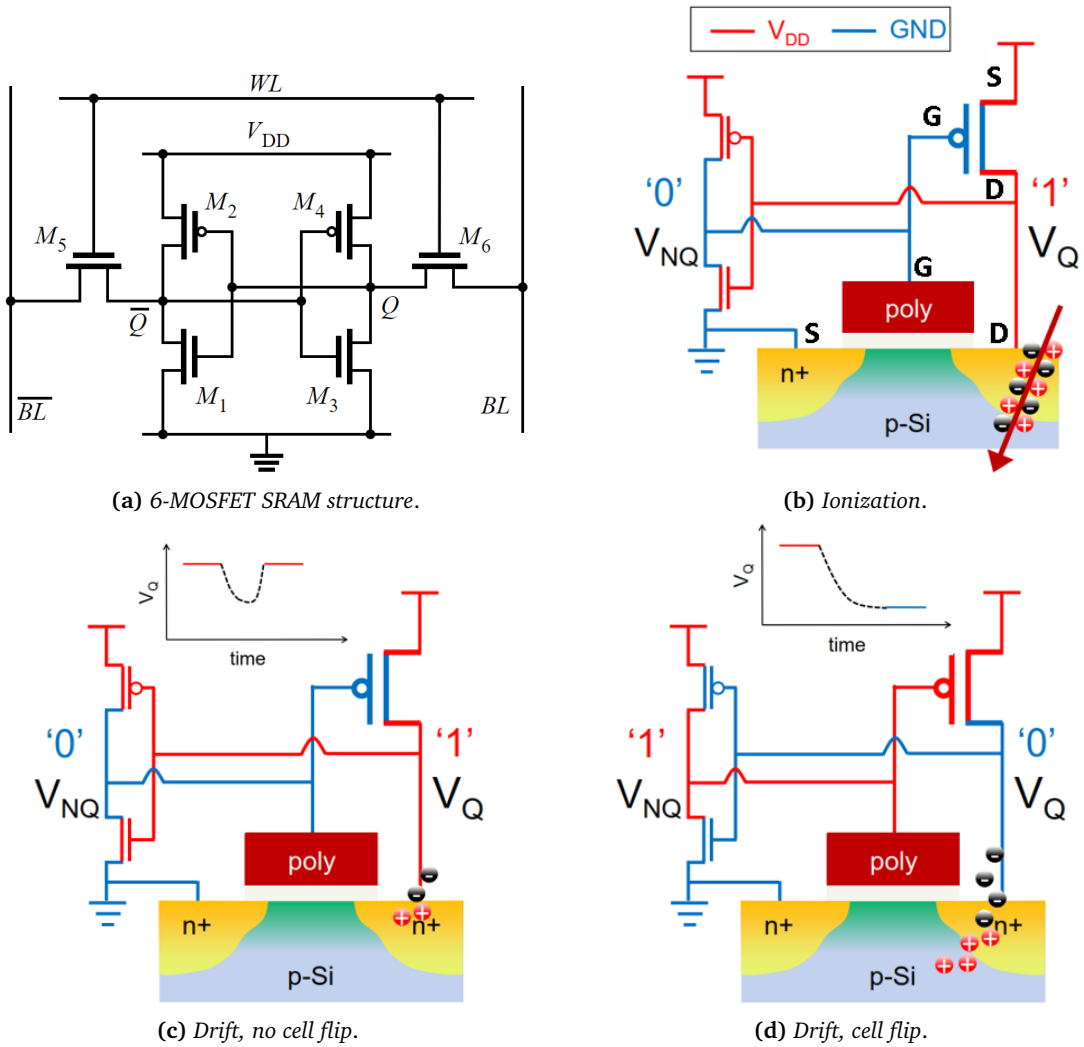

(a) *6-MOSFET SRAM structure.*

(b) *Ionization.*

(c) *Drift, no cell flip.*

(d) *Drift, cell flip.*

Figure 2.4: SEU mechanism on a 6 MOSFETs SRAM (from [6]).

2.2.2 Single Event Latch-up (SEL)

As opposed to SEUs, a Single Event Latch-up (SEL) is not a soft error but rather a potentially destructive event, owing to the activation of two parasitic bipolar transistors in the MOSFET substrate. In the event that the current, passing through these parasitic structures, is not detected and stopped in a short time by a control circuit, the component can be permanently damaged. The SEL mechanism is depicted in Fig. 2.5 that represents a CMOS inverter as that constituted by M1 and M2 in Fig. 2.4a. For instance, considering the PMOS structure (equivalent consideration are valid for the NMOS), an ionizing particle passing through the N-well deposits a quantity of electric charge, in a similar way as it happens for an SEU. The consequent current flows through the well, which can be modelled as a resistor R_W (see Fig. 2.5b), and when the voltage drop on this resistor satisfies $V_{EB} > 0.7$ V the parasitic PNP transistor Q1, formed by the P-source, N-well and P-substrate, can turn on (see Fig. 2.5a). Consequently, the current supplied by Q1 produces a potential drop on the substrate resistance R_S

and likewise it can activate the transistor Q2. The current passing through R_W increases as it is required by Q2, hence Q1 is switched-on more and more, in a loop that leads catastrophic damage due to the high current.

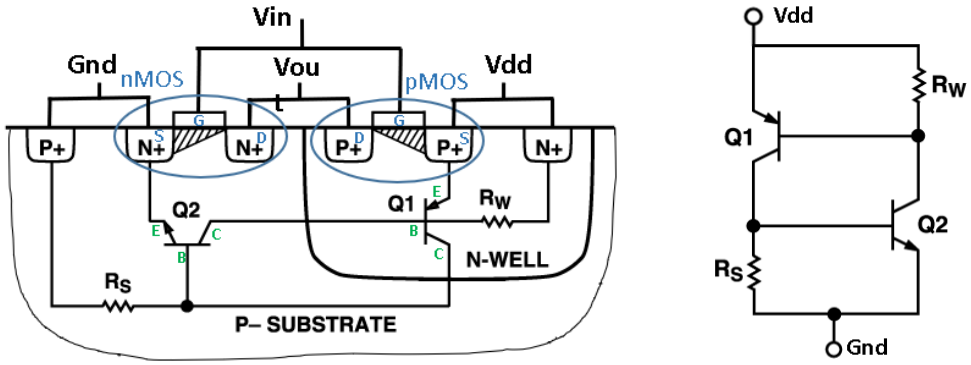

(a) *Inverter structure*. **(b)** *Parasitic transistor*.

Figure 2.5: Single Event Latch-up principle.

The SEL cross section (differently from that of SEU) increases when the applied voltage is higher, because the electric fields are larger and the required voltage to turn on the parasitic transistors can be provided with less deposited charge.

2.3 SEE Response Function

The SEE qualification approach for components to be used in the complex high-energy accelerator environment is based on the characterization of mainly two individual cross sections: high energy protons at 200 MeV or equivalent energies (σ_{HEH}) and thermal neutrons (σ_{thN}) [8], [9]. Based on these values, for reasons explained hereafter, the SEE response as a function of energy is assumed to be a step function from 20 MeV for charged hadrons, a Weibull-like response for intermediate energy neutrons (0.2-20 MeV) and a function decreasing as $E^{-1/2}$ for thermal neutrons, as expected for processes dominated by neutron capture. The detailed definition, assumptions, and explanation of the three terms are presented in the following sub-sections. The response introduced above is schematically shown in Fig. 2.6, where 200 MeV is considered to be an energy well representative of the energy-saturated SEE cross section. The response can then be folded with the spectra of interest (LHC, avionics, etc.), yielding the expected operational SEE rate. More details concerning this approach can be found in [10], [11].

Furthermore, neutron and proton SEU cross sections above 50 MeV are considered to be the same in the JEDEC standard [12], and even above 30 MeV in [13]. For this reason, proton data are used in substitution of neutron cross sections above 20 MeV, because as will be explained in Chapter 5, monoenergetic neutron beams above this energy are typically not employed.

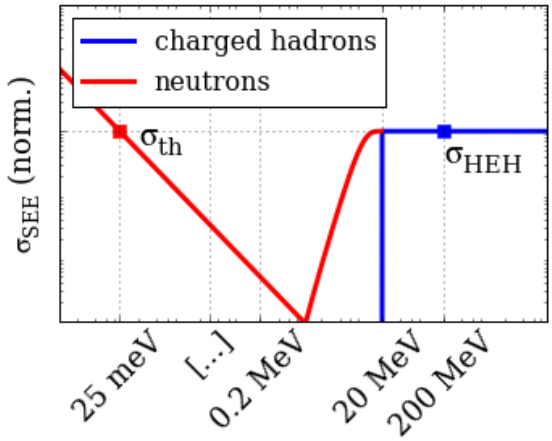

Figure 2.6: Typical SEE cross section response as a function of the energy, with the thermal neutron and high energy hadron cross sections, the latter typically referred to protons (see Section 2.3.1).

2.3.1 High-Energy Hadrons (HEH)

Hadrons are subatomic particles composed of quarks and anti-quarks and according to their composition they can form protons, neutrons, pions or kaons. This class of particles with energy above 20 MeV is hereafter referred to as High Energy Hadrons (HEH). The definition is based on the fact that electronics in the LHC are subjected to a mixed-field radiation environment composed, among others, of these particles. Ions are not considered in the definition because they are not produced. Hadrons above 20 MeV are considered equally effective in inducing SEUs because of their similar inelastic cross sections in silicon [10], [14], and this fact is proved regarding neutrons and protons and assumed for pions and kaons. Hence, SRAM memories are assumed to be equally sensitive to HEH, namely, a flat cross section is assumed above 20 MeV [10] (cross section in saturation), as shown in Fig. 2.6. Moreover, HEH induce SEEs mainly through inelastic nuclear interactions with matter.

Charged hadrons (protons, pions, kaons) below 20 MeV can still ionize atoms, as the Coulomb barrier for nuclear reactions is around a few MeV (for instance, regarding protons see Section 2.1). However, since proton ranges at these energies are limited, they will either not pass through the package or they will reach the sensitive volume with an energy below the SEE threshold for indirect ionization [10]. Indeed, protons with energies greater than 10 MeV are not able to directly ionize atoms, as their stopping power is little. Furthermore, the proton SEU cross section of integrated devices (nm scale) shows an increase up to a factor of 3 passing from 10 to about 2 MeV, typical characteristic of the proton direct ionization. This behaviour indicates the transition from nuclear reactions, where the cross section is consistent with that from spallation facilities, to direct ionization, where the cross section has order of magnitude of the physical technology of the cell in [cm^2/bit] [15]. In addition, protons around 1 MeV can still induce SEEs through direct ionization in devices with low Qc (<1 fC), although they can be neglected in most of the cases for what regards accelerator applications [16]. Hence, below the threshold of 20 MeV the SEU contribution due to charged hadrons, compared to hadrons with greater energies, can be neglected as far as accelerator applications are concerned.

The integrated differential flux of hadrons above 20 MeV is defined in Eq. 2.4 as the HEH flux, and measured in units of $\left[\frac{particles}{cm^2 \cdot s}\right]$.

$$\varphi_{HEH} = \int_{20MeV}^{\infty} \sum_{i=1}^{3} \frac{d\varphi_i(E)}{dE}\, dE = \int_{20MeV}^{\infty} \frac{d\varphi_{HEH}(E)}{dE}\, dE \tag{2.4}$$

Where i is one of the three hadrons normally considered in the LHC: neutrons, protons and pions. The respective fluence $\left[\frac{particles}{cm^2}\right]$ is obtained in Eq. 2.5 integrating the flux over the time.

$$\Phi_{HEH} = \int_{t_0}^{t_1} \varphi_{HEH}\, dt \tag{2.5}$$

It has to be noted that since the flux is typically not constant over the time, in both test facilities and accelerators, it can be found normalized by bunch of particles $\left[\frac{particles}{cm^2 \cdot spill}\right]$, primary particles $\left[\frac{particles}{cm^2 \cdot pp}\right]$ or calculated as average flux from the fluence.

2.3.2 Intermediate energy neutrons (HEHeq)

Neutrons below 20 MeV can still induce a significant amount of upsets, and hence they are taken into account. For these intermediate energies, the SEU cross section is strongly energy-dependent and is determined experimentally in monoenergetic neutron facilities [11]. Therefore, in addition to the aforementioned HEH flux, intermediate energy neutrons, defined between a threshold energy E_{th} and 20 MeV, must be taken into account, weighting their differential flux with the Weibull function of a reference SRAM memory [10], [11]. This response function, to characterize the SEU sensitivity of electronics, is described through the HEH equivalent (HEHeq) flux and reported in Eq. 2.6.

$$\varphi_{HEHeq} = \int_{E_{th}}^{20MeV} w(E) \cdot \frac{d\varphi_n(E)}{dE}\, dE + \int_{20MeV}^{\infty} \frac{d\varphi_{HEH}(E)}{dE}\, dE \tag{2.6}$$

Here, $w(E)$ is the Weibull response to intermediate energy neutrons from E_{th} to 20 MeV, $\frac{d\varphi_n(E)}{dE}$ and $\frac{d\varphi_{HEH}(E)}{dE}$ are the neutron and HEH differential fluxes, respectively.

The generic Weibull function is expressed in Eq. 2.7, where E_{th} is the aforementioned threshold energy below which the SEU cross section is considered to be zero, and S (shape) and W (width) are two fit parameters.

$$w(E) = 1 - e^{-\left(\frac{E-E_{th}}{W}\right)^S} \tag{2.7}$$

The threshold energy (E_{th}) was originally set to 0.2 MeV, to consider the lowest onset energy of (n, α) inelastic interactions in materials typically found in microelectronics. This threshold corresponds to that of nitrogen, according to the $^{14}N(n,\alpha)^{11}B$ reaction, which can be used as a dopant and in insulation layers [10]. However, as will be shown in this work,

also elastic processes can deposit enough energy in sub-micron technologies to trigger SEUs, for energies even below 0.2 MeV. In the following, low energy neutrons are defined as those neutrons below the lowest threshold energy for inelastic interactions that produce charged particles in ^{28}Si, which is 2.75 MeV for (n, α) reactions. Hence, low energy neutrons are defined as part of the intermediate energy neutrons extended to lower energies but excluding the contribution of thermal neutrons. It is to be noted that the physical spectra in the LHC are composed of both HEH and intermediate energy neutron contributions, and Φ_{HEHeq} aims to describe it as well as possible. The respective HEH equivalent fluence [cm^{-2}] is shown in Eq. 2.8.

$$\Phi_{HEHeq} = \int_{t_0}^{t_1} \varphi_{HEHeq}\, dt \tag{2.8}$$

Multiplying the Weibull function of the memory by its cross section in saturation, the SEU cross section as a function of the energy can be calculated in Eq. 2.9.

$$\sigma(E) = \sigma_{sat} \cdot (1 - e^{-\left(\frac{E-E_{th}}{W}\right)^S}) = \sigma_{sat} \cdot w(E) \tag{2.9}$$

The choice of using a Weibull to fit experimental data was initially adopted for heavy ion cross sections, and later extended to protons [17]. Although different functions could be used to fit proton and neutron data, the JEDEC standard [12] suggests using a Weibull function even for neutron cross sections. Therefore, Weibull functions are employed in this work for both protons and neutrons.

The Weibull function used for the HEHeq flux calculation in Eq. 2.6 considers a 4 Mbit Toshiba TC554001AF (400 nm) bulk SRAM memory as reference response [10], whose parameters are reported in Table 2.2 (the Toshiba response is also implemented in FLUKA for the HEHeq calculation). The HEHeq flux is therefore based on the Toshiba memory, which originally was the only studied memory to be significantly sensitive to intermediate energy neutrons [18], namely the curve decreasing (see Fig. 2.6) compared to a 90 nm Cypress CY62157EV30LL-45ZSXI was the most shifted to lower energies. However, one of the implications emerging from this thesis will be that the Toshiba response is not anymore the worst-case for sub-micron technologies.

Table 2.2: Weibull fit parameters for the Toshiba memory so far used for the intermediate energy neutron response and implemented in FLUKA for the HEHeq calculation.

Memory	E_{th} [MeV]	W [MeV]	S
Toshiba	0.2	9.25	3.02

Intermediate energy neutrons are not considered for the SEL response, because the produced secondaries have a low range compared to that of HEH. The collection volume of an SEL is much larger than that of an SEU, therefore secondary fragments from neutrons below 20 MeV will typically not deposit enough energy to trigger an SEL.

2.3.3 Thermal neutrons

Thermal neutrons (denoted as ThN in some cases in the following) compose the radiation background typically present in accelerator, terrestrial and even avionic environments. In addition, medical applications for radiotherapy are another consistent source of thermal neutrons, where its flux can be millions of times higher than that of the natural background [19].

Thermal neutrons are absorbed by the ^{10}B isotope inducing a nuclear reaction (sometimes referred to as fission), with the ejection of an alpha particle, a ^{7}Li ion and gamma radiation, according to the $^{10}B(n,\alpha)^{7}Li$ reaction depicted in Fig. 2.7 from [20]. During the reaction,

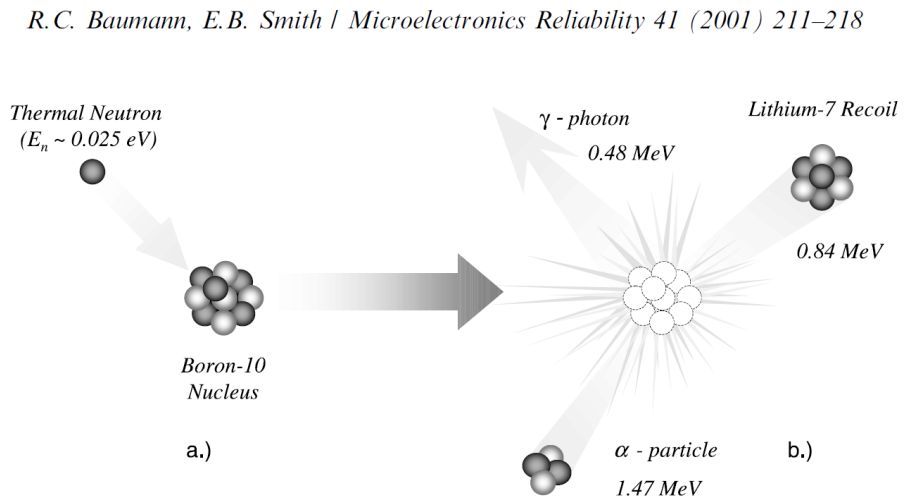

Figure 2.7: a) Nuclear reaction of ^{10}B with a thermal neutron, b) reaction products: photon, ^{7}Li ion and the α particle, potential treat for inducing SEUs.

alpha and ^{7}Li are emitted in opposite directions to conserve the momentum, and both are capable of ionizing silicon atoms, the charge is collected in the SV and the SEU can be triggered. Therefore, the thermal neutron sensitivity of electronics is due to a physical interaction with ^{10}B, which depends on the boron amount and location inside the device, as well as on its critical charge.

The alpha particle is ejected with energy of 1.47 MeV, while the lithium nucleus with either 0.849 MeV (94% of the times) or 1.014 MeV (6% of the times). The respective ranges in silicon are of about 5 µm for alpha particles and 2.5 µm for lithium ions [21]. The deposited charge as a function of the penetration depth for both ions is essentially the same up to 1 µm [22]. The gamma photon is emitted with 478 keV, and has a negligible probability of inducing charge.

It is worth noting that high energy neutrons are much less efficient in inducing boron capture and fission, because the boron capture cross section shows very large values (~3838 barns [20]) around the thermal region of 25 meV, and decreases as $E^{-1/2}$ with increasing energy (see Fig. 2.6).

Boron is formed of two isotopes: ^{10}B (19.9% of natural abundance) which is unstable when exposed to thermal neutrons, and ^{11}B (80.1%) that also reacts with thermals but pro-

ducing gamma radiation and not alpha particles, as most of isotopes do after absorbing a thermal neutron. Boron has been used as p-type dopant in silicon and in the past for the formation of dielectric layers of BoroPhosphoSilicate Glass (BPSG), where boron was added to PSG to reduce its reflow temperature and stress. Fission events in the substrate have a higher probability of inducing SEUs since the generated charge could be collected in the SV, whereas events in the BPSG generate charge partially lost, as the alpha and lithium range is <5 μm [20]. Since ThN were the main source of SEUs in the 1990s [19], the presence of ^{10}B has been avoided in recent technologies with the removal of BPSG (for instance it can be replaced by a Chemical Mechanical Polishing (CMP) process [23]). However, it is still present inside electronic devices as p-doping (boron implantation is not selective on the ^{10}B and ^{11}B isotopes), and near the Back End Of Line (BEOL) structure as coating of the tungsten plugs connecting the drain to the copper layers [19, 23, 24]. These atoms of ^{10}B originate from the B_2H_6 etcher gas used to improve the adhesion of tungsten in the trench contacts [22, 25].

The thermal neutron equivalent flux is defined from [26] in Eq. 2.10 as the product of the differential neutron flux and a weighting function, which decreases as the inverse square root of the energy (this leads the first decreasing curve of Fig. 2.6). As it can be inferred, this definition not only includes neutrons at thermal energies of 25 meV, but rather a wider spectrum, in a similar way as for the HEHeq definition.

$$\varphi_{ThN} = \int_0^{\infty} w_{ThN}(E) \cdot \frac{d\varphi_n(E)}{dE}\, dE = \int_0^{\infty} \sqrt{\frac{0.025eV}{E[eV]}} \cdot \frac{d\varphi_n(E)}{dE}\, dE \tag{2.10}$$

2.3.4 SEU cross sections

The SEU cross section of a device varies as a function of the particle energy and particle types. The number of measured events N_{SEU}, expressed in Eq. 2.11, is defined as the integrals of the product of the SEU cross sections $\sigma_i(E)$ by the differential fluences of interest $\frac{d\Phi_i(E)}{dE}$ (which are the integral over time of the differential fluxes of hadrons).

$$N_{SEU} = \sum_{i=1}^{M} \int_0^{+\infty} \sigma_i(E) \cdot \frac{d\Phi_i(E)}{dE}\, dE \tag{2.11}$$

Where i denotes the particle type of interest. However, the quantities that are typically measured are the ThN and HEH cross sections. Therefore, the energy-dependent cross section

of formula 2.11 is decomposed as a function of constant cross sections in Eq. 2.12.

$$\begin{aligned} N_{SEU} &= \sum_{i=1}^{M} \int_0^{+\infty} \sigma_i(E) \cdot \frac{d\Phi_i(E)}{dE}\, dE \\ &= \int_0^{+\infty} \sigma_{ThN}(E) \cdot \frac{d\Phi_{ThN}(E)}{dE}\, dE + \int_0^{+\infty} \sigma_{HEH}(E) \cdot \frac{d\Phi_{HEHeq}(E)}{dE}\, dE \\ &= \sigma_{ThN} \int_0^{+\infty} w_{ThN}(E) \cdot \frac{d\Phi_{ThN}(E)}{dE}\, dE + \sigma_{HEH} \int_0^{+\infty} w_{HEH}(E) \cdot \frac{d\Phi_{HEHeq}(E)}{dE}\, dE \\ &= \sigma_{ThN} \cdot \Phi_{ThN} + \sigma_{HEH} \cdot \Phi_{HEHeq} \end{aligned} \tag{2.12}$$

The energy dependence information of the cross sections is enclosed in the weighting functions $w_{ThN}(E)$ and $w_{HEH}(E)$. The former is the same used in the thermal neutron flux definition in 2.3.3 where it assumes the value 1 at 25 meV, while the latter term $w_{HEH}(E)$ is 1 above 20 MeV and formed by the Weibull function $w(E)$ below this energy, as graphically represented in Fig. 2.6. Hence, the expected upset rate can be expressed with constant terms, where σ_{ThN} and σ_{HEH} are the ThN and HEH SEU cross sections, respectively.

2.4 R-Factor

The R-factor is in general defined as the ratio between the thermal neutron and HEH fluences for a given environment. It is a dimensionless quantity that expresses the number of thermal neutrons relative to the HEH, which are present in a specific area subject to the analysis. All LHC locations are defined through R-factors, in order to assess whether electronics can operate in that specific radiation environment. The R-factor can refer either to fluences measured in the studied location, or fluences calculated through simulations.

The previous R-factor definition is more a theoretical quantity, because the mixed-field in the accelerator is also composed of the intermediate energy neutrons. Therefore, The R-factor definition is better expressed in Eq. 2.13 as the ratio between ThN and HEHeq fluences that are measured through the Radiation Monitor (RadMon) system.

$$R_{eq} = \frac{\Phi_{ThN}}{\Phi_{HEHeq}} \tag{2.13}$$

2.5 LHC Radiation Monitor (RadMon)

Radiation levels in the tunnel and shielded areas are monitored through the RadMon v6 system [27], which is fully developed at CERN. The RadMon is an independent system to measure the HEHeq and thermal neutron fluences, as detailed in [9] and about 400 devices are installed in the LHC to constantly monitor the radiation levels. It is based on two embedded COTS SRAMs, which are differently sensitive to HEHeq and ThN: a 4x8 Mbit Cypress CY62157EV30LL-45ZSXI (90 nm) and a 4x4 Mbit Toshiba TC554001AF (400 nm). The Cypress memory is mostly sensitive to HEH, while the Toshiba memory to ThN fluxes (to note that the Toshiba reference is the same used for the HEHeq calculation in Section 4.2). HEHeq and ThN fluences [cm^{-2}] are retrieved by solving the system of equations in 2.14 (expressions from Eq. 2.12).

$$\begin{cases} N_{SEU1} = \sigma_{HEH1} \cdot \Phi_{HEHeq} + \sigma_{ThN} \cdot \Phi_{ThN} \\ N_{SEU2} = \sigma_{HEH2} \cdot \Phi_{HEHeq} + \sigma_{ThN} \cdot \Phi_{ThN} \end{cases} \tag{2.14}$$

Where N_{SEU1} and N_{SEU2} are the measured upsets from Cypress and Toshiba, respectively. Upsets number and cross sections are the known terms while the fluences are unknowns. The HEHeq fluences are memory dependent, however, the system provides an accurate measurement because these memories are not particularity sensitive to intermediate energy neutrons so that most of the fluence is due to HEH (>20 MeV). Hence, the two HEHeq fluences can be considered to be the same and the system of equations can be solved.

RadMon cross sections at varying voltage

In LHC areas with high levels of radiations, the RadMon Toshiba memories are powered to 5 V, the highest voltage, in order to minimise the sensitivity to SEUs. While the HEH cross section increases linearly at decreasing voltage, the thermal neutron cross section shows an exponential increase, rather than linear [28]. As seen in Section 2.3.3, the energy deposition because of thermal neutrons is due to alpha and ^{7}Li ions produced in the ^{10}B reaction. When the device is powered at 5 V, the critical charge required to trigger an SEU is higher than that necessary at 3 V, hence the charge released by the ions can trigger more upsets with the lowest voltage.

2.6 Approach to Study SEEs Through Simulations

SEEs are extensively studied through simulations, with the aim of understanding the physical processes and interactions that yield to trigger the events that are measured experimentally. The general approach to study what happens inside a semiconductor and surrounding layers, three elements need to be known:

1) Particle spectrum of the radiation environment of interest. As will be outlined in the following, the LHC is characterized by very broad particle spectra, ranging from thermal up to several GeV of energy and particle species, depending on the location (tunnel, alcoves). Similarly, the atmospheric and ground level neutron spectra are the most widely studied in literature, because of avionic telecommunication and automotive applications. It is not known with good accuracy and it varies with position and altitude, with energies from thermal up to a few GeV. Other important radiation environments are those found in space, medical, and fusion applications. In the following chapters, some connections between one and the other environment with RHA implications are presented, as results valid for the accelerator can also be applied elsewhere.

2) Secondary ions generated from the neutron-matter interaction, their energy, LET, and range. In general, light ions receive higher energy from the incident neutron and therefore they have a higher range, but typically lower LET. Whereas heavy ions are emitted with energy close to the Bragg peak, lighter ions have to travel before reaching the peak, therefore light ions will not generate a lot of critical charge nearby the production point [29]. GEANT4, FLUKA, MCNP and PHITS are the software typically employed to derive all secondary products of interaction. The entire Chapter 4 is dedicated to the inelastic interactions n-Si, which are the most effective for inducing SEEs above about 10 MeV. At lower energies, elastic reactions become also an important SEU contribution and they are studied in Section 7.3.2.

3) How secondary ions interact with matter and trigger SEEs. The approach consists to calculate the charge deposited by the particle and then collected inside the SV of the component. When the critical charge overcomes a certain threshold a SEE is triggered; the study is carried out calculating LET and ion range to assess if the ion track crosses the SV and deposits enough charge. Indeed, in micron technologies, the charge is not locally deposited at the generation point [29], but range and LET must be carefully evaluated. In this work, the deposited energy was calculated through FLUKA, a Monte Carlo tool developed at CERN used to study the particle-matter interactions [30–33]. In addition, the G4SEE tool, also developed at CERN and based on the GEANT4 toolkit, was employed for simulations of neutrons below 20 MeV.

2.7 LHC Layout

A brief introduction regarding the LHC layout is described in this section (with some information taken from [34]), showing some photographs of relevant locations taken during LS2 in spring 2019, as these areas are the subject of the SEE analysis. Based on the radiation environment, the LHC can be subdivided into two main categories: tunnel and shielded alcoves. The LHC tunnel is composed of arcs, Insertion Regions (IR) also called Long Straight Sections (LSS), and the Dispersion Suppressor (DS) connecting the first two parts. The whole LHC ring is depicted in Fig. 2.8b with its layout divided in 8 octants, each one composed of

the repetition of the tunnel parts expressed above, as illustrated in Fig. 2.9. Each octant has a specific function (RF cavities, beam cleaning, etc.) and four of them host an Interaction Point (IP), also called experiment, where the two beams travelling in opposite directions are made to collide. For brevity, the IPs are also called "Points" and numbered: ATLAS (P1), CMS (P5), ALICE (P2) and LHCb (P8).

There is a total of 8 arcs, each one composed of 42 half-cells which are periodic parts of 3 series of dipole magnets followed by one quadrupole. Fig. 2.8a shows a dipole magnet in the arc of octant 5, below which a quench protection system is directly installed. Arcs are consecutively numbered and those of interest in this study are the half-cells of the DS from 8 to 13 included, and the arcs from 14 to 34. Moving from the arc towards the IP, the DS, which prepares the beam to the LSS to avoid dispersion, is composed of four quadrupole magnets each one separated by 2 dipoles. The LSS prepares the beam for the collision and a photograph can be seen in Fig. 2.10.

(a) *Quench protection systems directly installed below the dipoles in the arc of the LHC tunnel.*

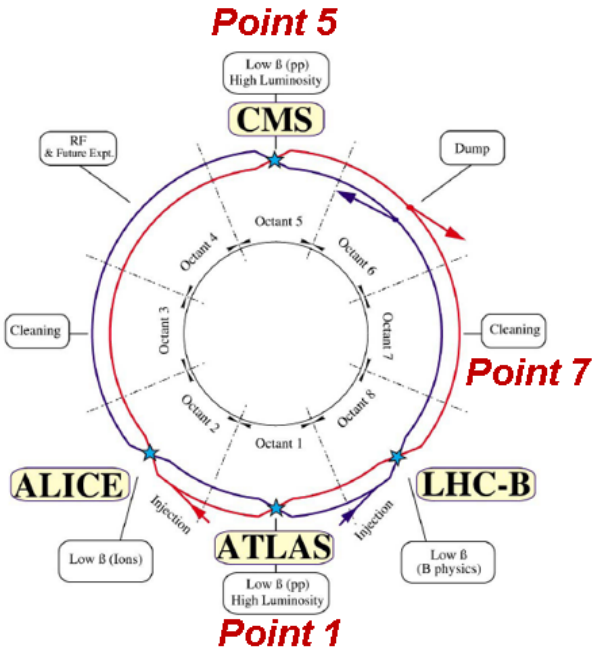

(b) *LHC layout.*

Figure 2.8: Photograph of the LHC tunnel near CMS (left), and LHC layout (right).

Shielded alcoves are located parallel to the tunnel, next to the IPs (see Fig. 2.9) and are normally symmetric with respect to it. They can be heavily shielded such as the UJs (junction), with 200 cm of cast iron/concrete, located at only 50 m from the IP. A picture of UJ14, just before the ATLAS experiment is represented in Fig. 2.11a, showing a variety of machine components in the tunnel (to the left) and the thick concrete shielding to protect the electronics in the alcove (to the right). For instance, the symmetric heavily shielded alcove to UJ14 is UJ16. Another alcove is the UL (liaison) that connects UJ to the service tunnel for the access. Other alcoves are lightly shielded, such as the RRs, with 40 cm of cast iron/concrete as can be seen in Fig. 2.11b. Although they are further away from the IPs, at about 250 m,

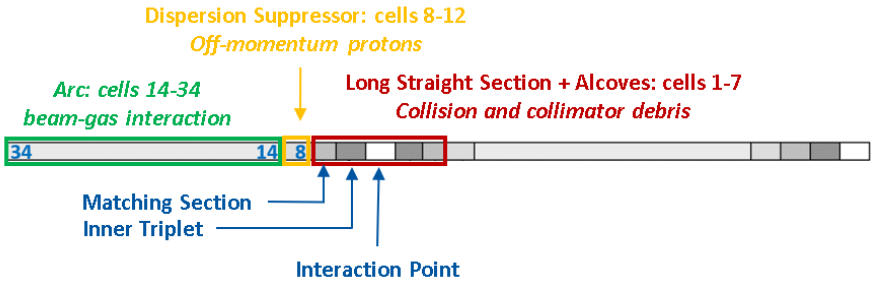

Figure 2.9: LHC layout of one octant, with the Long Straight Section (LSS), Dispersion Suppressor (DS) from half-cell 8-13, and the arc from half cells 14-34.

Figure 2.10: Photograph of the Long Straight Section (LSS) before the CMS experiment in 2019.

(a) *UJ14 alcove.* **(b)** *RR53 alcove.*

Figure 2.11: Photograph of the UJ14 (left) and RR53 (right) alcoves in 2019. The tunnel to the left of UJ14 just before the ATLAS experiment and the highly shielded alcove on its right. Similarly for the RR53 that is formed of 2 levels, one at the same level of the tunnel (lev0) and the other one above it (lev1). To notice the difference on the wall thickness between highly and lightly shielded alcove.

they can be close to collimators, one of the main source of radiation.

Both highly and lightly shielded alcoves can be found built in two levels, one at the same

height of the tunnel and the other alcove one floor above. In the RRs the upper level is above level 0 and the tunnel (like RR53 in Fig. 2.11b), while in the UJ the top level is just above level 0. Electronics are typically installed on both levels.

2.8 Summary

The main quantities used to describe radiation effects in electronics and used throughout the thesis are defined in this chapter, focusing on the accelerator context. After a brief introduction about LET, stopping powers and range, some differences between neutron and proton nuclear cross sections, that justifies the definition of the HEH fluence, are explained through the Coulomb barrier. An overview regarding SEEs in electronics was presented explaining the physical mechanisms for SEU and SEL, which are the topic of the thesis.

The approach to describe the SEE response function of components, that need to operate in the mixed-field radiation environment found in the LHC, was presented showing the three principal quantities concurring to the SEE cross section. To this regard, HEH, intermediate energy neutron, HEHeq and thermal neutron fluences were defined as they are the subject of study of the thesis.

In addition, the RadMon system used to measure the HEHeq and thermal neutron fluences along the LHC is presented. The typical methodology to study SEEs through simulations, in order to understand the physical processes that yield to trigger the events, was exposed. Finally, a brief introduction regarding the LHC layout was described, as the tunnel and shielded alcoves will be the subject of the SEE analysis as far as the accelerator is concerned.

Chapter 3

Sources of Ionizing Radiation and Operational Environments

Every place in our world, and more in general in the universe, is characterized by a radiation environment. Whatever it is considered, from our own house, the inside of an aeroplane, a beach at sea level, to more specific applications such as the LHC at CERN, medical equipment for radiotherapy [35] or telecommunication satellites, is characterized by a set of particle spectra. Every environment can be composed of several species of particles, with different intensity fluxes and energies. As will be detailed, these particles interact with electronic devices, nowadays used for everyday application, leading to ionization of the matter and the consequent production of electron-hole pairs. As a final effect of this generated current, soft and destructive errors can be induced in electronics, therefore compromising the working operations of devices. This work will mainly focus on accelerator, ground level and avionic applications, as neutrons are the primary threats for electronics in these environments. Moreover, other environments are characterized by neutrons, such as the nuclear fission and fusion reactors, planetary surfaces as mars and the moon [36]. With the aim of describing these problems, a preliminary overview regarding the ionizing radiation sources is described in the following.

3.1 Radioactive Decays

In radioactive decays, atoms lose energy by emitting alpha, beta, and gamma radiation. Among them, alpha particles, which are formed of two protons and two neutrons, usually possess high energy. In silicon, they are characterized by short range and high LET, so that they can release all the energy in a very small volume of material and ionize its atoms. Once the alpha particle releases its energy, it acquires two free electrons becoming a stable helium atom. For this reason, the alpha particle is commonly represented as "^4He" or called "He ion" neglecting other He isotopes which are less abundant. The presence of impurities inside the materials of electronic components may be an important source of alpha particles. For

instance, uranium and thorium atoms emit alpha particles in the range of 4-10 MeV [20]. Furthermore, ^{210}Pb and ^{210}Po, which are present inside the lead-based solder used in some flip-chip packages, are sources of alpha particles, and since the solder bumps are very close to the sensitive area of the chip it may receive high quantities of alpha particles. In addition, gold used for bonding wires, ceramic packages and interconnect metallization can also be sources of alpha decays [20].

3.2 LHC Radiation Environment

The radiation levels in the accelerator mainly depend on the beam energy, intensity and luminosity. After energy, luminosity (L) is the most important parameter of a collider, expressed through Eq. 3.1.

$$\frac{dN_{event}}{dt} = L \cdot \sigma_{event} \tag{3.1}$$

As the probability of an event σ_{event} is physical, to observe more events in a fraction of time, only the luminosity can be increased. More luminosity implies more collisions, but the luminosity is a measure of how many particles are squeezed in a given space and time. Not all these particles will collide, but the more the luminosity the more likely they are to collide. Luminosity is measured in unit of fb^{-1}/s, where 1 fb corresponds to roughly 10^{14} proton-proton collisions at TeV of energy [34]. It is typically integrated over time (for example 1 year) yielding the integrated luminosity.

The present data analysis of the LHC radiation environment refers to the current machine operating at about 50 fb^{-1}/year [34]. With the High-Luminosity LHC (HL-LHC) upgrade, the nominal annual integrated luminosity will be of 250 fb^{-1}/year and the radiation levels are expected to, in first approximation, scale linearly. The enormous amounts of electronic Commercial Off The Shelf (COTS) components used inside the LHC accelerator are primarily installed either inside shielded alcoves or, when the cabling length is an issue (e.g. high-speed communication, high current powering), directly in the tunnel. They are all subjected to radiation levels that can vary by a considerable amount for each location in terms of fluence and particle types.

The LHC presents three main sources of radiation:

1) Collision debris (or luminosity debris) from interaction points. During the collisions in the experiments, an enormous quantity of particles is generated, with an average multiplicity of 120 particles every single proton-proton collision [34]. In ATLAS, for instance, about 40 millions of collisions occur every second. Most of these particles are stopped in the detector layers of the experiments, but a fraction of radiation travels in the tunnel and surrounding areas.

2) Beam interaction with collimators. Collimators are special machine elements that clean the beam by removing the halo protons around the main bunch. Indeed, protons travelling inside the pipe are only a few cm apart from the superconducting magnets, hence

to avoid losses and to reduce the possibility of magnet quenching the beam must be collimated. Collimators are formed of a metallic jaw, which is put close to the beam to absorb the energy of protons in the beam halo. However, this interaction generates high quantities of secondary particles. Two of the eight insertion regions contain primary and secondary collimators, IR3 for momentum and IR7 for betatron cleaning [10] (see Fig. 2.8b), they are among the most radioactive locations in the LHC.

3) Beam interaction with residual gas inside the vacuum pipe. Although the vacuum levels inside the pipes where protons are travelling is in the order of 10^{-10}-10^{-12} mbar, protons still collide with the remaining gas molecules. The interaction generates hadronic and electromagnetic showers of secondaries, in a similar way as cosmic rays interact with the atmosphere (see illustration in Fig. 3.4).

As seen in section 2.5, radiation levels in the tunnel and shielded areas are monitored through the RadMon v6 system, and characterised through the R-factor (ratio between HEHeq and ThN). The following analysis is performed with data measurements from the tunnel and shielded alcoves, which as will be shown are characterized by different radiation environments.

3.2.1 Radiation levels in the LHC tunnel

RadMons in the tunnel are normally installed below the interconnections between dipoles and quadrupoles or near critical electronic devices, at a height of 70 cm below the beam. The arcs and DS near point 1 (P1, ATLAS) and point 5 (P5, CMS) have been analyzed with data from a total of 34 RadMons of which 11 are in the arcs and 23 in the DS. These data correspond to the 2018 proton operation and are presented in Table 3.1, subdividing the R-factors into 3 categories: measured annual fluence greater than 10^9 HEHeq/cm^2, between 10^8 and 10^9 HEHeq/cm^2 and lower than 10^8 HEHeq/cm^2. The useful information is the average,

Table 3.1: RADMON v6 HEHeq measurements and R-factors along the tunnel near point 1 and 5 subdivided in three yearly fluence intervals.

	Φ_{HEHeq} [HEHeq/cm^2/year]			R-factor		
area	Interval	average	max	average	min	max
DS	$>10^9$	$5.2 \cdot 10^{10}$	$1.7 \cdot 10^{11}$	3.5	0.7	7.6
ARC	10^8 -10^9	$1.6 \cdot 10^8$	$5.2 \cdot 10^8$	2.7	2.4	3.0
ARC	$< 10^8$	$3.6 \cdot 10^7$	$9.1 \cdot 10^7$	3.4	1.3	5.7

minimum and maximum R-factor values, and since these measurements in P1 and P5 yield compatible results, the data from the two points are merged. The highest fluences ($>10^9$ HEHeq/cm^2/year) are mainly in the DS, more precisely in the cells 8, 9, 11 and 13 and as shown in Table 3.1 the respective R-factors have a range of one order of magnitude, from a very low thermal neutron contribution (0.7) to a considerable one (7.6) with respect to the HEHeq. If considering only cell 8, for which the 2018 levels were relatively large due to the

debris collimator settings, the fluence results in $1.7{\cdot}10^{11}$ HEHeq/cm^2/year, the maximum one recorded among all the cells (as in Table 3.1) with a corresponding average R-factor of 4.6. The intermediate fluence values between 10^8 and 10^9 HEHeq/cm^2/year comes from only two entries. The fluences below 10^8 HEHeq/cm^2/year are measured along the LHC arcs. Their average R-factor is comparable with that of the high fluences in the DS, but with a minor spread. These average R values are compatible, within the uncertainties, to the FLUKA simulations shown in Fig. 3.1 for a typical cell in the arc. Below the dipole interconnections (MBx), where the RadMons for this analysis are installed, the simulated R-factor is 5.2. As a summary remark, the radiation environment in the tunnel is characterized by a large spread between the R-factors and by relatively large average and maximum values, significantly larger than those for standard ground and avionic applications (shown in Section 3.3). R-factors are high owing to the neutron scattering in the tunnel walls, which act as a moderator. A typical spectrum of neutrons in the tunnel can be seen in Fig. 3.2 and compared in the following to the spectrum of an alcove.

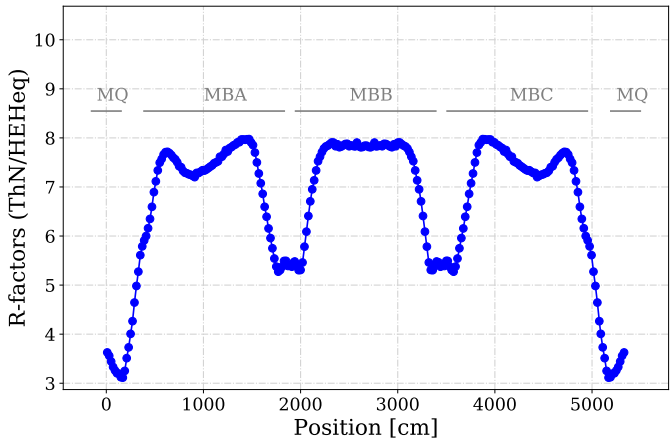

Figure 3.1: FLUKA simulated R-factors along cell 20, composed of 3 dipoles (MBx) and the quadrupole (MQ). RadMons are installed among the interconnections.

3.2.2 Radiation levels in shielded alcoves

Alcoves in the proximity of an interaction point, as seen in Section 2.7, can be heavily shielded, such as UJ and UL, with 98% of particles composed of neutrons, or lightly shielded, such as RR, with a neutron contribution varying from 70% to 90% [14]. The remaining contribution is almost equally shared between protons and pions. These percentages refer to HEH fluences mainly composed of neutrons, protons and pions, above 20 MeV.

RadMons in the shielded areas are typically installed on the concrete wall separating the tunnel from the alcove, or on the ceiling on top of the electronic racks. In some cases, an additional device is placed in the tunnel near the shielding for fluences comparison. To give a relevant example, Fig. 3.3 shows the planimetry of UJ14, the heavily shielded alcove in the proximity of P1 introduced in 2.7 (Fig. 2.11b is a photograph of the same location). As can be seen (Fig. 3.3), the electronic racks are disposed perpendicularly to the tunnel and the

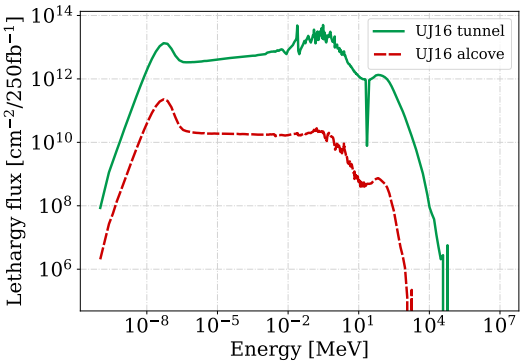

(a) *Both axes are in logarithmic scale.*

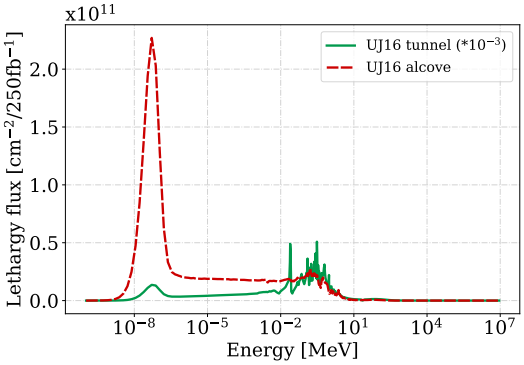

(b) *The y axis is in linear scale and the tunnel spectrum is divided by a factor 1000 in order to overlap the two spectra above 0.1 MeV.*

Figure 3.2: FLUKA simulated neutron spectra in the UJ16 shielded alcove and in the adjacent LHC tunnel. Lethargy fluxes in log and linear scales.

RadMon is placed near the entrance (which cannot be completely closed for safety reasons), where the fluence is expected to be higher, and on the opposite side in UL14, where the fluence is expected to be lower. It is to be noted that most sensitive equipment in the UJs were relocated to the ULs during the Long Shutdown 1 (LS1, 2013-14) owing to the lower radiation levels. The RRs, however, still host a vast quantity of electronic racks for critical systems.

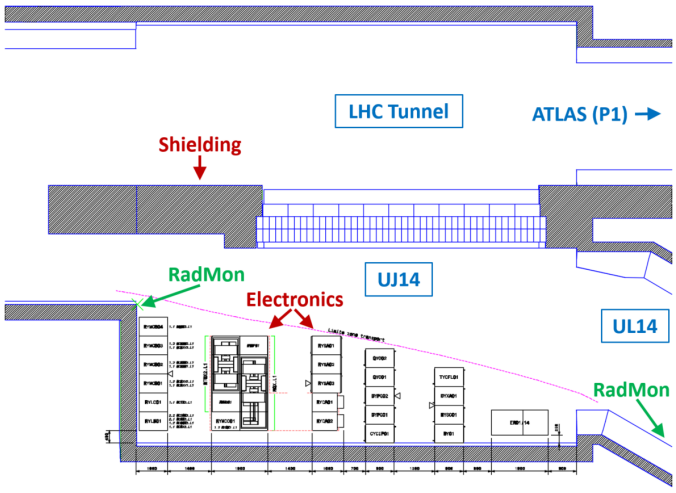

Figure 3.3: UJ14 and UL14 planimetry, with the thick iron-concrete shielding separating the tunnel from the alcove in which the electronic racks are placed. RadMons are installed at positions where the fluences are expected to be the highest and the lowest.

R-factor measurements for the alcoves in P1 and P5 are presented in Table 3.2. While the UJs and the ULs are at several tens of meters of distance from the experiments, the RRs are 250 m away from them and consist in two-level floors (LEV0, LEV1), both parallel to the tunnel, and of which LEV0 is at the same level as the accelerator beam. As can be seen, thermal neutrons in the RR tunnel side have similar fluxes as the HEHeq ones, and the R-

Table 3.2: R-factors for the alcoves in P1 and P5 during 2018. P1 is in between UJ14 and UJ16, which are symmetric alcoves as RR13 and RR17. The same applies in P5 for RR53 and RR57.

Alcove	RadMon position	R	Φ_{HEHeq} [HEHeq/cm^2/y]	Point
RR13	TUNNEL	1.3	$2.3 \cdot 10^9$	P1
RR13	LEV0	9.6	$1.6 \cdot 10^8$	P1
RR13	LEV1	5.0	$3.2 \cdot 10^8$	P1
UJ14	LEV0	52.5	$2.7 \cdot 10^8$	P1
UL14	LEV0	18.4	$1.3 \cdot 10^7$	P1
UJ16	LEV0	44.6	$2.7 \cdot 10^8$	P1
UL16	LEV0	31.0	$1.0 \cdot 10^7$	P1
RR17	LEV0	11.1	$1.6 \cdot 10^8$	P1
RR17	LEV1	4.5	$3.2 \cdot 10^8$	P1
RR53	TUNNEL	0.5	$6.7 \cdot 10^9$	P5
RR53	LEV0	4.1	$4.0 \cdot 10^8$	P5
RR53	LEV1	1.3	$8.8 \cdot 10^8$	P5
RR57	TUNNEL	0.5	$5.3 \cdot 10^9$	P5
RR57	LEV0	5.7	$3.3 \cdot 10^8$	P5
RR57	LEV1	2.7	$6.6 \cdot 10^8$	P5

factor significantly increases by almost a factor 10 inside the alcoves, especially in those at the same tunnel level. The thermal contribution is even higher inside the UJs: up to 52 times the HEHeq in the proximity of the alcove entrance. This is due to the fact that highly energetic neutrons are thermalized by the shielding and can scatter through the maze entrance. Moreover, the relative thermal neutron fluxes decrease when moving toward the ULs. Finally, the respective HEHeq yearly fluences inside both the UJ and UL alcoves are about one order of magnitude lower than in the tunnel. This aspect has strong implications for electronic components sensitive to thermal neutrons, as will be shown in Chapter 7.

The simulated neutron spectra for the alcove UJ16 and the corresponding tunnel are shown in Fig. 3.2a in unit of lethargy per 250 fb^{-1} of luminosity, in logarithmic scale. As can be seen, the shielded alcove reduces the flux by about 3 orders of magnitude. Three different peaks can be distinguished: those corresponding to thermals (around 25 meV), evaporation ($\sim$1 MeV) and spallation ($\sim$100 MeV) neutrons. To better observe the thermal neutron contribution, Fig. 3.2b shows the same lethargy graph in linear scale (thus, with the areas below the curves representing the integral fluxes in the different energy ranges), with the tunnel spectrum values divided by a factor 10^3 in order to overlap the two HEH parts. Two effects are now more evident: the HEH flux is almost negligible compared to the thermal peak, and the neutron thermalization when passing from the tunnel to the alcove. Flux and energy are reduced by the concrete and iron shielding resulting in a relatively higher flux of thermal neutrons.

Moreover, the simulated R-factors can be computed from these spectra. For this, the thermal neutron fluence is obtained by folding the spectra with the inverse square root of the

energy (see Eq. 2.10). The HEHeq fluence is retrieved through Eq. 2.6 using the Weibull fit of the Cypress SRAM (the memory more sensitive to HEH) embedded in the RadMon. As a result, inside the UJ16 alcove the simulated R-factor results of 32.3, while it is around 1 in the adjacent tunnel. Considering the fact that the scoring region in the FLUKA simulation of UJ16 is just behind the shielding with a volume of 12x2x1 m, while the RadMon is confined in a much smaller volume in a slightly different position (R = 44.6 from Table 3.2), and the thermal spectrum strongly depends on the exact location and material composition, the two R values are compatible.

As a general fact, electronics installed in the LHC alcoves are mainly affected by SEEs, whereas devices in the LHC tunnel are subjected from both SEEs and cumulative effects (TID, DD).

3.3 Atmospheric Radiation Environment

The atmospheric radiation environment is of great interest especially for avionic and ground level (e.g. automotive, IT) applications, and shares some similitudes to the accelerator neutron spectra of shielded areas, even though the fluxes in the latter are much larger. In this section, an overview regarding the cosmic rays is presented, followed by the terrestrial spectra at different altitudes extracted from simulations and compared to the data available in the standards.

3.3.1 Cosmic rays down to ground level

The main source of natural radiation comes from highly energetic cosmic rays, which are composed of protons (83%), alpha particles (16%) and heavy ions (1%) [37]. When entering the atmosphere, they interact with the air molecules, i.e. nitrogen (78%) and oxygen (21%), producing a shower of secondary particles, which in turn generates other particle cascades. This process is depicted in Fig. 3.4. These secondaries can be considered composed of pions and muons, both short-life particles, protons and electrons, which are attenuated by Coulomb interaction with air, and neutrons [29]. Among these particles, neutrons can easily reach the lower part of the atmosphere, down to ground level, due to the fact they have no charge and are characterized by relative high fluxes. Other particles such as muons and protons can also reach ground level, but their impact on microelectronics is much less significant than that of neutrons [3].

According to the IEC1 standard [37], a neutron flux above 10 MeV at ground level (New York City) results in 20 n/cm^2/h, 300 times lower than that at 12 km (avionic altitude), although it is reported as 450 times lower (13 n/cm^2/h) in both JEDEC and IEC2 standards [12, 38]. The altitude plays a fundamental role in terms of fluxes and particle composition. The highest neutron flux is at around 18.3 km, called the Pfotzer maximum. In addition to neutrons, protons present a similar high energy spectrum and are capable of inducing

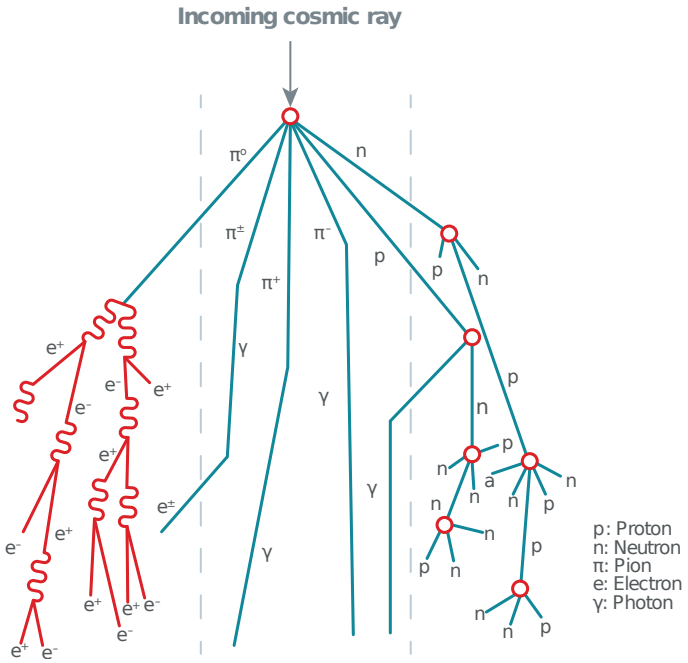

Figure 3.4: Cascade of secondary particles generated by the interaction of cosmic rays with air (the representation is modified from [3]).

SEE. Their fluxes are lower than those of neutrons at ground level and increase with altitude, showing the Pfotzer maximum at around 16.8 km. The proton flux in the atmosphere is about 20-30% of the neutron flux up to 400 MeV, while they are comparable at higher energies [37]. These conclusions come from measurements performed at around 3-4 km altitudes.

Latitude is another important parameter affecting the interaction of cosmic rays with the atmosphere, and it is related to the earth's magnetic field. At the poles, where the magnetic field is parallel to the particle direction, cosmic rays can easily penetrate the atmosphere, whereas at the equator the former is perpendicular to the latter and thus the interactions are reduced [37].

3.3.2 Neutron and Proton fluxes

Neutron and proton spectra were extracted through the Model for Atmospheric Ionizing Radiation Effects (MAIRE) tool [39] considering a medium geomagnetic index (Kp) of 4 on the 1^{st} of July 2016 for altitudes up to 20 km. Fig. 3.5 shows the differential fluxes of neutrons (Fig. 3.5a) and protons (Fig. 3.5b) at different altitudes over Geneva in Switzerland (375 m altitude, 46.2° latitude, 6.2° longitude) and at 1 meter above sea level in New York City (NYC). In both cases the flux attenuation moving from 20 km to sea level is noticeable. The neutron and proton fluxes are reduced by three orders of magnitude below 1.5 GeV and 400 MeV, respectively. Above these energies, the attenuation is four or more orders of magnitude.

A comparison between neutron and proton spectra is shown in Fig. 3.6a at ground level and at 12 km and 20 km of altitude over Geneva. Three ground level spectra are presented:

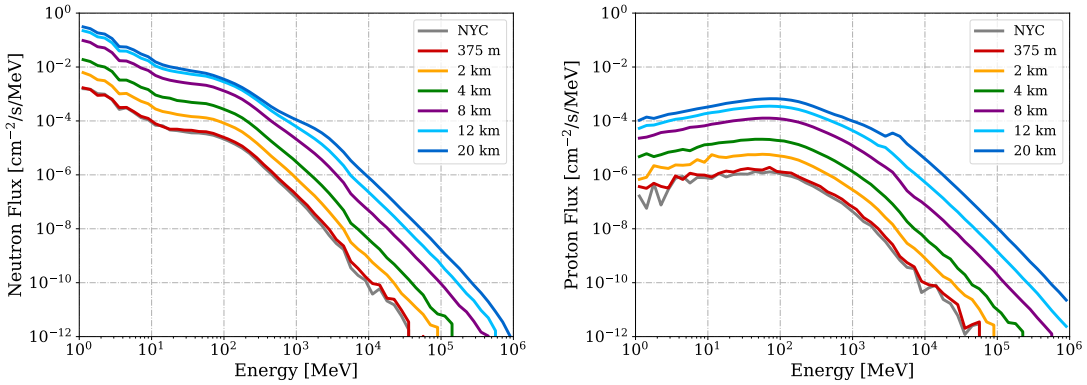

Figure 3.5: Differential spectra of neutrons (a) and protons (b) above 1 MeV at different altitudes over Geneva in Switzerland and at 1 m above sea level in New York City (NYC). Simulations retrieved through the Model for Atmospheric Ionizing Radiation Effects (MAIRE).

in Geneva (simulations, 375 m above sea level), NYC (simulations, 1 m above sea level) and NYC (measurements performed in November 2002 reported in the JEDEC standard). The simulation overestimates the measured NYC flux around 100 MeV by up to 80%. Proton fluxes are lower than those of neutrons below 2.5 GeV and higher above this threshold; this effect is particularly visible at 20 km of altitude, where protons above 2.5 GeV are 5 times greater than neutrons. Fig. 3.6b depicts the variation of neutron and proton fluxes with the altitude, calculated above 1 MeV and normalized at 12 km. These simulated values are compared to the Boeing model from IEC1, which are reported in the standard from 1 to 10 MeV. Although this energy range covers only a small portion of the spectrum, the standard states that the same altitude variations apply for neutrons above 1 MeV and indeed, the trend is compatible with that from the simulations. The maximum flux value corresponds to the Pfotzer peak at 18 km for neutrons, but it is not the case in regards to protons, which were supposed to present a peak around 16.8 km [37].

Fig. 3.7 depicts the integral fluxes of neutrons and protons, calculated above 10 MeV and 20 MeV. As can be seen, at 12 km of altitude, the proton flux above 10 MeV is 22% of the neutron flux, a factor of 3 higher than what the IEC1 standard alludes (6.7%).

A quick overview on how the hardness of the spectra evolves with the altitude is summarized in Table 3.3, through the $H_{10\%}$ **hardness factor**. This figure of merit is defined as the energy above which 10% of the HEH flux (> 20 MeV) is present in the considered spectrum [40,41]. It represents in a single value the information about the hardness of a spectrum for a direct comparison between different environments. The spectra, from which the $H_{10\%}$ were calculated, derive from the MAIRE simulations, which consider the contribution of neutrons and protons, and the JEDEC measurements, which only include neutrons. In addition, $H_{10\%}$ was calculated at the equator and pole for the same longitude of Geneva (6.2°), considering a latitude of 0° and 70°, respectively. As seen in Table 3.3, there is a general increase in the $H_{10\%}$ factor with altitude, showing the presence of larger relative fluxes of highly energetic particles. The $H_{10\%}$ values extends up to almost 1800 MeV (Table 3.3), which are also

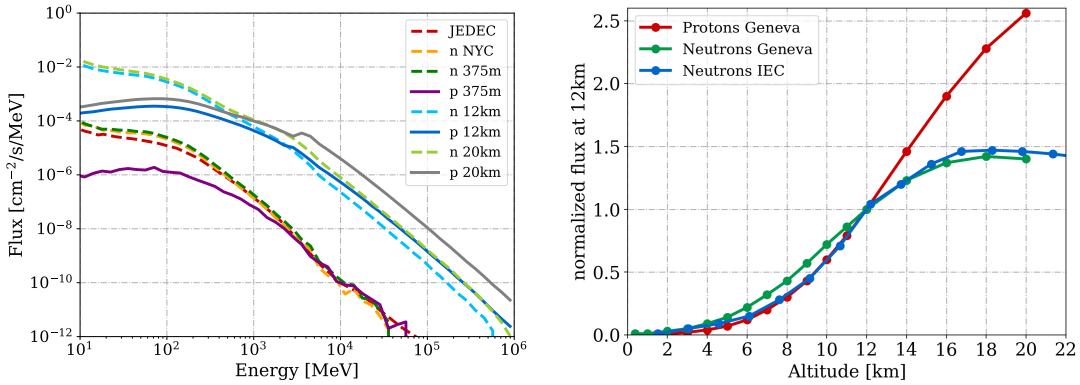

(a) **(b)**

Figure 3.6: (a): Comparison between neutron and proton differential spectra above 10 MeV at ground level (Geneva, NYC, JEDEC NYC), 12 km and 20 km over Geneva. (b) Simulated neutron and proton fluxes (above 1 MeV) vs altitude, normalized at 12 km for both protons and neutrons, in comparison to the Boeing model from the IEC1 standard (which is calculated from 1 to 10 MeV).

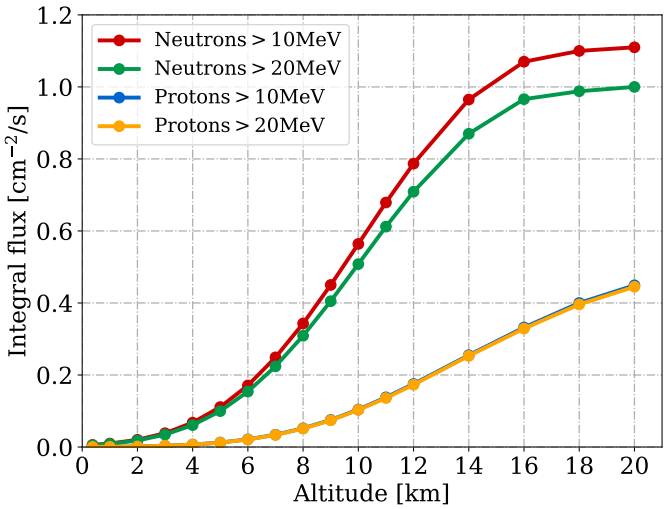

Figure 3.7: Integral neutron and proton fluxes, above 10 MeV and 20 MeV, for different altitudes above Geneva.

typical in accelerator environments. For comparison, the ChipIr spallation facility (ground level neutron-like spectrum) provides the hardness of 283 MeV [41].

It is important to highlight that, as shown in Table 3.3, it is not only the flux that changes in the neutron and proton spectra with altitude in the atmosphere, but also the energy spectra shape. Indeed, as will be shown in Section 7.4, this aspect has strong repercussions when estimating the SEE rate for aviation applications.

Table 3.3: Calculated spectral hardness factor at different altitudes over Geneva in km, compared to the NYC standard (JEDEC) and at varying latitude (0°, equator), (70°, pole).

Altitude (km)	**JEDEC**	**0.356**	**4**	**8**	**12**	**12 (Equator)**	**12 (Pole)**	**20**
$H_{10\%}$ (MeV)	525	450	566	805	1275	1420	1014	1790

3.3.3 Thermal neutrons in the atmosphere

The thermal neutron flux in the atmosphere, defined in this context as the flux below 1 eV, is lower than that of High-Energy Neutrons (HEN) of a factor that varies from 4 to 6, mainly due to their absorption by atmospheric nitrogen [37, 42]. HEN are defined in this context in comparison to ThN, for terrestrial and atmospheric applications, as neutrons with energy greater than 10 MeV [19].

Thermal neutrons - Ground level

At ground level, while the flux of neutrons above a few MeV is constant, epithermal and thermal neutrons strongly depend on the surrounding environments, because neutrons below 1 MeV are mainly produced from scattering with buildings and materials. For this reason, the thermal neutron flux is not constant and homogeneous, and measurements are needed to characterize them in the location of interest. Water, weather conditions, solar activities, latitude/longitude, etc., can vary the thermal neutron flux. For instance, during rainstorms the thermal neutron flux can double, whereas the snow decreases their flux [19].

Both thermal and HEN fluxes are attenuated with a shielding (buildings). However, materials containing hydrogen, such as water, increase the ThN flux by moderating fast neutrons.

Thermal neutrons - Avionics

The HEN spectrum inside commercial aircraft, which generally fly at 12 km of altitude, can be considered the same as outside. Contrarily, thermal neutron fluxes can be more than 10 times higher inside the plane, yielding the thermal flux up to 2 times higher than that of HEN. This is due to the presence of H inside many materials such as fuel, human bodies and equipment, which thermalizes neutrons. Therefore, the thermal neutron flux strongly depends also on the atmospheric humidity and on the presence of water masses. For terrestrial environments (ground level, New York City) the thermal flux is measured as 6.5 [n/cm^2/h] and the HEN one as 13 [n/cm^2/h] from the JEDEC standard [12], whereas inside an aircraft (12 km of altitude) the IEC standard considers a thermal to HEN ratio of 1.1 [42].

Summarizing, the R-factor for the ground level and avionic environment can be considered of 0.5 and 1.1 respectively.

3.4 Summary

The sources of ionizing radiation in accelerator and atmospheric environments were described in this chapter. Neutrons are the main constituents of the mixed-field present in the accelerator because they are produced due to collision debris from the experiments and the beam interaction with collimators and residual gas molecules inside the vacuum pipes. The thermal neutron and HEHeq fluences were characterized with the R-factor, in the tunnel and shielded alcoves of the LHC, through measurements performed with the RadMon system and benchmarked with FLUKA simulations. It turned out that the thermal neutron fluence can be up to a factor of 50 larger compared to the fluence of HEHeq in shielded alcoves.

In addition, neutron and proton fluxes at varying altitude in the atmosphere were assessed thorough simulations based on FLUKA and compared to the data in the JEDEC and IEC standards. Indeed, the cascade of secondary neutrons generated in the atmosphere from the interaction of cosmic rays occurs in a similar way as in the accelerator, when the beam interacts with the residual gas molecules. Other similitudes are shared between atmospheric and accelerator environments such as the highly energetic particles produced, that were quantified through the hardness factor $H_{10\%}$, showing their larger presence at increasing altitude. Moreover, differently from the accelerator, thermal neutrons in the atmosphere have essentially the same flux as that of high energy neutrons, resulting in R-factors of 0.5 and 1.1 for the ground level and avionic environments, respectively.

Chapter 4

Neutron Inelastic Interactions in Silicon

The following chapter is devoted to the inelastic interactions of neutrons in silicon, which are the most effective in inducing SEEs above 10 MeV [5], while the contribution of elastic scattering is studied in Section 7.3.2. The first sections aim to introduce basic aspects governing the interaction of neutrons with matter and introduce the study about the ion contributions to the SEE cross section from state of the art knowledge. Neutron inelastic interactions in Si will be studied in detail, allowing us to draw several conclusions about their contribution to the SEE cross section. In addition, this analysis assesses the potentiality of FLUKA for these simulations, from which the inelastic cross sections are calculated and compared to those extracted from nuclear databases and publications.

Inelastic interactions of neutrons in Si nuclei are simulated with FLUKA at the single interaction level (based on a production Monte Carlo code), for neutron energies from 10 MeV up to 1 GeV. The secondary products generated by the reactions are analyzed and counted by means of a python script developed in the scope of this thesis, considering all produced isotopes with atomic number from 1 to 15. In addition, neutrons, pions (total contribution of positive, negative and neutral ones) are counted. As the neutron kinetic energy approaches 1 GeV, more exotic particles are generated (mostly electrons and positrons), but they are less than two per million of the secondaries.

4.1 FLUKA Models

The nuclear effects of hadron-nucleus interactions are treated in FLUKA through the Pre-Equilibrium Approach to NUclear Thermalisation (PEANUT) model [30], that includes different models, each one operating in a certain energy range. Indeed, the evolution of a nuclear reaction, from high to low energies, is simulated in steps depending on the involved energies. The Generalized IntraNuclear Cascade (GINC) Monte Carlo model is used for high

energies and as long as all particles are emitted, absorbed or decay and all secondaries have energy below roughly 30-50 MeV [43]. Below this energy threshold, a transition to a pre-equilibrium stage model is implemented. The final step evaluates how the excited fragments de-excite, that can be through evaporation (A<25), fission, or Fermi break-up for light nuclei (A<18) [44]. These equilibrium processes are critical for the production of neutrons, as well as for the residual nuclei distributions that are directly associated to the activation of materials and to dose studies. The GINC model is very sophisticated and more details can be found in [30].

In the standard FLUKA tool, the neutron transport below 20 MeV is performed through a multi-group algorithm, which consists of dividing the energy range of interest in interval groups. There are 260 energy groups with corresponding cross sections, spaced with about the same logarithmic width. Inelastic (and elastic) cross sections are obtained by group to group transfer probabilities called down- or up-scattering matrix, which are calculated through a Legendre polynomial expansion [30]. Moreover, for some isotopes such as ^{10}B, ^{6}Li the point-wise cross section can be implemented (continuous treatment of the cross section).

However, the neutron physics for the inelastic simulations presented throughout this chapter relies on a FLUKA driver named Preex. This driver (based on PEANUT) samples the individual hadron-nucleus nuclear interactions without the need of running the full tracking in a simulation. Hence, the neutron physics below 20 MeV is also treated through Preex and does not rely on the aforementioned standard FLUKA treatment. In the following, the term "simulation at single interaction level" will be used to denote the simulations performed through the Preex tool.

4.2 Physical Interactions of Neutrons with Matter

The nuclear interactions of neutrons and materials found in electronic devices are defined and explained in this section. In general, neutrons impinging against silicon (or other nuclear species typically present inside electronics, such as oxygen) can produce secondary ions from both elastic and inelastic processes. In case of elastic scattering only silicon (recoils) are produced, while with inelastic collisions, in addition to possible silicon ions, other secondaries normally lighter than the target element can be created.

A nuclear reaction (or non-elastic) is defined as the process in which the incoming nucleon penetrates the target nucleus, which is excited and subsequently deexcited by the emission of one or more photons, n, p, or other nuclear fragments. The term "reaction" suggests that some collision partner changed its internal state, therefore elastic processes are excluded from this definition to avoid confusion.

The customary notation for a nuclear reaction is given by X(a,b)R, where "X" is the target, "a" the projectile, "b" the ejectile, and "R" the residual nucleus. For instance, ^{28}Si(n,α)^{25}Mg means that a neutron impinges on a silicon atom (^{28}Si abundance is 92%) and the reaction produces a magnesium residue with the emission of an alpha particle. When a neutron im-

pinges on a nucleus, mainly four types of interactions are of interest, and the probability of each one depends on the target nucleus and the energy carried by the neutron, which plays a drastic role in determining the output of the reaction.

1. **Elastic collision (scattering)**. The neutron collides against the nuclide and is deflected, as a result of which the target nuclide recoils with a kinematically determined energy, namely they rebound with different speeds than the original ones (see Fig. 4.1). The total kinetic energy of the system before and after the collision is unchanged and the residual nucleus remains at ground state (hence not excited). For instance, for the Si(n, n)Si elastic process, the silicon atom that was stationary in the lattice after the collision acquires energy and starts moving, while the neutron loses part of its energy and hence is slowed down.

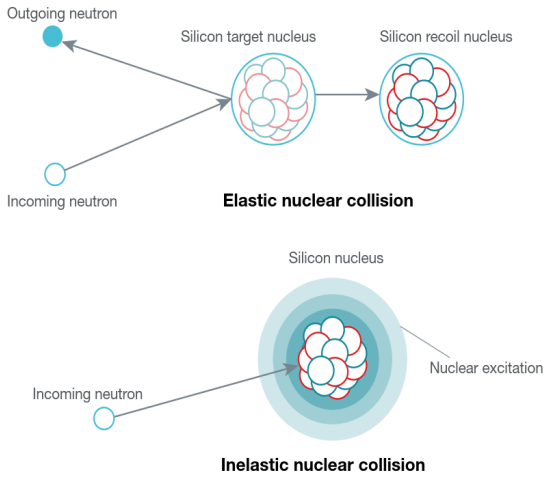

Figure 4.1: Elastic and inelastic collisions between incoming neutron and silicon target (from [3]).

2. **Inelastic interaction (nuclear reaction)**. Its definition is not unique in literature and in this work it is acquired from [45] and [3] with some adaptations.

   The term "inelastic interaction" will be used to indicate any process that changes the nature or internal state of any of the collision partners. Hence, for both processes where the target nucleus is promoted to an excited state but still retains its original Z and A (though it can be left in an excited state) such as the (n,n') reactions, and for processes where Z and A change.

   The impacting neutron is absorbed by the target nucleus and the total kinetic energy of the system is not conserved but results lower than the initial one (see Fig. 4.1). The difference in energy is transferred to the nucleus, which is promoted to an excited state. This excess of energy can be released in different ways, depending on the target nucleus and incident neutron energy. From thermal neutrons up to a few keV the nucleus typically de-excites emitting gamma radiation (except in the particular case of point 3 below), while with incident neutron energies up to several MeV the nucleus breaks into one or more light ions (or particles) (a) and a heavier residue (R). Above

100 MeV the impacting neutron no longer interacts with the whole nucleus, but rather with a single proton or neutron, resulting in its emission with high energy (**spallation**). In this work, inelastic interactions includes also reactions where (a) and (R) have almost the same weight, as for the Si(n,C)O reaction.

Inelastic processes are referred to as threshold reactions because the projectile neutron needs to have a determined kinetic energy below which a certain reaction does not happen. For instance, typical inelastic interactions in silicon are ^{28}Si(n, α)^{25}Mg and ^{28}Si(n, p)^{28}Al, whose lowest threshold energy is 2.75 MeV and 4.00 MeV, respectively [29]. Moreover, the energy loss with inelastic interactions is normally greater than with elastic scattering, even if the probability of occurrence is lower for inelastic collisions.

3. **Thermal neutron reaction**. Thermal neutrons can even spontaneously break a nucleus into smaller nuclei and not just induce gamma emission. For instance, this reaction occurs even inside our smartphone because of the ^{10}B isotopes contained inside electronic components, as seen in Section 2.3.3. This reaction is sometimes referred to as "fission reaction" in literature, although the term is ordinarily intended for heavy elements such as the ^{235}U, whose fission (either spontaneous or induced) releases two or more neutrons.

4. **Capture reaction**. The neutron in the capture reaction is absorbed by the target nucleus producing the next isotope of mass A+1, which results in an excited state and it deexcites by emitting gamma radiation. Typical example is ^{28}Si(n, γ)^{29}Si, that is the main reaction induced by neutrons below 1 MeV [24].

The difference between elastic and inelastic nuclear cross sections can be seen in Fig. 4.2 extracted from the TENDL database [4]. Below 10 MeV both cross sections present a resonance, and below roughly 8 MeV the nuclear elastic scattering is the dominant mechanism.

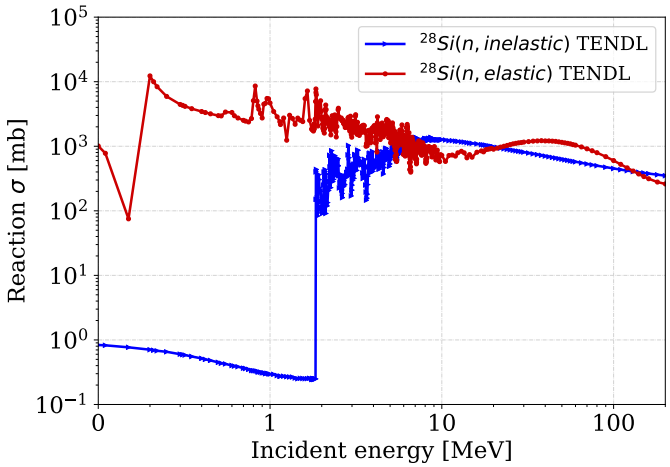

Figure 4.2: Elastic and inelastic nuclear cross sections in ^{28}Si from the TENDL library.

4.3 Ion Contributions to the SEE Cross Section

The main contributions to trigger SEEs, from secondary produced ions and materials in electronics, are explained in this section from state of the art knowledge of different publications.

Primarily, it is important to know if simultaneous ions ejected in the course of a single reaction can contribute to induce charge in a correlated way in the SV (the following considerations are presented from [29]). At high energies, even though the neutron elastic cross section is non-negligible, the recoil momentum of elastic scattering is small and therefore their contribution to SEUs is expected to be negligible. The n-Si inelastic interactions causing SEUs, considering a spherical SV, are mainly generated within a ray that is up to 5 times the SV dimension (4 μm of distance from the SV centre, considering a 0.25 μm technology with a spherical SV with ray of 0.7 μm). Beyond that distance, the probability of emitting two particles inside the same SV is rare as only one particle usually has the right direction to reach it. Although 92% of SEUs inside the SV come from the generation of 2 or more ions, less than 2% are due to the combined contribution from the same reaction. Furthermore, this value decreases with technology scaling, hence only single ions can be considered for SEU simulations [29].

4.3.1 H and He ions contribution to the SEU cross section

Even though in some works [15, 46] the Si ion recoiled by elastic scattering of neutrons below 10 MeV was considered the major contributor to SEUs, because the elastic scattering is the dominant mechanism (see Fig. 4.2), more recent researches highlighted the importance of light ions against elastic recoils. From [47], which explores in detail the charge deposition mechanisms due to neutrons below 10 MeV in 25 nm bulk SRAM, it turns out that H and He ions (protons and mostly alpha particles) are the main cause of SEUs, and the results are outlined in the following. Moving from higher to lower energies, the SEU neutron cross section shows a sharp decrease around 7 MeV. In addition, around the same energy, the production cross section of protons and alpha generated from n-Si reactions increases, and although they are lower than those of elastic scattering, the former can induce more upsets [47]. This phenomenon depends on the incident neutron energy, critical charge (Qc) and silicon target thickness (bulk), hence not only as far as the SV is concerned but all the material around it.

Reference [47] calculates the SEU cross section through PHITS simulations, considering a 1000 μm x 1000 μm silicon target area. For instance, with neutrons of 10 MeV and low Qc (0.1 fC), by varying the bulk thickness, H and He ions dominate the SEU cross section above 2 μm with respect to Si ions (considering both elastic and inelastic processes). Moreover, they are the cause of increasing the SEU cross section over the cell thickness from 0.5 to 200 um, after which it saturates because these ions have reached the maximum emission energy. This behaviour is explained through the Si, H and He emission energies and the corresponding range in silicon. Silicon ions have a maximum range of 1.4 μm, and therefore only those

produced in the proximity of the SV can induce SEUs. H and He ranges, instead, are much larger (up to 300 μm for H) and therefore these ions even produced far from the SV can reach it, and consequently the SEU cross section increases with the thickness. This explains also why below 2 μm of bulk thickness the Si elastic scatterings are dominant. However, increasing Qc (0.6 fC) the H contribution to the SEU cross section is significantly reduced.

As seen, the thickness of the overlayers above the SV plays a primary role to determine the ion contribution to deposit charge in the sensitive areas. In a real case with other layers and the package thickness, the contribution from H and He to the SEU cross section is expected to be even higher, because they can travel a longer distance. As a result, to predict SEU with simulations is essential to define a sufficient interaction volume resembling the one present in the memory structure, especially for low critical charge devices (and therefore for high scaled technology), in which light ions such as H and He play a major role on the SEU cross section [47].

4.3.2 SiO_2 (BEOL) contribution to the SEU cross section

Another important contribution, in addition to the secondary ions generated in the silicon SV, concerns the SiO_2 insulator used as passivation layer, gate oxide and shallow trench isolation. The probability of reaction (elastic and inelastic) with silicon is higher than with oxygen in terms of cross section, namely n-Si reactions happen more often than n-O one. However, in SiO_2 the oxygen nuclei are double than the silicon ones, and 60% of the nuclear reactions from 5 to 150 MeV occur in oxygen [48]. Moreover, the respective recoils are produced with greater energy in oxygen than in silicon because of their masses; in general, the energy transfer (not the LET) is greater with lighter target nuclei than heavy ones.

Below incident neutron energies of 50 MeV, the n-O reactions produce recoils with higher average LET and longer ranges than n-Si, hence oxygen is likely to induce more SEUs. Above 50 MeV instead, n-O produces recoils with lower LET but higher ranges and nothing can be said. The passivation layers of SiO_2 leads to increase the SEU cross section of 25% from simulation [48], and of a factor of 3 [49] or 2 [50] from measurements with 14 MeV neutrons. For bulk technology, this aspect implies that an irradiation from the front side of the memory yields higher cross section than performing it from the bottom, because in the latter case, the secondary ions produced by the SiO_2 are ejected mainly in the opposite direction of the SV and therefore SEUs are induced by n-Si reactions, which are less efficient. In conclusion, n-O reactions can deposit more energy in the SV, and their secondaries, having higher ranges than those of n-Si, can reach the SV from farther.

4.4 Nuclear Cross Sections in Silicon

The nuclear cross sections of neutrons in ^{28}Si and ^{29}Si are extracted through different libraries such as the Evaluated Nuclear Data File (ENDF) [51], a database based on measure-

ments, and depicted in Fig. 4.3. As the exhaustive list of cross sections is not contained in a single library, they can derive from different libraries, which are reported in the legend of the plots: ENDF/B-VIII.0 (USA, 2018), JENDL-4.0 (Japan, 2012) and JEFF-3.3 (Europe, 2017). The contribution of (n, α), (n,p), (n,d) and (n,t) cross sections are shown for ^{28}Si and the only (n, α) for ^{29}Si.

As can be seen in Fig. 4.3, the threshold energy can be quite low for (n, α) and (n,p) reactions in ^{28}Si, and even lower regarding the former in ^{29}Si. The threshold energy values of some reactions are calculated with FLUKA and compared in Section 4.5. In addition, from Fig. 4.3 it can be observed that the (n, α) cross section using different libraries (ENDF or JENDL for ^{29}Si) can be different at low energies, hence, the threshold limit of some reactions may be difficult to establish.

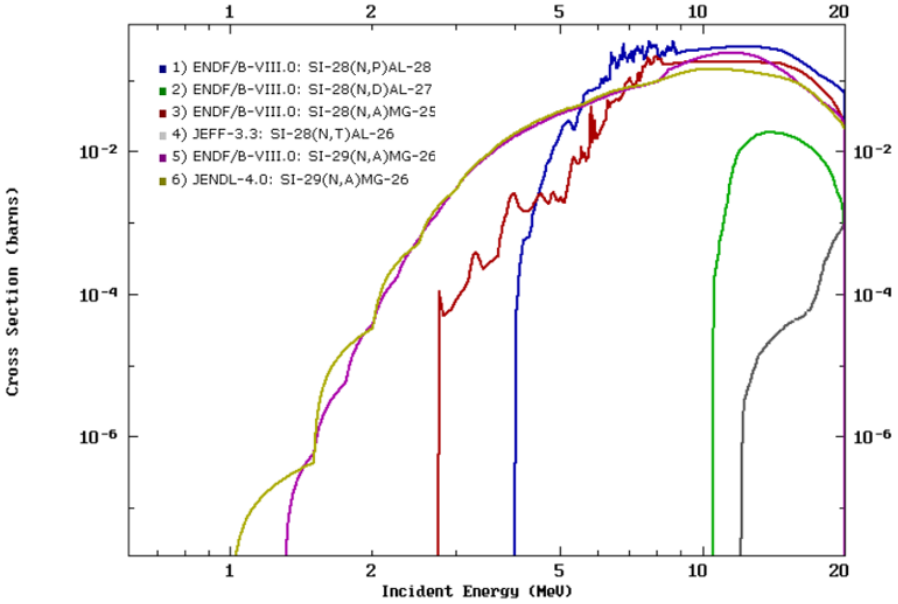

Figure 4.3: Inelastic nuclear cross sections as a function of the incident neutron energy, for different reactions in ^{28}Si and ^{29}Si, from the ENDF and JENDL database. Noteworthy the low threshold value for the (n, α) reactions in ^{29}Si.

4.4.1 Inelastic cross sections in FLUKA

Given a certain reaction channel, its respective cross section can be calculated as the product of the neutron reaction cross section (including all channels) times the ratio of events for the channel under scrutiny divided by the total number of events, through Eq. 4.1.

$$\sigma_{reaction} = \sigma(Si) \cdot \frac{N_{reaction}}{N_{tot}} \tag{4.1}$$

FLUKA has a parametrization for the reaction cross section (all channels) which governs the probability for a neutron to interact with a Si nucleus inelastically. These FLUKA models

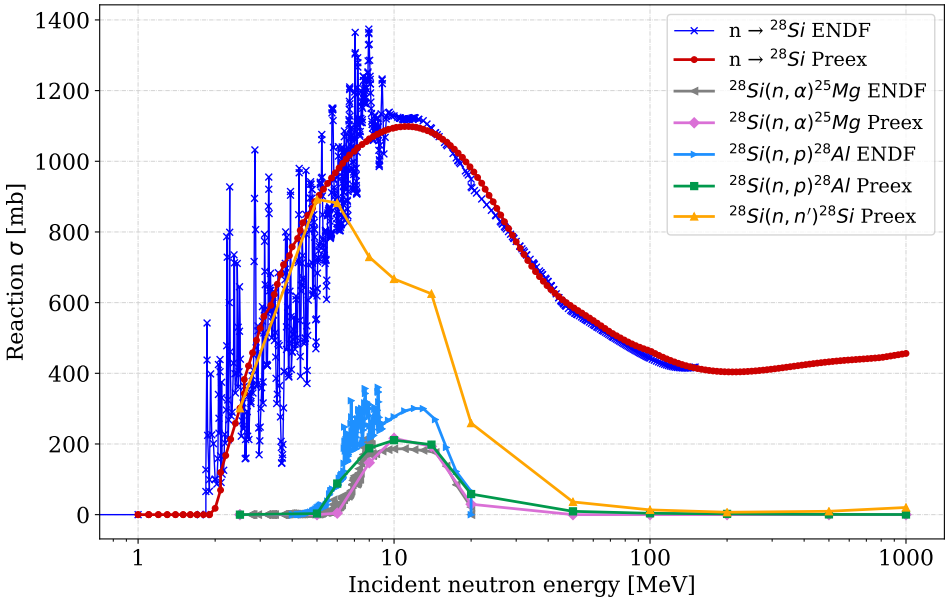

Figure 4.4: Inelastic cross sections as a function of the incident neutron energy from the interaction of neutrons in ^{28}Si, extracted from ENDF and the FLUKA simulations at the single interaction level (denoted as Preex).

are used to generate the final state when E > 20 MeV, while below this energy the aforementioned group cross section treatment is implemented. In the FLUKA simulations at single interaction level, every incident neutron is forced to produce a nuclear reaction (differently from a transport Monte Carlo simulation), and then the nuclear cross sections are extracted through Eq. 4.1.

The silicon cross section $\sigma(Si)$ is extracted from FLUKA at the individual interaction level (adopted cross section) for the ^{28}Si isotope and for the three main reactions (see Section 4.4.2) which are produced with incident neutrons of 10 MeV, namely ^{28}Si(n, α)^{25}Mg, ^{28}Si(n, p)^{28}Al and ^{28}Si(n, n$'$)^{28}Si, as a function of the incident neutron energy. The (n, α) cross section, for instance, is calculated in Eq. 4.2 as follows:

$$\sigma_{Si(n,\alpha)^{25}Mg} = \sigma(^{28}Si) \cdot \frac{N_{Si(n,\alpha)^{25}Mg}}{N_{tot}} \tag{4.2}$$

where $N_{tot} = 10^6$ reactions. The FLUKA (single interaction level) cross sections, expressed in mb, are shown in Fig. 4.4 in comparison to the same cross sections extracted from the ENDF database [51]. FLUKA and ENDF data points are calculated considering isotopically pure ^{28}Si (however, the difference is negligible even considering natural silicon). The ENDF ^{28}Si cross section below 10 MeV presents many resonance peaks, which are instead considered a monotonic decreasing function in FLUKA at single interaction level (PEANUT). This happens because Preex is forced to use a continuous model also below 20 MeV, while the ENDF database is based on measurements (for the sake of completeness, the standard FLUKA model implements the multi-group treatment at these energies).

The sum of the three cross section reactions in Fig. 4.4 gives the $\sigma(^{28}Si)$ up to 10 MeV, and represents 94% and 36% of the total reactions at 14 and 20 MeV, respectively. This aspect is in accordance with what will be shown in Section 4.4.2 and specifically in Table 4.1, where the reaction channels above 20 MeV are so populated that these three reactions, in addition to the fact that they are rarer at higher energies, have a negligible contribution above 20 MeV. Indeed, the secondary ions such as Mg, Al, alpha, etc. are still produced with higher energies, but through different reactions, as the silicon nucleus after the collision will result more fragmented.

4.4.2 Nuclear reaction channels

The nuclear reactions examined with FLUKA at the single-interaction level from the interaction of 10^6 incident neutrons of 10, 14, 20 and 100 MeV in natural silicon are listed in Table 4.1, showing the absolute number of reactions and their relative percentage on the total (that coincides to the 10^6 incident neutrons). As can be seen, these reactions cover completely the 10 and 14 MeV cases, but with 100 MeV they represent only 26% of the total reactions. Indeed, the higher the energy the more likely other channels (with more secondaries) are. In addition, the separate contribution of the most abundant produced isotopes for the (n, α) and (n,p) reactions is shown on the top rows of Table 4.1.

Table 4.1: Absolute number of fundamental reactions occurring with 10^6 incident neutrons of 10 and 14 MeV, and differences between 20 and 100 MeV. Percentages are calculated with respect to the total number of reactions (10^6).

	10 MeV		14 MeV		20 MeV		100 MeV	
Reaction	**Events**	**%**	**Events**	**%**	**Events**	**%**	**Events**	**%**
^{28}Si(n, a)^{25}Mg	181539	18.2	164001	16.4	28346	2.8	17	0.0
^{28}Si(n, p)^{28}Al	177101	17.7	169472	16.9	55575	5.6	7776	0.8
Si(n,a)Mg	185369	18.5	170223	17.0	30701	3.1	1532	0.2
Si(n,na)Mg	0	0.0	21023	2.1	153092	15.3	21266	2.1
Si(n,p)Al	179332	17.9	174092	17.4	59451	5.9	14292	1.4
Si(n,n')Si	628082	62.8	558142	55.8	254886	25.5	27153	2.7
Si(n,2n)Si	7217	0.7	40677	4.1	46945	4.7	43606	4.4
Si(n,np)Al	0	0.0	28455	2.8	423330	42.3	138162	13.8
Si(n,d)Al	0	0.0	7388	0.7	29076	2.9	15013	1.5
Si(n,C)O	0	0.0	0	0.0	522	0.1	87	0.0
Total	1000000	100	1000000	100	998003	99.8	261111	26.1

For incident energies of 10 MeV only 4 types of reactions occur: Si(n, n′)Si, Si(n, α)Mg, Si(n, p)Al and Si(n,2n)Si. With energies of 14 MeV, there are a total of 7 reactions, and in addition to the previous ones, also Si(n, np)Al, Si(n, nα)Mg and Si(n, d)Al. However, these latter three additional reactions represent only 7% of the total, so that in first approximation the 10 and 14 MeV cases can be considered very similar. Most of the important reactions are three: Si(n, α)Mg, Si(n, p)Al and Si(n, n′)Si. For both incident energies, more than 55% of reactions are the Si(n, n′)Si, and in equal percentage of 17% the ^{28}Si(n, α)^{25}Mg and ^{28}Si(n, p)^{28}Al re-

actions. The other Mg and Al isotopes, for the (n, α) and (n,p) reactions, are negligible, as shown comparing the events of Table 4.1.

With higher incident energies, the open channels significantly increase, so that with 20 MeV for instance, the reactions are at least 12 (that cover more than 99.7% of the total), with Si(n, 2α)Ne, Si(n, 2p)Mg, Si(n, C)O, $Si(n,p\alpha)Na$ and Si(n, t)Al in addition. With 20 MeV the percentage of produced reactions change substantially. The Si(n, np)Al is the most frequent reaction (42%) followed by the Si(n, n$'$)Si and Si(n, nα)Mg (26% and 15%, respectively). Therefore, increasing the primary neutron energy from 14 to 20 MeV, the (n,np) and (n, nα) reactions rapidly increase, which were negligible with 14 MeV and absent with 10 MeV. Differently, the Si(n, α)Mg and Si(n, p)Al reactions that were very important until 14 MeV represent a minor percentage with 20 MeV. However, the additional neutron produced in the latter reactions can be neglected from a deposited charge point of view, and hence the types of secondaries produced with indecent neutron energies from 10 to 20 MeV can be considered the same.

Increasing the incident neutron energy up to 100 MeV, the 8 reactions listed in Table 4.1 cover only 26% of the total. The channel for the Si(n,C)O reaction, of interest because two quite heavy fragments are produced with similar Z, is open with 20 MeV. However, with incident neutrons from 100 MeV most of carbon and oxygen are produced in other reactions not listed in Table 4.1.

Therefore, a complete analysis based on the types of produced reactions can be performed only until 20 MeV. In the following, the analysis is detailed carried out for the Si(n, α)Mg reaction at 10 and 14 MeV, because as seen it is one of the fundamental reactions at these energies and it was experimentally observed in a silicon diode (see Section 4.5). The analysis of the other single reactions is performed through the energy distribution of the products (Section 4.6). With higher energies, it is more adequate to study the quantity and energy of secondary products, rather than the single reactions (see Section 4.8).

4.5 Nuclear Reactions - Q Values and Threshold Energies

Given a generic nuclear reaction, where a projectile (p) impinges against a target (T) producing a residual nucleus (R) and the associated ejected particle (e), the reaction can be written as:

$$T(p,e)R \tag{4.3}$$

By applying the conservation law of the total energy and by calling i and f the initial and final energies, respectively, the initial energy has to be equal to the final one:

$$\sum_{i=1}^{N}(m_i c^2 + E_i) = \sum_{f=1}^{M}(m_f^{'} c^2 + E_f) \tag{4.4}$$

Where (m) is the rest mass and (E) the kinetic energy. As target plus projectile are the initial quantities and ejectile plus residual the final ones, Eq. 4.3 can be rewritten by applying Eq. 4.4:

$$m_T c^2 + E_T + m_p c^2 + E_p = m_R c^2 + E_R + m_e c^2 + E_e \tag{4.5}$$

The energy conservation of the initial and final products allows one to introduce the Q value as the difference between initial and final relativistic masses, which can be expressed in terms of kinetic energies [45]:

$$Q = m_i c^2 - m_f c^2 = E_f - E_i = (E_R + E_e) - (E_T + E_p) \tag{4.6}$$

The Q values of nuclear reactions are typically negative, namely $m_f > m_i$ and $E_f < E_i$ because the initial kinetic energy is converted into nuclear mass or binding energy [45]. In particular, for the FLUKA simulations at interaction level (Preex), as the target (silicon) is static, the initial kinetic energy is given by the only projectile (neutron), while the final energy is shared by the reaction products.

Secondary products are generated from many nuclear reactions, which depend on the incident neutron energy, as introduced in Section 4.2. When the primary neutron energy increases, more reaction channels can open, and consequently secondaries are generated from more reactions. Table 4.2 shows the ground state Q values and threshold energies E_{th} for the (n, α), (n,p), (n,d) and (n,t) reactions in the isotopes of natural silicon, extracted from FLUKA. Noteworthy, the threshold energies are slightly larger than the Q values (in absolute terms) because E_{th} is the energy required with respect to the laboratory (target nucleus at rest), while Q is relative to the centre of mass frame. Among the 3 isotopes, ^{28}Si is the most common, constituting 92.2% of natural silicon, while ^{29}Si and ^{30}Si represent 4.7% and 3.1%, respectively. For instance, many (n, α) reactions have the ground state $Q_0 = -2.65$ MeV and the reaction can be triggered by a neutron when its energy is larger than 2.75 MeV (see Table 4.2). However, although ^{29}Si is less abundant, the (n, α) reaction requires the incident neutron to have only 33 keV of energy and the very little Q value (-32 keV) indicates that the final products can have almost the incident neutron energy, to be shared between α and Mg. However, the same threshold is found to be around 1 MeV and 2 MeV from the ENDF and JENDL database, respectively (see Fig. 4.3). Q (absolute) values and threshold energies are instead increasing for the (n,d) and (n,t) reactions for heavier silicon isotopes.

Table 4.2: Q values and kinetic threshold energies for the (n,a), (n,p), (n,d) and (n,t) reactions for the three isotopes of natural silicon, retrieved from FLUKA.

		(n,a)	**(n,p)**	**(n,d)**	**(n,t)**
Si-28	Q_0 [MeV]	-2.65	-3.86	-9.36	-16.16
	Ek_{th} [MeV]	2.75	4.00	9.70	16.75
Si-29	Q_0 [MeV]	-0.032	-2.90	-10.11	-11.58
	Ek_{th} [MeV]	0.033	3.00	10.46	11.98
Si-30	Q_0 [MeV]	-4.20	-7.78	-11.28	-14.46
	Ek_{th} [MeV]	4.34	8.04	11.66	14.95

In the following, the cases with primary energies of 10 and 14 MeV will be analyzed in more detail, investigating the Si(n, α)Mg reaction, which is the most important at these intermediate energies as it presents the lowest E_{th}. To this regard, Table 4.3 shows the excited states of typical reactions occurring with neutrons of 14.1 MeV that were measured by a SiC pin diode in [52]. For every reaction, different excited states are shown with the respective (total) final energy of the products. For instance, for the ^{28}Si(n, α)^{25}Mg reaction, the final energy of the products at ground state is $E_i + Q_0 = E_\alpha + E_{Mg} = 11.3$ MeV. This energy will be shared between Mg and α in a continuous mode, while the excited state energies for the ^{25}Mg residual are discrete. This concept, which links the Q value to the nuclear reaction is explained in the following, taking the Si(n, α)Mg reaction as an example.

Table 4.3: Final energies of the excited states for different reactions, occurring with neutrons of 14.1 MeV and measured by a SiC pin diode (from [52]).

REACTION	BRANCH	ENERGY (keV)
^{12}C(n,α)^{9}Be Q=-5701.2 keV		
	Ground State - α_0	8298.8
	1st Excited State - α_1	6614.1
	2nd Excited State - α_2	5869.4
^{12}C(n,p)^{12}B Q=-12586.5		
	Ground State - p_0	1413.5
	1st Excited State - p_1	460.36
^{28}Si(n,α)^{25}Mg Q=-2653.7 keV		
	Ground State - α_0	11346.3
	1st Excited State - α_1	10761.26
	2nd Excited State - α_2	10371.56
	3rd Excited State - α_3	9734.533
	4th Excited State - α_4	9381.69
	5th Excited State - α_5	8544.83
	6th Excited State - α_6	7941.1
	7th Excited State - α_7	7932.33
	8th Excited State - α_8	7438.6
	9th Excited State - α_9	7375.6
	10th Excited State - α_{10}	7286.7
	11th Excited State - α_{11}	7069.5
	12th Excited State - α_{12}	6986.9
^{28}Si(n,p)^{28}Al Q=-3859.9 keV		
	Ground State - p_0	10140.1
	1st Excited State - p_1	10109.46
	2nd Excited State - p_2	9167.72
	3rd Excited State - p_3	9126.474
	4th Excited State - p_4	8767.15

The impinging neutron that triggers an inelastic interaction in silicon needs to have larger energy than the reaction threshold. When the inelastic interaction occurs, part of the kinetic energy is converted into mass and this process requires a Q quantity of energy, which is discrete for low states but can be continuous for higher ones. The output products of the reaction are normally a heavy residual (Mg), which is left in an excited state and a lighter particle (alpha). The residue (Mg) can be produced in many nuclear excited states, the more excited it is created, the less kinetic energy is left available to be shared, in a continues mode, between the products (alpha and Mg). More energy from the incoming neutron is required for higher excited states of the same reaction so that the final energy of secondaries decreases (see

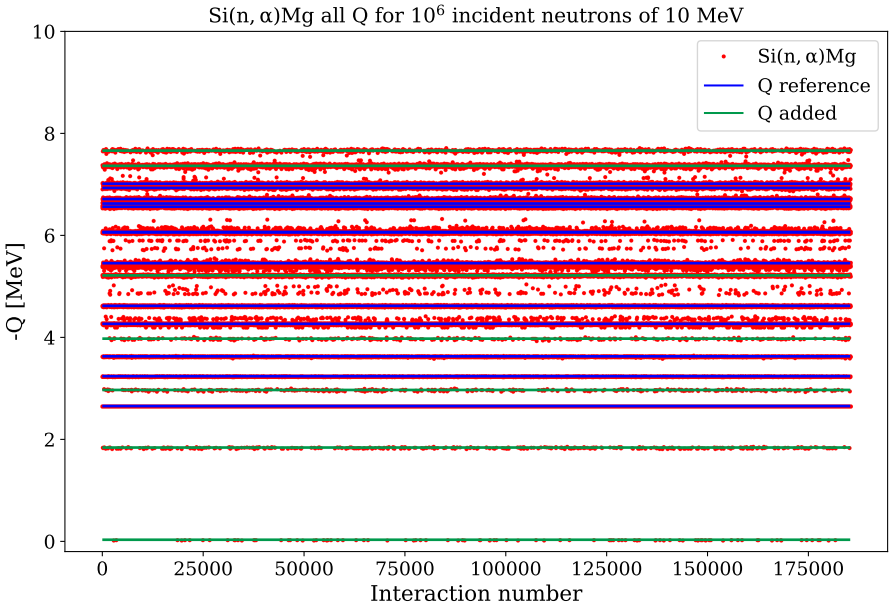

Figure 4.5: Q values for the Si(n, α)Mg reaction considering all isotopes - 10 MeV incident neutrons.

Table 4.3).

4.5.1 Q values (n,α) reactions - 10 MeV incident neutrons

For every interaction x, the energy of every product is used to calculate the corresponding Q value according to Eq. 4.7.

$$Q(x) = E_i - (E_\alpha(x) + E_{Mg}(x)) \tag{4.7}$$

Where E_i is 10 MeV in this case. Every Q value is shown in Fig. 4.5 with a red dot, for 10^6 incident neutrons in natural silicon, for every Si(n, α)Mg reaction, hence considering all Mg isotopes produced (^{25}Mg, ^{26}Mg, ^{27}Mg). In addition, in the same figure, the Q reference values[1] from Table 4.3 are represented with blue lines, while the green lines identify other Q values that are not included in the previous reference but are shown from the FLUKA (single interaction level) analysis. As can be noticed (Fig. 4.5), a minor number of Q values in the graph are scattered, and in general, the ones close to a Q line have a certain spread. Therefore, to consider a Q value (red dots) belonging to a certain line a spread margin was set to ±2%. It is interesting to note that the lowest Q value is at -0.032 MeV, followed by -1.84 MeV and then -2.654 MeV (lowest state of Table 4.3). These low values are owing to the ^{26}Mg isotope from the ^{29}Si(n, α)^{26}Mg reaction, as the target in the FLUKA simulation is composed of natural silicon (^{28}Si, ^{29}Si, ^{30}Si), while Table 4.3 considers only ^{28}Si. Fig. 4.6 depicts the three isotope contributions separately, for the three reactions ^{28}Si(n, α)^{25}Mg, ^{29}Si(n, α)^{26}Mg

[1]Although Table 4.3 shows the values for the 14.1 MeV case, the same reaction channels are open also with 10 MeV, because the threshold energy is lower than with 14.1 MeV.

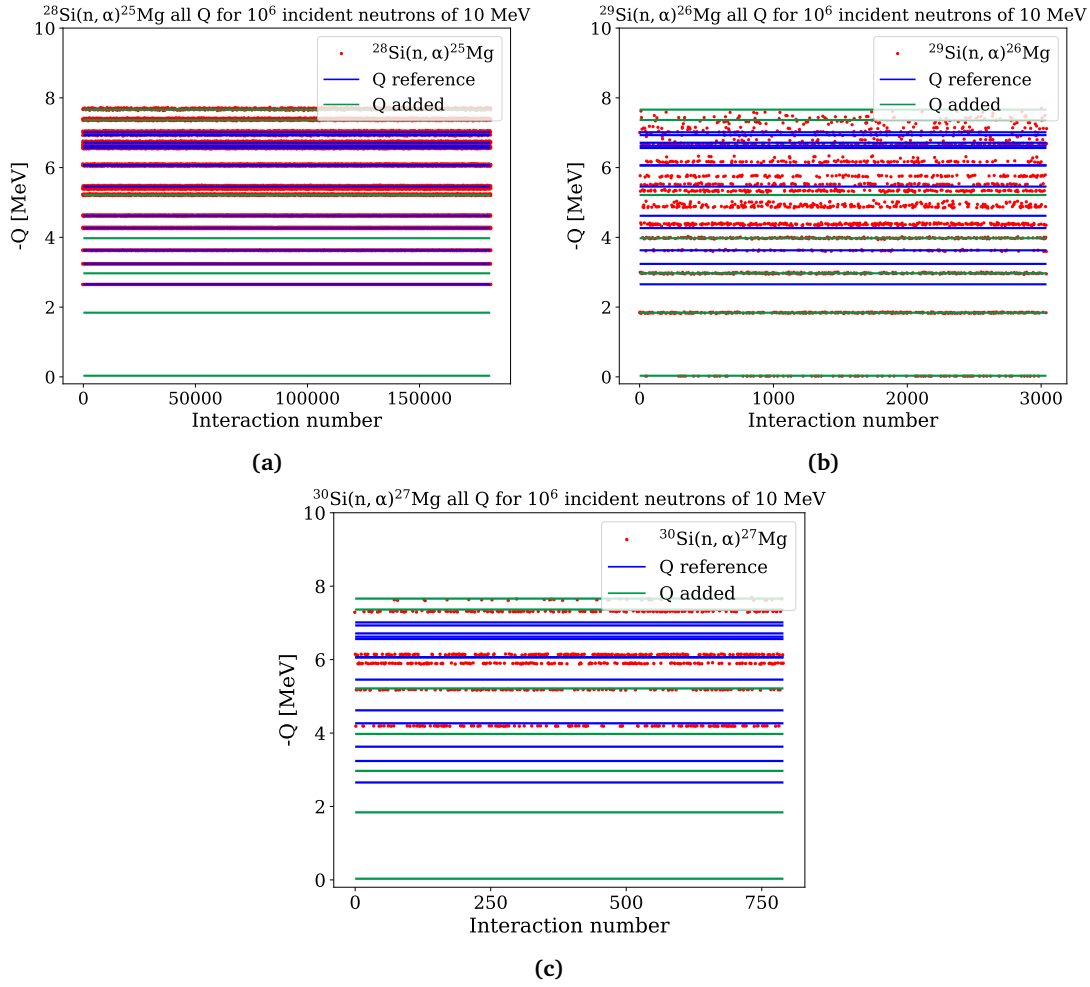

Figure 4.6: Q values for the Si(n, α)Mg reaction with the separation of the three Mg isotopes (^{25}Mg, ^{26}Mg, ^{27}Mg) - 10 MeV incident neutrons.

and ^{30}Si(n, α)^{27}Mg, respectively. Moreover, Table 4.4 shows the number of events associated to every Q state for these reactions, with their respective percentage on the total Q values (therefore the percentage is considering also those Q states that are not grouped in one of the "reference" or "added" states). Regarding the added Q Values, they are calculated considering the average Q values among the ^{28}Si(n, α)^{25}Mg reaction, which are the most abundant and exhibit a "line", with a spread of ±2%. These added Q values are shown in italic in Table 4.4. The sum of all the considered Q value events is calculated at the bottom of Table 4.4 and the Q_{tot}(%) percentage refers to how many Q value events are counted in this way, with respect to the overall Q. For instance, considering the Si(n, α)Mg reaction with all isotopes, the considered Q values (for a total of 184367 events) cover 99.5% of the total reactions (that are 185369). The events not counted do not appertain to any of the considered Q with the spread margin imposed, and are visible like scattered points in Fig. 4.5 and 4.6.

As can be noticed, 100% of the Q events are considered and belonging to a Q state line for the ^{28}Si(n, α)^{25}Mg reaction (see Table 4.4 and Fig. 4.6a), hence the majority of scattered Q

points in Fig. 4.5 are due to the interaction with ^{29}Si and ^{30}Si. Regarding these two isotopes, some other Q lines can be distinguished in Fig. 4.6b and 4.6c, but their events are negligible compared to those of ^{28}Si, except for the values with very low Q, which are already included in the analysis. Indeed, although the ^{29}Si abundance is only 4.7% in natural silicon, it presents the lowest Q values of 0.032 and 1.84 MeV, and secondaries can be a potential threat for inducing SEEs, because they share almost the initial neutron energy. However, ^{29}Si(n, α)^{26}Mg reactions are solely 1.6% the total (n, α), while the ^{28}Si(n, α)^{25}Mg and ^{30}Si(n, α)^{27}Mg cover 97.9% and 0.4%, respectively. As summarized in Table 4.4, with incident neutrons of 10 MeV, most of the excited states (19%) are at ground energy level (-2.654 MeV), and other relevant contributions around -4 and -6 MeV. The excited states at -6.059 and -6.068 MeV are too close in energy to be distinguished, hence the former Q assembles most of the Q values around these energies.

Table 4.4: 10 MeV incident neutrons - number of events for every Q value of the Si(n, α)Mg reaction and its isotopes. Q values in italic were added according to the FLUKA simulations, in addition to the ones of Table 4.3. Q_{tot}(%) refers to the Q values considered in this table with respect to the overall Q values of the same reaction, which includes also the scattered Q not appertaining to one of the considered lines.

-Q	$Si(n,a)Mg$		$^{28}Si(n,a)^{25}Mg$		$^{29}Si(n,a)^{26}Mg$		$^{30}Si(n,a)^{27}Mg$	
MeV	**N**	**%**	**N**	**%**	**N**	**%**	**N**	**%**
2.654	34986	18.9	34986	19.3	0	0.0	0	0.0
3.239	13175	7.1	13175	7.3	0	0.0	0	0.0
3.628	11037	6.0	10946	6.0	91	3.0	0	0.0
4.265	26055	14.1	25845	14.2	71	2.3	139	17.6
4.618	22637	12.2	22637	12.5	0	0.0	0	0.0
5.455	13507	7.3	13341	7.3	166	5.5	0	0.0
6.059	21415	11.6	21088	11.6	134	4.4	193	24.4
6.068	4	0.0	0	0.0	4	0.1	0	0.0
6.561	12963	7.0	12771	7.0	192	6.3	0	0.0
6.624	5431	2.9	5418	3.0	13	0.4	0	0.0
6.713	32	0.0	0	0.0	32	1.1	0	0.0
6.931	5618	3.0	5506	3.0	112	3.7	0	0.0
7.013	43	0.0	0	0.0	43	1.4	0	0.0
0.032	102	0.1	0	0.0	102	3.4	0	0.0
1.840	376	0.2	0	0.0	376	12.4	0	0.0
2.969	375	0.2	0	0.0	375	12.3	0	0.0
3.975	282	0.2	0	0.0	282	9.3	0	0.0
5.215	6882	3.7	6678	3.7	87	2.9	117	14.8
7.364	8079	4.4	7832	4.3	106	3.5	141	17.8
7.662	1368	0.7	1316	0.7	17	0.6	35	4.4
	N_{sum}	Q_{tot}(%)	N_{sum}	Q_{tot}(%)	N_{sum}	Q_{tot}(%)	N_{sum}	Q_{tot}(%)
	184367	99.5	181539	100.0	2203	72.5	625	79.1

4.5.2 Q values (n,α) reactions - 14 MeV incident neutrons

Similarly to the 10 MeV case, the Q values with 14 MeV incident neutrons are calculated and shown in Fig. 4.7 for the Si(n, α)Mg reaction considering all the isotopes together, and in Fig. 4.8 with the separate contribution of the three Mg isotopes. Table 4.5 shows the number of events associated to every Q values, as explained for the 10 MeV case in Section 4.5.1. Already at first glance, the Q values in Fig. 4.7 are many more than those expected from Table 4.3 (from [52], which refers to primary neutron energy of 14.1 MeV). The FLUKA output shows a continuum of Q states below about -7.7 MeV, and this behaviour is more clear in Fig. 4.8a showing only the Q values of the ^{28}Si(n, α)^{25}Mg reaction. Indeed, as previously observed also in the 10 MeV case, most of the scattered points are due to ^{29}Si and ^{30}Si (see Fig. 4.8b and 4.8c), but they are almost negligible compared to the ones from ^{28}Si. This difference is due

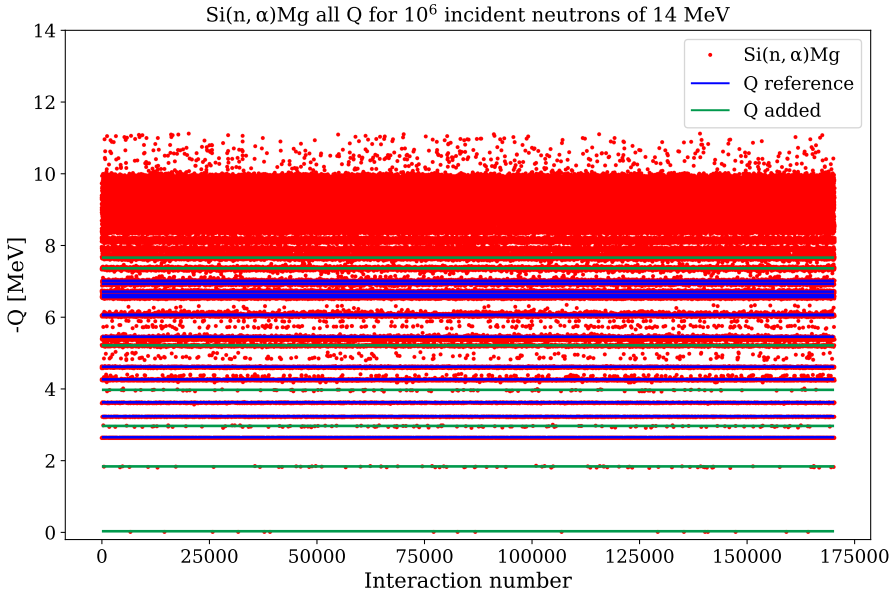

Figure 4.7: Q values for the Si(n, α)Mg reaction considering all isotopes - 14.0 MeV incident neutrons.

to the fact that in Table 4.3 the largest excitation energy for ^{25}Mg is set to 4.359 MeV, which can be calculated as the difference between the final energy at ground state (11.3463 MeV) and that at the 12^{th} excited state (6.9869 MeV), while the Mg structure is more populated, as shown in [53]. Below -7.3 MeV, the nucleus is no longer bound, becoming unstable for neutron emission. Considering all isotopes of the Si(n, α)Mg reaction, the clear Q state lines cover 61% of the total, therefore the remaining 39% are due to the continuum states, which are a substantial amount. This observation is experimentally shown in the silicon diode presented hereafter.

4.5.3 Silicon diode measurements

A silicon diode (Micron Semiconductors) was employed to measure the energy deposition spectrum of the secondary products generated with neutron beams, which deposit energy

Table 4.5: 14.0 MeV incident neutrons - number of events for every Q value of the Si(n, α)Mg reaction and its isotopes. Q values in italic were added according to the FLUKA simulations, in addition to the ones of Table 4.3. $\%Q_{tot}$ refers to the Q values considered in this table with respect to the overall Q values of the same reaction, which includes also the scattered Q not appertaining to one of the considered lines.

-Q	$Si(n,a)Mg$		$^{28}Si(n,a)^{25}Mg$		$^{29}Si(n,a)^{26}Mg$		$^{30}Si(n,a)^{27}Mg$	
MeV	**N**	**%**	**N**	**%**	**N**	**%**	**N**	**%**
2.654	5559	3.3	5559	3.4	0	0.0	0	0.0
3.239	2494	1.5	2494	1.5	0	0.0	0	0.0
3.628	2583	1.5	2555	1.6	28	0.6	0	0.0
4.265	7680	4.5	7611	4.6	41	0.9	28	1.8
4.618	8692	5.1	8692	5.3	0	0.0	0	0.0
5.455	7293	4.3	7111	4.3	182	3.9	0	0.0
6.059	15737	9.2	15386	9.4	165	3.5	186	12.1
6.068	6	0.0	0	0.0	6	0.1	0	0.0
6.561	13234	7.8	12958	7.9	276	5.9	0	0.0
6.624	5391	3.2	5347	3.3	44	0.9	0	0.0
6.713	197	0.1	138	0.1	59	1.3	0	0.0
6.931	7293	4.3	7081	4.3	212	4.5	0	0.0
7.013	93	0.1	1	0.0	92	2.0	0	0.0
0.032	17	0.0	0	0.0	17	0.4	0	0.0
1.840	82	0.0	0	0.0	82	1.8	0	0.0
2.969	124	0.1	0	0.0	124	2.6	0	0.0
3.975	105	0.1	0	0.0	105	2.2	0	0.0
5.215	3322	2.0	3177	1.9	74	1.6	71	4.6
7.364	12675	7.4	12226	7.5	240	5.1	209	13.6
7.662	11242	6.6	10859	6.6	262	5.6	121	7.9
	N_{sum}	$Q_{tot}(\%)$	N_{sum}	$Q_{tot}(\%)$	N_{sum}	$Q_{tot}(\%)$	N_{sum}	$Q_{tot}(\%)$
	103819	61.0	101195	61.7	2009	42.9	615	40.0

in the sensitive volume of the device. The results for the 14.8 MeV monoenergetic neutron beam measured at FNG in Frascati (see Section 5.4 for the facility description) are exposed in this section. Given its large sensitive area of 2 x 2 cm^2 and thickness of 300 µm, the diode is capable of detecting all secondaries produced from the reactions occurring at 14.8 MeV, which are discussed in the previous sections. Indeed, as will be shown in Section 4.8, the range of secondaries produced with these energies are mostly within the SV dimensions of the diode.

A picture of the diode can be seen in Fig. 4.9b, where it is visible the large silicon surface directly exposed without other layers of materials that could possibly contaminate the beam. As the diode is very sensitive to light, during the experiments the diode box was closed with an aluminium lid, which is thin enough for not attenuating the beam. The setup is schematically depicted in Fig. 4.9a from [54]. The diode was reversed biased at -120 V through a Source Measure Unit (SMU). The diode signal is a current pulse that is pre-amplified and sent to the CAEN digitizer, which converts the current signal in voltage V(t). The collected charge (Q_{coll}) is calculated offline through Eq. 4.8 from the wave-forms, pre-amplificator gain (G=43.9 dB = 157) and resistance (R=50 Ω).

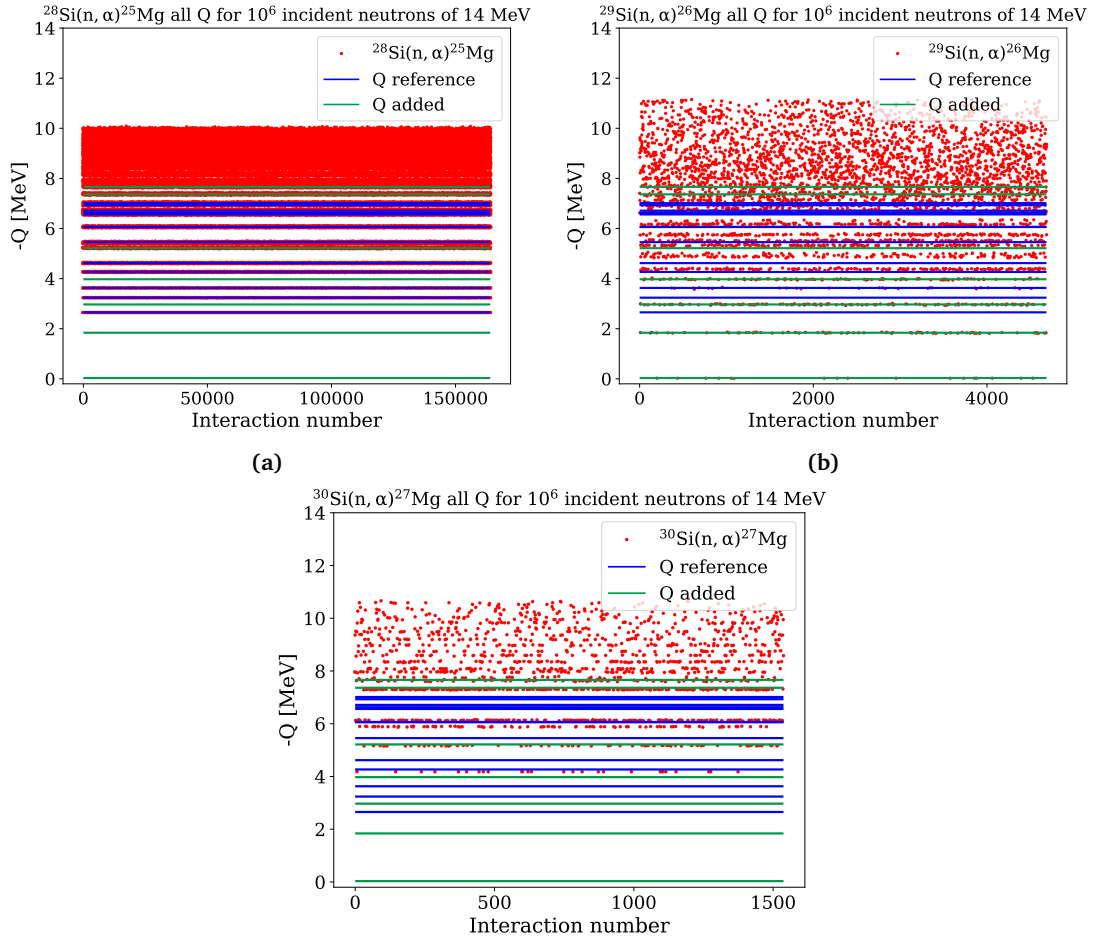

Figure 4.8: Q values for the Si(n, α)Mg reaction with the separation of the three Mg isotopes (^{25}Mg, ^{26}Mg, ^{27}Mg) - 14 MeV incident neutrons.

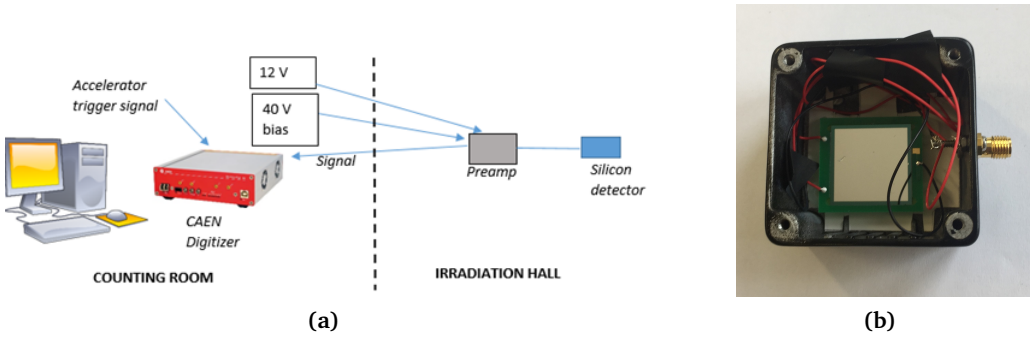

Figure 4.9: (a): Diode setup from [54]. (b) Picture of the diode inside its aluminium box, to notice the large active area 2x2 cm^2 (during the experiments the box is closed by a lid to avoid light detection.

$$Q_{coll} = \frac{1}{G} \cdot \int_{t=0}^{t_{fin}} \frac{V(t)}{R} dt \tag{4.8}$$

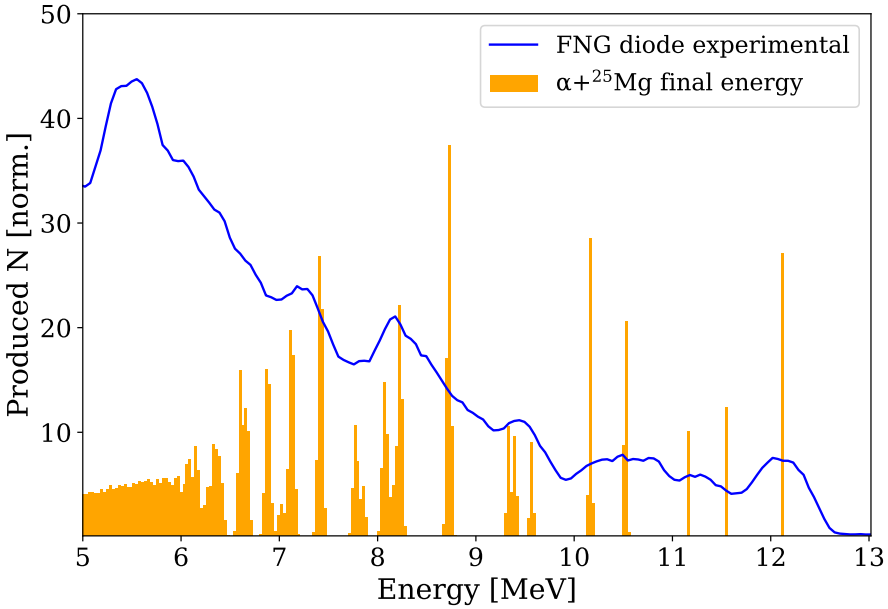

Figure 4.10: Spectrum of energy deposition measured by a 300 µm thick silicon diode with 14.8 MeV neutrons at FNG, and comparison to the inelastic final energy events calculated from FLUKA at single interaction level for the ^{28}Si(n, α)^{25}Mg reaction. Energy bins of 0.02 MeV.

The respective deposited energy is calculated through Eq. 4.9, where Q_{coll}/e is the number of electron-hole pairs produced (e elementary charge) and E_{eh} the average energy to produce an e-h pair in silicon (3.6 eV).

$$E_{dep} = \frac{Q_{coll}}{e} \cdot E_{eh} \tag{4.9}$$

Every E_{dep} is a count used to calculate the energy spectrum, which is shown in Fig. 4.10 measured with 14.8 MeV neutrons at FNG. The final energy of the inelastic events simulated in FLUKA for the ^{28}Si(n, α)^{25}Mg reaction are added for comparison (the values are arbitrarily normalized to fit in the same plot). Some of the Q values previously discussed are well visible in the experimental spectrum, for example, the ground state at $E_f = 14.8 - 2.65 = 12.15$ MeV. Other Q values can be distinguished, but the measured spectrum incorporates also the contribution of the other two main reactions occurring at 14 MeV: Si(n, p)Al and Si(n, n′)Si. The ground state of the ^{28}Si(n, α)^{25}Mg reaction is so well visible because is the only state that does not overlap with other excited states. For instance, the Si(n, p)Al ground state has final energy of 10.9 MeV (see values in Table 4.3 considering to add an offset of 0.7 MeV to the final energy values). In addition, as seen in the previous sections, the inelastic simulations from FLUKA are the result of a production Monte Carlo without any particle transport. Noteworthy the fact that results from a pure reactions point of view (production Monte Carlo) can explain experimental observations, which are only possible by means of sensitive devices, such as silicon diodes or diamond detectors [55].

4.6 Energy Distribution of Single Reactions

The energy distributions of the most relevant reactions (considered from Table 4.1) with two products are presented below (FLUKA simulations at the single interaction level), as the available energy after the nuclear interaction is differently shared among the secondary products of a certain reaction in a continuous mode. The energy binning is set to 0.2 MeV for primary energies of 10, 14, 20 MeV and to 1 MeV for 100 MeV. Therefore, the absolute comparison on the events number can be done only with same binning, although the main purpose of the graphs is to compare the shape of the spectra and see how the energy is shared between the products.

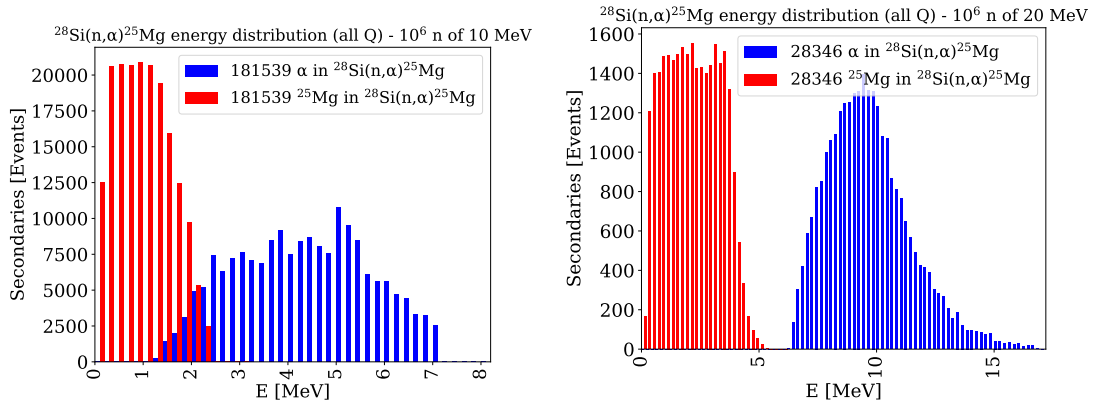

(a) **(b)**

Figure 4.11: Energy distribution of ^{28}Si(n, α)^{25}Mg secondaries, for incident energies of 10 and 20 MeV.

Regarding the Si(n, α)Mg, the energy distributions at 10 and 14 MeV is shown for the ^{28}Si(n, α)^{25}Mg reaction (Fig. 4.11). It can be noticed that increasing the incident neutron energy from 10 to 20 MeV the energy distribution of alpha particles is shifted to higher energies more significantly than that of Mg ions. Indeed, the maximum emission energy of both alpha and Mg increase, but the minimum energy rises only for the alpha, while the heavy Mg ion has a continuous spectrum down to almost 0 MeV. For this reason, while with primary neutrons of 10 MeV the two products can have same energies (between 1 and 2.5 MeV in Fig. 4.11a), with 20 MeV their spectrum do not overlap anymore. Showing the energy distribution of the corresponding ground state Q value (in Fig. 4.12a), the energy of Mg and alpha are well confined and the number of events is quite constant over the energy. Comparing Fig. 4.11a to Fig. 4.12a the fact that the energy of some secondaries overlap is to be attributed to Q values other than the ground state.

Furthermore, comparing the same figures, it is mainly the alpha particles that have a broader distribution of lower energies while Mg covers the same energy ranges, for both the ground state and all Q value distributions. Therefore, in the 10 MeV case for instance, the alpha particles associated to the Q=-2.6537 MeV have an average energy of 6 MeV, while the average energy is 4 MeV considering all the Q states (LET and ranges of 0.5 MeV $\cdot$ cm^2/mg, 32 μm and 0.7 MeV $\cdot$ cm^2/mg, 18 μm, respectively). However, even if Mg ions have lower

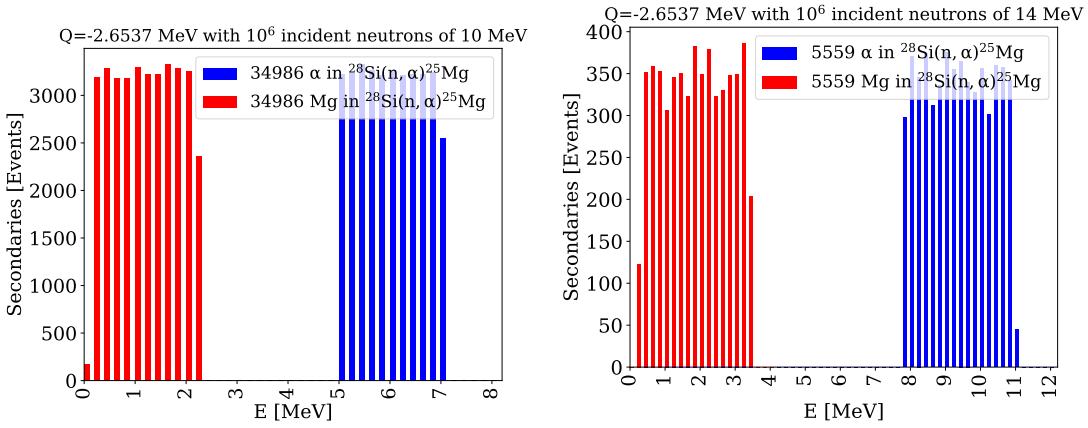

(a) **(b)**

Figure 4.12: Energy distribution of α and Mg ions for the ground state Q value at -2.6537 MeV, for incident neutron energies of 10 and 14 MeV.

energy, they have very high LET compared to the alpha particles. For example, with incident neutrons of 10 MeV, Mg has average energy around 1.1 MeV corresponding to a LET of 4.6 MeV $\cdot$ cm^2/mg and range of 1.6 µm. This aspect wants to highlight that not only the ground state is important for the associated energy deposition but especially the other excited states, since the associated average LET is higher than that of the ground state.

A similar behaviour to that of ^{28}Si(n, α)^{25}Mg is shown in Fig. 4.13 for the ^{28}Si(n, p)^{28}Al reaction, considering all Q values. Again, moving from primary energies of 10 to 20 MeV, the distribution of the lighter ion (proton) quickly shift towards higher energies, while Al receives less energy. The Si(n, n$'$)Si distributions are shown in Fig. 4.14 where two n' peaks are especially visible with 14 and 20 MeV, which imply there are at least two main Q values.

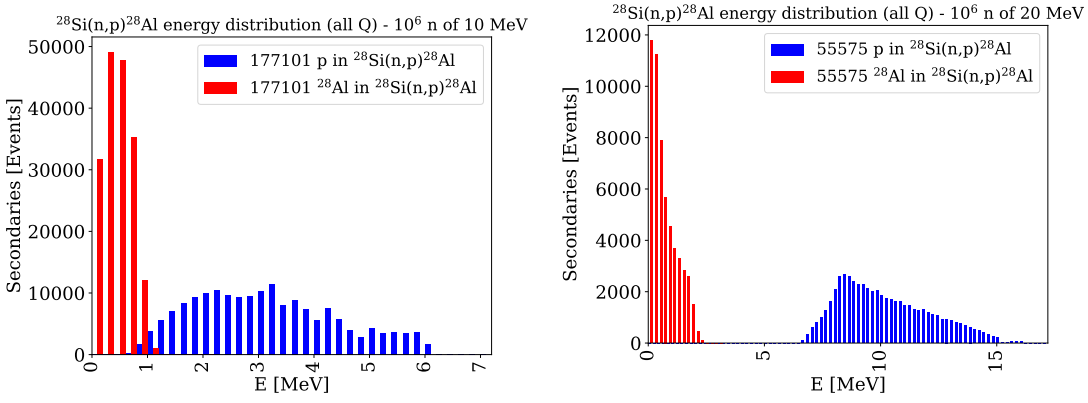

(a) **(b)**

Figure 4.13: Energy distribution of ^{28}Si(n, p)^{28}Al secondaries, for incident energies of 10 and 20 MeV.

The energy distributions of these reactions at 14 MeV, as well as that of Si(n, d)Al and Si(n, C)O at 20 and 100 MeV are shown in Appendix B.1 (Figures B.3, B.1 and B.2). Once again, it is confirmed that the energy is mostly shared to the lighter ion, and when the reaction

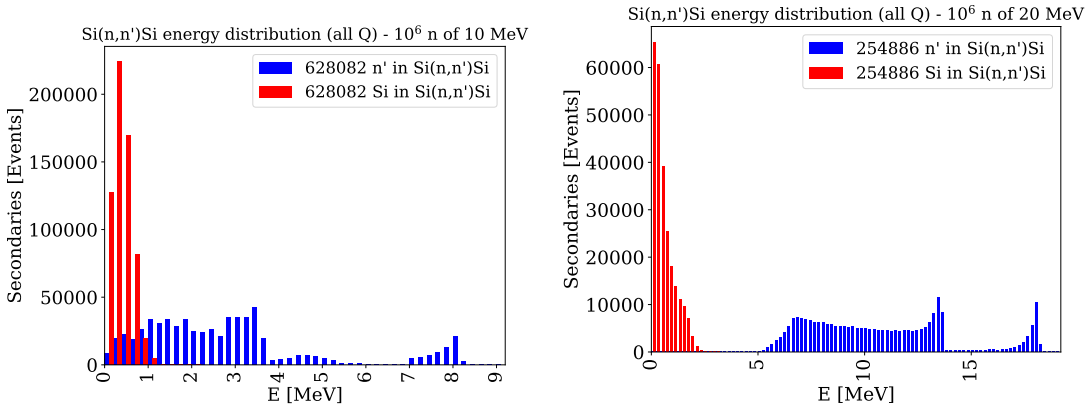

Figure 4.14: Energy distribution of Si(n, n′)Si secondaries, for incident energies of 10 and 20 MeV.

products have similar masses the energy is instead shared almost equally.

4.7 Contribution of Produced Ions in Depositing Energy for SEU

As seen in the previous sections, several reactions are produced with a monoenergetic neutron beam, generating different ions with different energies and probabilities. These ions concur in depositing energy in silicon, which is directly linked to the critical charge needed to trigger a SEE, according to their LET and range. Based on the energy distribution of secondaries and their properties formerly analysed (and others presented in Section 4.8), this section exposes some considerations on the impact that ions yield in depositing charge in the SV of a device.

As introduced in Section 2.3.1, the neutron SEU cross section is assumed saturated above 20 MeV, and experimental measurements on several SRAMs confirm this trend, as will be shown in Section 7.3.2. Table 4.6 provides an idea on how the SEU cross sections of several SRAMs decrease with energy decreasing, from the experimental data obtained at 17, 14 and 8 MeV in two facilities providing monoenergetic neutrons: FNG and PTB (see Chapter 6). In addition, the SEU cross section in saturation measured with high energy protons (>180 MeV) is reported for comparison. As can be seen, the SEU cross section at 8 MeV can result from being almost in saturation to 6 times lower with respect to the 17 MeV value, while at 14 MeV the ratio ranges around a factor of two.

The simulations on the inelastic interactions explain the general increase of the SEU cross section as a function of the energy. As exposed in Section 4.4.2 the open reaction channels between 10 and 20 MeV are mainly three: Si(n, xα)Mg, Si(n, xp)Al and Si(n, xn′)Si, where "x" is an additional neutron in some cases. Aiming at identifying those ions that contribute most in depositing energy, secondary neutrons can be neglected as they have to indirectly

Table 4.6: SEU cross sections of SRAMs measured at FNG and PTB with 17, 14 and 8 MeV monoenergetic neutrons and ratio with respect to the values at 17 MeV. The cross section in saturation was measured with high energy protons (>180 MeV).

Device	$\sigma_{17\text{ MeV}}$ [cm^2/bit]	$\sigma_{14\text{ MeV}}$ [cm^2/bit]	$\frac{\sigma_{17}}{\sigma_{14}}$	$\sigma_{8\text{ MeV}}$ [cm^2/bit]	$\frac{\sigma_{17}}{\sigma_{8}}$	σ_{sat} [cm^2/bit]
ISSI 40 nm	$1.91{\cdot}10^{-14}$	$9.81{\cdot}10^{-15}$	1.9	$7.77{\cdot}10^{-15}$	2.5	$1.40{\cdot}10^{-14}$
Cypress 65 nm	$8.19{\cdot}10^{-14}$	$4.60{\cdot}10^{-14}$	1.8	$6.49{\cdot}10^{-14}$	1.3	$7.73{\cdot}10^{-14}$
Cypress 90 nm 8 Mbit	$1.25{\cdot}10^{-13}$	$5.06{\cdot}10^{-14}$	2.5	$2.02{\cdot}10^{-14}$	6.2	$2.16{\cdot}10^{-13}$
ESA M. 250 nm	$2.37{\cdot}10^{-14}$	$1.84{\cdot}10^{-14}$	1.3	$5.63{\cdot}10^{-15}$	4.2	$2.60{\cdot}10^{-14}$

interact one more time with matter. Moreover, in first approximation also secondary protons can be neglected with respect to Al, because as will be shown in the energy distributions of Section 4.8, the range of protons at the energy corresponding to their production peak is 2 μm with LET of 0.11 MeV $\cdot$ cm^2/mg, similar to that of Al (1.1 μm) but with LET of 3.3 MeV $\cdot$ cm^2/mg.

Therefore, four ions can be considered of major importance: Mg, alpha, Al and Si. Table 4.7 shows their production percentage, energy, LET and range at the production peak and the maximum range for each ion, calculated for incident neutron energies of 10, 14 and 20 MeV. In addition, the corresponding reaction cross section is calculated from Eq. 4.1. As can be seen, in the 20 MeV case, the range of Mg, Al and Si are within 3.5 μm, while the alpha particle can reach up to 120 μm. Analogous considerations can be done for the 14 and 10 MeV cases, where the maximum range of the heavier ions is even lower. Therefore, the three heavier ions are only generated relatively close to the SV within a few μm, while the alpha particles can reach the SV even if generated far from it.

Table 4.7: Main secondary ions produced with incident neutrons of 10, 14 and 20 MeV with corresponding energy, LET and range at the production peak (p) or maximum (max). The ion's percentage is referred to the significant secondary particles and the maximum range and reaction cross section are calculated from 10^6 interactions. Mg and α ions are the products from the same reaction.

E_{inc} [MeV]	Ion	(%)	E_p [MeV]	LET_p [MeV $\cdot$ cm^2/mg]	$Range_p$ [um]	$Range_{max}$ [um]	$\sigma_{reaction}$ [mb]
10	Mg	16	1	4.3	1.5	2.4	203
	α	16	4	0.7	18	24	203
	Al	15	0.5	2.5	0.8	1.3	196
	Si	53	0.4	2.5	0.5	1	687
14	Mg	16	1.4	5.5	1.8	2.9	209
	α	16	5	0.6	24	70	209
	Al	17	0.75	3.3	1.1	1.8	222
	Si	51	0.6	3.3	0.8	1.3	655
20	Mg	16	1.5	5.7	1.9	3.4	201
	α	16	5.5	0.6	28	120	201
	Al	42	0.75	3.3	1.1	2.3	560
	Si	26	0.5	2.9	0.7	1.7	330

As can be deducted from Table 4.7, aluminium ions are expected to give the largest contribution in depositing energy in silicon at 20 MeV and hence to the neutron SEU cross section, while silicon ions are instead more effective at 10 and 14 MeV.

Impact of alpha particles in depositing energy

FLUKA simulations were carried out to calculate the effect of alpha particles on the deposition of energy inside a SV, as their range is up to two orders of magnitude larger than the range of the other ions generated with energies below 20 MeV. In fact with the approximation introduced above, all ions produced within 3.5 µm from the SV are assumed to have unitary weight, but an additional contribution needs to be accounted for alpha particles. For this purpose, a silicon target with a surface of 54 x 54 μm^2 was considered (which are typical dimensions for SEU simulations for SRAM) and several simulations were performed by varying its thickness (z) from 5 to 150 µm. The SV is modeled with a 10 x 10 matrix composed of 100 RPPs, each one with dimensions of 0.5 x 0.5 x 0.5 μm^3. Fig. 4.15a shows the energy deposition events by varying the target thickness in one side with respect to the location of the RPPs. To this regard, the notation "a-b µm" is used to denote the silicon thickness before (a) and after (b) the RPPs along the z-direction, parallel to the beam. The neutron beam of 20 MeV was simulated covering the whole target surface and corresponding to a fluence of $6 \cdot 10^{13}$ n/cm^2 ($3.4 \cdot 10^4$ n/cm^2/pp).

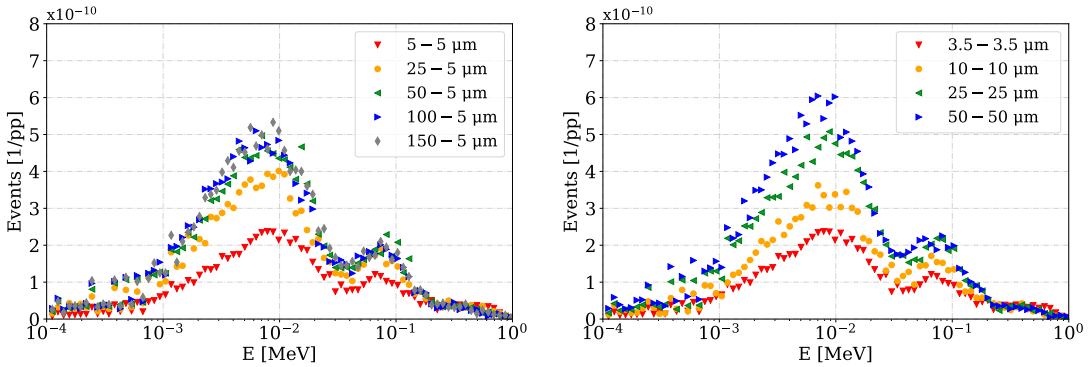

(a) **(b)**

Figure 4.15: Events of energy deposition normalized per primary particle, for 20 MeV incident neutrons in silicon. Several thicknesses of the silicon target are considered and shown in the notation of "a-b µm", where "a" and "b" are the thicknesses before and after the RPPs, respectively.

As can be seen (Fig. 4.15a) the energy deposition significantly increase from 5 to 25 µm of thickness and it saturates after 50 µm. Considering this observation, the deposited energy was calculated considering the full two z-sides of the geometry and the distributions are shown in Fig. 4.15b for several thicknesses. Even with 25-25 µm the events shape is similar to that of 50-50 µm, and considering that the higher the energy of the distribution, the larger the weight on the events, the two are very similar. In addition, only energies above a certain value can be considered inducing SEUs depending on the critical charge of the device. For this evaluation, devices with Q_c greater than 0.5 fC are considered, corresponding to an energy of 11 keV.

Hence, the event probabilities are summed above 11 keV and the results are reported in Table 4.8, where the increase of energy deposition events is shown with respect to the 5-5 μm case (in percentage). In first approximation, the additional alpha particle contribution with respect to the heavier ions with incident neutrons of 20 MeV can be calculated comparing the events with target thickness of 5-5 and 50-50 μm, and the difference results of 95%.

Another interesting information can be extracted from Table 4.8 regarding the effects of alpha particles with respect to the beam direction. The beam was simulated travelling from the left to the right of the z-axis, hence the particle fluence will invest first the region "a" and after the region "b". Comparing the cases where the silicon target was only considered before (50-5 μm) or after (5-50 μm) the RPPs to the full thickness (50-50 μm), the additional contribution is +72%, +36% and +95%, respectively. Therefore, alpha particles are ejected with a vector component in forward direction with respect to the beam for 67% of the times, and backwards the remaining 33% of the times.

Table 4.8: Sum of deposited energy events above 11 keV for several target thickness, from the distributions of Fig. 4.15 and differences with respect to the 5-5 μm case.

Thickness a-b [um]	5-5	25-5	50-5	100-5	150-5	10-10	25-25	50-50	5-50
Events ($\cdot 10^{-9}$)	3.4	4.8	5.9	5.6	5.9	4.5	6.2	6.7	4.7
(%) to 5-5 μm	-	+41	+72	+63	+73	+32	+82	+95	+36

4.8 Energy Distribution of Secondary Products at Several Incident Energies

As shown in Section 4.4.2, the study of secondary particles generated by neutrons in silicon can be performed from a single reaction point of view until 20 MeV. Above this energy the reaction channels are too many to be studied individually, hence it is more convenient to analyze the secondaries from the overall contribution of all the possible reactions. The goal through this study is to retrieve information on the ion contribution that potentially induce SEEs, and explain why the SEU cross section does not increase anymore with increasing the neutron energy up to 1 GeV.

In the following section the energy distribution of the produced secondaries is presented, for incident neutron energies of 10, 14, 20, 50, 100, 200, 500, 1000 MeV in natural silicon. Energy distributions are shown for all the possible produced ions, from the alpha (Z=2) to Phosphorus (Z=15). The number of events in the axis ordinate is the absolute value of the produced ions, with a statistic of 10^6 incident neutrons in silicon (each neutron is forced to produce a nuclear reaction). The data shown on these graphs are discrete quantities, every point can be though as the bar of a histogram. To better enhance and follow the trend of every curve, the data points are connected by segments, only if the events per energy bin are larger than 5 (for incident neutrons $\geq$ 50 MeV). Hence, it has to be noted that the curves

are not continuous functions. The percentages reported on the plots for every energy are calculated considering the overall number of secondaries produced from (Z=1) to (Z=15), including neutrons and silicon from the Si(n, n′)Si reaction, protons and pions (if generated). As energies can range of different orders of magnitude depending on the ion, the plots are shown in logarithmic and linear scales. In the logarithmic graphs all the events are included (even the very rare ones consisting in just a single entry), whereas in the linear plots the axis energy was limited in order to see the general ion trend with higher resolution. To this regard, and for an adequate view of the graphs, the energy binning was set to 0.25 MeV and 0.1 MeV for the logarithmic and linear plots, respectively (otherwise, it will be specified in the figure caption). Therefore, the absolute event value of the two plot types cannot be compared because directly dependent on the energy binning. Moreover, all produced isotopes are considered together for every ion. The respective LET and range of the ions extracted from SRIM [2] are depicted in every plot.

4.8.1 Secondary ions: from P (Z=15) to Li (Z=3)

In the following subsection, the analysis of the energy deposition of ions from phosphorus to lithium is exposed. Most of the corresponding energy distributions, from which these considerations are drawn, are reported (and referenced) in Appendix B.2 for readability of the section.

Although secondary products from n-Si reactions are generally composed by atomic number smaller or equal to 14 (silicon), with high incident energies (>200 MeV) even phosphorus P (Z=15) can be produced. Its amount is however negligible compared to that of other ions (see Fig. B.5).

Si ions (Fig. B.6) are produced in high percentage (∼ 30%) at low energies below 20 MeV, but above 100 MeV they constitute only less than 2% of total ions. For incident energies of 10 and 14 MeV, the production of silicon involves only two possible reactions: Si(n, n′)Si and $Si(n, 2n')Si$, of which the former occurs 99% (10 MeV) and 92% (14 MeV) of the times, respectively. With higher energies other reaction channels may open, for example $Si(n, 3n')Si$ or $Si(n, \pi^- n' p)Si$. However, the reaction Si(n, n′)Si happens most of the times, where the incident neutron gives part of its energy to the silicon atom. Even in terms of absolute quantities (see the linear plot of Fig. B.6), silicon ions are produced primarily with low incident energies (<20 MeV). The majority of secondary silicon have energies below 1 MeV.

Al ions (Fig. B.7) are mostly produced with incident neutrons of 20 MeV (19.5% of the total), with an absolute value 3 times larger than with 10 and 1000 MeV. The majority of secondary Al have energies below 2 MeV.

Mg (Fig. 4.16) is still produced with relatively large percentages on the total ions, with the absolute maximum with incident neutrons of 100 MeV, a factor almost twice as many as the case with 10 MeV and 1000 MeV. Once again, as with aluminium, the produced quantities (absolute values) at 10 MeV and 1000 MeV are essentially the same.

The relatively heavy ions (Si, Al, Mg) produced from the interaction of neutrons in silicon

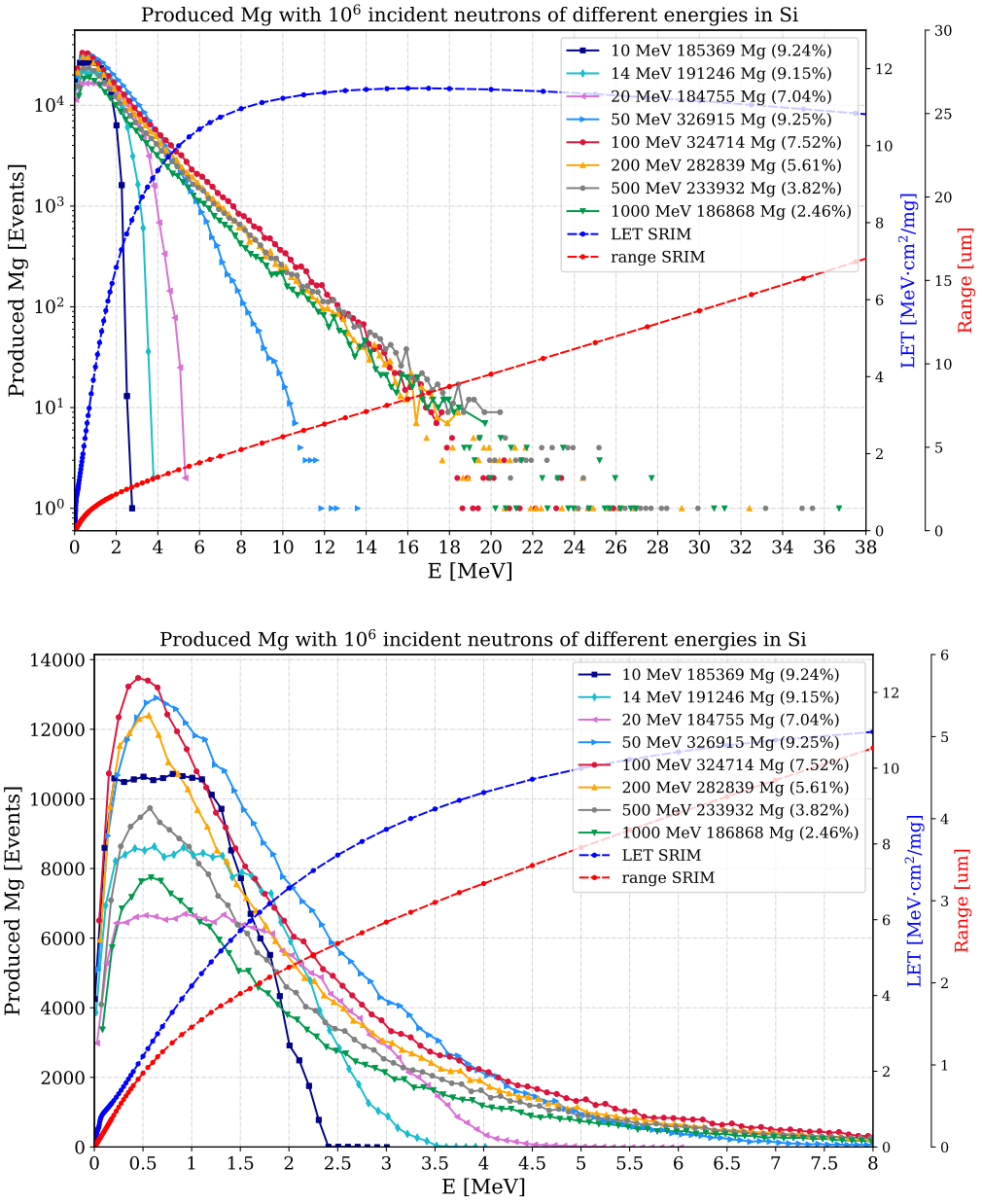

Figure 4.16: Energy distribution of Mg ions in log and linear scale, with energy bins of 0.25 and 0.1 MeV, respectively.

show a similar shape for incident neutron energies above 100 MeV, as can be seen in the respective logarithmic plots (Fig. B.6 - 4.16). Considering incident energies of 100, 200, 500 and 1000 MeV the curves decrease almost linearly, therefore exponentially in linear scale, and the absolute number of ions produced from 100 MeV are always in larger quantity, followed by the 200, 500 and 1000 MeV curves. In addition, the maximum production peak (see the linear plots of Fig. B.6 - 4.16) with 100 MeV is up to 2 times higher than that with 1000 MeV and the proportion is maintained similar for higher ion energies. Hence, increasing the incident neutron energy above 100 MeV does not imply to produce more relative heavy ions.

Na and lighter ions are not produced with 10 and 14 MeV. Na and Ne are produced in the highest absolute quantity with incident neutrons of 100 MeV, with higher relative percentage compared to silicon (both around 2.5%). Curve shapes and proportions for incident neutrons above 100 MeV still apply, as with heavier ions.

The number of secondaries produced with 100 MeV (with respect to the other incident energies) is not the highest anymore from F (Fig. B.10) to lighter ions, where higher incident energies, in particular 1000 MeV, are instead able to generate more light fragments. F and N (Fig. B.10-B.12) compose less than 0.54% of the total ions, while O and C can reach up to 1.5% (Fig. B.11-B.13). Therefore, although as a general behaviour ions with higher atomic number (Z=14) are produced in larger quantities with respect to those with lower values, for adjacent ions in the periodic table this is not always the case (as F and O or N and C). In addition, with lighter ions such as O (Fig. B.11) or C (Fig. B.13), the ratio between the number of secondaries created from incident neutrons of 1000 and 100 MeV increases with increasing of the ion emission energy (while it was almost constant with heavier ions). For instance, the aforementioned ratio for C ions on its maximum (3 MeV) is 2, and one y-decade lower (16 MeV) the ratio is 4. This effect accentuates more and more with B, Be and Li. The maximum amount of B and Be from 1000 MeV is less than 0.7% and for Li it is 1.3%. As far as B is concerned, 40% of its produced isotopes are ^{10}B, differently from the 20% abundance found in natural boron. However, they are produced in small proportion when compared to the bulk materials, and therefore they can be neglected for potential interactions with thermal neutrons.

4.8.2 Secondary ions: He (α), deuteron and tritium

He ions are produced in relatively high percentage on the total ions, around 9% with incident neutrons from 10 to 100 MeV and up to 15% with 1000 MeV (Fig. 4.17). Most of He ions are constituted by alpha particles, which amount depends on the incident neutron energy. Alpha particles are at least 90% of the total He ions (with 1000 MeV) and their percentage increases with lower incident energies (95% with 100 MeV). Their maximum energy at which they can be created is very close to the incident neutron energy, hence their spectrum is wider than with heavier ions. This aspect proof that the energy of the incident neutron can be almost entirely transferred to light ions. The peak of secondary He, for all incident energies, is produced at 4-5 MeV with a LET of 0.65 MeV $\cdot$ cm^2/mg and rage of 21 µm. However, the alpha ranges can largely vary up to the order of mm when their energy is greater than 300 MeV. In absolute terms, one alpha particle is generated every two incident neutrons of 100 MeV, while more than one alpha is produced with 1000 MeV. the alpha particles are twice as many passing from 20 to 100 MeV and these aspects will be used to draw some considerations concerning SEE.

Similar considerations can be drawn for deuteron and tritium ions, where Fig. B.17 shows their combined contribution (therefore, protons are not included in this graph, they are separately shown in Fig. B.18), with the difference that below primary energies of 100 MeV they are poorly produced compared to alpha, and above 100 MeV they compose about 6% of the

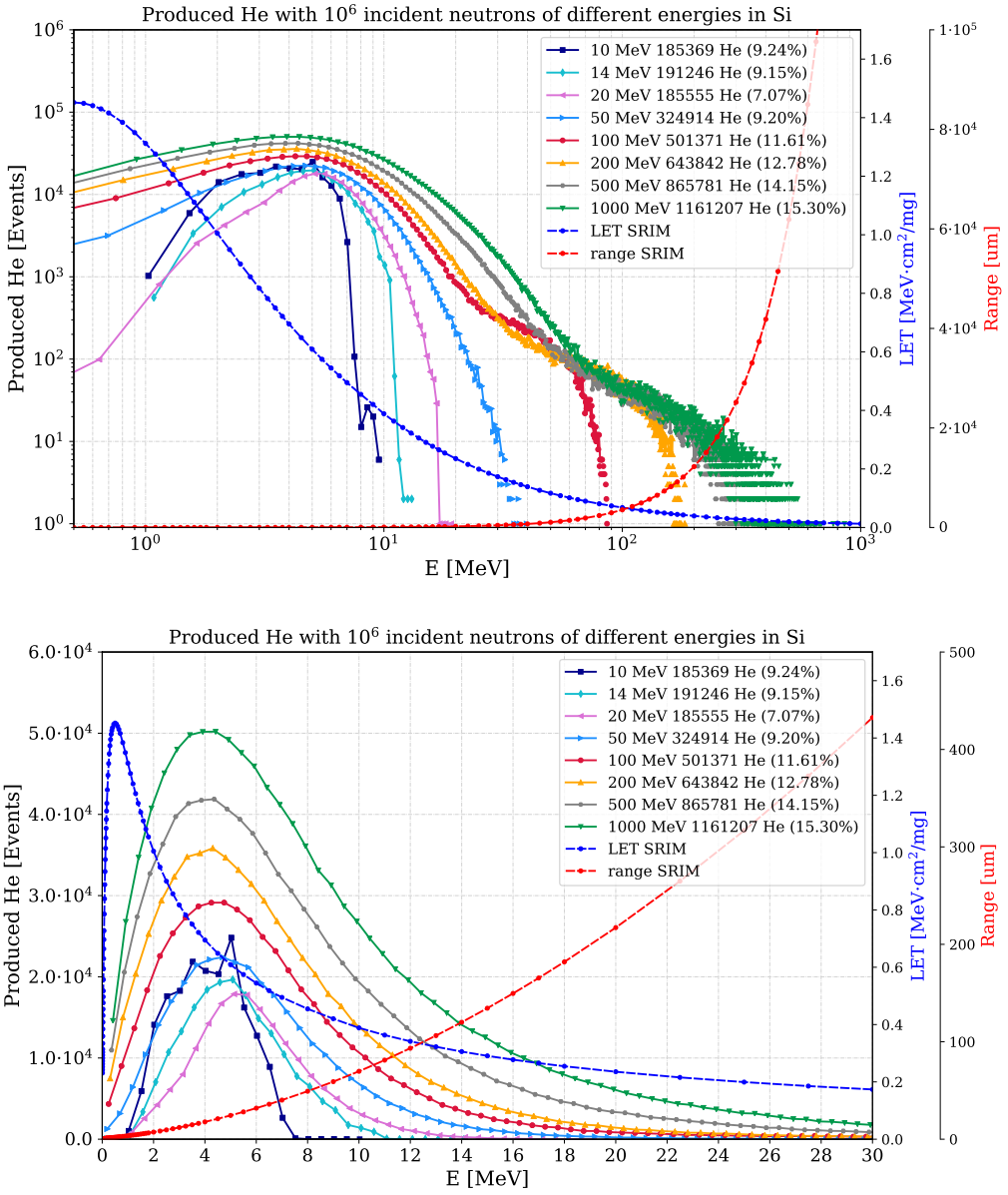

Figure 4.17: Energy distribution of He ions in log and linear scale, with energy bins of 0.5 MeV. LET and range from SRIM are relative to α particles

total ions (Fig. B.17). Considering the overall H ions, protons constitute 80% of them above incident neutrons of 100 MeV, followed by about 18 % of deuteron and less than 4% of tritium.

4.8.3 Secondaries: neutrons and protons

It is worth to bear in mind that these spectra are discrete quantities resulting from a energy binning in this case of 0.5 MeV (both logarithmic and linear scales, for neutrons and protons). The connecting segments between two points are only the mean to better follow the general trend of the distribution. Therefore, the events with very low energies (from 0 to 0.5 MeV)

are all counted in the first point, but this does not imply that there are not particles with lower energies than 0.5 MeV. This aspect is particularly important for protons where low energies can play a significant role in inducing SEEs but less meaningful for ions (shown before).

Secondary neutrons can be in part those incidents, which lost energy in the inelastic interaction, and the others are produced from reactions. As shown in Fig. 4.18 the neutron spectra (spallation) vary from 0.5 MeV up to the incident particle energy, and they are produced with the highest percentage (more than 30%) among secondaries (linear plot in Appendix, Fig. B.4). The lowest energy at which neutrons are produced can be considered 1 keV, where less than 20 events occur with a binning of 10 eV. For almost every incident neutron of 20 MeV another neutron is produced as a secondary, and above 50 MeV the secondary neutrons are more than the primary ones, up to a factor of 2.4 with 1000 MeV. As can be noticed, their production is relatively large from low energy (1 MeV) to about 70% of the primary energy. For instance, with the primary energy of 100 MeV the number of secondary neutrons with 70 MeV is only 18 times less than those at the maximum production around 1 MeV. In turn, these secondary neutrons can interact with the silicon atoms and generate other cascades of secondaries.

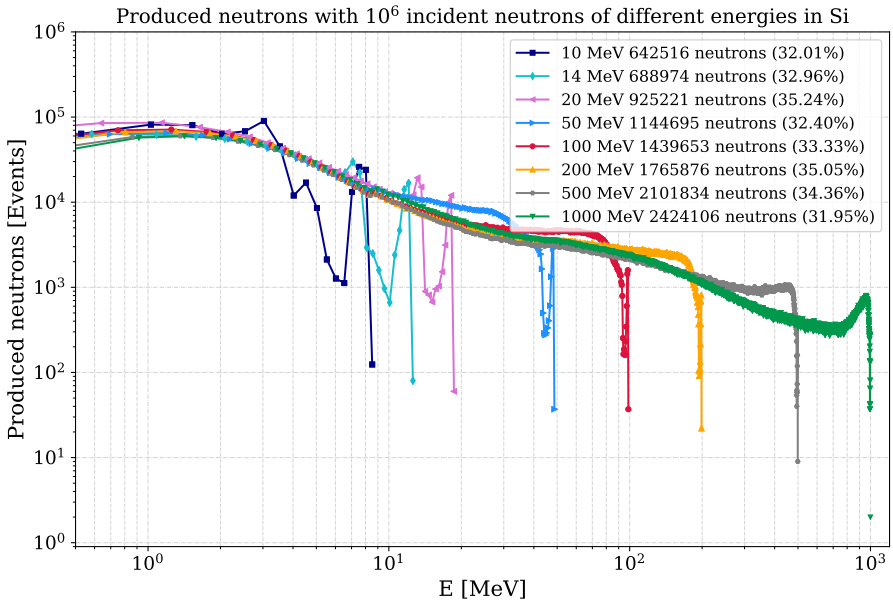

Figure 4.18: Neutron energy distribution (spallation) in log scale, with energy bins of 0.5 MeV

Secondary protons, similarly to neutrons, show a wide spectrum from 0.5 MeV up to the primary energy, but they are produced in minor percentage, especially from 50 MeV and lower incident neutron energies, to reach up 27% with 1000 MeV (See Appendix Fig. B.18). The peak of production is around 2-3 MeV and, as with neutrons, they are considerable from low energies up to 70% of the primary energy value, with an attenuation between these energies of about 2 orders of magnitude. In absolute terms, for every incident neutron of 100 MeV one proton is produced, and the proportion increments with increasing the primary energy up to a factor of 2 with 1000 MeV. Less than 10 events are produced below 10 keV (binning of 10

eV) and it can be considered as the lowest energy for the proton production.

4.8.4 Conclusions

As exposed in the previous sections, the properties of secondary produced ions by varying the incident neutron energy are not trivial to extract, but some conclusions from this analysis are provided below.

In a certain reaction producing one of the ions, as a general fact, the impacting neutron transfers most of its energy to lighter ions rather than to heavier ones. Secondary alpha, for instance, can have transferred up to 96% of the incident neutron energy (with 10 MeV), while the heavier silicon only up to 12%. Increasing the incident energy up to 1000 MeV these percentages decrease to 66% and 2%, respectively.

Lighter ions (from H to B) have the production peak with energy higher than that of the Bragg peak, hence when travelling inside silicon losing energy the LET of these ions will increase. Heavier ions instead are produced mostly with energies to the left of the Bragg peak, therefore their LET can only decrease with the distance.

Secondary ions produced with primary energies above 100 MeV have similar distributions, in shapes and quantities, from Si to F, whose ions present the greatest LET. Moreover, Si, Na and Ne ions are produced in similar percentages, and Al and Mg are produced with the highest amount compared to all the other ions (until Li). Therefore, given their similar distribution and importance above 100 MeV, the simulations explain in a qualitative way the reason why the experimental SEU cross section is normally saturated above 100 MeV, and testing with higher energies does not significantly impact its value. While heavier ions are more important in inducing SEUs until about 100 MeV, above this energy their percentage of production decrease and intermediate and lighter ions are produced in increasing quantities, so that the SEU cross section above 100 MeV is saturated because of a balance between heavier and lighter ions. This aspect is further analysed in Section 4.9.

4.9 LET and Energy of Secondary Ions

Aiming at better quantifying the contribution that secondaries yield to ionize atoms, the events from the distributions shown in the previous Section 4.8 are grouped in LET intervals of 1 MeV $\cdot$ cm^2/mg up to 15 MeV $\cdot$ cm^2/mg, for single incident energy.

Every ion, including its possible isotopes, from Z=14 (Si) to Z=1 (H), is represented with a coloured bar. Notably, most of the He ions are α particles and H ions are protons, deuteron and tritium. For graphical reasons, the bars of the ions Z=[14,8] and Z=[7,1] are respectively overlapped, showing the ion's bar with fewer events in front. The energy to LET conversion is performed through the SRIM database [2], associating every energy of secondaries to the closest energy of the SRIM tables and consequently its LET (electronic stopping power). It has to be noted that this LET is the theoretical value possessed by the ion as soon as it is created.

Moreover, the corresponding graph of secondaries grouped in energy intervals is shown as well, where the energy bins differ based on the different incident neutron energy. These energy intervals can be read directly from the ticks of the x-axis. Fig. 4.19 shows the LET (top figure) and energy (bottom figure) of all the secondary products generated in inelastic interactions, with incident neutrons of 10 MeV in silicon. The statistic considers 10^6 neutrons, each of which creates an inelastic interaction (Production Monte Carlo). Every event with LET_x is counted in one of the intervals where $LET_i < LET_x < LET_{i+1}$ for $i = [0, 14]$. For instance, all events with a LET between 0 and 1 MeV $\cdot$ cm^2/mg are shown in the first bar of the graph. The absolute number of secondaries and their relative percentage on the overall products are shown in the legend. In addition, secondary neutrons, protons and pions are included in the graph in a separate box. The relative percentage is calculated on the total produced ions. To notice that H and He ions consider also those more rare isotopes different from protons and alpha particles, respectively. The evolution of produced ions using incident neutrons energies of 10, 14, 20, 50, 100, 200, 500, 1000 MeV is shown in the case of 10 and 100 MeV in Figs. 4.19 and 4.20, respectively. The plots regarding the other energies are reported in Appendix (from Fig. B.19 to Fig. B.24) and the following results are drawn also on the basis of these data.

As can be noticed, only relatively heavy ions are produced with primary neutrons of 10 MeV (Fig. 4.19): Si, Al and Mg, in addition to the alpha particles, where for this energy they are generated from the Si(n, α)Mg reaction. The same ions species are produced with incident neutrons of 14 and 20 MeV, although a negligible amount of O and C is generated with the latter energy from the Si(n, C)O reaction. As the primary energy increases, more and more secondary ion species are generated. Even with 50 MeV (Fig. B.21) all ions are produced, from silicon to lithium. The amount of lighter ions becomes greater by increasing the incident neutron energy, while the quantity of heavier ions decreases. Silicon ions, for instance, are produced in high percentage (>10%) on the total amount until incident neutrons of 20 MeV, and their production decreases down to 1% with 1000 MeV. However, the silicon LET is the largest among all the ions with incident energies higher than 50 MeV, and up to value of 14 MeV $\cdot$ cm^2/mg above 100 MeV. Below 50 MeV the magnesium LET is instead the greatest. As a general behaviour for all the incident energies, Si, Al and Mg ions have the highest LET values.

Some considerations are drawn from the LET graphs of Figures 4.19 to B.24, moving from the highest to the lower LET values, and observing that once an ion is generated with a certain LET, it is always produced with lower LET values (in different quantities).

- For incident neutron energies until 20 MeV (see Fig. 4.19, B.19, B.20): Similarly to what shown in Section 4.6, and summarizing the results, the main ion contributions are given by Si, Al and Mg. Mg is the ion with the greatest LET, and the main difference between incident energies of 10, 14 and 20 MeV is on the quantity of produced Mg with high LET. For instance, a non-negligible amount of Mg is produced below LET of 8, 9 and 10 MeV $\cdot$ cm^2/mg with primary neutrons of 10, 14 and 20 MeV, respectively. In addition, Mg ions are the ones receiving the largest energy by the neutron, that on average is

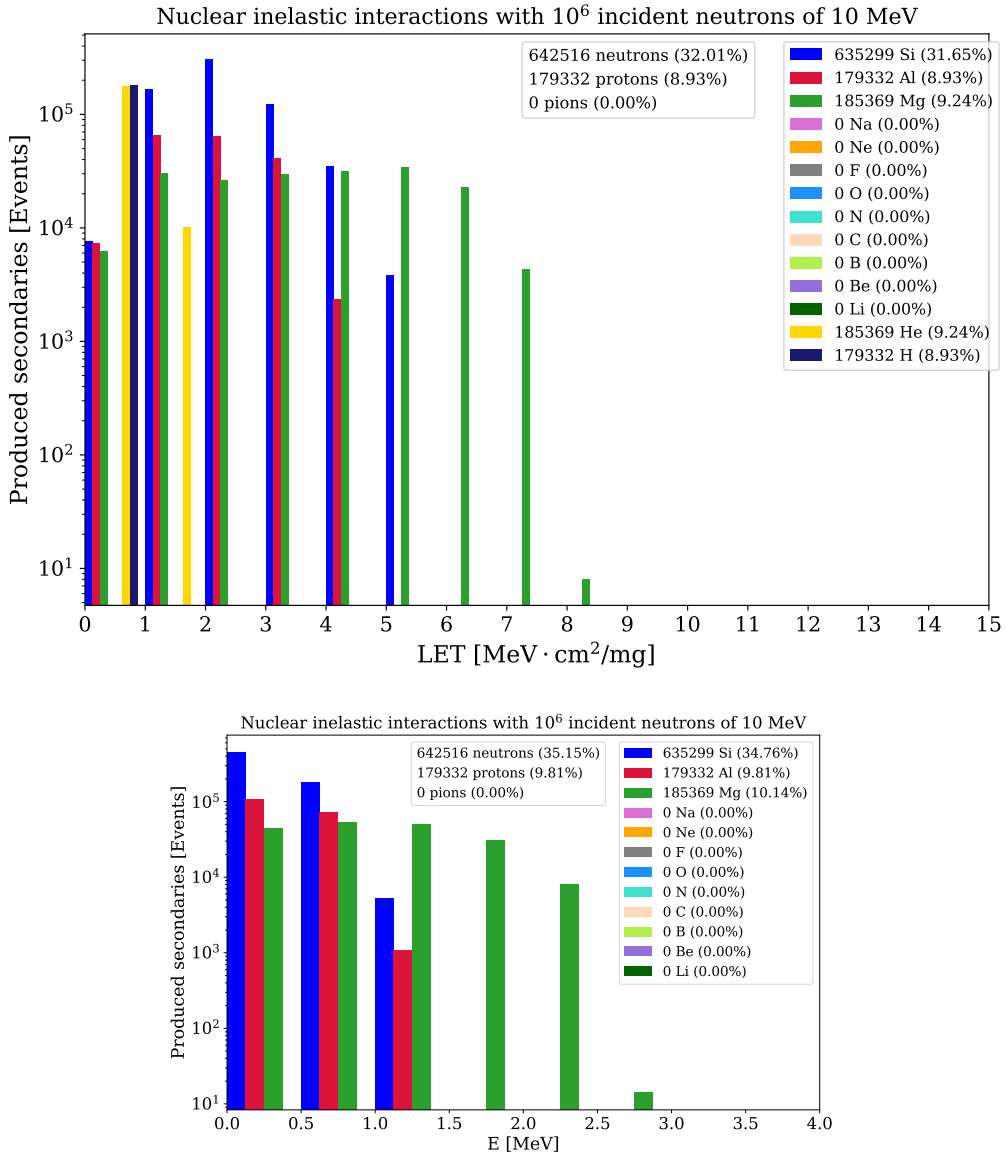

Figure 4.19: LET and Energy of secondary ions produced in inelastic interactions of 10 MeV neutrons in Si.

twice as many as the other heavy ions (Si, Al). Similar considerations can be done for Si ions, the most abundant after Mg, where LETs are non-negligible below 6, 7 and 8 MeV · cm^2/mg for the three energies, respectively. He ions (mostly alpha particles) are generated in the same quantities and LET values. An important difference regards H ions, which are composed mostly of protons, as with these intermediate energies deuteron and tritium ions are negligible (absent with 10 MeV): protons are 10% and 20% of the total ions with primary energies of 14 and 20 MeV, respectively.

- Between 20 MeV and 50 MeV (considering Fig. B.20 and B.21): There is a transition on the highest ion's LET passing from Mg (at 20 MeV) to Si (at 50 MeV), although most of the transferred energy is still ceded to Mg (considering these two ions). Lighter ions

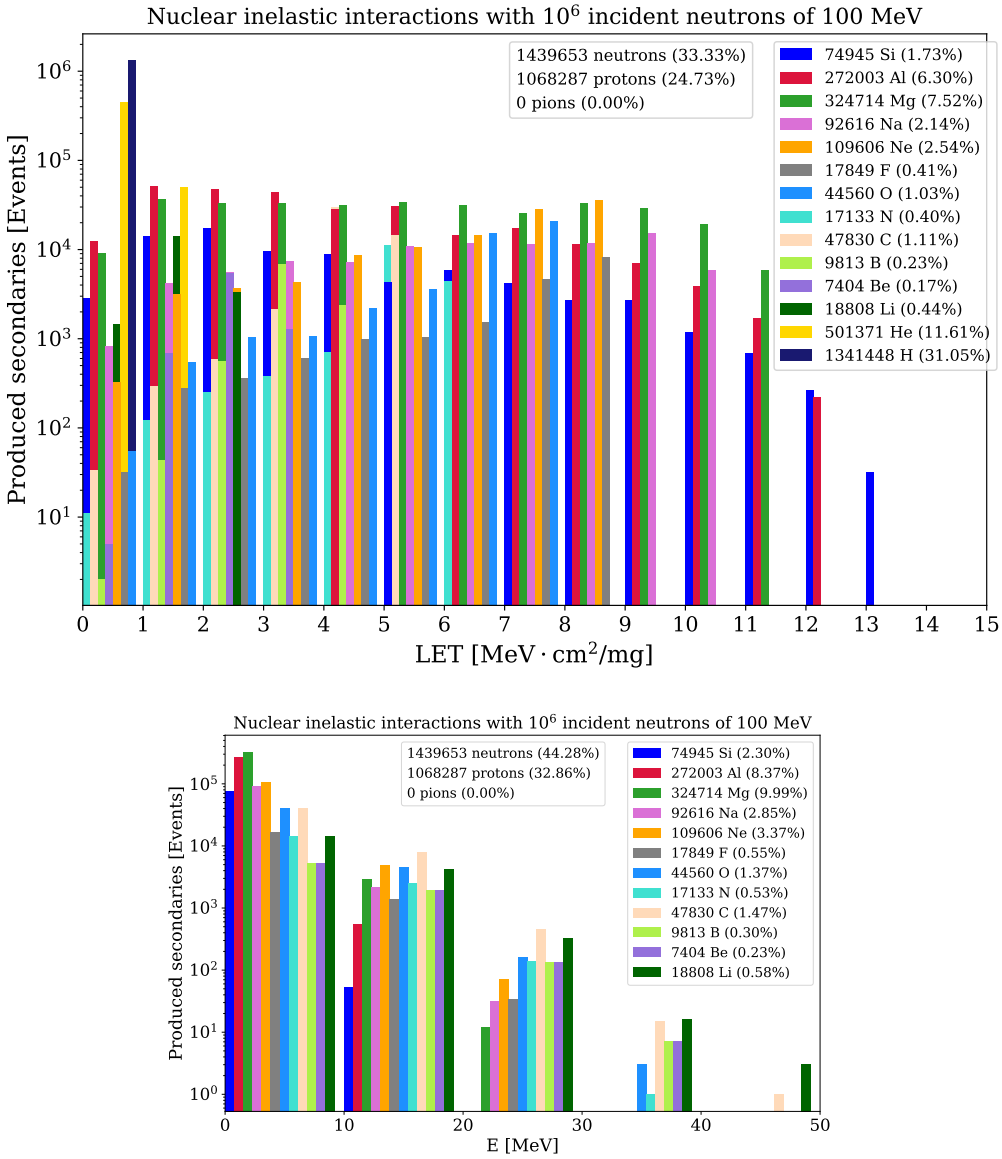

Figure 4.20: LET and Energy of secondary ions produced in inelastic interactions of 100 MeV neutrons in Si.

start to be produced, in addition to Si, Mg and Al. Even though LET and quantities of lighter ions are still lower with respect to the heavy ions, Na, Ne, O and C can have an impact, as together represent about half (5%) the quantity of Mg (10%) produced with 50 MeV. Between these range of energies, He ions and in particular alpha particles increase of 75% (absolute terms), and also H ions increase their production of 100%.

- For incident neutron energies above 50 MeV (see Fig. B.21 - Fig. B.24): Only Si, Al and Mg are produced with LET above 11 MeV · cm^2/mg (and below 14 MeV · cm^2/mg). Between 9 and 11 MeV · cm^2/mg, in addition to the three previous ions, Na is produced in amounts with the same order of magnitude of the others. Below 9 MeV · cm^2/mg, Si, Al, Mg maintain a quite constant production for the various LET intervals down to

1 MeV $\cdot$ cm^2/mg, while Na events tend to decrease with lower LET values. In addition, Ne and F are produced in consistent quantities between 8-9 MeV $\cdot$ cm^2/mg, as well as O between 7-8 MeV $\cdot$ cm^2/mg.

Above 100 MeV of primary neutron energies, the production of Ne in the LET range of 8-9 MeV $\cdot$ cm^2/mg is the greatest among ions. Moreover, the contribution of O is the highest between 7-8 MeV $\cdot$ cm^2/mg for incident energies above 500 MeV. The lighter ions (Z<8) are produced below 7 MeV $\cdot$ cm^2/mg, but the production of most of them can be different orders of magnitudes lower than that of Al and Mg, with some exceptions. Above incident energies of 100 MeV, C ions in the range 4-5 MeV $\cdot$ cm^2/mg have the largest production among ions. B, Be, Li ions are produced in considerable quantities for LET below 4 MeV $\cdot$ cm^2/mg mostly above 500 MeV. It is worth noting that, differently from the heavy Si, Al and Mg, those ions with Z<12 (starting from Na) have their peak of production around the highest LET, and the events decrease with lower LET values.

In terms of energies instead, as can be seen in the energy graphs of Fig. 4.19 and 4.20 (and those in Appendix for the other incident energies from Fig. B.19 to B.24), the lighter ion is always produced with the greatest energy.

4.9.1 LET and Energy of the overall secondary ions

The overall contribution from all the ions produced at different incident neutron energies with their LET and energies is shown in Fig. 4.21. In the LET graph, every interval of LET groups the events from all the ions, from Z=15 (P) to Z= 1 (H) considering all isotopes. In the corresponding energy graph, instead, He and H ions are excluded for graphical reasons, since their energies range up to almost the incident neutron energy, but the single ions contributions can be seen in Fig. 4.17, B.17, B.18 for He, D+T and protons, respectively.

It is clear that primary energies of 100, 200, 500, 1000 MeV generate almost the same quantity of secondaries per LET intervals, and in particular, 100 MeV produce the greatest amount of secondaries between 7 and 13 MeV $\cdot$ cm^2/mg. Most of the secondaries with the highest LET between 13 and 14 MeV $\cdot$ cm^2/mg are not generated with the highest incident energy of 1000 MeV, but rather with 200 and 500 MeV (even with 100 MeV the events are larger than with 1000 MeV). Therefore, as an important remark, incident neutron energies above 100 MeV, and up to 1000 MeV, do not generate larger quantities of high LET secondaries. Decreasing the neutron beam energy below 100 MeV, the LET of secondaries drops quickly. Below LETs of 1 MeV $\cdot$ cm^2/mg the number of reaction products is larger with increasing of the primary energy, especially due to He and H ions, which are produced in larger quantities at higher energies.

These graphs will be used for some considerations on the difference between SEU and SEL cross sections. For instance, above incident neutrons of 20 MeV, ions with LET greater than 10 MeV $\cdot$ cm^2/mg are negligible.

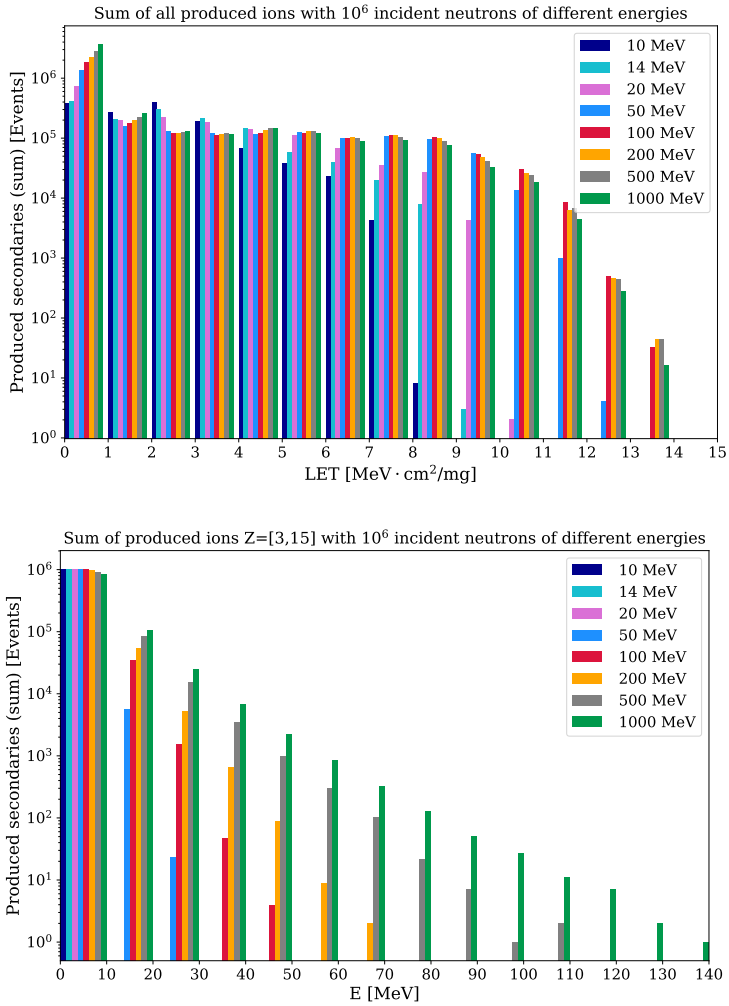

Figure 4.21: LET and Energy of the overall secondary ions produced in inelastic interactions n-Si. He and H ions are excluded in the energy graph (bottom).

4.9.2 Conclusions

At the beginning of the inelastic interaction study, with some approximations, it was possible to identify what ions are more important for increasing the SEU cross section from 10 to 20 MeV (Section 4.7). At 20 MeV, where the SEU cross section is almost already saturated, the major contributors in depositing energy in the SV resulted to be Al, followed by Mg, Si and alpha particles.

Studying the energy distributions (Section 4.8) of secondaries it was shown why the SEU cross section does not increase above 100 MeV and ions produced in higher percentage were identified.

To have a better picture, from the presented analysis by grouping the produced ions in LET intervals, other considerations were done on the ions contributions in depositing energy in Si and some conclusions can be drawn regarding the SEU cross section between 20 and

100 MeV. As the SEU cross section is almost saturated at 20 MeV but the production of ions widely varies from 20 to 100 MeV, some ions will contribute less and others will contribute more in depositing energy in the SV. This fact is especially valid for Al ions, which are largely produced at 20 MeV (20%) and rapidly decrease already at 50 MeV (10%) and more with higher energies. Their place is taken by the conjunct contribution of lighter ions which are more and more produced at increasing energy, particularly Na, Ne, O, C and alpha.

In addition, for incident neutron energies above 100 MeV, this behaviour happening from 20 MeV is more accentuated, where the heavier ions (Si, Mg, Al) are less produced and their contribution to the SEU cross section will be replaced by the lighter ones (Na, Ne, O and C).

4.10 Difference Between SEU and SEL Cross Sections

SEU and SEL mechanisms were explained in Section 2.2 and both cross sections were experimentally measured in SRAMs with high energies (protons above 100 MeV and spallation facilities) and with 14 MeV neutron beams. As already shown (see Table 4.6) the SEU cross section measured at 14 MeV compared to that in saturation is in general lower but on the same order of magnitude. Contrarily, the two SEL cross sections differ about 2 orders of magnitude, as shown in Table 4.9 from [11], for several SRAMs (specifications in Table 6.3). Hence, while the SEU cross section measured with 14 MeV neutrons is almost its value in saturation, enabling the use of such beams for the SEU characterization, SEL cross section cannot be reproduced otherwise than with high energy beams.

Table 4.9: SEL cross sections comparison, measured with 14 MeV neutrons, high energy protons (200 MeV) and mixed-field (CHARM) from [11] and tests performed in 2018.

Memory	$\sigma_{14\ MeV}$ [cm^2/dev]	$\sigma_{200\ MeV}$ [cm^2/dev]	σ^{CHARM}_{HEH} [cm^2/dev]
ISSI	$<1.92{\cdot}10^{-10}$	$2.30{\cdot}10^{-8}$	$1.69{\cdot}10^{-8}$ (M0)
Brilliance	$<1.63{\cdot}10^{-10}$	$3.15{\cdot}10^{-8}$	$2.18{\cdot}10^{-8}$ (M0)
Lyontek	$<7.88{\cdot}10^{-11}$	$4.60{\cdot}10^{-8}$	$2.49{\cdot}10^{-8}$ (M0)
Alliance	not tested	$3.40{\cdot}10^{-10}$	$4.32{\cdot}10^{-10}$ (R10)

This experimental observation can be physically explained through the inelastic interaction analysis exposed in this chapter, and additional Monte Carlo simulations which implement models capable of extracting the SEU and SEL cross sections experimentally measured.

4.10.1 SEU and SEL RPP models

These models (in a similar way as introduced in Section 4.7) consist of a silicon target with a certain volume dimension that contains the RPP resembling the SV of the device, in which the energy deposition is calculated. The silicon target is large enough with respect to the SV to account for those ions with long-range (such as alpha particles) that can travel and deposit

energy even far from the generation point. The RPP representing the SV is located several μm deep in silicon to consider the Back-End-Of-Line (BEOL), and to enhance the simulation time performance multiple RPPs can be considered instead of one, in a matrix disposed of 10 x 10 RPPs. A model of example for SEU (B) and for SEL (C) are considered for the study, whose geometric characteristics are reported in Table 4.10. For completeness, the characteristics for the models employed in Sections 5.9 and 7.3.7 to describe the 40 nm ISSI (Model A) and the 0.18 μm Samsung memories (Model D), are reported in the same table. The Monte Carlo simulations were carried out with FLUKA where the beam was covering the whole target surface (xy) and travelling along the z-direction.

Table 4.10: Geometric parameters of SEU and SEL models (the first 6 μm along z for the BEOL of Model A were composed of SiO_2 and the remaining 0.35 μm of Si). Deep refers to the location of SV with respect to the z axis.

Model	Note	Target [μm]			deep [μm]	RPPs	SV [μm]		
		x	y	z			x	y	z
A SEU	ISSI 40 nm	24.5	24.5	6.35	6	1	0.25	0.25	0.25
B SEU	example	54	54	10	5	10x10	0.5	0.5	0.5
C SEL	example	260	100	11	6	10x10	20	4	2.5
D SEL	Samsung 0.18 μm	40	40	37	7	1	20	4	1.8

The energy deposition is scored in the SV and the corresponding events are normalized by the total number of primary particles and number of RPPs (representing the SV). To this regard, the simulation output is a histogram of these events, where each event is merely the probability to deposit energy in the corresponding energy bin. This event probability is calculated through several FLUKA user routines described in [56] and it is associated with the probability of triggering a SEE.

The SEE cross section for given threshold energy is calculated by summing all the events of the bins with higher deposited energy than the energy bin in consideration, through Eq. 4.10. In fact, if a SEE is triggered by a certain deposited energy (E_{dep}), it will be triggered also by higher E_{dep}, hence the probability will be the sum of all single probabilities associated to a single energy bin.

$$\sigma_{Eth} = \frac{1}{\Phi} \cdot \sum_{E_d=i}^{bin(max)} Events(E_d) \tag{4.10}$$

In Eq. 4.10, the fluence Φ [cm^{-2}] is that simulated, corresponding to the inverse of the x-y target surface.

The distribution of this cross section can be shown as a function of the LETeq (see Eq. 4.11), which is the LET calculated from E_{dep}, the silicon density $\rho = 2.33 \cdot 10^3\ mg/cm^3$ and the thickness SV_t of the SV. Otherwise, it can be plotted as a function of the critical charge Qc

through the conversion factor of 22.5 MeV/pC (see Chapter 2).

$$LETeq = \frac{E_{dep}}{\rho \cdot SV_t} \qquad [MeVcm^2/mg] \tag{4.11}$$

The final SEU cross section is normally extracted from this distribution considering a certain Qc, while the SEL cross section is calculated by weighting every event of the histogram with the heavy-ion Weibull response function of the memory concerned (see Eq. 4.12).

$$\sigma_{SEL} = \frac{\sigma_{HI}^{sat}}{\Phi \cdot SV_{xy}} \cdot \sum_{E_d=bin(min)}^{bin(max)} Events(E_d) \cdot w(E_d) \tag{4.12}$$

Where σ_{HI}^{sat} is the HI cross section in saturation, $w(E_d)$ the associated Weibull function as a function of the deposited energy and SV_{xy} is the surface of the SV. Equations 4.10 and 4.12 can be rewritten in terms of integrals as shown in Eq. 4.13 and 4.14, respectively.

$$\sigma_{SEU} = \frac{1}{\Phi} \cdot \int_{E_{crit}}^{+\infty} \frac{d(Events(E_d))}{dE} dE_d \tag{4.13}$$

$$\sigma_{SEL} = \frac{\sigma_{HI}^{sat}}{\Phi \cdot SV_{xy}} \cdot \int_{0}^{+\infty} w(E_d) \cdot \frac{d(Events(E_d))}{dE} dE_d \tag{4.14}$$

Here, E_{crit} in the SEU equation is the energy corresponding to the critical charge of the device.

These methods will be explained in more detail in Sections 5.9.3 and 7.3.7, as the purpose of the present study is to compare the SEE cross sections retrieved through Eq. 4.10 to have the same metric.

4.10.2 SEE simulated cross sections

The SEE cross sections are shown in Fig. 4.22 for model B and C of Table 4.10 simulated with monoenergetic neutron beams of 20 and 100 MeV and with the JEDEC ground level spectrum for the SEL model. The choice of using 20 MeV instead of 14 MeV relies on the fact that FLUKA treats neutrons below 20 MeV as a multi-group structure and the point-wise neutron cross section is not available for these energies. However, using 20 MeV is not limiting, as the SEU cross section is even closer to that in saturation, and for SEL the cross section is still very little compared to the saturated value [57].

The SEU cross section can be directly extracted from the area of the plot highlighted in green, corresponding to a Qc from 0.5 to 1.5 fC (typical for SRAM memories with technology of nm/µm).

The main difference between SEU and SEL cross sections is due to the dimensions of

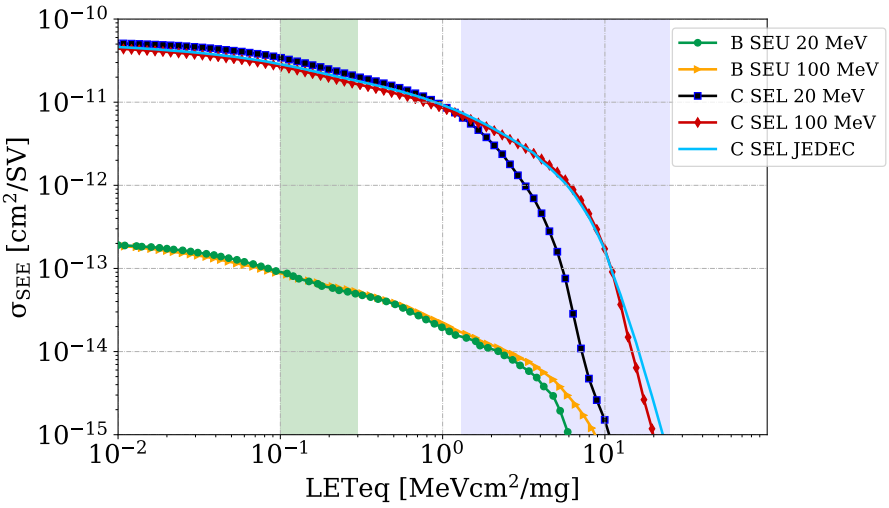

Figure 4.22: SEU and SEL simulated cross sections using RPPs models with incident neutron energies of 20 and 100 MeV.

the respective SV. As far as SEU simulations are concerned, the SV is two-three orders of magnitude smaller with respect to that of SEL models and the resulting cross sections are about two orders of magnitude higher for SEL. This result can be expected, as a bigger SV will have the capability of collecting more charge released by the produced secondaries. To notice that the final SEL cross section is calculated weighting more the higher E_d (hence higher LETeq), as the Weibull function would cut the lower values. Therefore, the reason why the SEL cross section is not reproduced with lower energies has to be found in the area of the plot highlighted in blue.

Focusing on the SEL C model, and on the basis of the produced secondaries seen in the previous Sections, the difference between the 20 and 100 MeV curves can be attributable to two reasons:

1) The probability of depositing energy (and trigger events) in a certain energy bin is much higher with 100 MeV, up to two orders of magnitude for deposited energies larger than 13 MeV (22 MeV $\cdot$ cm^2/mg). This is mainly due to the conjunction contribution of the **lighter ions** produced (mainly Na, Ne, C, O), which are absent with 20 MeV, plus the increasing amount of alpha particles (twice as many at 100 MeV) and higher LET of heavier secondaries.

2) The quantity of deposited energy is larger with 100 MeV, as the E_d cut off corresponds to a maximum energy of 22 and 10 MeV (38 and 17 MeV $\cdot$ cm^2/mg) for incident neutron energies of 100 and 20 MeV, respectively. This shift is mainly due to the **heavier fragments** (generated with larger incident neutron energies, as seen in the analysis in the previous Sections) that have greater LET values and therefore can deposit more energy in the SV. Also, the lighter generated fragments will have an impact (especially Na, Ne, F) but not as much as for the vertical shift.

These two effects are also visible in the SEU model B around 7 MeV $\cdot$ cm^2/mg (comparing 20 and 100 MeV in Fig. 4.22), but these events of higher E_d have much less impact on the SEU cross section.

Therefore, both the lighter ions produced at 100 MeV (not present with 20 MeV) and the heavier ions produced with larger LET values are more important for SEL than for SEU. This fact is related to the dimensions of the respective SV, LET and range of secondaries. Those ions that have the capability of realising a lot of charge in an SEL SV, will only release part of this charge in an SEU volume, because of its smaller dimensions. Indeed, increasing the incident neutron energy from 20 to 100 MeV, both heavier and lighter ions produced will have longer range than the dimensions of an SEU SV and hence will release more energy in an SEL volume.

In addition, Fig. 4.22 also shows that the atmospheric SEL cross section (JEDEC C Model) can only be obtained with 100 MeV, precluding the use of lower energies.

4.11 Summary

This chapter detailed exposed and analyzed the inelastic interactions of incident neutrons from 10 MeV to 1 GeV in silicon, retrieved through FLUKA at the single interaction level. The aims of this comprehensive study were to explain the behaviour of the SEE cross sections experimentally measured as a function of the energy and to explore the potentiality of FLUKA in performing these simulations.

The nuclear cross sections in silicon as a function of the incident neutron energy were calculated with FLUKA and compared to those from nuclear databases showing a good agreement. In addition, the reaction channels that open at increasing neutron energy from 10 to 20 MeV were analysed, showing that the important contributions are given by the (n, xα), (n, xp) and (n, xn) reactions. Among them, the Q values of the (n, α) reactions with incident energies of 10 and 14 MeV were calculated observing how different silicon isotopes can exhibit different threshold energies to initiate a nuclear reaction. Specifically, the ^{29}Si isotope showed an E_{th} of only 33 keV, compared to the 2.75 MeV of ^{28}Si normally considered in literature, implying that low energy neutrons can possibly open this reaction channel and the produced secondaries can deposit energy in the SV of an electronic device. It was shown that the Q states even with 14 MeV present a continuum below -7.3 MeV and they are not discrete values anymore as with 10 MeV, and different excited states were experimentally measured through a silicon diode. The energy distributions of single reactions were represented and a qualitative analysis on the contribution of ions to the SEU cross section was exposed for energies of 10, 14 and 20 MeV. It turned out that Al ions are expected to give the largest contribution in depositing energy in silicon at 20 MeV, while silicon ions are instead more effective at 10 and 14 MeV. Alpha particles yield also an equivalent contribution as that of heavy ions due to their longer range and capability of reaching the SV even when generated far from it, and this additional contribution was calculated to be +95%.

For incident neutron energies larger than 20 MeV the study of the secondaries was performed considering the overall contributions from all the reactions, and the energy distributions for every ion were analysed. As experimentally observed, the SEU cross section is fundamentally saturated above 20 MeV even if the production of ions widely varies from 20 to 100 MeV, hence some ions will contribute less and others will contribute more in depositing energy in the SV (Section 4.9). Al ions for instance, which are largely produced at 20 MeV (20%), rapidly decrease already from 50 MeV (10%) and more with higher energies. Their place is taken by the conjunct contribution of lighter ions which are more and more produced at increasing energy, such as Na, Ne, O, C and alpha. In addition, for incident neutron energies above 100 MeV, this behaviour happening from 20 MeV is more accentuated, where the heavier ions (Si, Mg, Al) are less produced and their contribution to the SEU cross section will be replaced by the lighter ones (Na, Ne, O and C). Moreover, Sections 4.8 showed that secondary ions produced with primary energies above 100 MeV have similar distributions, in shapes and quantities from Si to F, whose ions present the greatest LET. This aspect and other considerations from Section 4.9 could explain that the SEU cross section is normally saturated above 100 MeV, and testing with higher energies does not significantly impact its value, because of a balance between the heavier and lighter ions produced.

Finally, the inelastic interaction analysis along with RPP FLUKA models used to calculate the SEU and SEL cross sections were combined in Section 4.10 to understand why the SEL cross section in saturation, differently from that of SEU, is not reproduced with 14 MeV neutron beams, and the conclusions are summarized as follows:

1) More deposited energy is needed to trigger an SEL with respect to an SEU because the dimensions of the SEL SV are much larger. This aspect reflects also the physical dimensions of the effect: an SEU regards dimensions of MOSFETs whose PN areas are smaller compared to the dimensions of an SEL, which involves well, substrate and drain/source contacts (see representation in Fig. 2.5a).

2) The ions contributing to the SEU cross section vary at increasing incident neutron energy, passing from Si, Al, Mg at incident energy of 14 MeV to an additional contribution from lighter fragments such as Ne, Na, O, C at 100 MeV. However, although more ions are contributing to the SEU cross section, the energy deposition in the SV at increasing energy is almost constant, deriving by a balance between the increasing amount of lighter ions produced and the decreasing amount of heavier ions (Si, Al). Ions with LET greater than 10 MeV $\cdot$ cm^2/mg are not very important for SEUs, because their production with 14 MeV is absent compared to that at 100 MeV, but the deposited energy do not significantly change (see Section 4.9.1). For the same reason, also the double amount of alpha particles produced (with 100 MeV) do not have an evident effect on the deposited energy in SEU SV.

3) The same ions (as for SEU) are produced in an SEL volume, but their importance in triggering an SEL is differently weighted owing to the larger dimensions of the SV with respect to the SEU case. As the incident neutron energy increases from 14 to 100 MeV,

ions produced with large LET values are very important as they will be able to release most of the energy in an SEL volume (while only partially in an SEU one). These ions are mainly Si, Al, Mg (produced with larger LETs at 100 MeV) plus the contribution of Ne and Na ions (only produced at 100 MeV in relevant quantities). Also, C and O ions produced with 100 MeV (absent with 14 MeV) will have a relevant impact, as well as the increased number of alpha particles. Indeed, given their longer range will release more energy in an SEL volume.

4) As a conclusion, recalling the initial problem and assumptions, the saturated SEL cross section is not reproduced with 14 MeV neutron beams, resulting in two orders of magnitude lower, for two main reasons. Owing to the larger amount of deposited energy necessary for SEL with respect to SEU, which is linked to the bigger dimensions of the SV, only with 100 MeV this energy can be provided by the heavier fragments that have higher LET and by the lighter ions produced in significant quantity. For SEU these two contributions are less meaningful because of its smaller SV, in which these ions only release a small fraction of their energy (owing to the ions' range) and this increase of energy deposition (at 100 MeV) is compensated by the decreasing of Si and Al ion production.

Chapter 5

Radiation Test Facility and Calibration Approach

The SEE failure rate for electronic components to be used in the LHC accelerator has to be quantified in dedicated test facilities capable of reproducing the spectra found in the LHC, or by assuming a certain SEE response function. As seen, neutrons are the primary particles constituting the radiation environment inside the LHC. Their fluxes can be tens of times higher than the mixed-field of protons, electrons, muons, pions and kaons that together characterize the locations of the accelerator in which electronics are installed. For instance, the LHC environments can be recreated in the CHARM mixed-field facility at CERN. Nevertheless, neutrons are also the main concern for ground level and avionic applications, as once produced in the atmosphere, due to their nature they can travel until interacting with nuclei of atoms in semiconductor devices. Both accelerator and atmospheric environments are characterized by a wide neutron spectrum, from thermal (25 meV) up to several GeV of energies.

As explained in Chapter 2.3, the generalized SEE response function of electronics is based on the measurement of thermal neutrons and high energy SEE cross sections. To this regard, several R2E test campaigns were conducted in facilities providing neutron beams, to study SEEs and verify the compatibility of results between different facilities. Indeed, some facilities are more available and economic than others, hence a comparison is required to assess to which extent they can be interchangeable. In addition, tests at intermediate neutron energies were performed to assess the response of state of the art SRAMs, and evaluate the lower energy to which they can yield a non-negligible contribution to the SER.

This chapter describes different monoenergetic and spallation test facilities employed for the thesis work and a summary of the neutron and proton test campaigns is shown in Table 5.1. Some facilities are located at CERN and others in several institutes and research centres across Europe. An overview regarding the SEE qualification approaches is given hereafter before the description of the facilities.

Table 5.1: Main test campaigns conducted in the scope of this thesis.

Facility	Location	Particles	Energy	Test campaign
ILL	Grenoble (FR)	Thermal neutrons	23 meV	2019
Am-Be	CERN (CH)	Neutron spectrum	up to 11 MeV	2018-2020
PTB	Brunswick (DE)	Monoenergetic neutrons	144 keV - 17 MeV	2020
FNG	Frascati (IT)	Monoenergetic neutrons	2.5, 14.8 MeV	2019
ChipIr	Didcot (UK)	Neutron spectrum	up to 700 MeV	2018,2019
CHARM	CERN (CH)	Mixed-field spectra	up to a few GeV	2018
PSI	Villigen (CH)	Protons	30 - 200 MeV	2018
RADEF	Jyvaskyla (FI)	Protons	3 - 52 MeV	2018
TOP-IMPLART	Frascati (IT)	Protons	18.9, 29 MeV	2019

5.1 SEE Qualification Approaches

Different procedures for neutron SEE qualification of electronics can be distinguished, and are described in this section as methods. The standards for testing electronics for ground level applications are defined in JEDEC JESD89A [12], and those for avionics in IEC 62396-1 [37] and IEC 62396-2 [38]. In the following, Methods 1, 2, 4 and 5 come from the standards, while Method 3 is a development of Method 2, proposed in the context of this thesis. Test approaches used for the LHC are based on these standards with some expansions and are also the outcome from the studies of this thesis.

1. Method 1 (M1): Spallation neutron source. The source provides a neutron spectrum over a wide energy range, from thermal up to high energy neutrons. Among the neutron sources, it has the closest shape to the atmospheric spectrum. Although energies in the atmospheric spectrum can be as high as 100 GeV, these facilities can normally provide energies only up to roughly 1 GeV. However, the atmospheric flux at such high energies is several orders of magnitude lower than that at around 100 MeV and therefore its impact is considered to be negligible. The SEU and SEL cross sections measured in such facilities encompass the information of a very wide spectrum in a single value. Thus, it is not possible to extract the energy contributions separately, such as the thermal neutron and high energy hadron (HEH) cross sections. The SEE cross section is calculated based on the neutron flux greater than 10 MeV and can be used to estimate the SER only in environments with similar spectra. The most well-known facilities are WNR in Los Alamos (US-NM), TRIUMF in Vancouver (CA) and ChipIr in Didcot (UK).

2. Method 2 (M2): Mono-energetic proton and neutron beams up to 200 MeV. The JEDEC standard [12] suggests of performing the characterization with at least four different energies: 14, 50, 100 and 200 MeV and then, from these experimental points, calculate the memory response through the Weibull fit. Tests with 14 MeV should be carried out with a neutron beam, whereas above 50 MeV both neutron and proton beams can be used, as their nuclear cross sections are similar. The SEE rate is calculated through the

integral of the operational spectrum folded with the memory response, which is also valid for avionic applications [37]. The main advantage of this method relies on the fact that the SEE rate can be calculated for every environment (given its spectrum), such as for accelerator applications, or space (e.g. trapped protons).

3. Method 3 (M3): Mono-energetic beams/simulations up to several GeV. This method, which derives from [56] and was validated for the SEE neutron studies presented in Section 7.4, is not outlined in the standards and it overcomes some limitations of M2. Indeed, M2 makes the important assumption that the component SEE cross section is saturated above 200 MeV. However, as shown in [40, 57, 58], some devices with a strong energy dependence due to the presence of high-Z materials near the sensitive volume show an increasing SEE cross section above 200 MeV, and up to several GeV before the saturation. The information about the material composition of the device can be extracted through the Scanning Electron Microscope (SEM) technique, as it was performed in [56]. Therefore, the characterization should be performed up to GeV energies in order to assess the SEE impact from high energy particles in the atmosphere. Despite their fluxes being an order of magnitude lower than those around 100 MeV, the fact that the SEE cross section is still increasing above 200 MeV plays an important role, as will be detailed in this thesis. Tests with such high energies can be performed for example in the CERN high energy accelerator mixed-field facility (CHARM) at CERN, which provides a 24 GeV proton beam extracted from the Proton Synchrotron (PS). Otherwise, the device SEE cross section can be calculated through simulations with a FLUKA Monte Carlo model as introduced in Section 4.10.1. The model is employed to calculate the deposited energy inside the memory sensitive volume needed to trigger a SEE, and it has been validated for protons [58] and neutrons [41]. It requires the input of the following information:

   - The geometrical parameters of the sensitive volume.
   - The layers of surrounding materials, especially the amount of possible tungsten or other high-Z materials, which is the direct cause of the SEE cross section increase with energy.
   - The experimental heavy ion SEE response of the component, or the information of its critical charge or threshold LET, and saturation cross section.

4. Method 4 (M4): Using a reference flux (for avionics). According to the IEC1 standard for avionic applications [37], as in most practical cases the SEE cross sections as a function of energy are not known for applying M2, a simplified approach can be implemented. It consists of using a reference flux (from a Boeing model), considered at 12 km of altitude and 45° of geographic latitude, integrated above 10 MeV. This flux results in 5600 neutrons/cm^2/h, which is rounded to 6000 cm^{-2}/h to include the effects of protons (therefore, the proton contribution is considered 6.7%). The flux is said to be conservative of a factor 2 compared to in-flight measurements. The expected SEE rate for avionics is then calculated by multiplying this flux value by the device SEE cross section, preferably characterized with a white neutron spectrum (M1) or monoenergetic

beams (M2), in the case of technologies above 150 nm. It is also acceptable to consider the SEE cross section measured at the highest test energy (200 MeV) since the SEE rate will be conservative [38]. If the feature size is below 150 nm, the contribution of neutrons between 1-10 MeV should also be included using a flux of 9200 neutrons/cm^2/h. It is worth noting that this simplified approach for avionics is very similar to that used in accelerator environments, which consists of multiplying the 200 MeV SEE cross section by the HEH (or HEHeq) fluence of interest [41, 59].

5. Other methods. In addition to the previous methods, the standards mention real-time and quasi-monoenergetic neutron measurements. The real-time method consists of observing SEEs under nominal conditions without accelerated tests, but it is not very practical since it would take years (or the testing of a vast number of components) to obtain meaningful statistics. The quasi-monoenergetic neutron beam is characterized by a main peak at nominal energy and by a tail at lower energies, and the difficulty lies in distinguishing between the SEEs induced by the neutron peak and the tail [26]. Due to the aforementioned complications, these two methods were not taken into account in this work.

The summary of these methods is shown in Table 5.2.

Table 5.2: Test methods summary.

Method	Description	SER calculated for	Facility example	Test time
M1	Spallation source	Same spectrum environment	WNR, ChipIr	hours
M2	Monoenergetic beams	All environments	PSI, PTB	hours
M3	M2 + sim [GeV]	All environments	-	hours
M4	Reference flux	Same spectrum environment	-	-
M5	Real-time	Same spectrum environment	-	years

Since neutron beams with energy greater than 20 MeV are typically not employed, high energy testing can be performed with protons, whose beams are easier to generate and work with. However, there are two major issues using protons instead of neutrons:

- The chip package can attenuate the proton beam energy.
- After a few krad the SEU sensitivity can be affected by the total dose (TID effect), and devices may fail due to Displacement Damage (DD) before that happens [60].

The previous methods concern intermediate-high energies (above 10 MeV), as the SER contribution due to lower energies was regarded as negligible, according to the standards. However, as it will be shown in the SER result chapter, also the qualification with thermal and intermediate energy neutrons below 10 MeV is fundamental for accelerator applications. Moreover, the latter can be a threat even for avionic and ground level applications. Thermal neutron beams are obtained from reactors, while intermediate energy neutrons from nuclear reactions, for instance (d,d), (d,t), (p,t) or (p, Li).

The test facilities employed in this work are described in the following, with the respective cross-calibrations carried out with the ESA SEU Monitor, which is a rad-hard detector here employed to assess the beam flux and homogeneity (over 19.8x19.8 mm^2), thanks to the upset map measured by four sensitive dies. This result is used to calculate the fluence uncertainty of the beam ($\sigma_{fluence}$); the complete description of the detector and the procedure is reported in Chapter 6. Hence, the cross-calibration is a method to verify the beam flux and homogeneity, evaluate the fluence uncertainty, and compare them with the values provided by the facility.

5.2 ILL - Thermal Neutrons

The R2E test campaign was conducted in July 2019 in the scope of this thesis.

The thermal neutrons flux can be as high as 50 times the HEHeq flux (or more) inside shielded areas in the LHC (see Section 3.2.2). Hence, the experiments held at ILL aimed at identifying and studying components presenting a high thermal neutron cross section, for a subsequent comparison to the HEH one. This helped to define whether thermal neutrons shall be considered or neglected in the RHA approach currently applied at CERN.

The Institut Laue Langevin (ILL) runs a nuclear reactor located in Grenoble with a total thermal power of 58 MW [61, 62]. The fuel element is highly enriched uranium, cooled and moderated with heavy water (D_2O) to produce a very intense neutron flux ($1.5{\cdot}10^{15}$ $n/cm^2/s$). Neutrons are produced in the reactor from the fission reactions of Uranium nuclei: prompt neutrons have energy corresponding to ~2.1 MeV (20000 km/s), and they are slowed down to thermal energy ~25 meV (2.2 km/s) by heavy water in order to produce new fission reactions.

Neutrons are extracted through 20 beamlines extended by guides and providing neutron beams to more than 40 experimental areas (Fig. 5.1). One of them delivers thermal neutrons to the D50 instrument, a facility for electronics irradiations, with an average energy of 13 meV. The neutrons available in D50 are produced by the ILL horizontal cold source (thermal neutrons moderated by liquid deuterium at 20 K) and transmitted along a 100 m long neutron-guide. The captured flux (i.e. equivalent flux of 25 meV neutron) delivered on D50 is adjustable up to 10^{10} $n/cm^2/s$. The neutron spot size may be easily adapted for local irradiation (1 mm^2) to global irradiation of a homogeneous square section of about 50 cm^2 by means of motorised borated carbon (B4C) slides. The typical neutron spectrum available at D50 is shown in Fig. 5.2.

The neutron flux is measured with dedicated ^3He detectors and is periodically monitored by the activation of five gold foils with a diameter of 10 mm. The neutron beam homogeneity, calibrated through a CCD camera in the highest flux position of D50 (used in this work), was measured to be within 90% of the maximum intensity over an area of 15x15 mm^2 [63].

During a previous R2E test campaign in February 2017 the thermal neutron flux was $1.37{\cdot}10^8$ $n/cm^2/s$ [63], whereas in July 2019 it was measured to be 10^9 $n/cm^2/s$ (seven times higher) [64]. Indeed, some upgrades have been performed on the beamline: the D50

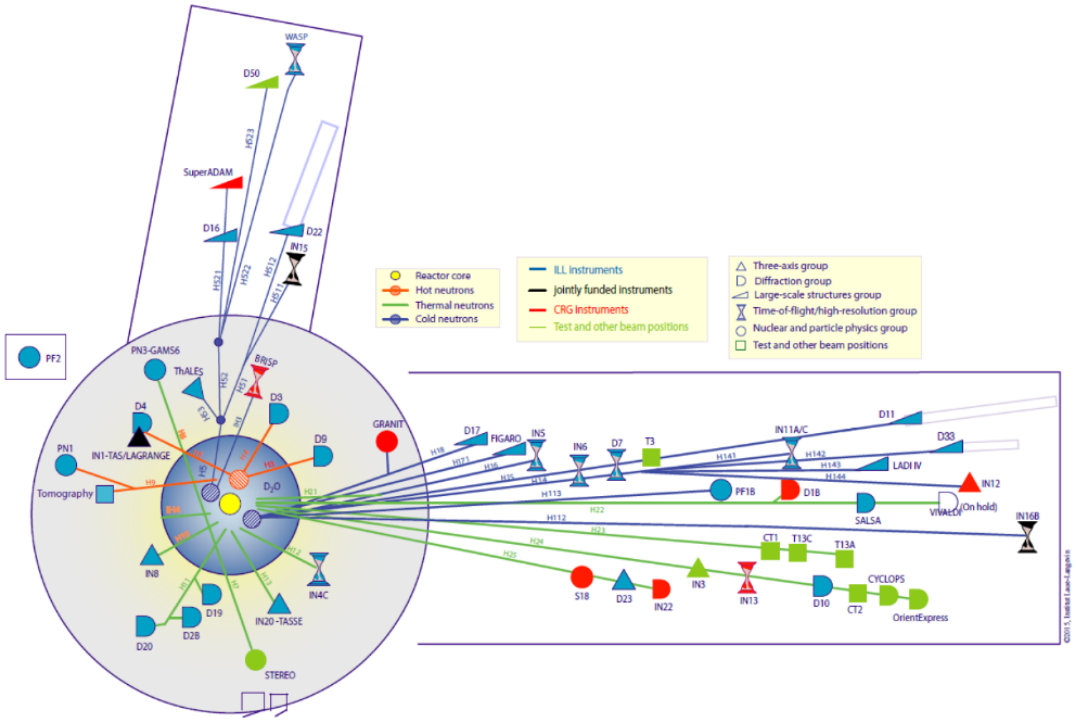

Figure 5.1: Experimental areas and beamlines at ILL [61].

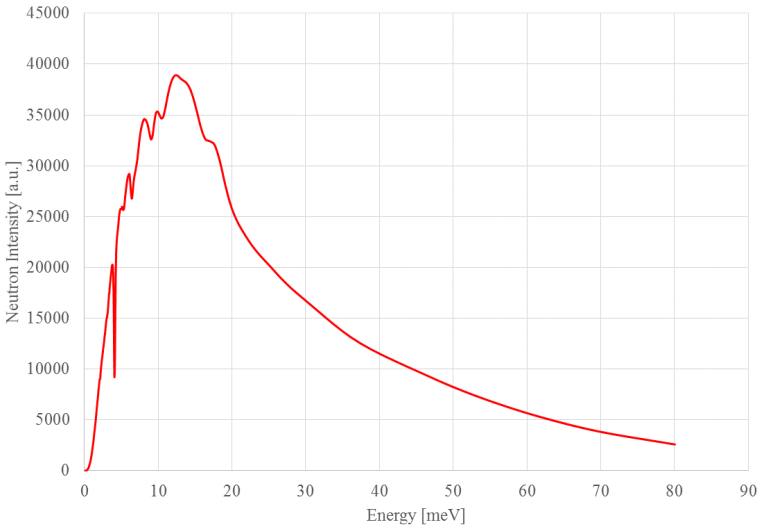

Figure 5.2: ILL-D50 thermal neutron spectrum (Courtesy of J. Segura-Ruiz).

collimator was realigned, its aluminium window replaced and an optional graphite slide, of either 5 or 10 mm at the end of the guide, was not used in order to increase the flux by an additional 20%. With these beamline settings, considering an irradiation chamber opening of 30 mm diameter and the reactor power of 51.5 MW, the flux was measured by three different gold foil calibrations on June 13^{th}, August 2^{nd} and August 27^{th} 2019. These measurements showed a thermal neutron flux of 10^9 n/cm^2/s, which is therefore retained for the post-

irradiation analysis.

Electronic boards are installed on a movable table inside the irradiation room, which can be controlled remotely in both vertical and horizontal axes. The alignment is performed through a laser and a camera.

Cross-calibration

The cross-calibration and the fluence uncertainty assessment were performed through measurements with the ESA SEU Monitor without lid (date code 1817), as explained in Section 6.1.2.

Table 5.3 reports the upsets measured by each die of the ESA Monitor, their larger percentage ratio, and fluence uncertainty calculated at one standard deviation from the upset measurement. The values from the previous calibration, carried out in February 2017, are also shown for comparison. Both measurements were taken by placing the centre of the ESA Monitor in the centre of the beam as indicated by a laser system. As one can see, the actual beam homogeneity, qualified by the die to die variation, was improved with a maximum difference between dies of 31.8%, instead of 90.5%. This is attributed to be a result of the mentioned beam guide replacement. The fluence uncertainty of the beam results of $\pm 1\sigma_f = \pm 11.8\%$, hence $\pm 2\sigma_f = \pm 24\%$.

Table 5.3: Number of SEUs measured in each die of the ESA Monitor (no lid). Comparison between current (2019) and previous calibration (2017) (from [65]).

Test date	φ [n/cm^2/s]	die0	die1	die2	die3	die-die var. (%)	$\pm 1\sigma_{fluence}$(%)
July 2019	$1.37 \cdot 10^8$	2203	1896	1672	1825	31.8	11.8
Feb. 2017	$1.00 \cdot 10^9$	637	538	707	1025	90.5	29.0

5.3 TOP-IMPLART LINAC - 18.6 and 29 MeV Protons

The R2E test campaign was carried out in December 2019 in the scope of the thesis.

The TOP-IMPLART is a linear accelerator in Frascati (ENEA), designed for proton therapy, which provided 18.5 and 29 MeV protons. Since requirements for proton therapy are normally stricter than those for electronics, spot size and homogeneity of the beam are very accurate. The ESA SEU Monitor was employed to cross-check the beam homogeneity and compare the results with other proton testing. SEU measurements were performed with COTS memories, measured with and without the chip package, to study its impact on the cross section. Indeed, as explained in Chapter 7, protons generated by the interaction of neutrons with the chip package may lead to an increasing of the low energy neutron cross section. Hence, devices were directly tested with a proton beam of intermediate energy.

The Terapia Oncologica con Protoni - Intensity Modulated Proton Linear Accelerator for

Radio Therapy (TOP-IMPLART) is a S-band LINAC currently providing up to 35 MeV protons [66–68]. The accelerator is under construction with the final aim of providing 150 MeV for proton therapy applications, and currently working on radio-biological studies. The accelerator is structured in pulses with length of 3 μs and a typical repetition frequency of 25 Hz. The current can be turned between about 1 and 50 μA. The beam energy after the vacuum window is 35 MeV with a very small spot size, resulting in less than 4 mm in diameter with a homogeneity of ±5% [66]. A lead scattering foil was used to irradiate targets and the subsequent expansion of the beam in air enables to obtain a large enough spot size and homogeneity to cover an area of 2x2 cm^2. Therefore, the beam was degraded from 35 MeV to obtain 29.0 and 18.6 MeV, with fluxes of up to $4.2 \cdot 10^7$ and $6.7 \cdot 10^7$ cm^{-2}/s, respectively.

Online dosimetry is performed through two ionization chambers, located at the accelerator exit and 15 cm before the DUT, respectively. The ionization chambers are calibrated offline with a Faraday cup and a micro diamond dosimeter, since reliable dosimetry is one of the key points of the facility, owing to the radio-biological requirements.

Cross-calibration

Given the high interest on the beam homogeneity assessment, several ESA Monitor measurements were performed at the highest and lowest flux intensities for every energy. Table 5.4 reports the fluence standard deviations calculated from N ESA Monitor measurements, for the two fluxes operated by the machine and used during the tests. The homogeneity was very good and will be considered as $\pm 2\sigma_f = \pm 10\%$

Table 5.4: ESA Monitor beam homogeneity assessment at 29 and 18.6 MeV with two fluxes intensities. N indicates the number of repeated measurements and the standard deviation is the final value from the multiple measurements.

E [MeV]	φ [cm^{-2}/s]	N	$\pm 1\sigma_f$(%)
29.0	$1.30 \cdot 10^7$	2	4.0
29.0	$3.90 \cdot 10^7$	3	2.6
18.6	$1.77 \cdot 10^7$	3	4.4
18.6	$7.10 \cdot 10^7$	4	5.1

5.4 FNG - 2.5 and 14.8 MeV Monoenergetic Neutrons

The test campaign was conducted in November 2019 in the scope of this thesis.

The Frascati Neutron Generator (FNG) is located at the ENEA centre in Frascati (Italy) and can provide 14.8 and 2.5 MeV monoenergetic neutrons [69], which are of interest for characterizing SEU cross sections at intermediate neutron energies. As it was the first R2E test campaign carried out at FNG, particular attention was dedicated to cross-calibrate the beam and assess its employment for radiation to electronics testing.

The facility was originally designed for experiments on the thermonuclear fusion and it is available for electronics testing. Neutrons are generated accelerating a deuteron beam (up to 300 keV), against either a tritium target to produce 14.8 MeV or a deuteron target to obtain 2.5 MeV. The respective fusion reactions are shown in Eq. 5.1.

$$\begin{aligned} D + T &\rightarrow n + {}^4He \\ D + D &\rightarrow n + {}^3He\ (50\%) \\ &\rightarrow p + T\ (50\%) \end{aligned} \tag{5.1}$$

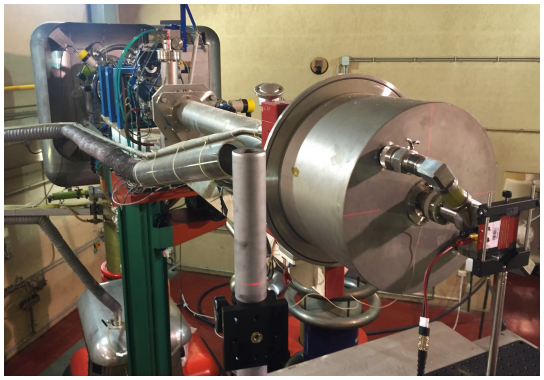

(a)

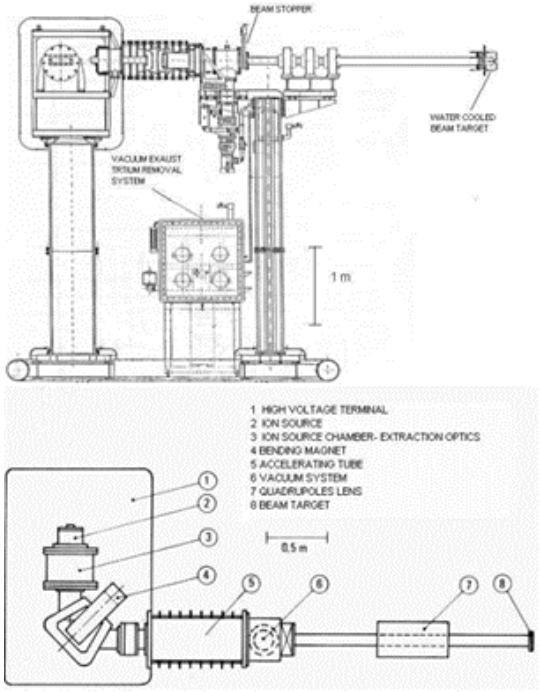

(b)

Figure 5.3: (a): Picture of the FNG target and DUT installed in front of it during the test campaign in November 2019. (b): FNG machine – side and top views from [69]

Fig. 5.3 depicts the machine side and top views, which are described hereafter from [69, 70]. Following the parts numbering in Fig. 5.3, the deuteron ion beam is produced by a duoplasmatron source (2), a vacuum chamber which creates the plasma by means of filaments and an electron arc. The beam is extracted (3) from the source and it is composed by D, D_2 and D_3. A 90-degrees bending magnet (4) of 1.6 T is used to select only the mono-atomic D ions. These ions are then accelerated up to 230 keV, through a uniform gradient accelerating tube (5). The beam passes through a triplet quadrupole (7) to be focused on the target (8). The latter is composed of a copper cup, covered by 4.4 μm of titanium on the bottom, which contains tritium or deuterium, according to the desired neutron energy. A water-cooling

system is used to dissipate the power on the target (900 W maximum). The target is placed at 2 m from the accelerating tube and neutrons are generated almost isotropically. During the irradiation, some tritium is released into the vacuum system, and it is removed with a tritium removal system. The target is more than 4 m far from walls, floor and ceiling, in order to minimize as much as possible the neutron scattering. To this regard, the irradiation hall is 11.5 x 12 m^2 wide and 9 m high, so to reduce the spectrum contamination from moderation and neutron thermalization.

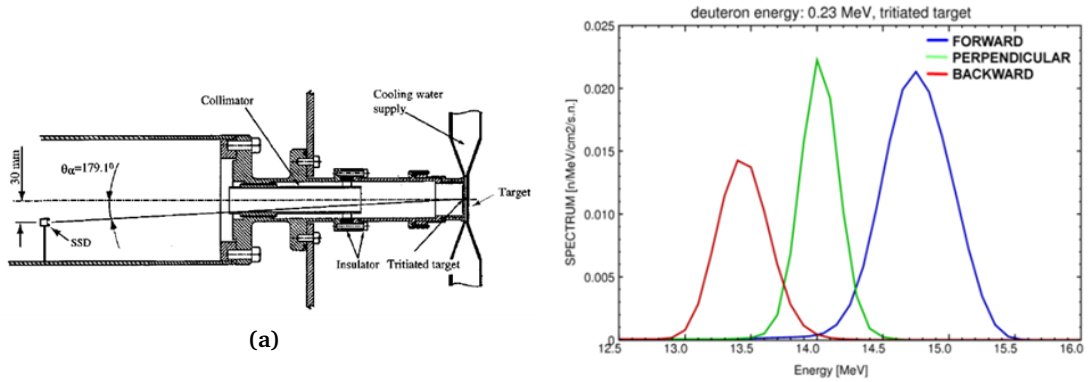

(a) **(b)**

Figure 5.4: (a): FNG target and SSD counter position (from [69]). (b): FNG 14.8 MeV neutron spectrum at different angles with respect to the target (from [69]).

The neutron flux is assessed counting the alpha particles (at 14.8 MeV) or ^{3}He ions (at 2.5 MeV) that are produced in the fusion reaction by means of a Silicon Surface barrier Detector (SSD), which is placed inside the vacuum system, as shown in Fig. 5.4a, with accuracy within 3%. Moreover, a fission chamber and a plastic scintillator counting are used, and these detectors are routinely calibrated through a set of activation foils, whose activity is measured through a germanium detector. The isotropic neutron yield of 14.8 MeV and 2.5 MeV is measured to be up to $1 \cdot 10^{11}$ n/s and $1 \cdot 10^{9}$ n/s, respectively. The neutron beam in the forward direction to the target has the peak energy at 14.8 MeV and a spectrum ranging from about 14 to 15.5 MeV, as shown in Fig. 5.4b. In addition, in the same Figure, the spectrum in the perpendicular and backward direction with respect to the target is depicted, showing that the spectrum is shifted to lower energies down to 13 MeV in the latter case.

The homogeneity of the beam is calculated from simulations provided by the facility. For instance, the homogeneity of the 14.8 MeV beam at 2.5 cm from the target, shown in Fig. 5.5, is within 20% over a spot diameter of about 3 cm.

The tests were performed at different distances from the target, in particular at 2.5 cm, the closest test position with a suitable homogeneity, presenting a flux during the tests (considering the target ageing) up to $3 \cdot 10^{8}$ cm^{-2}/s and $4 \cdot 10^{6}$ cm^{-2}/s for 14.8 and 2.5 MeV, respectively. The DUTs were installed on an optical plate, aligned to the centre of the beam by means of a laser.

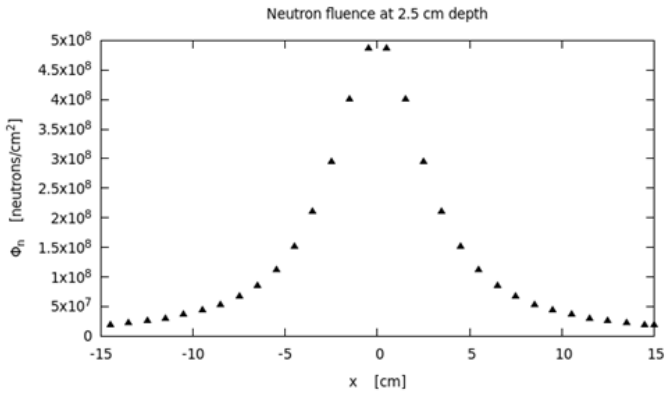

Figure 5.5: FNG 14.8 MeV neutron beam profile at 2.5 cm of distance from the target in perpendicular direction (Courtesy of S. Fiore).

Cross-calibration

Cross-calibration and fluence uncertainty assessment were performed through the ESA SEU Monitor (see Section 6.1.2) without lid (date code 1817). The ESA Monitor motherboard was installed at 2.5 cm from the target. As the 14.8 MeV flux was very high, the test time to obtain more than 3000 events was very short (less than 2 minutes) and the same measurement was repeated three times. Differently, at 2.5 MeV the flux during the irradiation was about 34 times lower than that at 14.8 MeV and the ESA Monitor cross section is 2 orders of magnitude less sensitive at this energy, hence the SEU statistics was limited.

Table 5.5 reports the upsets measured by each die of the ESA Monitor (worst-case between 4 runs) and the fluence uncertainty retrieved from their spread, as explained in Section 6.1.2. For both energies, the beam homogeneity was good resulting in 4.4% and 9.6% (1 standard deviation) for 14 and 2.5 MeV, respectively. The final fluence uncertainty will be considered as $\pm 2\sigma_f = \pm 10\%$ even for the 2.5 MeV, as the ESA Monitor measurement had little statistics to rigorously estimate the fluence uncertainty, which therefore relies on the value provided by the facility calibration.

Table 5.5: ESA SEU Monitor beam homogeneity assessment at 14 and 2.5 MeV. Fluence uncertainty (1 standard deviation) retrieved from the upset spread between dies.

E [MeV]	φ [n/cm^2/s]	die0	die1	die2	die3	$\pm 1\sigma_{fluence}$(%)
14.8	$1 \cdot 10^{11}$	1038	953	966	944	4.4
2.5	$1 \cdot 10^{9}$	21	18	20	17	9.6

5.5 PTB - Monoenergetic Neutrons from 144 keV up to 17 MeV

The test campaign was carried out in September 2020 in the scope of this thesis.

Low and intermediate energy neutron measurements were performed at the accelerator facility PIAF of the Physikalisch-Technische Bundesanstalt (PTB), the national metrology institute of Germany [71–74]. PTB can provide a very broad set of neutron energies, from 24 keV up to 19 MeV [73], and therefore extremely interesting for the studies of the thesis. The facility not only permitted to accurately characterize devices at several intermediate neutron energies but even to assess their response below the 0.2 MeV threshold, set as the lower limit in the HEHeq flux calculation.

5.5.1 PTB description

The neutron field produced from the target can be distorted by scattering with floor, walls and ceiling. Hence, to reduce the neutron scattering, the irradiation room has dimensions of 24 x 30 m and 14 m of height, and the beamline is located in the middle of a pit accessible by means of an aluminium grid, as seen in Fig. 5.6.

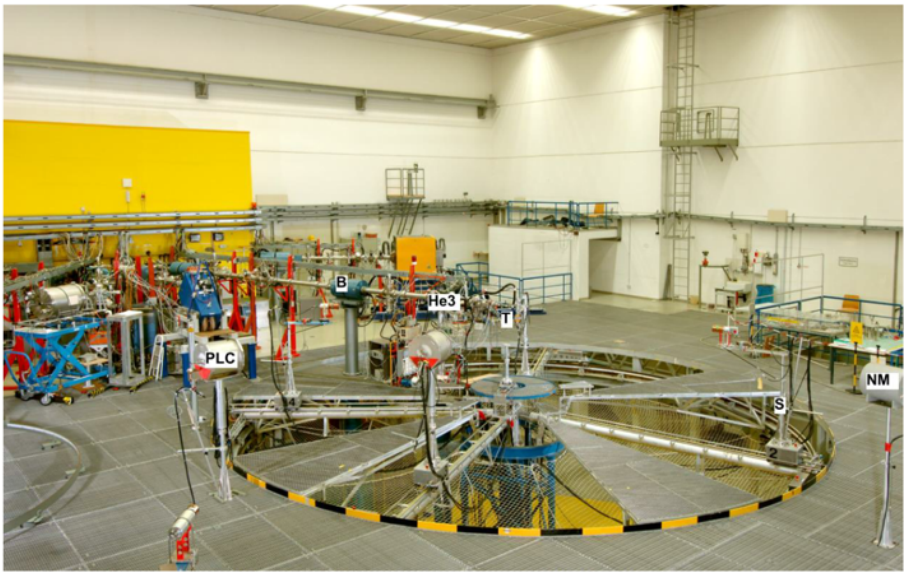

Figure 5.6: PTB irradiation room and several detectors. The beamline is in the middle of the pit to reduce the neutron scattering (courtesy of Ralf Nolte).

Monoenergetic neutrons are typically produced without any collimator to avoid distortion of the spectrum, with an emission angle of 0° with respect to the ion beam. In PTB, they are produced from nuclear reactions of light ion beams (protons or deuteron gas) with a light nuclei target (lithium, deuteron or tritium) [71]. For instance, neutrons of 0.144 MeV are produced by the interaction of 1.943 MeV protons with a Lithium target, and they were used

to assess the sensitivity of the devices below the threshold of 0.2 MeV.

For stability and security reasons, targets are in a solid-state and in the form of a mixture with titanium, so that T and D targets are actually Ti(T) and Ti(D), respectively. They are produced at high temperatures by absorption of tritium or deuterium in titanium layers, and they are very sensitive to the overheating by the ion beam. For this reason, the target is cooled by cold air instead of water, to avoid degradation of the neutron spectrum. Lithium targets (metallic form) are manufactured by a proper machine and delivered in vacuum to the target station, because lithium is highly reactive with water and carbon dioxide [71]. Furthermore, the tritium in the Ti(T) target used for the 17 MeV can decay to ^{3}He, and produces protons with the incoming deuteron beam via the ^{3}He(d, p)T reaction. In order to stop these protons (maximum energy of 17 MeV), an aluminium foil of 0.5 mm was interposed between the beam and DUT. Detailed information about the neutron production and relative fields in PTB as presented in Section 5.5.2.

Table 5.6 reports the list of neutron energies (E_n) used for the tests, with the corresponding reaction in the form Target (Projectile, Ejectile) and projectile energy. Energies measured at FNG (see Section 5.4) are also reported for completeness and comparison. In addition, the closest distance of DUT to the target and the relative average flux, both during the tests, are included (the latter reported as the highest among runs). It has to be noted that 2.5 MeV neutrons, tested in PTB and FNG, are produced through different reactions. Ions are accelerated either with a 3.75 MeV Van de Graaff generator (for lower energies) or a cyclotron (for higher energies).

Table 5.6: Neutron reactions produced in PTB and FNG, with corresponding projectile energy, closest distance of DUT to the target and average flux, both during the tests.

Facility	E_n [MeV]	Reaction	E_{proj} [keV]	d [cm]	φ_n [cm^{-2}/s]
PTB	0.144	Li(p,n)	1943	5.5	$4.0 \cdot 10^5$
PTB	1.2	T(p,n)	2047	5.5	$1.8 \cdot 10^6$
PTB	2.5	T(p,n)	3356	5.5	$1.9 \cdot 10^6$
FNG	2.5	D(d,n)	300	2.5	$3.8 \cdot 10^6$
PTB	5	D(d,n)	2406	6.6	$8.2 \cdot 10^5$
PTB	8	D(d,n)	2524	6.6	$2.7 \cdot 10^6$
FNG	14.8	T(d,n)	300	2.5	$1.2 \cdot 10^8$
PTB	17	T(d,n)	1264	5.5	$5.2 \cdot 10^5$

The flux is measured through four yield monitors. The Long counter (NM) is the most stable and sensitive detector, composed of a ^{3}He tube and located at 16° with respect to the beam (see Fig. 5.6). The Pangher long counter (PLC) located at 100° and a ^{3}He counter located at 145°, which mainly measures the neutrons scattered from the hall to determine the room neutron return. Finally, the integrated beam current is a means to measure the beam charge, from which the neutron fluence is calculated (this latter monitor was used for the analysis).

Cross-calibration

The ESA Monitor was tested at 17, 8 and 5 MeV, however, the die statistics was insufficient to estimate the fluence uncertainty (less than 50 upsets per die were measured mainly because of the low flux), and hence the fluence uncertainty relies on the facility calibration during the runs. It was performed through the PLC monitor, measured with the DUT setup in position and with an empty field, namely with the setup removed from the test position to assess its impact on the monitor. The calibration considers the standard deviation of the PLC to charge monitor ratio, resulting in $\pm 2\sigma_f \leq \pm 5\%$ for all energies. A conservative value of $\pm 2\sigma_f = \pm 10\%$ is considered for the analysis.

5.5.2 Monoenergetic beams and neutron production in PTB

A neutron field or beam produced by a nuclear reaction is monoenergetic if the neutron energy is a unique function of the neutron emission angle under ideal conditions, i.e. massless DUT and negligible energy loss of the projectile in the reactive layer. This requires that the nuclear reaction has exactly one exit channel with only two particles and no excited states involved.

Under realistic conditions, however, the energy distribution of the monoenergetic neutron produced at a given emission angle exhibits a finite width which reflects the energy loss of the projectile in the reactive target layer. In addition, these 'monoenergetic' neutrons are accompanied by neutrons of lower energy which result from scattering of primary 'monoenergetic' neutrons in the DUT. Usually, experimental conditions are selected such that the relative width of the energy distribution of the monoenergetic neutrons and the relative contribution of scattered neutrons are only a few per cent each.

If the kinematic conditions mentioned above are not met, i.e. several exit channels are possible, the resulting neutron field is called quasi-monoenergetic even if the monoenergetic exit channel is dominating. In such cases, the monoenergetic component is accompanied by lower-energy neutrons resulting from other reaction channels, e.g. breakup reactions of the target or projectile nuclei with more than two particles in the exit channel. This is typical when producing neutron energies above 20 MeV through the ^{7}Li(p, n)^{7}Be reaction, resulting in a spectrum composed of a main peak and a lower energy tail [60].

At the PTB ion accelerator facility PIAF, monoenergetic neutron fields with mean neutron energies at 0° between 144 keV and 8 MeV and between 14.8 MeV and 19 MeV are produced using the nuclear reactions ^{7}Li(p, n)^{7}Be, ^{3}H(p, n)^{3}He, ^{2}H(d, n)^{3}He and ^{3}H(d, n)^{4}He. The deuteron beam energy employed for producing the 8 MeV field using the ^{2}H(d, n)^{3}He reaction is already above the threshold for the breakup reaction ^{2}H(d, np)^{2}H, which corresponds to a neutron energy of 7.70 MeV for the monoenergetic channel ^{2}H(d, n)^{3}He. However, the breakup cross section at this energy is so small that the field is practically monoenergetic. In the energy region between 8 and 14.8 MeV no useful monoenergetic neutron producing reaction is available. In this energy region, the neutron energy distributions produced by bombarding Deuterium targets with deuterons always exhibit a monoenergetic component

and a more intense breakup component at lower energies [71]. Hence, only neutrons in the energy region 144 keV to 8 MeV and 14.8 to 19 MeV are monoenergetic and can be employed to investigate the sensitivity of electronics.

As discussed above, the neutron energy distributions at the position of the DUT are composed of the primary monoenergetic beam and the spectrum of neutrons scattered in the target assembly. This contribution was calculated through simulations provided by the facility (considering a disc of 1 cm^2) and resulted in less than 4% with respect to the main neutron fluence (1.1% at 144 keV). The cutoff energy in these simulations was 2 keV.

Thermal neutrons (around an energy of 25 meV) are not produced with the primary neutron field and are only part of the room-return background that results from neutron thermalization in the walls. However, the large dimensions of the hall and the low-mass grid floor are specifically designed to reduce as much as possible the neutron room return, thus thermal neutron fluxes at the DUT position are negligible.

5.6 Am-Be Source - Neutron Spectrum up to 11 MeV

The Americium-Beryllium (Am-Be) is a neutron source located at CERN, typically used for radiation protection purposes [75], and the study performed in [65] verified its suitability for electronics testing. The source is extremely useful for screening and the preliminary study of components, given its high availability and easy accessibility, a spectrum of intermediate energy neutrons up to 11 MeV and the fact that electronics is not activated after the exposure.

The facility is composed of the irradiation room shown in Fig. 5.7. The source, which is stored at the bottom of the room, can lift through the aluminium pipe (see right Fig. 5.7) by means of compressed air, reaching the exposure position. In this way, the source remains in the middle of the wide room, enabling an isotropic irradiation with negligible neutron scattering.

Figure 5.7: Am-Be irradiation room to the left and source exposure position to the right.

Neutrons are generated after the absorption by the beryllium of alpha particles, which are emitted from the americium. The source has an activity of up to 888 GBq, which provides an isotropic neutron yield of $5.03 \cdot 10^7$ [n/s] ±5% ([75]). The neutron spectrum has a peak around 3 MeV and reaches a maximum energy of 11 MeV, as shown in the FLUKA simulation of Fig. 5.8a, representing the neutron spectrum around the source capsule (cylinder: 7.62 cm high and 2.54 cm of diameter) and at 5 cm of distance from the source centre. The flux attenuation follows a r^{-2} law, as proved in the FLUKA simulation of Fig. 5.8b that was benchmarked with the ESA Monitor measurements, considering its SEU cross section in saturation (200 MeV PSI) and its intermediate-energy neutron response. As introduced in Section 2.3.2, intermediate energy neutrons are weighted with a response function to obtain the HEHeq flux, defined in Eq. 2.6. Therefore, the HEHeq flux was calculated using the Weibull function of the ESA Monitor, weighted with the neutron flux simulated in FLUKA enabling a direct comparison with the measurements, which resulted in agreement within 15%. The HEHeq flux calculated at 5 and 10 cm from the source is reported in Table 5.7 when using the Toshiba and ESA Monitor response.

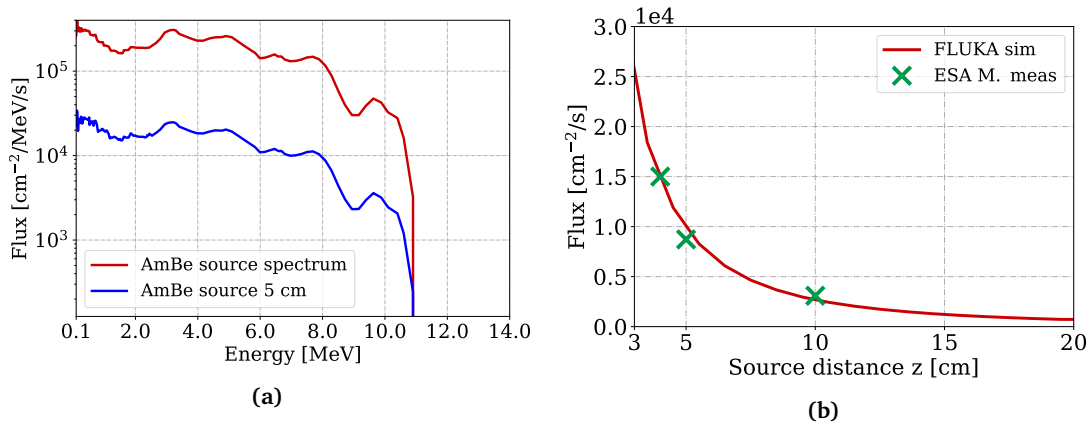

Figure 5.8: (a): Americium-beryllium neutron spectrum on the source capsule and at 5 cm of distance (test position used in this work). The source is located at CERN and provides a maximum energy of 11 MeV. (b) Flux attenuation as a function of the distance, FLUKA simulation and ESA Monitor measurement.

Table 5.7: HEHeq fluxes at 5 cm and 10 cm of distance from the centre of the source, retrieved from FLUKA (Toshiba response) and by applying the ESA Monitor Weibull response to the FLUKA neutron spectrum.

	Response	5 cm	10 cm
HEHeq $[n/cm^2/s]$	Toshiba (FLUKA)	$1.84 \cdot 10^4$	$5.05 \cdot 10^3$
	ESA M.	$9.32 \cdot 10^3$	$2.61 \cdot 10^3$

Other sources can be employed to produce neutron spectra with lower energies as reported in Table 5.8 from [72] (to note that the Am-Be characteristics in this table do not concern the source located at CERN, which instead presents a mean energy around 4.5 MeV).

Table 5.8: Mean energies and neutron energies corresponding to the 10% and 90% of the spectral fluence distribution of several neutron sources. The calculated and measured De Pangher long counter efficiencies are shown for completeness (Table from [72]).

Source	Mean energy/MeV	$(E_{10} - E_{90})$/MeV	Source of spectral data	Calculated response/cm^2	Measured response/cm^2	Measured/calculated
^{124}Sb–Be	0.0215	0.017 to 0.024	Ryves [68]	3.23 ± 0.04	3.24 ± 0.02	1.003 ± 0.014
^{241}Am–Li	0.451	0.032 to 1.06	Tagziria [69]	3.40 ± 0.05	3.46 ± 0.04	1.017 ± 0.019
^{238}Pu–Li	0.537	0.126 to 1.00	IAEA [70]	3.38 ± 0.05	3.45 ± 0.02	1.021 ± 0.016
^{241}Am–F	1.49	0.73 to 2.20	Tagziria [71]	3.46 ± 0.05	3.50 ± 0.04	1.012 ± 0.019
^{252}Cf	2.13	0.4 to 4.6	ISO [72]	3.40 ± 0.05	3.31 ± 0.02	0.974 ± 0.016
^{241}Am–Be	4.16	0.75 to 7.61	ISO [72]	3.27 ± 0.04	3.22 ± 0.02	0.985 ± 0.014

5.7 ChipIr - Atmospheric like Neutron Spallation Spectrum up to 700 MeV

Two test campaign were carried out in March 2018 and March 2019 in the scope of this thesis.

ChipIr (for Chip Irradiation) is a neutron facility located at the end of the ISIS spallation neutron source beamline, at the Rutherford Appelton Laboratory (Didcot, UK) [76]. The facility is currently the reference European spallation source, and the instrument is dedicated to the irradiation of microelectronics, specifically tailored to the study of SEEs.

Spallation neutron production occurs when energetic protons (>100 MeV) interact with atomic nuclei. This process takes place in the upper atmosphere, through the interaction of primary cosmic rays, but also in a spallation source like ISIS, where protons are accelerated up to 700 or 800 MeV in the ISIS synchrotron and are collided against a tungsten target to produce neutrons. During the present tests the cut off energy was of 700 MeV. The fast neutron ($En > 1\ MeV$) beam is then collided with a secondary scatterer, to optimize the hard atmospheric-like spectrum and minimizes the gamma-ray flux. For this reason, a spallation source can be used to reproduce an atmospheric like spectrum, with the resulting spectrum extending up to the energy of the proton accelerator. In the case of ChipIr, the design of the instrument is optimized to mimic the atmospheric neutron spectrum, with a flux roughly nine orders of magnitude higher than the natural one to enable accelerated testing of electronic devices [77].

The neutron flux in ChipIr was measured in [76] using multi-foil activation. This method consists in the irradiation of samples with a known amount of target nuclei and the measuring of the activation rates, which are correlated to the neutron flux through the activation cross sections. The neutron flux can be measured by combining the activation data of different reactions. Depending on the activation cross section, each reaction is induced in different proportions by neutrons belonging to different parts of the energy spectrum. By properly choosing the set of activation reactions, a wide energy range of the neutron flux can be measured. Fig. 5.9 shows the differential neutron flux obtained from the unfolding of the foil

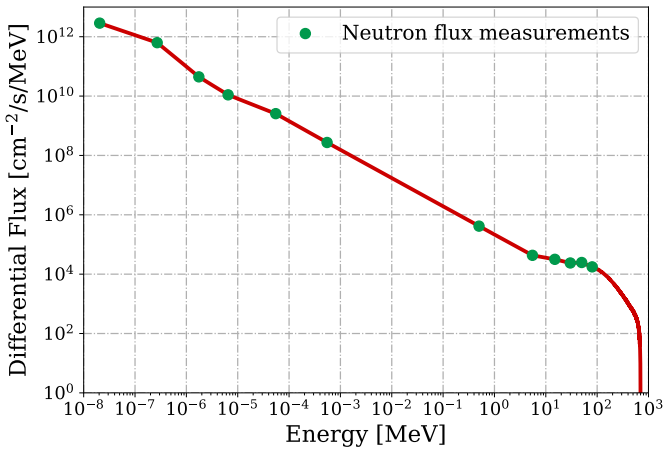

Figure 5.9: ChipIr spectrum in differential flux from activation foil measurements and interpolation with power functions up to 100 MeV. The 100-700 MeV interval is retrieved through MCNP simulation. Both axis are in logarithmic scale.

activation measurements up to 100 MeV, which consist of 12 flux values (green points). The spectrum from 100 to 700 MeV is retrieved through MCNP simulations because measurements in this range of energies are difficult to carry out and less accurate.

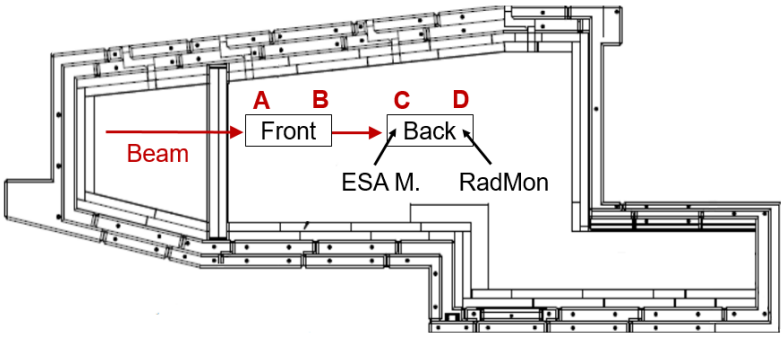

Figure 5.10: ChipIr irradiation room and test positions (top view).

The choice of a passive method for the spectrum measurements was mainly motivated by the complex time structure of the source. The ISIS source is pulsed at 10 Hz on the target and the pulse has a double structure with two bunches 70 ns wide and 360 ns apart. This does not allow for spectroscopy with time of flight (TOF) technique for neutrons over 10 MeV, because of the short time between bunches and the fact that the beamline is only 15 meters long, which would lead to high uncertainty. Furthermore, high instantaneous fluxes can result in a strong pile-up for many active detectors, whereas the passive method is not affected by these complications. However, active detectors are also used in ChipIr, as a silicon diode through which the real-time flux can be retrieved considering the operating conditions of the facility. The beam mapping and profiling are performed with diamond and Gas Electron Multiplier (GEM) detectors, which demonstrated an excellent uniformity in 70x70 mm^2 wide beams, and an average flux of $3.56 \cdot 10^6$ n/cm^2/s (E>10 MeV) at the actual test position, 320 cm far from the beam output (as depicted in Fig. 5.10 with label "C").

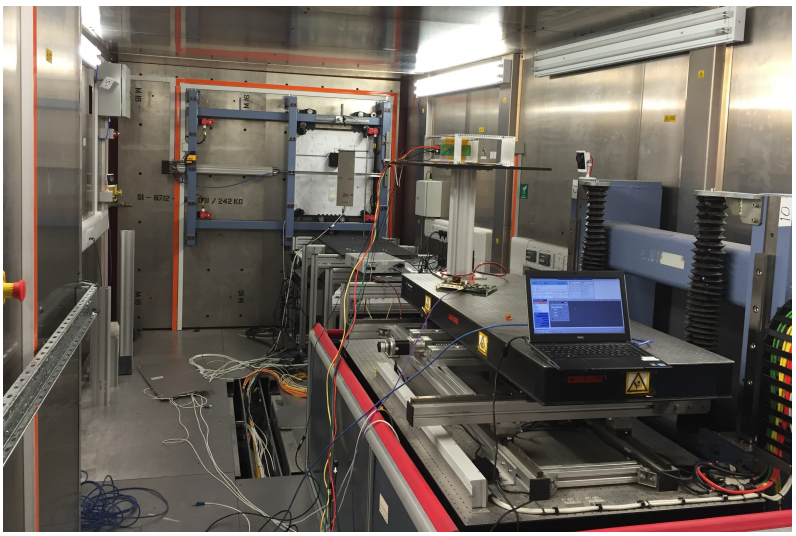

Figure 5.11: Photograph of the irradiation room and setup preparation, for the tests conducted in March 2018. The "back" optical table position (see Fig. 5.10) used for the tests is visible in the foreground, with the DUTs installed in position C.

As ChipIr presents a neutron spectrum up to high energies, similar to that found in the LHC, a dedicated analysis was performed to assess until what extent ChipIr can mimic the high-energy accelerator environments, and compared to the mixed-field of CHARM. This study, which includes a new calibration approach to study the spectra of such as facilities, is exposed in Section 5.9.

Cross-calibration

In both test campaigns (2018, 2019) the beam was characterized and compared with the ESA Monitor without lid (date code 1817), installed in position C (see Fig. 5.10). Table 5.9 compiles the homogeneity assessment, where the data from 2019 are the result of three different runs. Hence, the $\pm 2\sigma_{fluence}$ uncertainty for CHipIr will be considered as ±10%.

Table 5.9: ESA SEU Monitor beam homogeneity assessment at ChipIr during two test campaigns. Fluence uncertainty (1 standard deviation) retrieved from the upset spread between dies.

Test	Date code	die0	die1	die2	die3	$\pm 1\sigma_{fluence}$(%)
2018	1330	284	282	273	271	2.3
2019	1817	1288	1187	1220	1158	4.6

5.8 CHARM - Mixed Field

Electronics tests were conducted during May-June 2018 in the scope of this thesis.

The CERN High energy AcceleRator Mixed Field (CHARM) is a CERN facility operating since 2014, where the radiation environments found in the LHC (and future HL-LHC) accelerator can be reproduced. It has been intensively used for testing electronic components and systems, in a mixed-field radiation environment obtained using different combinations of shielding, target and test positions.

As further detailed in [78], CHARM receives a 24 GeV proton beam extracted from the Proton Synchrotron (PS), which interacts with a 50 cm target (typically of copper) generating a mixed-field composed of neutrons, protons, pions and electromagnetic showers (see Fig. 5.12). It is similar to a spallation facility but charged particles are not removed from the field. CHARM normally operates from May to November, according to the PS operation cycle.

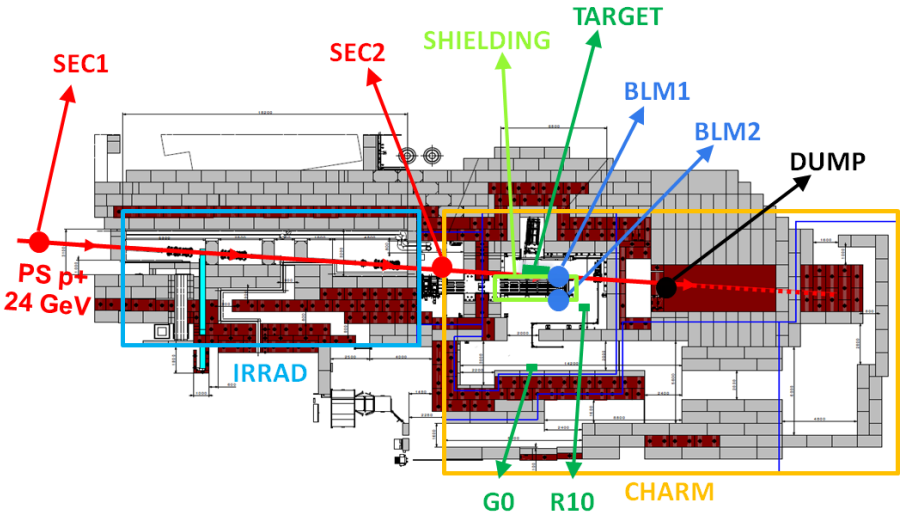

Figure 5.12: Top view of the CHARM facility downstream IRRAD, showing the 24 GeV proton beam delivered by the PS. The SEC1 and BLM monitors are indicated on the illustration, as well as G0 and R10 test positions employed in this work.

Inside the CHARM irradiation area, there is a movable shielding composed of four blocks of concrete-iron-iron-concrete, which can be combined in different ways in order to obtain a broad variety of spectra relevant not only to high-energy accelerator applications, but also to ground level, avionic and space environments [26]. As seen in Fig. 5.13, a broad variety of test positions are available, most of them inside the main irradiation chamber (numbered from 1 to 13) and a few along the corridor (M0, G0). As personnel cannot access the main irradiation room (but only the corridor) due to radiation protection constraints, systems and equipment are installed on a proper rack, which is carried by an automatic guided vehicle. In addition, a movable shuttle (Montrac) is designed to carry small setups inside the chamber by means of a rail. A photograph of the irradiation room and corridor at CHARM is shown in Fig. 5.14.

When the shielding blocks are inside the chamber, the energy and intensity of the mixed-field decreases and there is a greater relative contribution of neutrons, thus mimicking the conditions in the LHC alcove areas. The locations inside the chamber present harder spectra compared to those in the corridor, and the former do not exceed an R-factor of 3, whereas

locations in the corridor present larger R-factor values. Position M0, which is shielded by the wall, showed the highest relative flux of thermal neutrons (largest R-factor) and was studied in [65]. Measurements in the scope of this thesis were performed in R10 and G0 (see Fig. 5.13), located at 30° and 87° with respect to the incoming beam on the target, which are characterized by a hard and soft spectrum, respectively. All test positions at CHARM are calibrated through the R-factor, measured by the RadMon system described in Section 2.5, and the facility was modelled in FLUKA, simulating R-factors, doses, particle spectra, etc. [79].

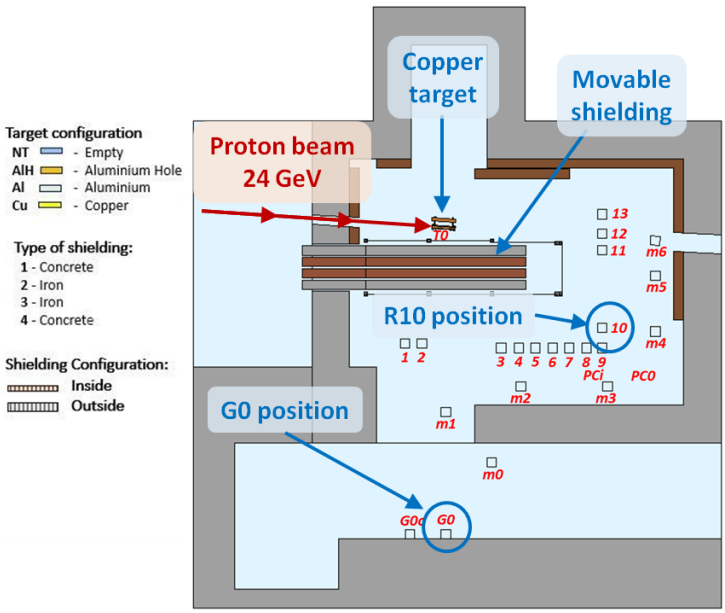

Figure 5.13: Horizontal cut of the CHARM facility seen from the top. Several test positions (numbered) are available inside the main irradiation chamber (from 1 to 13) and in the corridor (G0, M0) with the numbered positions inside the main chamber; M0 and G0 (0) in the corridor were the locations neutron-dominated used in the experiments.

The notation $XX - abcd$ is used to denote the shielding configuration, where XX is the metal target (Copper Cu, Aluminium Al, Aluminium-holes Alh) and abcd is the shielding status: C=concrete, I=iron, O=out. For instance, the notations Cu-OOOO and Cu-CIIC are used to indicate the non-shielding and full-shielding configurations with copper target, respectively.

The proton beam extracted from the PS has a time structure in spills, each of which has a length of approximately 350 ms. A group of 3 spills, spaced from 4 to 6 seconds, are typically injected to CHARM, in a cycle repeated about every 40-50 seconds and arranged in a super-cycle of 30 bunches. With the aim of calculating the particle fluence on a specific position it is essential to accurately measure the delivered Protons On Target (POT), measured by a calibrated secondary emission chamber (SEC1), which is placed upstream the IRRAD facility (see Fig. 5.12). The number of POT is retrieved by multiplying the SEC1 value by $1.84 \cdot 10^7$ [80], which was calibrated using aluminium activation foil measurements placed directly in the beam [81]. Since the beam delivered to CHARM passes through the upstream facility IRRAD, the beam characteristics can be affected by its operation, as evaluated in [65]. Whereas the SEC1 detects all protons in the primary beamline, the mixed-field at CHARM is

generated only when the target is placed in the beam. The latter aspect is monitored by a set of detectors, such as the Beam Loss Monitor (BLM) ionization chambers placed inside the irradiation room (indicated as BLM1 and BLM2 in Fig. 5.13) and the RadMon system.

Access to CHARM during the operation period normally takes place on the morning of every Wednesday. The beam is turned off two days before the access to cool down the facility. Since 2019, the LHC and its injector chain, including the PS and the operation at CHARM are in long shut down (LS2), in order to consolidate and upgrade the machine, especially in view of the HL-LHC.

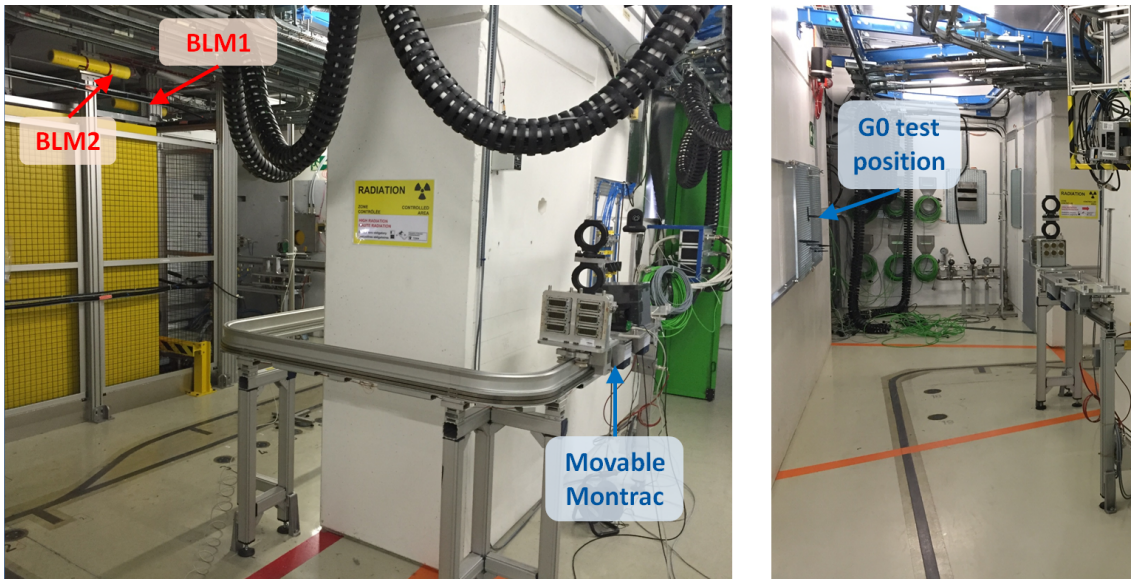

Figure 5.14: Photographs of CHARM. In the left picture are shown the main irradiation room seen from the corridor, with the two BLMs, the shielding configuration in position (yellow block) and the Montrac which can move through the rail. In the right picture is visible the corridor with the G0 test position, and a RadMon installed on the top right of the wall. The black line passing through the floor is the path for the automated guided vehicle.

5.9 Flux and Spectral Hardness Calibration of Neutron Spallation and Mixed-Field Facilities

5.9.1 Introduction

The approach of calibrating neutron environments through well-known SEU based SRAM memories is applied to a neutron spallation and mixed-field facility. The availability of a method to compare different radiation environments is essential because differences in neutron and HEH spectra can play an important role when determining the SER. Neutron facilities are typically calibrated through activation foil methods, where different elements are irradiated by the beam and the activation from the produced reactions is measured. This method is

precise but requires many runs, samples and a lengthy data analysis, and in addition becomes even more complex in mixed-field facilities, where a broader range of particle types is present.

The approach applied in this work for the characterization of both spallation and mixed-field facilities lies in employing SEU and SEL based detectors. They rely on calibrated SRAM memories which are sensitive to a broad range of energies. The difference of this method compared to the activation foil technique lies on the fact that in the latter, the flux is retrieved in energy intervals, whereas these memories are sensitive to the entire spectrum. SRAM detectors are easy to deploy, they actively record the number of events and knowing their SEE cross sections to HEH and thermal neutrons, they provide online the respective fluences. Since the cross section is energy-dependent, when calibrating a new spallation or mixed-field facility the memory response as a function of energy is required for considering all the portions of the spectrum.

In this framework, the ChipIr neutron facility of the ISIS spallation source, in the UK [76] was investigated in order to verify its capability of reproducing the SEU and SEL cross sections typically observed in mixed-field environments, such as those measured at CHARM [78]. ChipIr is particularly interesting for evaluating the calibration method, since it can provide a broad spectrum ranging from thermal neutrons up to 700 MeV. Its large beam size capability is also especially attractive for board and system level tests.

The first phase of the study was dedicated to the cross-calibration of the facility with standard SRAM-based detectors: the ESA SEU standard Monitor (see Section 6.1.2) and the RadMon system (see Section 2.5), the same used throughout the LHC ring for monitoring the HEHeq and thermal neutron fluences. These two detectors rely on SEU measurements and are commonly used for calibrating different facilities. The results have been compared with the calibration carried out through multi-foil activation measurements reported in [76].

In a second phase of the study, memories with a strong energy dependence on the cross section were tested against SEL, both at ChipIr and CHARM, to correlate the spectral hardness of the facilities, and those of the LHC alcoves. Based on considerations from nuclear reactions, the SEL cross section is typically assumed in saturation above 150 MeV [82]. However, for components presenting high-Z materials such as tungsten near the sensitive volume areas and a relatively large LET threshold, the SEL cross section is expected to increase up to a few GeV [40]. Owing to this unusual nature, these memories are differently sensitive to high energies and consequently can be employed as a means of calibrating different spectral hardnesses. Moreover, the behaviour of memories up to the expected saturation value of roughly 3 GeV can be estimated through a Monte Carlo simulation model [58]. The applicability of the model, which was initially employed for monoenergetic proton beams, has been verified for particles spectra in Section 5.9.3.

5.9.2 ChipIr Flux cross-calibration

The cross-calibration of ChipIr was carried out through the ESA SEU standard Monitor and the RadMon system. The approach for the SRAMs consists in extracting the portion of the

spectrum, retrieved from the activation foil measurements, to which the calibrated memory is sensitive thanks to the knowledge of its response function. This flux is then compared to the expected flux obtained from the SRAMs measurement, as their cross sections to HEH and thermal neutrons are known. The same can be seen in terms of cross sections, comparing the measured cross section in the spallation facility (using the HEHeq fluence) to that in saturation (200 MeV).

The differential flux up to 100 MeV shown in Fig. 5.9 was extracted from measurements reported in [76]. These measurements have been interpolated with power functions, with the approximation of considering linear the curve between two points of the graph (seen in logarithmic scales), to obtain the desired resolution in energy for the consequent calculations. The remaining part of the spectrum up to 700 MeV was calculated through MCNP simulation, as previously stated in Section 5.7. The expected HEHeq fluxes by applying Eq. 2.6 are reported in Table 5.10, where the fluxes are obtained by weighting the facility spectrum with the SRAM Weibull functions, and therefore they are not directly measured by the memories. The Weibull parameters used in the calculation were retrieved for ESA Monitor, Cypress and Toshiba in dedicated studies [26].

Table 5.10: ChipIr theoretical HEHeq fluxes of the spectrum retrieved through Eq. 2.6 for the three memories, and fluxes above 10 and 20 MeV. The values are normalized by the operating factor, "o". Total uncertainty within 23%.

$\varphi_{HEHeq}\ [cm^{-2}/s/o]$			$\varphi_{>10\ MeV}$	$\varphi_{>20\ \mathrm{MeV}}$
ESA M.	Toshiba	Cypress	$[cm^{-2}/s/o]$	$[cm^{-2}/s/o]$
$3.54 \cdot 10^6$	$3.63 \cdot 10^6$	$3.46 \cdot 10^6$	$3.57 \cdot 10^6$	$3.25 \cdot 10^6$

These fluxes account for the facility operating conditions (denoted with "o" in the measuring unit) which can change from different runs and times. They are mainly dependent on the position of the DUT with respect to the reference position and the possible systematic offset between monitoring diode and spectrum calibration. The diode flux is a normalized value, calculated by multiplying its counts by a calibration factor (dimensionless), so that o_{factor} is ideally 1. The operating condition is thus defined as the ratio between the flux recorded by the facility diode, and the flux above 10 MeV from the original calibration, as expressed in Eq. 5.2.

$$o_{factor} = \frac{\varphi_{diode}}{\varphi^{\text{calib.}}_{>10\ \mathrm{MeV}}} \tag{5.2}$$

Its value during the tests was of 0.97 and 0.85 for positions C and D, respectively (see Fig. 5.10).

As shown in Table 5.10, the HEHeq fluxes of the different memories, based on the neutron spectrum and respective response functions, are very similar to each other, with difference within 10% even considering the flux calculated above 10 MeV. This aspect implies that the memories sensitivity to intermediate energy neutrons in ChipIr only weakly affects the total

HEHeq flux, as will be also shown in the SER study in Section 7.3.

ESA SEU Monitor cross-calibration

The device was installed in position C (see Fig. 5.10) and measured with and without a thermal neutron absorber. To this regard, the sensitive dies of the ESA Monitor were covered with boron carbide (B4C) with the purpose of evaluating the thermal neutron impact on the measured upsets from Eq. 2.10. The thickness and properties of the material permit to completely absorb the neutron flux below 1 eV [11]. As shown in the first column of Table 5.11, the result on the SEU cross section by employing the boron carbide is less than 5% different with respect to that extracted without thermal neutrons absorber. This aspect, together with

Table 5.11: ESA Monitor SEU cross sections in [cm^2/bit] measured in different facilities. In brackets the measurement with boron carbide. CHARM position refers to R10. Uncertainties within 25%.

Memory	σ_{HEH}^{ChipIr}	$\sigma_{230\ MeV}^{PSI}$	σ_{HEH}^{CHARM}
ESA M.	$2.28 \cdot 10^{-14}$ ($2.17 \cdot 10^{-14}$)	$2.63 \cdot 10^{-14}$	$2.69 \cdot 10^{-14}$

the fact that the ESA Monitor SEU cross section to thermal neutrons is $3.36 \cdot 10^{-15}$ [cm^2/bit] (from measurements performed at ILL in Section 6.4), about one order of magnitude lower than that of HEH, allows to neglect the thermal neutron portion compared to more energetic neutrons. Therefore, the thermal term in Eq. 2.12 can be considered negligible and only the HEHeq flux will contribute to the upset rate as reflected in the cross section of Table 5.11 (the relative total uncertainties are within 25%, and were calculated considering the statistical and fluence uncertainties, as explained in Section 6.1). With the formalism presented in the introduction, considering the involved uncertainties, the difference of 14% between the cross section measured in ChipIr and that at 230 MeV monoenergetic protons assumed as saturation shows the validity of the approach. The respective flux value considering the 230 MeV saturated cross section is reported in Table 5.12 (first two columns) together with that calculated from the spectrum, the latter extracted from Table 5.10, multiplied by the respective o_{factor}.

Table 5.12: HEHeq and thermal neutron fluxes measured by the ESA Monitor (for position C) and RadMon (for position D), compared to those extracted from the spectrum through the SRAMs response. RadMon uncertainty are reported in percentage and absolute value for HEH and ThN, respectively.

φ_{HEHeq} [cm^{-2}/s]				φ_{ThN} [cm^{-2}/s]	
ESA M.	*Spectrum*	*RadMon*	*Spectrum*	*RadMon*	*Spectrum*
$2.97 \cdot 10^6$	$3.43 \cdot 10^6$	$3.09 \cdot 10^6$ ±21%	$3.09 \cdot 10^6$	$3.49 \cdot 10^4$ $0 - 2.8 \cdot 10^5$	$2.13 \cdot 10^5$

RadMon cross-calibration

The HEHeq flux measured by the RadMon, which was installed on position D (see Fig. 5.10), is reported in Table 5.12 in comparison with that measured from the spectrum considering the Cypress Weibull response (see Table 5.10) and the operating conditions. As can be seen, the agreement is very satisfactory within 1% between absolute values of RadMon and spectrum measurements, fully compatible with the 21% of uncertainty. This aspect, along with the ESA Monitor cross-calibration, confirms the assumption of considering the spectrum of 12 groups continuous through power functions. The thermal neutron flux measured by the Toshiba memory of the RadMon is reported in Table 5.12 and results in more than a factor of 5 lower than the corresponding one retrieved from the spectrum through Eq. 2.12. This difference can be attributed to two possible contributions: the RadMon was staked behind the ESA Monitor during the same run, therefore thermal neutrons flux may have been attenuated by the latter much more than the fast neutrons. Moreover, the associated thermal neutron uncertainty of the RadMon for this specific measurement condition only allows to provide an upper limit (see Table 5.12). The relative error is so high because of the uncertainty propagation on the HEHeq measurements. Indeed, if the ratio between thermal neutrons and HEHeq fluxes is low, as in this case ∼0.01, the uncertainty propagation of the thermal neutron cross section is negligible compared to the HEH one, and the latter weights with the low thermal flux. The Cypress memories measured a total of 16949 SEUs all due to HEHeq, while the Toshiba ones recorded 2555 SEUs, of which 81 can be attributed to thermal neutrons. In other words, for the thermal neutron measurement, the uncertainty in the very large HEHeq background contribution limits its sensitivity. It is to be noted, however, that for environments with a stronger relative thermal neutron contribution, the RadMon is capable of measuring their flux with an accuracy of 20-30%, acceptable for most applications.

5.9.3 Spectral hardness evaluation with SRAM memories through SEL measurements

The spectral hardness is quantified through the $H_{10\%}$ factor, representative of the energy above which 10% of the total HEHeq flux is still present in the spectrum [56]. The same factor was also used to characterize the atmospheric radiation environment at varying altitude in Section 3.3.2 (see Table 3.3). In a similar way, $H_{50\%}$ is also defined, considering 50% of the flux. These two factors are defined according to the flux above 20 MeV, and they represent a given spectrum with a single energy value, enabling an analogy with monoenergetic beams.

The reverse integral of the HEHeq flux as a function of the energy is a method to compare the hardness of different environments, and from which $H_{10\%}$ can directly be extracted. The reverse integrals of different accelerator environments and facilities are reported in Fig. 5.15 for soft and hard spectra, as well as the ground level one. The spectral hardness of the facilities in comparison to that of the LHC alcoves (UJ, RR) and ground level (JEDEC) are shown in Table 5.13. They are ordered from the softer to the harder one, according to the $H_{10\%}$ factor. The extremely energetic radiation environment of the LHC tunnel has also been included in

the table for the sake of completeness.

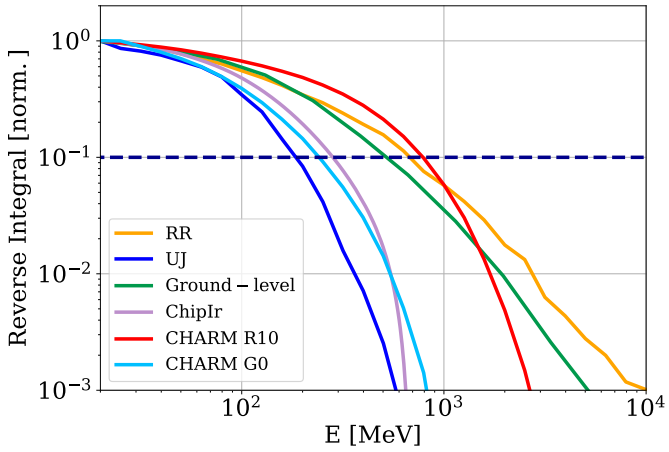

Figure 5.15: Reverse HEH flux integral as a function of the energy for ground level, LHC alcoves (RR, UJ), ChipIr and CHARM, with soft (G0) and hard (R10) spectra. The $H_{10\%}$ factors can be extracted from the intersection of the blue dashed line and and reverse integrals.

Table 5.13: $H_{10\%}$ and $H_{50\%}$ factors for different spectra in MeV.

	UJ	G0	ChipIr	JEDEC	RR	R10	Tunnel
$H_{10\%}$ [MeV]	183	194	283	525	690	790	1800
$H_{50\%}$ [MeV]	80	62	96	65	120	190	370

Samsung and Alliance SRAM memories were studied in [40] and showed a strong energy dependence, which enables their deployment as detectors sensitive to the shape of the energy spectrum. The SEE which enables the study is the latch-up, considering the HEH fluence (>20 MeV). The experimental SEL cross sections are shown in Table 5.14 for several facilities (230 MeV protons, ChipIr, CHARM) in comparison with the values retrieved from simulations explained in the following (including the operational environments ground level JEDEC, UJ, RR). Focusing on the measurements, both SEL cross sections of Alliance and Samsung SRAMs differ for more than one order of magnitude between soft and hard spectra.

When $H_{10\%}$ is higher than 200 MeV (i.e. typical maximum energy for standard proton monoenergetic testing and energy to which most of the cross sections are considered saturated), there might be a SEE underestimation in memories with strong energy dependence due to the contribution of higher energy particles [58].

The hard spectrum of R10 at CHARM compared to that of ChipIr explains the difference in the SEL cross section results (see Fig. 5.15). Therefore, soft and intermediate spectra such as that of G0 and ChipIr will lead to an underestimation of the SEL cross section for those components containing high-Z materials and operated in more energetic environments.

ChipIr presents a spectrum in between the softer G0 and the ground level one, and compatible with the ground level spectral hardness up to several hundred of MeV. The use of SEL

Table 5.14: Alliance and Samsung SEL cross sections calculated in different environments and facilities, for measurements (meas) and simulations (sim). The magnitude of the values is 10^{-11} [cm^2/chip]. Uncertainties are within 34%.

Mem $\cdot 10^{-11}$ [cm^2/chip]	σ_{HEH}^{UJ}	σ_{HEH}^{G0}	σ_{HEH}^{ChipIr}	$\sigma_{230\ MeV}^{PSI}$	σ_{JEDEC}	σ_{HEH}^{RR}	σ_{HEH}^{R10}
Alliance (meas)	-	5.1	7.1	34	-	-	43
Alliance (sim)	4.6	5.2	7.4	28	26	37	45
Samsung (meas)	-	-	6.8	44	-	-	61
Samsung (sim)	8.2	-	9.7	33	30	42	51

memories for characterizing spallation and mixed-field facilities has been shown to be valid by means of the hardness factor in addition to the following simulations.

SEL assessment through FLUKA model simulations

To support the observed energy dependence with the spectral hardness, the SEL cross sections of the present memories have been retrieved through the FLUKA model introduced in Section 4.10.1, by applying the model from [57,58]. It is a semi-empirical method applied to event-by-event energy deposition simulations that receive as input the operational spectrum. The model is then capable of extrapolating the SEL cross section up to several GeV, therefore applicable also to those environments, as the ground level or alcoves, where an actual measurement is typically unfeasible. Hereafter, the model from [58] is briefly described with some adaptations. In the cited publication, it was applied to monoenergetic protons, whereas in the present work its validity is assessed as regards a particle spectrum.

Samsung and Alliance memories (their specifics are reported in Table 6.3), both powered at 3.3 V, were measured using HI and the corresponding Weibull functions were calculated to describe the SEL cross section response versus LET. These are the experimental data that show a relatively high LET threshold of the memories. In fact, the LETs at which the Samsung and Alliance cross section is 1% of the saturated value, correspond to 18 and 15 $MeVcm^2/mg$, respectively (15 $MeVcm^2/mg$ is the upper limit LET for silicon fragments in silicon). The geometry of the Sensitive Volume (SV) consists of a surface of 4 x 20 μm^2 composed of 10 x 2 cells of 2 x 2 μm^2 each one. The deposited energy in the SV carried by the particles of the spectrum is evaluated event by event with the Monte Carlo FLUKA simulation tool [30]. The most important input parameters are the SV thicknesses, which was found to be 1.8 µm (Samsung) and 3.2 µm (Alliance) from the best fit of the model to the monoenergetic proton data. Moreover, the amount of tungsten in the metal layers around the SV, which turned out to be 0.48 $\mu m^3/cell$ for both memories, and is modelled with a thin layer above the SV. The SEL cross section for a given spectrum $\sigma_{SEL}(E_s)$ is computed through the integral of Eq. 5.3.

$$\sigma_{SEL}(E_s) = \int_0^{+\infty} \sigma_{HI}(E_d) \cdot p(E_s, E_d) dE_d \tag{5.3}$$

Where $\sigma_{HI}(E_d)$ is the HI cross section as a function of the deposited energy and $p(E_s, E_d)$

is the probability that a particle of the spectrum with energy E_s deposits an energy E_d in the SV.

The spectrum given as input is composed of neutrons, protons and pions in the case of RR, G0 and R10, and exclusively neutrons for the other spectra. The larger the SV thickness, the lower the resulting SEL cross section (from Eq. 5.3) for a given heavy ion response. Indeed, as seen in Table 5.14, the Alliance cross section is lower than that of Samsung, although this also depends on their HI response. This behaviour is explained by examining the two terms of the integral at varying SV thickness. $\sigma_{HI}(E_d)$ rises up proportionally with the energy until the saturation, whereas $p(E_s, E_d)$ decreases at increasing energy and at some point the two terms cross each other. The probability function increases by increasing the SV thickness because the secondary products can release more energy in a larger volume. On the other hand, the HI cross section curve shifts to higher energies because the deposited energy, which is proportional to the LET (constant) and thickness, is larger. The intersection of these two functions for the Alliance memory is lower than with the Samsung memory and consequentially the integral of the product results reduced.

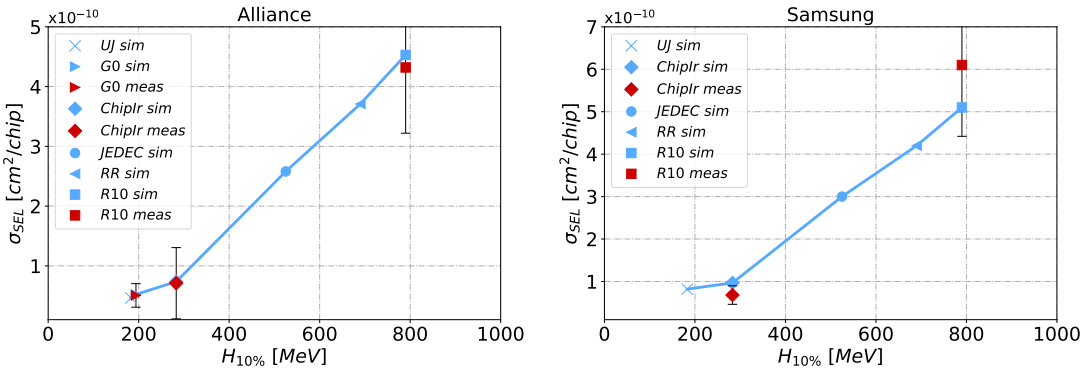

(a) **(b)**

Figure 5.16: Alliance (a) and Samsung (b) SEL cross sections as a function of the hardness factor $H_{10\%}$, retrieved through the FLUKA model and measurements. UJ and G0 values are almost overlaid in (a).

The energy dependence of these memories is shown in Fig. 5.16a and 5.16b with an evident increase of the SEL cross sections above a $H_{10\%}$ value of 200 MeV (numerical values are shown in Table 5.14 with the monoenergetic proton data). The SEL cross section is retrieved through the FLUKA model introduced above and compared with the relative measurements. Considering the statistical and systematic test uncertainties (2σ, depicted in Fig. 5.16), both Samsung and Alliance simulations are in good agreement with the measured values within 30% and 5% respectively, over a broad range of both energies and SEL cross sections. The corresponding agreement with protons from Table 5.14 is within 34% and 24%. This aspect permits to extend the validity of the model to spectra of particles. Moreover, retrieving the experimental values of JEDEC, UJ and RR is not feasible in practice, and therefore the simulation is the only way to estimate the SEL cross section dependence with energy. ChipIr showed to well estimate the SEL cross section of the alcove UJ, whereas RR or tunnel locations, which are characterized by harder spectra as R10, are more accurately reproduced in CHARM.

5.9.4 Conclusions

In this section, a spallation and mixed-field facility have been characterized through SRAM detectors supported by FLUKA simulations. The exposed method requires as input the calibrated SEU cross section in saturation of the memory detector, in addition to its Weibull fit in the intermediate energy (0.2-20 MeV) neutron interval. Moreover, the facility spectrum in terms of differential flux and its absolute normalization value, accounting for the operational conditions, are needed for the flux calculations.

A cross-calibration of the ChipIr neutron spallation facility has been carried out through SEU and SEL-based detectors. Concerning SEU measurements, the ESA Monitor and RadMon results showed to be in excellent agreement with the foil activation measurements on the intermediate and high energy neutron fluxes, within the systematic uncertainties. Thermal neutron measurements are limited by the RadMon sensitivity due to the small ratio between thermal and fast neutron-induced SEUs, however the upper limit is in agreement with the activation foil measurements.

In addition, the approach of determining the spectral hardness of spallation and mixed-field facilities through SEL measurements has been applied to ChipIr and CHARM. A FLUKA model has been successfully validated for extracting these SEL cross sections in these environments. For applications with hard operational spectra, SEL testing in soft energy environments can significantly underestimate the failure rate. Therefore, the assessment of the facility hardness in comparison with the operational spectra is essential. Whereas the ChipIr spectrum is designed for atmospheric-like neutron tests, we demonstrate that the spectral hardness enables for tests dedicated to some accelerator applications as shielded areas. However, tunnel and more energetic alcoves exhibit harder spectra, reproducible in CHARM. This cross-calibration allows the comparison of tests performed at ChipIr with tests performed at CHARM, which is at the present day the reference for the highly energetic accelerator environment testing.

5.10 Summary

The present chapter summarized several qualification approaches from the JEDEC and IEC standards, proposing a development of one method applied in Section 7.4. Indeed, the qualification approach applied at CERN introduced in Section 2.3 relies on these standards with some adaptations for the mixed-field environment found in the accelerator.

The characteristics and dosimetry of several monoenergetic and spallation test facilities employed for the thesis work were described. The cross-calibration by employing the ESA Monitor detector was carried out for every facility in order to verify the beam homogeneity, evaluate the fluence uncertainty, and compare them with the values provided by the facilities. A brief summary regarding the described test facilities, whose SEE measurements are reported in the next Chapters 6 and 7 is provided below: Thermal neutrons were provided by the D50 instrument at ILL (Grenoble, FR). Intermediate energy neutrons from 144 keV

up to 17 MeV were employed in PTB (Brunswick, DE) and FNG (Frascati, IT), and a neutron spectrum up to 11 MeV was provided by an Am-Be source (CERN). The characteristics and the production of monoenergetic beams, as opposed to quasi-monoenergetic beams, was exposed in Section 5.5.2, as these terminologies are not always coherent in the publications. Tests in a mixed-field environment were performed at CHARM (CERN) and measurements in an atmospheric-like neutron spectrum at ChipIr (Didcot, UK). In addition, complementary proton tests were performed in PSI (Villigen, CH), RADEF (Jyvaskyla, FI) and at TOP-IMPLART (Frascati, IT).

Finally, a proposed approach for calibrating and comparing neutron environments through well-known SEU and SEL based SRAMs was applied to a neutron spallation and mixed-field facility, through measurements and FLUKA simulations. This detailed analysis was carried out to compare ChipIr to CHARM and assess whether the former facility can be employed to mimic LHC environments, in substitution to CHARM for those periods when will not be available.

Chapter 6

SEE Measurements, setups and Uncertainty Evaluation

6.1 SEE Uncertainty Assessment

6.1.1 Methodology

The SEE cross section experimentally measured is affected by an uncertainty, which mainly derives from two independent contributions: the measured N events during the experiment and the particle fluence provided by the facility.

1. The uncertainty on the measured SEE is of statistical nature (σ_{stat}). According to [83], the uncertainty can be calculated on the basis of the absolute number of recorded events. Indeed, although more than 1000 events are typically measured per single test, when the beam flux and/or device cross section are very low, the number of events can be limited to several tens.

    - When $N_{SEE} > 50$, as these events occur subsequently in a fixed interval of time, their probability can be modelled as a Poisson distribution of parameter N, with standard deviation $\sigma_{stat} = \pm\sqrt{N_{SEE}}$. As the recorded upsets during the tests were generally more than 1000, the statistical uncertainty associated at one standard deviation is lower than 3%. When more than 1000 events are recorder, the probability can be also approximated to a Normal distribution of parameters $N(N_{SEE}, N_{SEE})$, and its standard deviation coincides to that of the Poisson.
    - When $N_{SEE} < 50$, an upper limit instead of the measured SEE number was used, considering 95% of confidence level from the tables reported in Appendix C.1 from [83, 84].

2. The uncertainty associated with the fluence ($\sigma_{fluence}$) is normally provided by the facility, according to the flux dosimetry performed with calibrated detectors. To this regard,

the instrument has a systematic error that affects the fluence value, and the beam has an uncertainty based on its homogeneity profile, which is specific of the test position where the DUT is installed. Most of the times, the uncertainty provided by facilities relies on the latter evaluation carried out with electronic devices or simulations. In addition, another important source of uncertainty is due to the positioning of the DUT with respect to the calibrated position, which is impractical to evaluate. The overall fluence uncertainty is not a systematic error in a strict sense, but only because on the whole, its value is provided from a quantity (fluence) not related with the actual experiment (SEE measurement). Therefore, considering the three contributions, a standard deviation can be attributed to the fluence uncertainty, which was typically considered of 10% at 2 standard deviations. However, as the comparison of SEE cross sections between facilities have suggested from experience, in order to account for all possible uncertainties described, a value of 10% at 1 standard deviation is more realistic in some cases. This observation is supported also by independent homogeneity measurements performed through the ESA Monitor, as described in Section 6.1.2. Therefore, for every facility, a cross-calibration was carried out in order to estimate as accurately as possible the fluence uncertainty.

Furthermore, especially with neutron irradiations, a fourth contribution to the fluence uncertainty may affect the measurement, which is related to the neutron scattering. In fact, neutron scattering from the air and structural materials surrounding the experiment, such as mechanical supports, walls, ceiling, floor, etc. contributes to the so-called room return, mainly composed of thermal and epithermal energy neutrons. For this reason, neutron irradiation rooms are normally very large, however, this fluence is not typically assessed by the facilities (except in PTB, see Section 5.5).

Hence, as can be deduced from this overview on the many uncertainties affecting a cross section measurement, its exact value is not straightforward to determine, and when comparing results obtained in different facilities they may not be in agreement within the uncertainties for these reasons.

While the statistical uncertainty can be reduced by increasing the events number (longer irradiation), the fluence uncertainty is fixed. To notice that the notation of uncertainties ($\pm 1\sigma$, $\pm 2\sigma$) has not to be confused with that of cross sections (σ_{SEE}).

The total uncertainty on the cross section measurement for a given device is calculated adding in quadrature the two contributions and expressed for 1 standard deviation ($\pm 1\sigma$) in Eq. 6.1. Noteworthy that this uncertainty is expressed in relative terms (as opposed to absolute terms). In the majority of cases, the final uncertainty is dominated by the fluence, as the statistical uncertainty was reduced by increasing the number of counts. Uncertainty values in this thesis are shown for $\pm 2\sigma$ unless otherwise specified.

$$\pm 1\sigma_{tot} = \sqrt{(\sigma_{stat})^2 + (\sigma_{fluence})^2} = \sqrt{\left(\frac{1}{\sqrt{N_{SEE}}}\right)^2 + (\sigma_{fluence})^2} \tag{6.1}$$

In addition, a third uncertainty will be considered in some cases, accounting for the sample to sample variation, In fact, samples even of the same reference can have a cross section variability, as described for instance in [9] for the Cypress memory embedded in the RadMon.

6.1.2 ESA SEU Monitor and fluence uncertainty assessment

The ESA SEU Monitor is a reference detector employed as a golden chip, that embeds a radiation monitor which consists of a 16 Mbit ATMEL SRAM, designed for space applications [85] and shown in Fig. 6.1a. The ESA Monitor has been calibrated in a large set of environments and was used in every facility to assess the beam homogeneity before performing the tests.

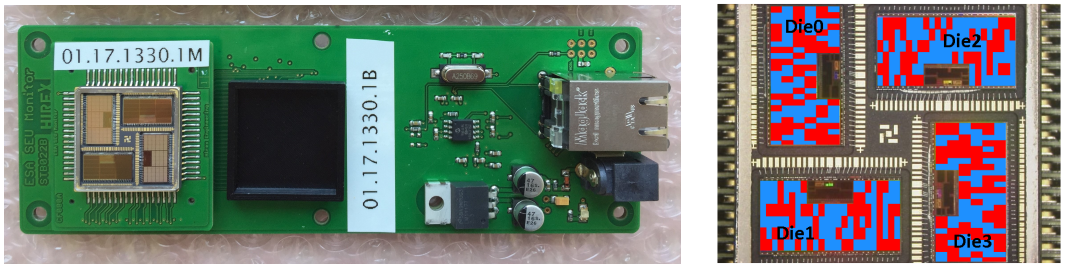

(a) (b)

Figure 6.1: (a): ESA Monitor motherboard with delidded memory (b): Homogeneity map shown in the software interface and disposition of the four dies, which cover an area of 19.8 x 19.8 mm^2.

Table 6.1 reports the ESA Monitor part references and date codes used since 2011 by the R2E group at CERN. As the memories are extremely fragile (bonding wires and active area are exposed), they can easily break during the tests. Therefore, a new purchase was made in 2018 with the new 1817 date code. However, although the reference is the same, SEU cross sections of different date codes may vary, because of the manufacturing silicon process. To this regard, a test campaign was performed at PSI and RADEF to calibrate the memory with several proton energies and compare the cross sections of different date codes, also to assess the compatibility of results with older date codes.

Table 6.1: ESA SEU Monitor specifications for different date codes.

Memory	Part reference	Date code	Tech	Size	Nominal voltage [V]
ESA Monitor	AT68166H-YM20-E	1817	0.25 µm	16 Mbit	3.3 ± 0.3
ESA Monitor	AT68166H-YM20-E	1330	0.25 µm	16 Mbit	3.3 ± 0.3
ESA Monitor	AT68166F-YM20-E	1104	0.25 µm	16 Mbit	3.3 ± 0.3
ESA Monitor	AT68166F-YM20-E	1036	0.25 µm	16 Mbit	3.3 ± 0.3

The ESA Monitor consists in a motherboard developed by HIREX, and housing the 16 Mbit SRAM (technology node of 0.25 µm) which is a multi-chip module, rad-hard against TID and SEL, and with MBU immunity. The memory is composed of four 4 Mbit dies which

cover an area of 19.8 x 19.8 mm^2, and the physical arrangement of SEUs is displayed through a dedicated software interface, thus enabling the analysis of the radiation field homogeneity as shown in Fig. 6.1b. The memory active area can be directly exposed to the beam by removing its cover lid protection and all tests in this thesis were performed without the lid unless otherwise specified. The peripheral electronics (e.g. micro-controller, voltage regulator, communication) installed on the motherboard is not rad-hard, as the monitor was initially designed for its use in collimated beams.

All four dies were written before the test with a checkerboard (CHKBD) pattern, namely with consecutive 0 and 1. After the irradiation, the memory was read to compare the binary data in each cell with the initial pattern, and every mismatch (bit flip) is counted as an SEU.

Fluency uncertainty assessment

In addition to providing the SEU cross section, the ESA Monitor was employed to cross-check the fluence provided by the facility and to calculate the associated uncertainty. The latter is calculated through the upsets recorded by the four dies, therefore it is an uncertainty on the homogeneity over ~2 x 2 cm^2, which area is larger than the chip dimensions of the other irradiated SRAMs. The fluence uncertainty of the beam is considered as the corrected standard deviation between upsets on the 4 dies divided by their average value (called relative standard deviation), and expressed in Eq. 6.2.

$$\sigma_{fluence} = \frac{\sigma_{corr}}{\bar{x}} \tag{6.2}$$

where σ_{corr} is the corrected standard deviation, and $\bar{x}$ the average between N samples (that are 4 in this case), defined in Eq. 6.3 and 6.4, respectively.

$$\sigma_{corr} = \sqrt{\frac{1}{N-1}\sum_{i=1}^{N}(x_i - \bar{x})^2} \tag{6.3}$$

$$\bar{x} = \frac{\sum_{i=1}^{N} x_i}{N} \tag{6.4}$$

The facilities provide as well the uncertainty on the profile homogeneity, which is typically of 10% (considering $\pm 2\sigma$). However, the uncertainty assessment through the ESA Monitor can be considered more accurate, because it is performed just before the tests. In addition, as the same reference detector is consistently employed, possible additional uncertainties deriving from the calibration of the different detectors used in the facilities are excluded. This aspect is important especially when comparing results from different facilities. Nevertheless, the upsets recorded by each die of the ESA Monitor have to present good statistics for an appropriate fluence uncertainty estimation. In the test results, the larger uncertainty was selected between that measured with the ESA Monitor and the one provided by the facility, also

to account for other uncertainties that are normally not included, as the DUT positioning.

ESA Monitor proton and neutron calibration

The new batch of ESA Monitor (1817) was calibrated in PSI (PIF) and RADEF with proton energies from 30 to 200 MeV and 3 to 52 MeV, respectively. Moreover, the 1330 and 1104 date codes were tested in PSI for comparison, and all references were measured 3 times to assess the repeatability of the experiment. In addition, the cross sections are compared to those of previous tests in PSI, TRIUMF and PTB with the 1036 date code from [56]. For the latter, some tests were carried out with the protective lid on the memory, which is composed of kovar, a nickel-cobalt alloy (while it is of plastic for the 1330 and 1817).

Fig. 6.2 shows the proton cross section comparison, numeric values can be found in [86]. Considering the tests at PSI without the lid, whereas the 1817 and 1303 date codes present, within the uncertainty, the same cross section values, the 1104 shows a generic lower cross section over all the 30 – 200 MeV range, up to 9.2%. The 1036 date code exhibits a lower cross section only at lower energies and results decreased up to 26% at 30 MeV. As regards the 1036 test with and without the kovar lid, only at low energy (30 MeV) its impact is non-negligible, which results in a reduced lid cross section of 15%.

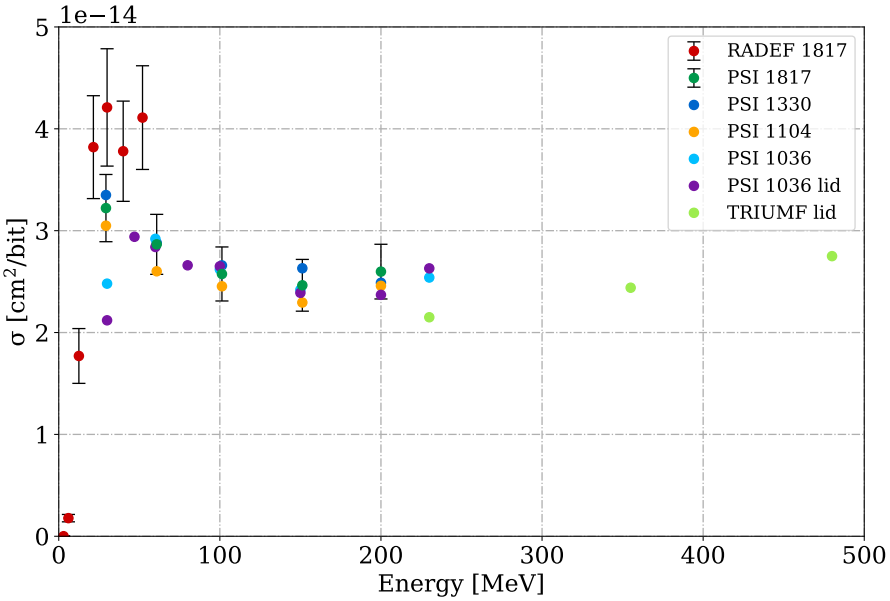

Figure 6.2: Proton tests comparison between date codes and facilities: RADEF – PSI –TRIUMF. Error bars showed only for RADEF 1817 and PSI 1817 for the readability of the graph.

Comparing the results obtained in PSI and RADEF both at 30 MeV for the same date code 1817 (no lid), the PSI cross section is 23.5% lower than that at RADEF. A similar behaviour appears at 230 MeV for the 1036 (with lid) in which the cross section retrieved in TRIUMF is 18% lower with respect to PSI (see Fig. 6.2). Since the statistical uncertainty is small for these runs, a possible explanation for these discrepancies is the difference on the flux calibration of

each facility and/or how the beam at a certain energy is degraded from the primary energy. The RADEF beam has primary energy of 55 MeV to produce 52, 40, 30 MeV and of 30 MeV to obtain the low energies of 21.5, 12.5, 6, 3 MeV. The PSI beam is produced starting from 200 MeV. For this reason, the cross section value at 30 MeV is supposed to be more accurate in RADEF, whereas at 230 MeV the PSI calibration is more precise than TRIUMF (for which a 480 MeV proton beam was degraded).

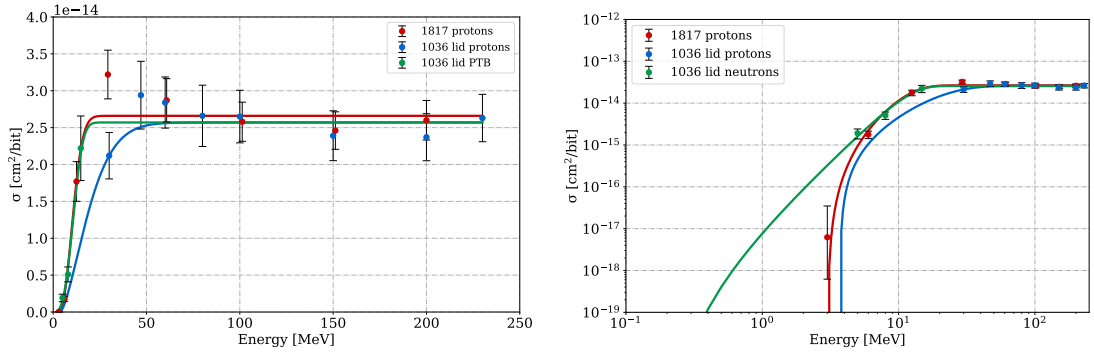

(a) **(b)**

Figure 6.3: PSI proton data for the 1817 and 1036 (with lid) date codes, PTB neutron data 1036 (with lid) and respective Weibull fits, in linear (a) and logarithmic (b) scales.

The cross sections measured with protons for the 1817 and 1036 (with lid) date codes are reported in Fig. 6.3 with the respective Weibull functions, whose parameters are shown in Table 6.2, according to equation 2.9.

Table 6.2: Proton and neutron Weibull parameters for the 1817 and 1036 (with lid) date codes.

Calibration	Date code	σ_{sat} [cm^2/bit]	E_0 [MeV]	w [MeV]	S
protons	1817	$2.66{\cdot}10^{-14}$	3.0	9.1	2.2
neutrons	1817	$2.60{\cdot}10^{-14}$	0.2	13.08	2.99
protons	1036 (lid)	$2.57{\cdot}10^{-14}$	3.7	18.3	1.53
neutrons	1036 (lid)	$2.57{\cdot}10^{-14}$	0.2	12.0	3.0

Regarding the 1817 date code, in addition to the PSI data, the points at 3, 6, 12.5 MeV measured at RADEF are considered for the Weibull calculation. The evidence that the 1817 Weibull is higher than that of 1306 at low energy (see Fig. 6.3) is derived by the fact that the 1306 date code shows a lower peak at 30 MeV and the impact of the lid further decreases this low energy point.

6.2 SEU and SEL COTS SRAMs

The Devices Under Test (DUTs) are Commercial Off The Shelf (COTS) SRAMs of different node sizes, because of their high interest for accelerator applications. Table 6.3 reports the list of SEU and SEL memories employed in this work, with their specifications. All devices

were irradiated at room temperature, normal beam incidence and from the top-side of the memory package. The date codes reported in Table 6.3 are employed in all tests except in some cases (date codes shown in brackets), for which the date code will be explicitly specified in the concerned test.

Table 6.3: COTS components employed in this work. SEU and SEL memory references, date codes, technology nodes and sizes are reported. The date codes shown in brackets are used only in a few measurements and will be explicitly specified in the concerned test.

SEE	Memory	Reference	Date code	Tech.	Size
SEU	ISSI	IS61WV204816BLL-10TLI	1650	40 nm	32 Mbit
	Cypress	CY62167GE30-45ZXI	1731	65 nm	16 Mbit
	Cypress	CY62157EV30LL-45ZSXI	1843 (1437)	90 nm	8 Mbit
	Cypress	CY62167EV30LL-45ZXA	1731 (1525)	90 nm	16 Mbit
	RADSAGA v1	Not commercial	na	65 nm	32 Kbit
SEL	Samsung	K6R4016V1D-TC10	na	0.18 µm	4 Mbit
	Alliance	AS7C34098A-10TCN	1339	0.20 µm	4 Mbit
	ISSI	IS61LV5128AL-10TLI	1246, 1303, 1416	0.18 µm	4 Mbit
	Lyontek	LY62W20488ML-55LL	1251	0.18 µm	16 Mbit
	Brilliance	BS62LV1600EIP55	9254	0.18 µm	16 Mbit

6.2.1 SEU setups

The first four SEU memories of Table 6.3 will be referred to as "Tester memories" and identified in the following as ISSI 40, Cypress 65 and Cypress 90 (8 or 16 Mbit) memories, respectively. The test setup consists of a daughterboard housing the SRAM memory, that is

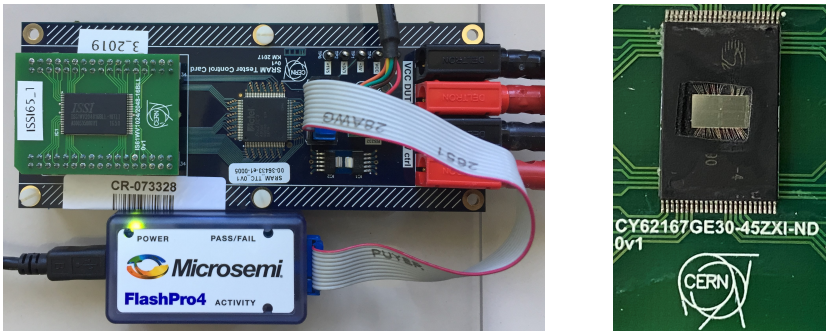

(a) **(b)**

Figure 6.4: (a): Tester motherboard with the mounted daughterboard embedding the SRAM memory. The FlashPro4 programmer is used to write the FPGA which controls the memory. (b): Delidded SRAM where the sensitive area is exposed (Cypress 65 nm).

installed on a tester motherboard developed at CERN as can be seen in Fig. 6.4a. The operations of writing/reading the memory are performed through a user GUI that communicates via a USB connection to a radiation-tolerant flash-based FPGA embedded on the motherboard. The memory is initially written with a check-board pattern and the reading is performed ev-

ery few seconds or minutes, according to the flux of the facility. The data of every address is compared to the initial pattern and every bit mismatch is counted as an upset and subsequently corrected. Each type of memory needs specific firmware to be loaded in the FPGA. The firmware also disables the ECC correction for the Cypress 65 memory, which is the only one embedding this functionality straight within the SRAM chip. The motherboard was powered at 5 V, while the memories were supplied at nominal 3.3 V unless differently specified.

The SRAMs were irradiated with their package and delidded in some cases, namely the package was removed via specific techniques, and the active area of the device directly exposed to irradiation as can be seen in Fig. 6.4b.

MBU analysis: In addition, the MBU analysis is performed in relevant cases directly from the raw data of the tester. MBU occurring in the same word of 16 bits (for all the tester memories) are reported in tables on the "MBU" column, considering a multiplicity of 2. When greater multiplicities are observed a separate table will be considered. When MBUs are recorded, the SEU column values, from which the cross sections are calculated, contains the sum of all upsets with whatever multiplicity. For instance, with 3 bit flips occurred in different words and 2 bit flips triggered in the same word of 16 bit (1 MBU) the SEU count will result of 5.

The RADSAGA SRAM is a non-commercial memory that was tested without the lid at 4 different core voltages: 0.3, 0.6, 0.9 and 1.2 V. Four different blocks are embedded in the SRAM, the first two blocks have a standard MOS threshold, and block 3 and 4 present a low and high threshold voltage, respectively. After setting the voltage and writing the memory through a LabVIEW interface, the beam was turned on and after the irradiation (beam off) the memory was read and the upset counted, because the memory is affected by noisy bits that show upsets even without the beam. However, these bits are localized and removed from the SEU count through a post-processing filter.

6.2.2 SEL setups

The SEL memories of Table 6.3 were soldered to the test motherboard in single unit (1x) or eight per motherboard (8x), in order to obtain enough SEL statistics in a reasonable time. The SELs are measured through *PsControl*, a LabVIEW interface developed at CERN.

Although an SEL is a potentially destructive failure, the setup consists in detecting the current increase and performing a power cycle when the latter exceeds a threshold, in such a way the latch-up is stopped before possible damages are caused. The current is kept over the threshold during a certain hold-time and after that, the voltage is set to zero for a reset-time. The sum of these two times is defined as the dead-time in which the setup is not sensitive to SEL, and therefore the corresponding fluence has to be removed from the analysis. To this regard, for those facilities operating with a time structure in spills, such as CHARM and ChipIr, the first spill that triggered the SEL is considered for half of its fluence. Indeed, assuming a uniform distribution over the spills in inducing a latch-up, the memory would be in dead-time half of the latch-up spill time (valid if the SEL probability per spill is small, so that only one latch-up per spill can occur). Every memory has a specific latch-up threshold and more details

can be found in [65].

The SEE cross section measurements performed in several facilities are reported in the following, with preliminary observations that will be used for the analysis in Chapter 7, and details on the carrying out of the tests.

6.3 ChipIr - Neutron Spallation up to 700 MeV

The SEU cross sections regarding the Tester are reported in Fig. 6.5, where the components were irradiated at different incident beam angles, from 0 to 90 degrees (the numerical values and ESA SEU Monitor cross sections can be found in Appendix in Table C.2). No significant difference was observed for the ISSI memory, while a maximum deviation of up to +24% and -18% was recorded between 90° and 0° for the Cypress 8 and 16 Mbit, respectively. The ESA Monitor cross section measured in 2019 is 8% lower compared to that obtained in 2018, compatible within the experimental uncertainty.

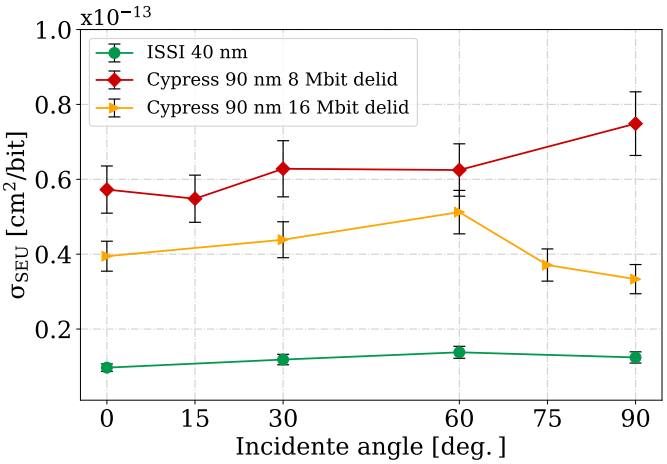

Figure 6.5: SEU cross sections as a function of the beam incidence angle for the three COTS tested SRAMs. Both Cypress memories were tested delidded.

6.4 ILL - Thermal Neutrons

Thermal neutron tests were carried out at ILL (see Section 5.2 for the facility description) to measure the cross section of different devices, as thermal neutrons are one of the main topics of this thesis. The results are shown in Fig. 6.6 for the nominal voltage (3.3 V) and will be used for the analysis in Chapter 7. The complete list of cross sections can be found in the Appendix in Table C.3.

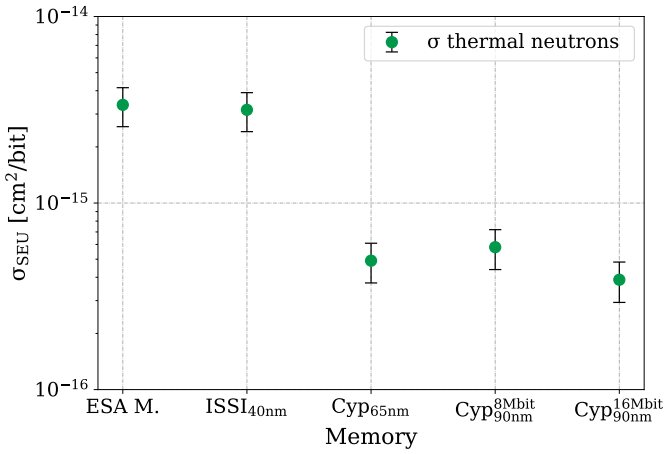

Figure 6.6: Thermal neutron cross sections measured at ILL with thermal neutrons at nominal voltages (3.3 V).

Thermal neutron cross section at varying voltage

Fig. 6.7 shows the thermal neutron sensitivity at different voltages (Vm) on the ISSI 40 nm memory tested at ILL (from the cross sections of Table C.3 in Appendix). The thermal neutron cross section is found to be constant from 3.6 V down to 2 V. Below this threshold, the sensitivity increases as the voltage decreases and the effect is exponential below 1 V. The cross sections of $3.15 \cdot 10^{-15}$ and $1.62 \cdot 10^{-14}$ cm^2/bit were measured at 3.3 and 0.733 V, respectively. Therefore, the thermal neutron sensitivity with the lowest applicable voltage is a factor of 5 higher compared to the nominal conditions. The same effect was also measured in the RadMon (see Section 2.5). When lowering the voltage, the critical charge needed to trigger an SEU is smaller and, alpha particles and ^7Li ions produced in the reaction with ^{10}B can deposit enough charge to cause an upset. The higher cross section shown at 1.57 V with respect to the adjacent points is likely attributable to an unknown readout malfunction associated with a previous reading.

When applying a voltage lower than 2.2 V (for both 16 Mbit Cypress) and 1.55 V (for the 8 Mbit Cypress) the reading through the tester GUI was not possible due to hardware limitations. Therefore, the thermal neutron enhanced sensitivity was not observed in these memories.

6.5 LINAC - 18.6 and 29 MeV Protons

As introduced in the facility description (see Section 5.3), in order to assess the package impact on the SEU cross section, all SRAMs were tested at 18.6 and 29 MeV protons with package and delidded, as can be seen in Figures 6.8 and 6.9, respectively (the corresponding tabulated values can be found in Tables C.4 and C.5 in Appendix). Regarding the ESA Monitor (1817), whose package is made of plastic, its SEU cross section resulted lower when the

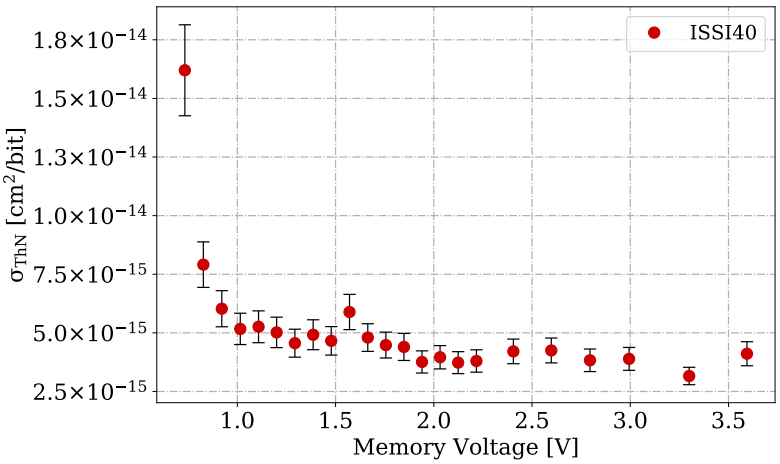

Figure 6.7: ISSI 40 nm thermal neutron cross sections at varying voltage (V_m), measured on the memory pins (nominal voltage: 3.3 V).

package was on the memory. This is the typical expected behaviour, since protons are normally stopped or at least slowed down in the package, and this effect is more accentuated when lowering the proton energy beam. However, for the ISSI, Cypress 65 and Cypress 90 8 Mbit memories the SEU cross sections measured at 29 MeV with the package resulted higher than those tested delidded, while at 18.6 MeV only the latter memory still presented this behaviour. Moreover, the higher sensitivity with the package resulted in a factor of 2 with both energies regarding the Cypress 90 8 Mbit memory. This fact may be attributed to at least two factors: the direct ionization, where higher energy protons are attenuated by the thickness of the package but can still pass through, and the production of secondaries from the beam-package interaction.

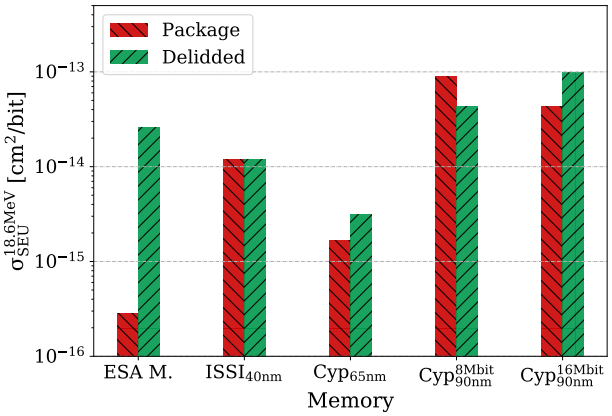

Figure 6.8: 18.6 MeV proton SEU cross sections of the memories tested with package and delidded at the TOP-IMPLART LINAC.

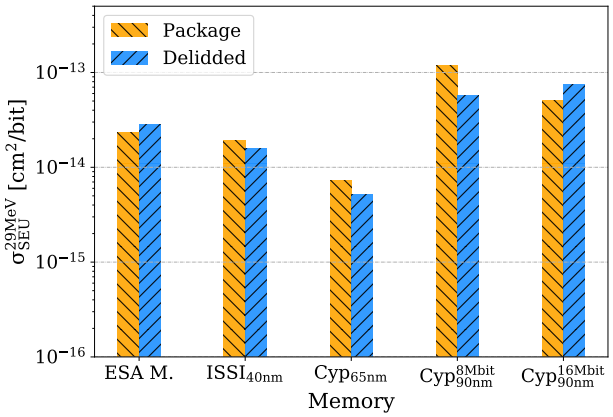

Figure 6.9: 29 MeV proton SEU cross sections of the memories tested with package and delidded at the TOP-IMPLART LINAC.

6.6 Am-Be Source - Neutrons Spectrum up to 11 MeV

During proton testing in Frascati with the TOP-IMPLART LINAC, some of the delidded SRAMs showed an SEU cross section higher than that of the memory with the package. Moreover, as hypnotized in [87], an increased low-energy neutron sensitivity may be due to elastic proton recoils produced inside the package. Therefore, the four SRAM references were measured irradiating the devices, both with their package and delidded, with the intermediate neutron spectrum of the Am-Be source up to 11 MeV (see Section 5.6). The SEU cross section results are presented in Fig. 6.10 (the numerical values are reported in Table C.6 of the Appendix) calculated using two different types of HEHeq flux. In the first two cross section

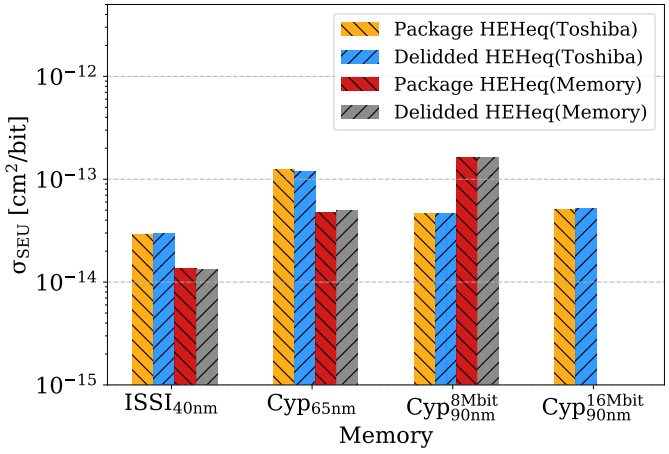

Figure 6.10: SRAM SEU cross sections measured at 5 cm of distance from the centre of the Am-Be neutron source, calculated considering the HEHeq flux from the Toshiba reference implemented in FLUKA, and the actual response of each memory. Memories tested with package and delidded (ISSI with package was at 5.6 cm from the source) and their cross section ratio.

bars, the HEHEq is calculated by weighting the Am-Be spectrum with the Weibull fit of the

reference Toshiba memory (also implemented in FLUKA), and the values are higher than the proton cross section in saturation at 200 MeV. Instead, using the HEHeq flux calculated from each memory response (third and fourth cross section bars), the results are compatible with those from high-energy protons, as expected.

As can be noted from Fig. 6.10 (or Table C.6), the package is shown not to have an impact on the cross sections, as the ratios are basically one for all the memories (by construction, independently from which method is used to calculate the cross sections). Moreover, the SEU counts as a function of the time were linear and the corresponding SEU logical distributions were randomly spread between the memory addresses.

The cross section results using one of the two HEHeq of Fig. 6.10 can be used as an example of a more general observation. The second HEHeq method requires the response function of each individual memory, which often is not known a priori, hence the use of a reference memory response is the only way to estimate the cross section in the Am-Be source. The HEHeq fluxes are reported in Table 6.4 for comparison. As can be seen, using the Toshiba response for the ISSI or Cypress 65 memories, for example, yields an underestimation of the flux up to a factor of 2.5 for the latter memory, and therefore an overestimation of the cross section.

Table 6.4: HEHeq fluxes retriever using the Weibull response function of each memory, at 5 cm of distance from the centre of the Am-Be source.

	Toshiba	ESA M. (1817)	ISSI 40	Cypress 65	Cypress 90 8 Mbit
HEHeq $[cm^{-2}/s]$	$1.84{\cdot}10^4$	$9.78{\cdot}10^3$	$4.00{\cdot}10^4$	$4.59{\cdot}10^4$	$5.21{\cdot}10^3$

6.7 FNG - 2.5 and 14.8 MeV Neutrons

The test campaign in FNG was carried out to measure the devices to intermediate energy neutrons and especially to observe their response at 2.5 MeV. Table 6.5 reports the tester SEU results for 2.5 and 14 MeV, installed at 2.5 cm from the target, the closest test position. The Cypress 90 nm 8 Mbit was also tested placing 5 mm of boron carbide (B4C) between the beam and the memory, and the cross section resulted to be unchanged. The same Cypress 8 Mbit reference memory CY62157EV30LL-45ZSXI, measured without B4C at LPSC but with date code 1443 (instead of 1843) was found to be $6.81 \cdot 10^{-14}$ cm^2/bit.

MBUs were recorded at 14.8 MeV especially in the Cypress 90 nm memory, with a multiplicity of up to 8 for the 16 Mbit version. The complete list of multiplicities is reported in Table 6.6. However, MBUs are still a smaller amount compared to SBU (multiplicity of one) resulting in 5% and 15% for Cypress 90 8 and 16 Mbit, respectively. It is to be noted that the same memory tested at 2.5 MeV did not record any MBU. Moreover, the Cypress 65 memory was also tested at 2.5 MeV, but as shown in Table 6.6, half of the upsets were MBU. This was caused by a hardware problem probably related to the ECC disabling.

Table 6.5: 14.8 and 2.5 MeV SEU cross sections for the tester SRAMs measured at FNG. The tests were performed at 2.5 cm from the target. The runs that recorded MBUs with a multiplicity greater than 2 are highlighter in bold.

E $[MeV]$	Device	Φ [n/cm^2]	SEU	MBU (2x)	σ_{SEU} [cm^2/bit]	$\pm 2\sigma$
14.8	ISSI 40	$1.11 \cdot 10^{10}$	3642	1	$9.81 \cdot 10^{-15}$	10.5
	Cypress 65	$1.00 \cdot 10^{10}$	7742	3	$4.60 \cdot 10^{-14}$	10.3
	Cypress 90 8	$1.00 \cdot 10^{10}$	4633	52	$5.06 \cdot 10^{-14}$	10.4
	Cypress 90 8 B4C	$1.00 \cdot 10^{10}$	4676	37	$5.06 \cdot 10^{-14}$	10.4
	Cypress 90 16	$1.00 \cdot 10^{10}$	5042	57	$2.99 \cdot 10^{-14}$	10.4
2.5	ISSI 40	$1.63 \cdot 10^{10}$	1201	0	$2.20 \cdot 10^{-15}$	11.5
	Cypress 90 8	$8.72 \cdot 10^{9}$	201	0	$2.75 \cdot 10^{-15}$	17.3

Table 6.6: MBU multiplicity for those runs of Table 6.5 (in bold) that recorded more than 2 MBUs. The events denoted with a multiplicity of "1" are SBUs and reported for completeness.

MBU	14.8 MeV			2.5 MeV
multip.	Cyp 90 8	Cyp 90 8 B4C	Cyp 90 16	Cyp 65
1	4031	4094	4318	45
2	52	37	57	16
3	20	11	51	4
4	9	10	30	0
5	3	2	35	0
6	1	1	21	0
7	0	0	4	0
8	0	0	1	0

Noteworthy that the ISSI and Cypress 90 nm cross sections are still relatively high compared to their value at 14.8 MeV. The 14.8 MeV to 2.5 MeV cross section ratio is 4 and 17 respectively, whereas for ESA Monitor the ratio is 126. The typical sensitivity of SRAMs shows a behaviour as in the latter case, with a difference of roughly 2 orders of magnitude. The final ESA Monitor SEU cross sections are reported in Table 6.7 including an additional test covering its active surface with 5 mm of boron carbide (B4C), to assess the thermal neutron percentage. The ESA Monitor cross section with the boron carbide is 23% lower than that without the absorber. In addition, the results from LPSC providing a similar beam of 14.2 MeV are reported in Table 6.7, showing a difference of about +32% between PTB and LPSC. This could be attributed to the date code of the memory, although with high energy protons, from 30 to 200 MeV, the date code does not significantly impact the SEU cross section.

The 14.8 MeV RADSAGA SRAM cross sections are reported in Fig. 6.11 (from the numerical values found in Table C.7 in Appendix) for the three threshold voltages, calculated from the 4 different blocks embedded in the SRAM. Specifically, block 1, 2, 3 and 4 consist in 7979, 8104, 8027 and 7903 bits respectively (at 0.3 V), after removing the noisy bits. The first two blocks have a standard MOS threshold, block 3 and 4 present a low and high threshold voltage, respectively. The closest position to the target for the RADSAGA SRAM installation was

Table 6.7: 14.8 and 2.5 MeV ESA SEU Monitor cross sections measured at FNG (2.5 cm from the target) in comparison to those tested at LPSC with 14.2 MeV. B4C refers to the test covering the memory with boron carbide.

Facility	E [MeV]	Date code	σ_{SEU} [cm^2/bit]	$\pm 2\sigma$ (%)
FNG	14.8	1817	$1.84 \cdot 10^{-14}$	10.2
FNG (B4C)	14.8	1817	$1.41 \cdot 10^{-14}$	10.8
LPSC	14.2	1330	$2.49 \cdot 10^{-14}$	13.8
LPSC	14.2	1104	$2.43 \cdot 10^{-14}$	12.3
FNG	2.5	1817	$1.51 \cdot 10^{-16}$	25.0

3.5 cm. The cross section increase is significant when lowering the voltage, up to 85% for the

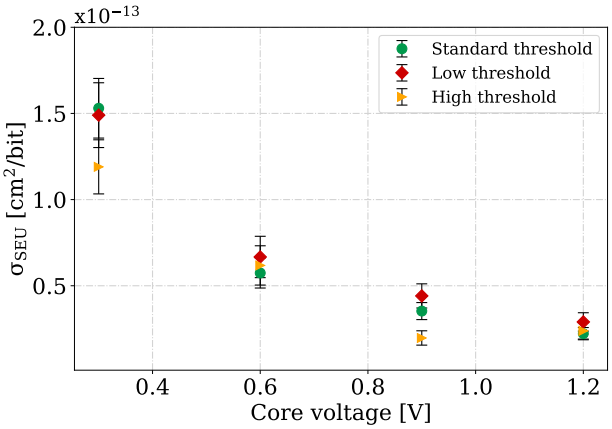

Figure 6.11: 14.8 MeV SEU cross sections for the RADSAGA v1 SRAM with standard, low and high voltage thresholds.

standard threshold.

6.8 PTB - Monoenergetic Neutrons from 144 keV up to 17 MeV

After the first observation on the high cross section measured at 2.5 MeV in FNG with the ISSI 40 memory, the same reference, Cypress 65 and Cypress 90 8 Mbit SRAMs were characterized with a broader range of intermediate energy monoenergetic neutrons in PTB (see Section 5.5 for the facility description), from 144 keV up to 17 MeV. Therefore, the sensitivity of the devices was assessed for energies below 0.2 MeV, which is the lowest threshold currently employed for the HEHeq flux calculation. The DUTs were installed at the closest position to the target corresponding to 6.6 cm for the D target and 5.5 cm for Li and T targets.

The ESA Monitor tabulated cross sections tested at 5, 8 and 17 MeV are reported in Ap-

pendix in Table C.8, whereas those of the Tester, whose memories were measured with chip-package and delidded from 144 keV to 17 MeV, in Table C.9. It is relevant to immediately note that the more integrated technologies were considerably sensitive even at 144 keV. The complete analysis, considerations and simulations about the SRAMs sensitivity to intermediate energy neutrons are reported in Chapter 7, while in the following section other important observations are outlined. The recorded MBU were zero or just a few for energies below 8 MeV (Table C.9), while at 17 MeV their proportion with respect to SBU was similar to that observed with 14.8 MeV at FNG (in Table 6.5).

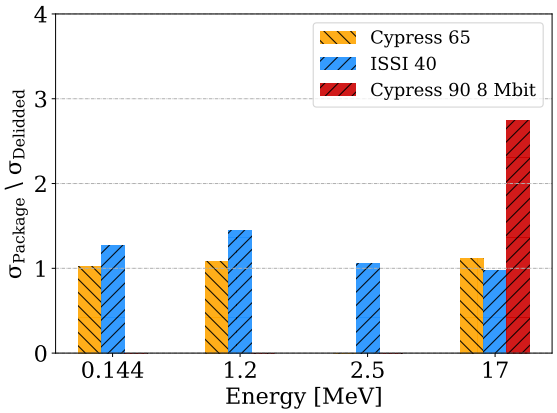

Figure 6.12: Ratio between SEU cross sections of the memories measured with package and delidded at PTB for different neutron energies.

As can be seen from Fig. 6.12 reporting the ratio between SEU cross sections of the memories with package and delidded, while the package does not significantly impact the cross section regarding the ISSI and Cypress 65 memories, its effect is instead relevant for the Cypress 90 8 Mbit, where the package increases the cross section of almost a factor of 3 with respect to the delidded measurement. This behaviour was also observed testing with intermediate energy protons at the TOP-IMPLART LINAC (see Figures 6.8, 6.9), while there was no difference by employing the neutron spectrum up to 11 MeV of the Am-Be source (Fig. 6.10). Thus, for the Cypress 90 nm 8 Mbit memory it seems that only neutrons above a certain energy (greater than 11 MeV) can produce secondary particles from the package capable of inducing SEEs.

In order to evaluate the beam attenuation at PTB, two Tester motherboards were installed in parallel on fixed positions, the one in front (5.5 cm from the target) facing directly the beam and a second DUT on the back (11.3 cm from the target). Table 6.8 shows the corresponding cross sections at 17 MeV with the front to back ratio. As can be seen, no significant difference was observed on the cross sections, except for the Cypress 65 memory that resulted 30% lower when installed in the back position, but within the experimental uncertainties.

Table 6.8: SRAM cross sections tested at 17 MeV in PTB, when installed in front position and in parallel to another tester motherboard, with their ratio.

17 MeV	σ_{FRONT} [cm^2/bit]	$\pm 2\sigma$ (%)	σ_{BACK} [cm^2/bit]	$\pm 2\sigma$ (%)	$\frac{\sigma_{FRONT}}{\sigma_{BACK}}$
ISSI 40 nm	$1.91 \cdot 10^{-14}$	15.0	$1.99 \cdot 10^{-14}$	22.5	0.96
Cypress 65 nm	$8.19 \cdot 10^{-14}$	12.1	$5.76 \cdot 10^{-14}$	22.0	1.42
Cypress 90 nm 8	$1.25 \cdot 10^{-13}$	13.6	$1.12 \cdot 10^{-13}$	19.7	1.12
Cypress 90 nm 16	$4.30 \cdot 10^{-14}$	13.7	$4.01 \cdot 10^{-14}$	23.5	1.07

6.9 Summary

This chapter outlined the multiplicity of uncertainties that can affect the SEE measurements and defined how they are calculated. To this regard, the ESA SEU Monitor employed as a golden chip for the cross-calibration of the facilities was described showing its calibration performed with protons and neutrons.

The SEU and SEL setups of the COTS components were described and the SEE cross sections, measured in the test facilities exposed in Chapter 5, were reported explaining the conditions of the tests. Preliminary observations and comparisons of the results were made in preparation for the analysis performed in the next Chapter 7. Noteworthy that the memory package can play an important role either in producing secondary particles or in attenuating the primary beam, hence in both cases affecting the SEU cross section. While this effect is more. This effect is particularly visible in the Cypress 90 nm 8 Mbit memory with both proton and neutron beams.

Chapter 7

SEE estimation and Radiation Hardness Assurance Implications

As seen in Section 3.2, neutrons are the primary particles constituting the radiation environment inside the LHC accelerator at CERN. Their fluxes can be tens of times higher than the broad mixed-field of protons, electrons, muons, pions, kaons, etc. that together characterize the radiation environment in the locations of the accelerator where electronics are installed. Furthermore, neutrons are also the main concern for ground level and avionic applications, as once produced in the atmosphere, owing to their nature they can travel until interacting with atoms in semiconductor devices. Both accelerator and atmospheric environments are characterized by a wide neutron spectrum, from thermal (25 meV) up to several GeV of energies. Most of SEEs are therefore associated to neutrons, which above a few MeV (and even below for elastic processes) can indirectly ionize the Sensitive Volume (SV) atoms of the device through elastic and/or inelastic reactions, depending on the initial particle energy and target material.

Based on the SEE measurements presented in Chapter 6 carried out in the facilities described in Chapter 5, and the radiation fields of accelerator and atmospheric environments presented in Chapter 3, the expected SEE rate in operation due to a certain energy range of neutrons with respect to the overall contribution are calculated in the present Chapter. Consequently from this study, several conclusions can be drawn regarding RHA implications for the accelerator and atmospheric applications. The outcome of this analysis is meant to outline some hints for potential drafting of a unified standard test approach for the accelerator. In fact, the current qualification standards applied at CERN do not systematically consider the issues induced by thermal and intermediate energy neutrons in electronics, essentially because they were not considered a treat in micron-technologies as opposed to highly energetic particles. However, with the technology node scaling, the contributions from these portions of neutron spectra pose serious SEE underestimations whether are not properly taken into account.

7.1 Environments Comparison

An overview comparison between the spectra of the operational environments of interest, with those reproduced in facilities, is shown in Fig. 7.1 and will be employed for the SER estimation. The differential spectra are shown for energies above 1 MeV normalized to the JEDEC NYC integrated flux above 10 MeV and corresponding to a fluence of $1.13 \cdot 10^5$ [n/cm^2/year]. The same spectra are shown in lethargy units in Fig. 7.2, highlighting the differences in the 1-10 MeV neutron fluxes for the various environments. As can be seen, the spectra shape below 10 MeV are visibly different, the accelerator fluxes being several times higher than that of the JEDEC standard. Neutrons at flight altitude (12 km) present instead lower fluxes between 1-10 MeV, while they have a harder spectrum (even more than the accelerator ones) at high energies.

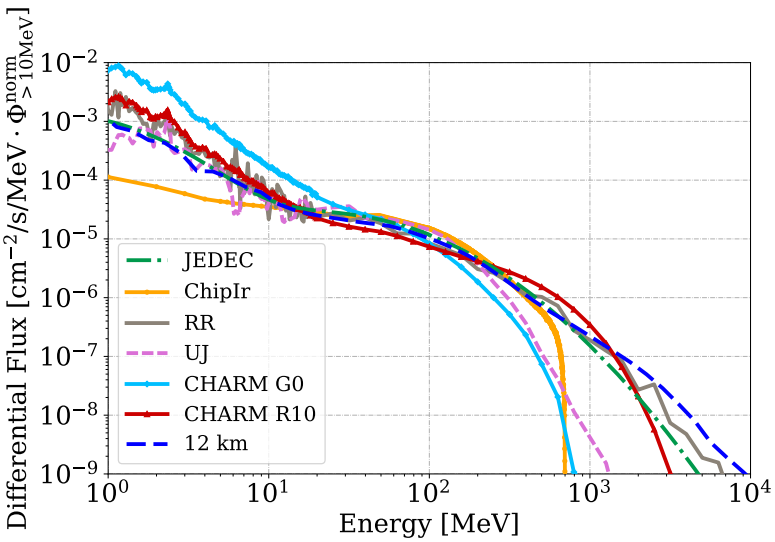

Figure 7.1: Differential spectra above 1 MeV normalized to the JEDEC NYC neutron flux above 10 MeV. The neutron spectrum at 12 km of altitude is compared to the ground level one. G0 and R10 represent a soft and more energetic mixed-field found in the CHARM facility, mainly composed of neutrons. RR is the actual spectrum of a shielded alcove inside the LHC.

The New York City (NYC) sea level neutron spectrum is calculated with the mathematical model from the JEDEC (JESD89A) standard [12]. In addition, the neutron spectrum at typical flight altitudes (12 km) is added to the analysis. The latter is calculated above Geneva from the simulations shown in Section 3.3.2, which are based on FLUKA and extracted through the MAIRE tool.

Regarding accelerator environments, as seen in Section 2.7, the RR and UJ spectra are those of two specific alcoves of interest along the LHC tunnel, formed by a light and heavy shielding, respectively. While the radiation field is mainly dominated of neutrons in the UJ (90%), the RR radiation environment is for instance composed of neutrons (71%), protons (13%) and pions (16%) in the RR7 alcove [56]. In fact, a large quantity of electronic devices is installed inside these shielded alcoves.

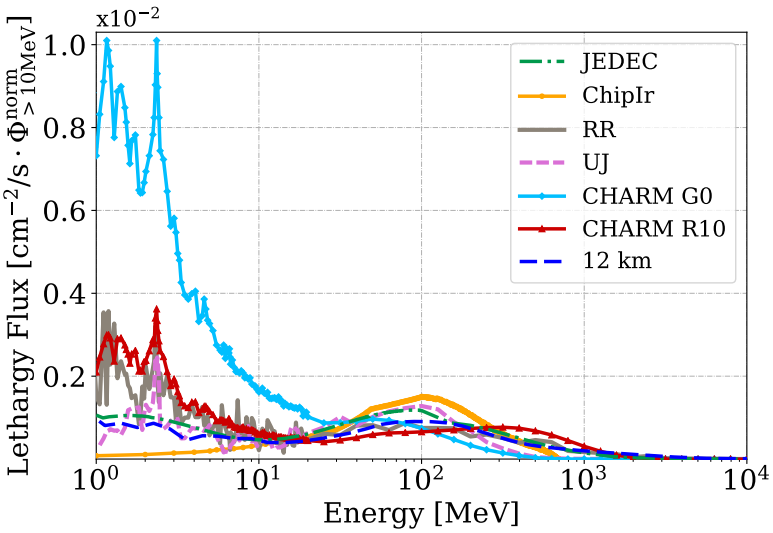

Figure 7.2: Lethargy spectra (linear y-axis) above 1 MeV normalized to the JEDEC NYC neutron flux above 10 MeV. The neutron spectrum at 12 km of altitude is compared to the ground level one. G0 and R10 represent a soft and more energetic mixed-field found in the CHARM facility, mainly composed of neutrons. RR is the actual spectrum of a shielded alcove inside the LHC.

In the same figure, three spectra found in two facilities are depicted for comparison. G0 and R10 spectra are produced in the CHARM facility at CERN (see Section 5.8) and they resemble the main radiation environments found in the LHC accelerator [78]. These mixed-field spectra are characterized by a soft and hard spectrum, respectively. In the calculation, G0 and R10 are both composed of neutrons, protons and pions above 20 MeV and only of neutrons below this energy, as the contribution of other particles to the SER is negligible below 20 MeV (as explained in Section 2.3.1). ChipIr, provides a ground level-like neutron spectrum up to 700 MeV (see Section 5.7) that derives from interpolated measurements as explained in Section 5.9, while the CHARM and LHC locations derive from FLUKA Monte Carlo simulations. The distinctions of these operational and facility environments have been outlined through the hardness factor ($H_{10\%}$) in Table 5.13.

7.2 Thermal Neutron-Induced SEUs with Respect to HEH in Accelerator and Atmospheric Environments

SEUs in electronic devices to be installed in LHC accelerator complex are typically associated to highly energetic particles, whereas as will be outlined in this section, thermal neutrons can play an equal or even dominant role for certain locations and components.

SV and contact size decrease according to the technology scaling, and consequently the amount of ^{10}B atoms is reduced. On the other hand, the critical charge to trigger upsets has decreased and, when lowering the supply voltage, the SEU rate can increase almost exponentially, as seen in Section 2.5 from [28]. These two competing effects typically cancel out and

the cross section per bit is roughly constant or slightly decreasing with the technology. However, the cross section per chip increases due to the integration and other factors, such as the actual proportion of boron, which depends on the manufacturing process. These are the reasons why thermal neutrons are becoming a major issue for the LHC accelerator but not least for avionic, terrestrial (see Section 3.3.3), medical and automotive applications. As shown in [88] evaluating the response of different CPUs and GPUs, thermal neutrons can contribute to the ground level Failure In Time (FIT) rate up to 59% of the total. Moreover, as presented in [19], at sea level, SEUs in 90 nm SRAM are basically due to neutrons above 10 MeV, but scaling down the technology to 28 nm (microprocessor cache) up to 41% of the SER is expected from thermal neutrons. At flight altitude inside an aircraft the SER contribution of thermal neutrons further increases up to 60% [19]. Therefore, it seems that thermal neutron fluxes have similar probabilities of inducing SEUs as the high energy neutrons, especially with the technology scaling.

This section will focus on the Soft Error Rate (SER) due to thermal neutrons along different locations of the accelerator in comparison to that from highly energetic particles. Whereas the standard component level qualification for accelerator parts is based on the response to high-energy (200 MeV) protons, the sensitivity to thermal neutrons is presently not investigated on a systematic basis. The aim of this study is to outline the crucial impact that thermal neutrons can have on accelerator applications, in comparison to those at ground level and avionics. The devices involved in this study consist of SRAM, FPGA and Flash memories, which have been tested in thermal and high-energy neutron facilities. Ionizing radiation and, in particular, neutron effects on NAND Flash memories have been extensively studied [88–92]. At sea level, the error rate due to radiation in NAND Flash is comparable to that induced by other mechanisms affecting reliability, such as program and read disturbs, random telegraph noise, etc. Radiation Hardness Assurance (RHA) implications are discussed in addition to the analysis of the results.

7.2.1 Thermal neutron SEU cross sections and SER estimation

In order to study the thermal neutron contribution to the overall SEU count, the thermal and HEH cross sections have to be measured. As seen in Chapter 5, the HEH cross sections can be obtained in different manners, with monoenergetic proton beams (PSI, RADEF), neutrons beams (FNG, PTB, LPSC) or with a broad energy spectrum (CHARM, ChipIr).

The involved test facilities for this study were LPSC [63] and the D50 instrument at ILL in Grenoble described in Section 5.2, which provide 14 MeV and thermal neutrons, respectively. In addition, CHARM and ChipIr were employed (see the facility description in Sections 5.8, 5.7). Both HEH and thermal neutron cross sections can be retrieved at CHARM by performing two differential measurements with and without a shielding of boron carbide, a thermal neutron absorber, as further explained in [11].

The SEU SRAMs presented in Chapter 6 were tested in different facilities, powered (on the memory pins) at 3.3 V. In addition, cross section data of the 28 nm Artix-7 (Xilinx) FPGA

from [93], which was powered at 1 V are used for the SER analysis. Furthermore, Flash memories from Micron of different NAND technologies of 20, 25, and 50 nm are employed for the analysis, and their internal structure can be organised in Multiple Level Cell (MLC) or Single Level Cell (SLC). The memories were programmed before the test and read after the irradiation at the University of Padova in the framework of [65]. A reference sample not irradiated was considered in order to subtract the possible errors that are not due to the irradiation.

The cross section comparison between facilities is reported in Fig. 7.3a for the SRAM memories. The results regarding the ISSI memory retrieved at CHARM can be found in [94]. As can be seen, the cross sections are compatible within a factor 2, which accounts for the measurement and facility calibration uncertainties. This allows considering a single cross section value representative of the HEH sensitivity of the memory. Similar reasoning can be made for the thermal neutron cross sections, which were measured at ILL (see Section 6.4 for the Tester cross sections) and with differential measurements at CHARM, as depicted in Fig. 7.3b. They are also compatible within a factor 2. At least two samples of the same reference were tested for the Flash memories and ESA Monitor, while for the SRAMs one sample was used. As shown in [9], for the same Cypress 8 Mbit reference, the $\pm 1\sigma$ standard deviation due to the sample to sample variation is calculated to be ~20%. It can be assumed a reasonable value for SRAMs and a conservative uncertainty for the other devices. The sample uncertainty would dominate the total uncertainty in ChipIr, LPSC and RADEF, yielding the overall error bars $\pm 1\sigma$ within 25%.

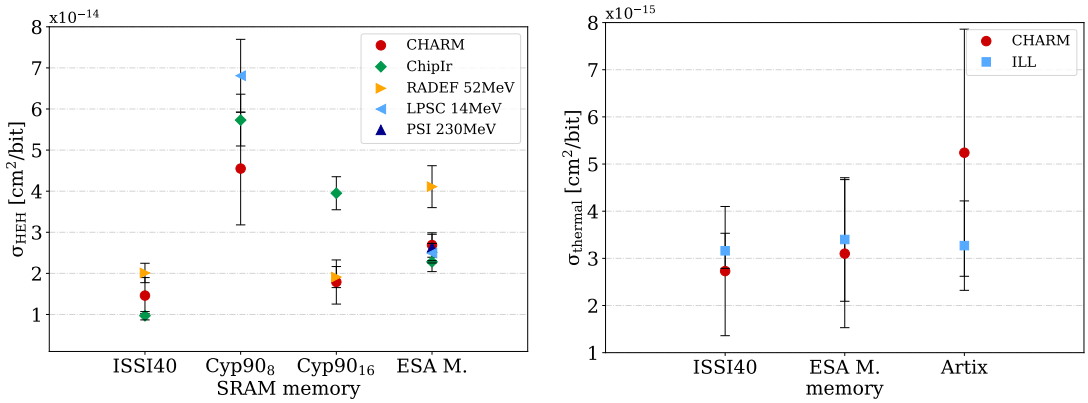

(a) *HEH cross sections* **(b)** *ThN cross sections*

Figure 7.3: (a): HEH cross section comparison obtained in different monoenergetic/spallation facilities for the three SRAM memories. (b): Thermal neutron cross section comparison obtained at CHARM, with a differential measurement, and at ILL. (a) and (b): Total error bars (accounting for statistical and fluence uncertainties) are reported for $\pm 1\sigma$.

The respective cross sections for the subsequent analysis are reported in Table 7.1 indicating the test facilities in which they were measured. For coherence, all thermal neutron cross sections are shown and measured at ILL. As the 25 nm SLC Flash memory showed a very low thermal neutron cross section (3 orders of magnitude lower compared to the others) and almost 30 times lower than the HEH one, its thermal sensitivity can be neglected and thus this

Table 7.1: Thermal neutron and HEH SEU cross sections used in the analysis for the tested memories and their ratio (the facility column reports the facility where the corresponding cross sections were measured). The memory size is expressed in Mbit (M) or Gbit (G).

Memory	Tech. [nm]	Size	Facility	σ_{HEH} [cm^2/bit]	σ_{ThN} [cm^2/bit]	$\frac{\sigma_{HEH}}{\sigma_{ThN}}$
ESA M.	250	16 M	PSI, ILL	$2.6 \cdot 10^{-14}$	$3.4 \cdot 10^{-15}$	7.7
ISSI	40	32 M	ChipIr, ILL	$9.7 \cdot 10^{-15}$	$3.2 \cdot 10^{-15}$	3.1
Cypress	90	8 M	ChipIr, ILL	$5.7 \cdot 10^{-14}$	$5.8 \cdot 10^{-16}$	99
Cypress	90	16 M	ChipIr, ILL	$4.0 \cdot 10^{-14}$	$3.9 \cdot 10^{-16}$	102
Artix7	28	1.4 M	LPSC, ILL	$9.7 \cdot 10^{-15}$	$3.3 \cdot 10^{-15}$	3.0
MLC Flash	50	4 G	LPSC, ILL	$7.1 \cdot 10^{-17}$	$2.1 \cdot 10^{-16}$	0.3
MLC Flash	25	8 G	LPSC, ILL	$2.6 \cdot 10^{-16}$	$5.2 \cdot 10^{-16}$	0.5
MLC Flash	20	16 G	LPSC, ILL	$8.6 \cdot 10^{-16}$	$1.1 \cdot 10^{-16}$	8.0
SLC Flash	25	32 G	LPSC, ILL	$4.2 \cdot 10^{-18}$	$1.5 \cdot 10^{-19}$	28

memory will not be included in the following analysis. For the other SRAMs, the HEH cross section is higher than the thermal neutron one by up to 100 times for both Cypress memories. Although at first glance the thermal neutron contribution might be neglected for these memories, it is of fundamental importance to know the operational environment in which they will be operating. As will be shown, in some LHC locations, thermal neutrons can still play a considerable role in inducing SEUs and for this reason, these memories are included in the analysis. It is noticeable that for the 50 and 25 nm Flash memories the thermal cross section is instead higher with respect to the HEH one, up to 3 times. This can occur also in SRAMs, such as in the Toshiba memory [10], and it depends on the amount of ^{10}B inside the device and its critical charge.

Based on the cross section data of Table 7.1 and the fluences of the radiation environments analysed in Chapter 3, the expected SEU rate, due to thermal neutrons and HEH, is calculated for the considered critical LHC locations. To this regard, the LHC locations that showed the largest SEU contributions are taken into account, corresponding to RR13 (tunnel), RR17 (LEV0), UJ16 and UL16 concerning the alcoves. The most meaningful results among the same memory type are reported in Table 7.2 showing the expected absolute upset values during one year of operation for the ISSI 40 nm, Artix 28 nm and 25 nm MLC Flash memories. SEUs are calculated by multiplying the respective memory cross section by the fluence of interest, and are expressed in Mbit for the SRAMs and FPGA and per Gbit for the Flash memories. For the former, the results are very similar because they have almost the same cross section ratio. The associated uncertainty on these values are mainly due to the uncertainty propagation from the HEH and ThN measurements of the RadMon and estimated to be up to 40% [10]. Therefore, the values are not directly comparable as the Flash memory capacity is higher. Considering all the results in units of Mbit, the Flash memories are the less sensitive (both to thermal neutrons and HEH) with respect to the SRAMs and the FPGA. However, the overall SEU count per memory is hundreds of times higher for the Flash memories. As can be seen, the most critical areas in terms of SER are the DS cell 8 and the UJ alcove for all the memories. The most important results are shown in Table 7.3 reporting the

Table 7.2: Example of expected SEUs due to thermal neutrons and HEH along the LHC ($N = \sigma \cdot \Phi$). Values for the ISSI and Artix memories are in [events/year/Mbit], whereas in [events/year/Gbit] for the MLC Flash 25 nm.

Location	N_{SEU} ThN			N_{SEU} HEH		
	ISSI	Artix	$Flash_{25nm}$	ISSI	Artix	$Flash_{25nm}$
RR Tunnel	10	10	1664	23	23	648
RR	6	6	987	2	2	2
UJ	47	47	7848	3	3	75
UL	1	1	173	0	0	3
DS cell 8	1489	1519	251129	668	659	18489
DS	45	46	7544	23	23	633
ARC	1	1	138	1	1	18

percentage of upsets caused by thermal neutrons with respect to the HEH. The contributions are calculated for the LHC areas and compared to those expected in ground level and avionic (inside an aircraft at 12 km of altitude) environments. For the latter, the R-factors were evaluated in Section 3.3.3, yielding the values of 0.5 and 1.1 for the ground level and avionic environment, respectively.

Table 7.3: Percentage contribution of thermal neutrons on the SEU rate with respect to the HEH. U is the RHA underestimation factor shown for accelerator locations and in comparison to the ground level and avionic (12 km) environments.

Environment	R-factor	ISSI 40 nm		Artix 28 nm		$Flash^{MLC}$ 25 nm	
		ThN (%)	U	ThN (%)	U	ThN (%)	U
RR Tunnel	1.3	30	1.4	30	1.4	72	3.6
RR	11.1	78	4.6	79	4.7	96	23.1
UJ	44.6	94	18.1	95	18.7	99	105.4
UL	31.0	91	11.1	91	11.5	98	62.7
DS cell 8	6.8	69	3.2	70	3.3	93	14.6
DS	6.0	66	3.0	67	3.0	92	12.9
ARC	3.7	55	2.2	56	2.3	88	8.4
ground level	0.5	10	1.1	14	1.2	50	2.0
avionic	1.1	19	1.2	27	1.4	69	3.2

In addition, the underestimation U-factor is defined in Eq. 7.1 as the ratio between the expected events in operation (due to HEH and thermals) and those usually calculated in qualification (due to HEH).

$$U = \frac{N_{oper}}{N_{qual}} = 1 + R \cdot \frac{\sigma_{ThN}}{\sigma_{HEH}} \tag{7.1}$$

Where R is the R-factor (ratio between thermal neutrons and HEHeq fluences) as defined in Section 2.4. The majority of qualification tests are often performed considering solely the HEHeq fluence contribution, neglecting the thermal neutron fluence. This is acceptable if the U-factor is close to 1, but when higher than 2 the SER underestimation, due to neglecting

thermal neutrons, is by definition also a factor higher than 2.

The overall percentage of SEUs induced by thermal neutrons for all the studied memories is graphically depicted in Fig. 7.4, where it is noticeable the very strong impact they can have on the SER. The respective U-factors are shown in Fig. 7.5. From Table 7.3 and Fig. 7.4 it is evident that electronics in the shielded alcoves (RR, UJ, UL) will mostly suffer due to thermal neutrons, since they can provoke up to 94%, 95% and 99% of the total upsets in the ISSI, Artix and MLC 25 nm Flash memory, respectively. Even in the Cypress memories, which are up to 100 times less sensitive to thermal neutrons than HEH, the former induce up to one-third of SEUs (in UJ). Thermal neutrons are also relevant throughout the LHC tunnel, with the highest contribution among the studies locations in cell 8 of the DS. However, in the tunnel, the impact of thermal neutrons on the ISSI memory and on the 28 nm FPGA is comparable to the HEH one. Only on the tunnel side of the RR the SER counts for the SRAMs and FPGA are comparable to those in avionic applications, which resulted in different factors lower than in most of the LHC (see Table 7.3). The same memories in ground level operation would instead present most of the issues with HEH rather than with thermal neutrons.

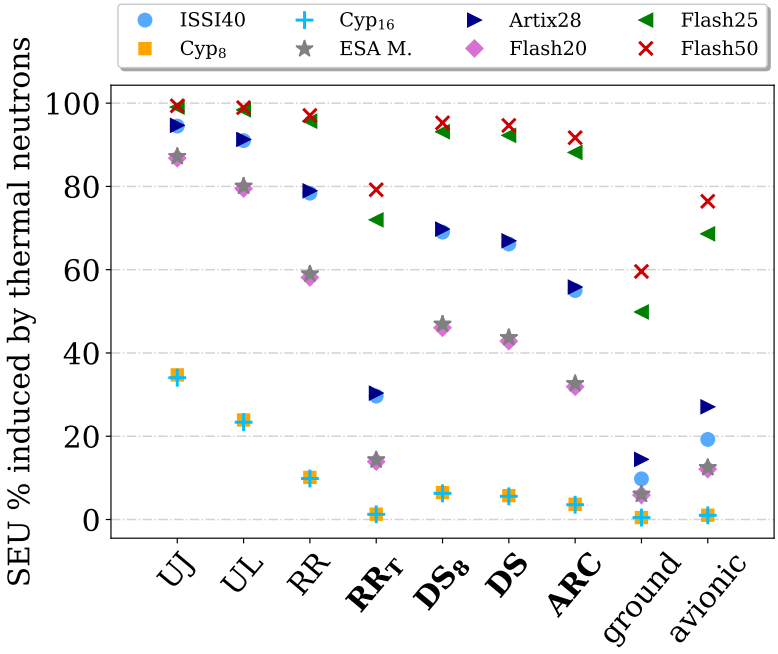

Figure 7.4: Estimated SEUs (in percentage) induced by thermal neutrons with respect to the HEH, for different LHC locations, ground level and avionic environments. RR_T refers to the tunnel, as well as the areas highlighted in bold. The estimated uncertainties to be up to 40%, mainly due to the RadMon fluence measurements.

7.2.2 Thermal neutron RHA implications

Based on the results presented in this section, the RHA implications for accelerator components and systems can be drawn. As the U-factor is basically above 2 in the alcoves and in most of the tunnel areas, the qualification of components against thermal neutrons has to be

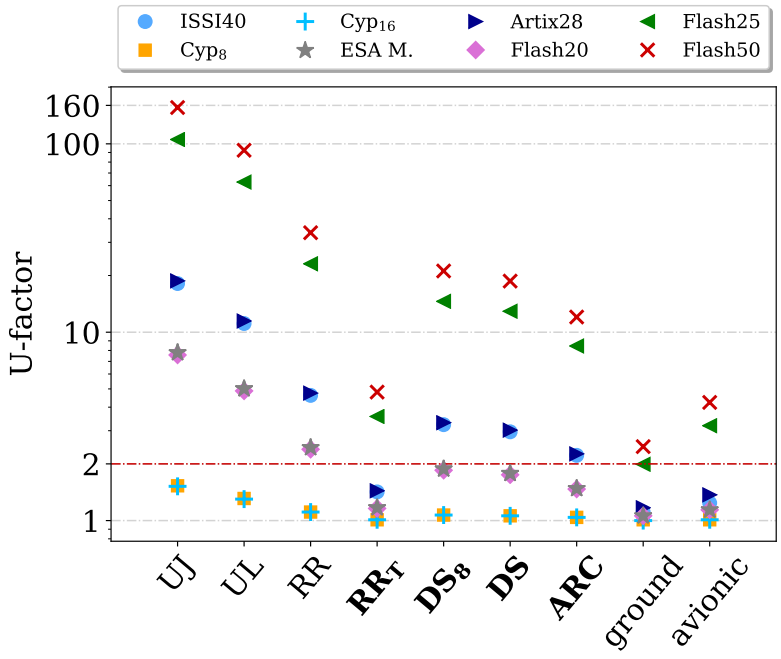

Figure 7.5: U-factors for different LHC locations, ground level and avionic environments. RR_T refers to the tunnel, as well as the areas highlighted in bold.

taken into account. Therefore, they should not be neglected, because they can be as important as the HEH or even more (when U>2). It is relevant to note that the current RHA does not include systematic thermal neutron tests at device level. For future applications, the thermal neutron qualification of critical components can be carried out through three different methods and the fourth method regards non-critical components:

1. Tests with a thermal neutron beam, such as that from a reactor as ILL. The advantage is given by the fact that the fluxes can be very high, implying short test periods and the certainty that the beam is solely composed of thermal neutrons without the contribution of higher energy particles. On the other hand, in this case, only single components can be tested at a time, since the beam size of these facilities is usually not suitable for board/system testing.

2. Mixed-field differential measurements at CHARM with boron carbide to retrieve the thermal neutron and HEH cross sections, as mentioned in section 7.2.1. Both cross sections are measured in the same facility with relatively high fluxes, and as seen in Fig. 7.3b, the thermal neutron cross sections are compatible with those measured with method 1. Furthermore, devices and systems can be tested, being the irradiation room large enough to host them. However, as explained in [11] there is the need of performing the test either with two identical memories/devices at the same time or in two different runs, in order to effectuate the differential measurements with and without the boron carbide absorber.

3. Mixed-field measurements at CHARM in a specific position with a known R-factor (ratio

between thermal neutron and HEHeq fluences). In this case, the thermal neutron and HEH cross sections remain unknown and only the total upset count including the two contributions is obtained. Thus, this method is suitable only for a specific R-factor in operation, which is compatible with that selected during the test. However, R-factors in CHARM can be selected to be large depending on the facility configuration and test position, and therefore be representative of the application environment. When the operational R-factor is known and a device/system has to be installed in that LHC location, the same R-factor can be reproduced in the CHARM facility, permitting its characterization for that specific environment. On the other hand, a new characterization is needed so far as the device has to operate in a different radiation environment.

4. For non-critical SRAM components, a safety margin can be applied to the SER calculated considering only the HEH cross section. Since the lowest ratio between HEH and thermal neutron cross sections resulted as low as 3 (see Table 7.1) a conservative approach is to consider unitary the ratio between the two cross sections.

The selection of one of these methods can be different based on the accelerator application and some remarks can be adduced for its comparison with space, ground level and avionic environments. Full boards or systems can be qualified only with methods 2 or 3 whenever their dimensions are larger than a few cm, the typical beam size in thermal neutron facilities for which the homogeneity is acceptable. If the electronics will be installed throughout the LHC method 2 is the best, because there will be different R-factors for all of which the respective SER can be calculated, whereas method 3 is enough whenever electronics will be installed in a specific location. For the accelerator, method 3 could introduce an SEU underestimation if the R-factor in operation is larger than that used experimentally. On the contrary, if method 3 is applied to retrieve the high energy cross section for space applications, where thermal neutrons are negligible, there would be an SEU overestimation, because the radiation field at CHARM always contains a portion of thermals neutrons, which can however be easily removed via boron carbide shielding. It is instead applicable for ground level and avionic applications since there are test positions with small R-factors (0.5, 1) as in those environments.

7.2.3 Conclusions

Recent studies already outlined the importance of thermal neutrons in ground level and avionic applications, since their impact on the SER increased in sub-micron technologies. As far as the accelerator environment is concerned, thermal neutron fluences can be tens of times higher than the fluences of high energy particles, especially in shielded areas. The ratio between thermal neutron and HEHeq fluences varies considerably along the LHC tunnel (DS, Arcs) up to a factor of 8, and reaches values up to 50 in the shielded alcoves (UJ, UL, RR), significantly larger than in terrestrial applications. FLUKA simulations confirm these data in agreement with the RadMon measurements.

The knowledge of the operational environment in which the device will be operating is essential, as for those locations with high thermal fluences, even if the thermal neutron sensi-

tivity of the memory is 1-2 orders of magnitude lower than that of the HEH, the resulting SER might be non-negligible. As in some of these critical areas the SEUs due to thermal neutrons can be very large, up to 95% of the total count in SRAMs and FPGAs, consequent RHA must be accounted for the component qualification. Besides the high energetic proton/neutron testing, thermal neutron measurements are therefore of primary importance.

The consequent qualification should be performed in thermal reactors for single components or in the CHARM mixed-field facility for components/boards/systems. In the latter, complete information about thermal neutron and HEH cross sections can be obtained with a differential measurement using boron carbide. Otherwise, when the installation area of electronics in the LHC is known a priori, a single measurement, suitable for a specific thermal/HEHeq fluence ratio in operation, can be performed for the qualification.

7.3 Impact of Intermediate Energy Neutrons with Respect to HEH SER in Accelerator and Atmospheric Environments

The ground level spectrum has high fluxes of neutrons below 10 MeV, and the sensitivity of electronics to this fraction of spectrum has increased in nanometric technologies, as previously shown in [46]. Indeed, the technology scaling leads to a general reduction of the threshold energy (the energy limit below which no SEUs are induced, reflected in the E_{th} parameter of the Weibull function) in SRAMs and FPGAs, with a ratio as low as 10 between saturated and 2.5 MeV neutron SEU cross sections, for the most sensitive parts presented in [95]. Therefore, the contribution to the Soft Error Rate (SER) from neutrons between 1-10 MeV has been recently investigated. To this regard, the minimum threshold energy currently imposed at 10 MeV in the JESD89 standard has been discussed to be shifted down to 1 MeV [96]. In the atmospheric environment, it was shown [15] that neutrons below 10 MeV can induce up to 13% of SEUs in 65 nm SRAMs and [95] reports a contribution of 10%. For power MOSFETs the SEEs in the relative 1-10 MeV range are reported to be up to 19% in [96], and in addition, it was concluded that the current E_{th} in the JEDEC standard should not be shifted down to 1 MeV, because it would lead to a higher measurement error comparable to the SER increase. Moreover, albedo neutrons (energies below 10 MeV) can also increase the SER in 45 and 28 nm technologies up to a factor of 20% in the former [97, 98].

The impact of intermediate energy neutrons, in the development of the thesis, was studied in two steps, shown in the following Sections 7.3.1 and 7.3.2, respectively:

1. In a first stage (Section 7.3.1), memories with feature size down to 65 nm were considered for the SER estimation, with their intermediate energy neutron responses deriving from previous publications. The SER induced by neutrons was assessed for several energy intervals between 1 and 100 MeV and compared to the SER considering the overall spectrum of different environments.

2. As the results of the first study suggested that neutrons below 20 MeV can yield a significant contribution to the SER in some cases, other targeted SRAMs with technology down to 40 nm were measured with 2.5 and 14 MeV monoenergetic neutron beams at FNG. Given the surprisingly high sensitivity of these components at low energies, a further test campaign was carried out in PTB to fully characterize these memories with neutron energies as low as 144 keV, benchmarking these results with simulations (Section 7.3.2).

7.3.1 SER induced by several energy intervals between 1-100 MeV

With the aim of evaluating the impact of intermediate energy neutrons on the total SER, four groups of energies have been treated: 1-3 MeV, 1-10 MeV, 1-20 MeV, and 1-100 MeV to give an insight to the high-energy behaviour. The SER was calculated for operational atmospheric and accelerator environments and compared to the SER retrieved in the CHARM and ChipIr irradiation facilities.

From the broad set of differential spectra shown in Fig. 7.1, the expected SEU count has been computed for the ESA Monitor, Toshiba and Cypress 90 nm, whose Weibull functions were retrieved in a dedicated study [26]. In addition, a 65 nm FPGA M2GL090 RAM presented in [57] is included in the analysis, being more sensitive to lower energies with respect to the SRAMs. In this study, energies solely above 1 MeV have been considered, and this choice is justified by the fact that the Weibull functions of these devices weight practically zero below this threshold. Figure 7.6*a* reports the percentage of SEUs of the four devices considering the ground level spectrum. In this case, except for the 65 nm FPGA, the sensitivity of the

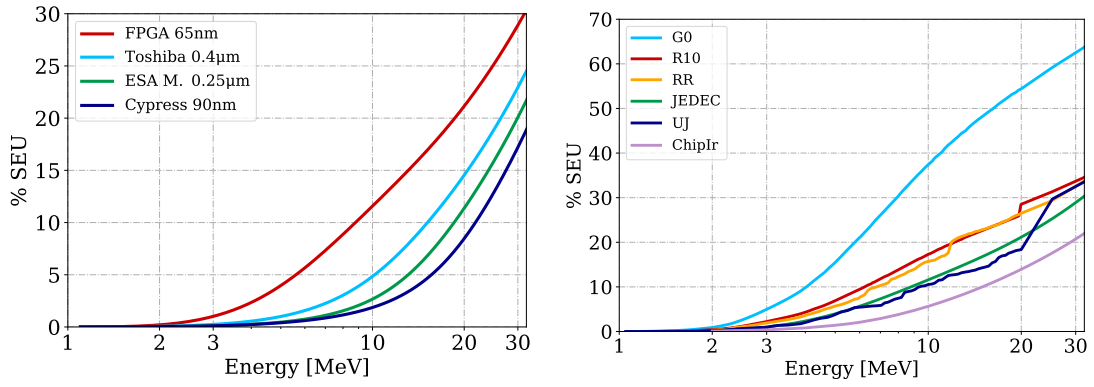

Figure 7.6: (a): SEU count (%) for the four devices in the ground level environment (JEDEC reference). (b): FPGA SEU count (%) for different operational (JEDEC, RR, UJ) and facility (CHARM: G0, R10 and ChipIr) environments.

other memories [cm^2/chip] does not increase with the technology integration. Figure 7.6*b* shows the SEU trends for the same FPGA memory in the accelerator (UJ, RR), ground level (JEDEC) and facility environments. Figures 7.7 and 7.8 show the complete result overview (the corresponding numeric values are reported in Appendix in Tables C.10, C.11, C.12 and

C.13). For every environment, the SEU count due to the relative energy range expressed as percentage (%) on the total upsets is reported (the percentage of the spectrum appertaining at the considered energy interval is shown in the respective tables in Appendix).

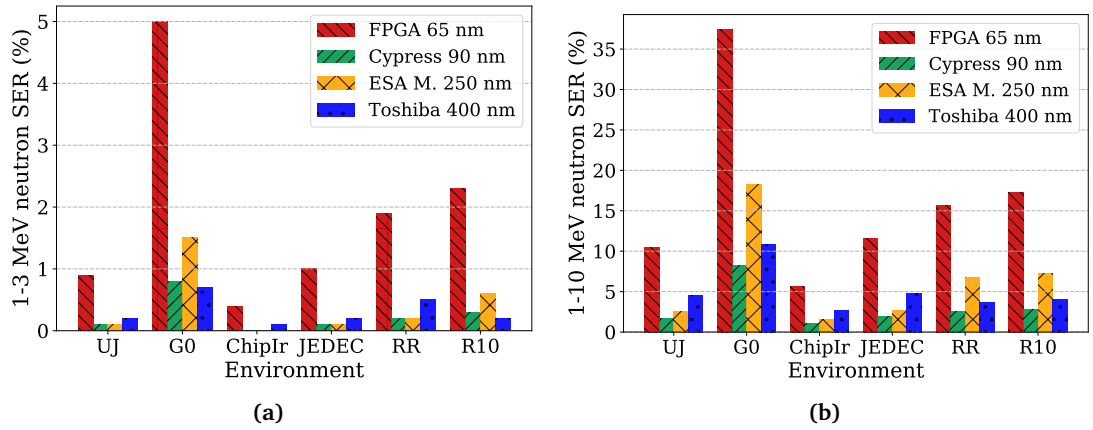

Figure 7.7: SEU (%) due to neutrons in the 1-3 MeV (a) and 1-10 MeV (b) energy interval, from the softer to the harder environment. The spectrum energy is considered >1 MeV.

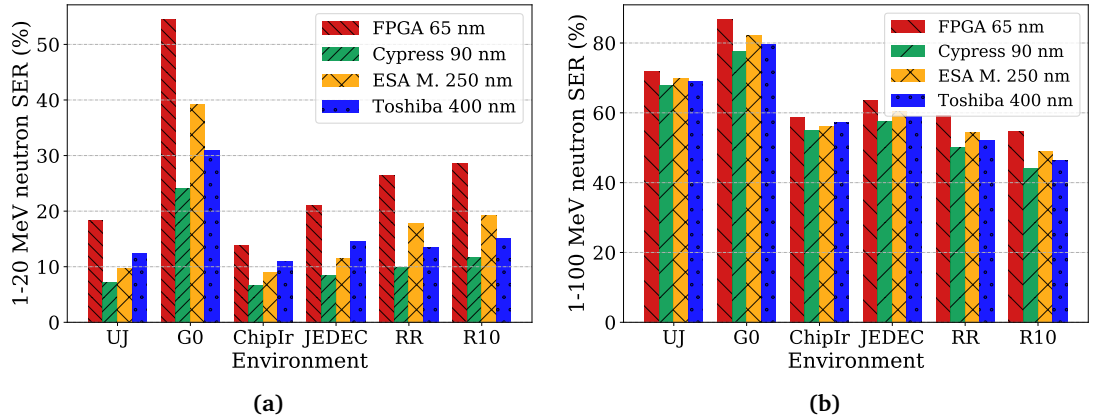

Figure 7.8: SEU (%) due to neutrons in the 1-20 MeV (a) and 1-100 MeV (b) energy interval, from the softer to the harder environment. The spectrum energy is considered >1 MeV.

As can be deducted, the 1-3 MeV neutron energy range has a negligible impact on the SER, 1-10 MeV yields an upset rate up to 12% as far as JEDEC, ChipIr and UJ are considered, while it is higher with the hard spectrum of R10 and RR up to 17% regarding the FPGA. The impact can reach up to 37% in the soft G0 location, but it has to be noted that 78% of its total spectrum is within the 1-10 MeV energy interval. Higher energies up to 20 MeV instead, constitute a large portion of the operational environments up to ∼40% for UJ and JEDEC and 56% concerning the RR. Although these percentages are similar to those from 1-10 MeV, the 1-20 MeV contribution starts to be significant for ESA Monitor, Toshiba and Cypress, increasing their SER by roughly a factor of 4 compared to the previous energy interval. The large relative 1-20 MeV neutron contribution to the total SEU count highlights the importance of having an accurate representation of the SEU cross section energy dependence in this range to realistically predict the SER.

Particles with energies greater than 100 MeV still induce about 40% and 30% of total SER, in the UJ and ground level environment, respectively. For all these energy-ranges up to 100 MeV, position R10 at CHARM is capable of perfectly reproducing the RR alcove spectrum both in terms of particle composition and SER.

Some consideration can be deducted from the portion of the spectrum contained in the four energy intervals. As far as intermediate energy neutrons are concerned, the LHC UJ alcove has a very similar particle composition to JEDEC. Up to 20 MeV, R10 and RR are mainly composed of intermediate energy neutrons for the 60% of the total particles, differently from the 20% of ChipIr, which is conversely dominated by high-energy neutrons, as it is also confirmed from Table 5.10.

Conclusions

The operational environments from the JEDEC reference and the LHC alcove UJ showed the same particle composition in terms of intermediate energy neutrons up to 20 MeV. Considering the SEU count retrieved from the spectrum and energy sensitivity of the memories down to 65 nm, the 1-10 MeV interval does not exceed 12% of the total SER in ground level application but it reaches up 17% in accelerator ones. The same trend appears for the 1-20 MeV energy range in which the LHC alcove shows up to 28% of total SER. The respective impacts increase up to 37% and 54% if considering soft, non-shielded spectra accelerator environments. Therefore, as general behaviour, intermediate energy neutrons yields a greater SER influence in accelerator applications rather than atmospheric ones, highlighting also the importance of the measured or assumed intermediate energy neutron response.

7.3.2 Focus in the 0.1-10 MeV energy interval

As introduced, this study continues the work on the basis of the results presented in the previous Section 7.3.1, focusing on lower neutron energies down to 0.1 MeV. To this regard, a broad collection of experimental data on state-of-the-art SRAMs tested with monoenergetic neutrons from 144 keV to 17 MeV is presented. Noteworthy that access to such beams (and hence publications of related results) is quite rare for electronics applications. The SRAMs concerned in the study are the ESA Monitor (1817), ISSI 40 nm, Cypress 65 nm and Cypress 90 nm memories (see Tables 6.1 and 6.3 for the specifications). These SRAMs, with same references and date codes, were irradiated in FNG and PTB (facility description in Sections 5.4 and 5.5, respectively), both with their package and delidded in some cases to assess its impact on the SEU cross section. In addition to the neutron tests, the SEU cross sections were measured with 18.6 and 29 MeV protons at the TOP-IMPLART LINAC (facility description in Section 5.3) and with 40, 50, 80, 124, 164, 184 MeV protons in the Kernfysisch Versneller Institute (KVI, The Netherlands). In both facilities, the tests were performed in air. KVI can provide primary energies of 190, 66.5 or 30 MeV which are degraded with aluminium slabs [99].

The SER due to neutrons between 0.1-10 MeV is computed for ground level, avionic

(12 km) and accelerator environments, including soft and hard spectra reproduced in the CHARM facility. SEU results have been benchmarked with those calculated from a model through Monte Carlo simulations. In addition, the study is performed also for neutrons in the 0.1-3 MeV range, whose contribution has always resulted negligible in previous publications [95] and in Section 7.3.1. Finally, the SER retrieved by applying the current memory response is compared to the events obtained from the HEHeq approximation, evaluating whether it can be still considered as valid.

7.3.3 Monoenergetic neutron and proton cross sections

The first neutron tests were carried out at FNG, where the ISSI memory was shown to have the 2.5 MeV SEU cross section only 6 times lower than that in saturation (considering 184 MeV protons at KVI). Subsequently, the same devices were measured in PTB, where a broader range of low and intermediate-energy neutrons is provided, with the aim of obtaining a better picture of the sensitivity of these memories as a function of the neutron energy. To this regard, the memories were also tested delidded (i.e. without the package) with some energies. Indeed, as shown in [87], the neutron cross section below 10 MeV of SRAMs can increase because of elastic interactions with the H atoms composing the package. These protons, which are ejected mainly in the same direction of the incoming beam [87] can reach the sensitive area of the device, and therefore contribute to increasing the SEU cross section. In fact, the memories studied in this work are sensitive to low energy protons [16].

The neutron SEU cross section measurements at FNG and PTB are shown in Figs. 7.9-7.11 for the ISSI, Cypress 65 and Cypress 90 memories and ESA Monitor, respectively. In addition, the delidded SEU cross sections are included in the same plots (the tabulated cross sections can be found in Appendix C.2).

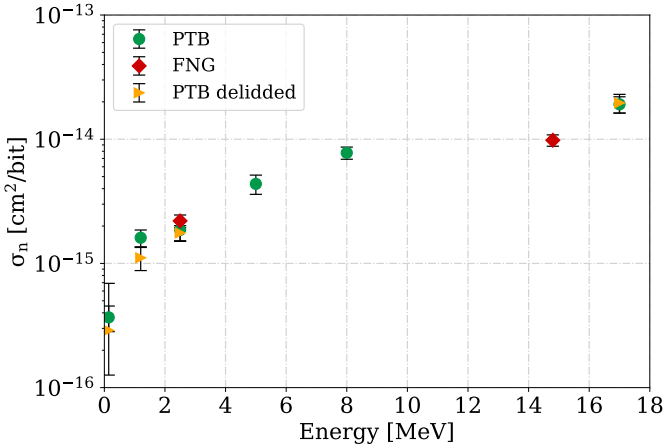

Figure 7.9: ISSI 40 nm neutron cross sections, measured at FNG and PTB. Comparison with the delidded memory for some energies. Error bars are reported with 95% of confidence level, including statistical and fluence uncertainties.

As can be seen, for the ISSI and Cypress 65 memories, the package does not have a signif-

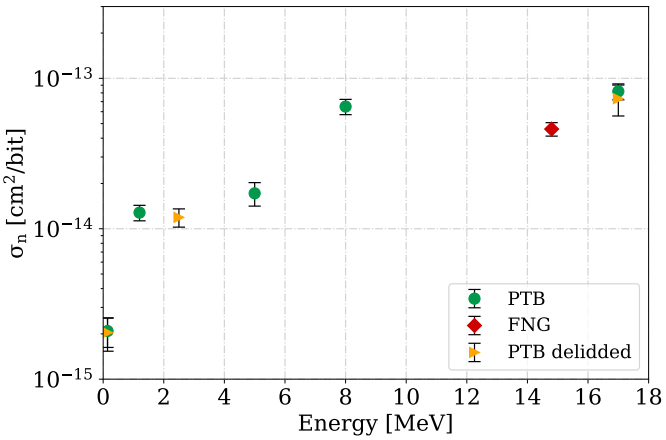

Figure 7.10: Cypress 65 nm neutron cross sections, measured at FNG and PTB. Comparison with the delidded memory for some energies. Error bars are reported with 95% of confidence level, including statistical and fluence uncertainties.

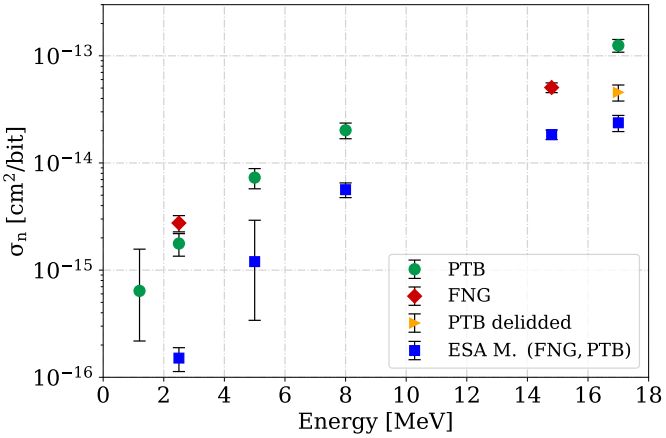

Figure 7.11: Cypress 90 nm 8 Mbit and ESA Monitor neutron cross sections, measured at FNG and PTB. Comparison with the delidded memory at 17 MeV. Error bars are reported with 95% of confidence level, including statistical and fluence uncertainties.

icant impact on the SEU cross sections. Table 7.4 reports the SEU cross section values at the energy extremes: low and intermediate-energy neutrons at 0.144, 1.2 and 17 MeV from PTB and high energy protons measured at 184 MeV in KVI for the ISSI and Cypress 65 memories, and at 150 and 200 MeV in PSI for the Cypress 90 memory (different date code) and ESA Monitor, respectively (from [100], [86]).

The ISSI and Cypress 65 memories show a relatively high cross section even at 1.2 MeV with respect to the saturated value, measured with 184 MeV protons. For instance, the Cypress 65 neutron cross section at 1.2 MeV is only 6 times lower than the high energy proton value in saturation (see Table 7.4). The complete set of ratios between high energy proton and neutron cross sections are shown in Fig. 7.12a, for the four memories. Even at 0.144 MeV, that is below the threshold energy of 0.2 MeV (so far considered the lowest onset energy to calculate the HEHeq fluence for the SEU estimation) the ISSI and Cypress 65 memories did

Table 7.4: Low energy neutron (0.144, 1.2 MeV), 17 MeV neutron and high energy proton saturated SEU cross sections for the tested memories and their ratio between high and low energies.

Memory	$\sigma^n_{0.144}$ [cm^2/bit]	$\sigma^n_{1.2}$ [cm^2/bit]	σ^n_{17} [cm^2/bit]	σ^p_{sat} [cm^2/bit]	$\frac{\sigma^p_{sat}}{\sigma^n_{1.2}}$
ISSI 40	$3.68{\cdot}10^{-16}$	$1.61{\cdot}10^{-15}$	$1.91{\cdot}10^{-14}$	$1.40{\cdot}10^{-14}$	8.7
Cypress 65	$2.09{\cdot}10^{-15}$	$1.28{\cdot}10^{-14}$	$8.19{\cdot}10^{-14}$	$7.73{\cdot}10^{-14}$	6
Cypress 90	-	$6.40{\cdot}10^{-16}$	$1.25{\cdot}10^{-13}$	$2.13{\cdot}10^{-13}$	333
ESA M.	-	-	$2.37{\cdot}10^{-14}$	$2.60{\cdot}10^{-14}$	-

not show a completely negligible SEU cross section, which is 38 and 37 times lower than the saturated values, respectively (see Fig. 7.12a). To further verify that neutrons of such low energies can still indirectly deposit enough energy to trigger an SEU, simulations were carried out and the results will be shown in Section 7.3.7.

Moreover, the thermal neutron effects on low energy neutron measurements are excluded, as the fields produced in PTB are monoenergetic, the spectra of neutrons scattered in the DUT are not composed of thermal neutrons, and the neutron background is negligible (see Section 5.5.2). Additional confirmation of this fact can be done considering the thermal neutron cross sections of the same SRAMs, which were measured in the nuclear reactor at ILL (described in Section 5.2). Indeed, given for instance the low thermal neutron SEU cross section of the Cypress 65 memory ($4.91 \cdot 10^{-16}$ cm^2/bit), very large fluxes would be needed in order to have a significant overall impact.

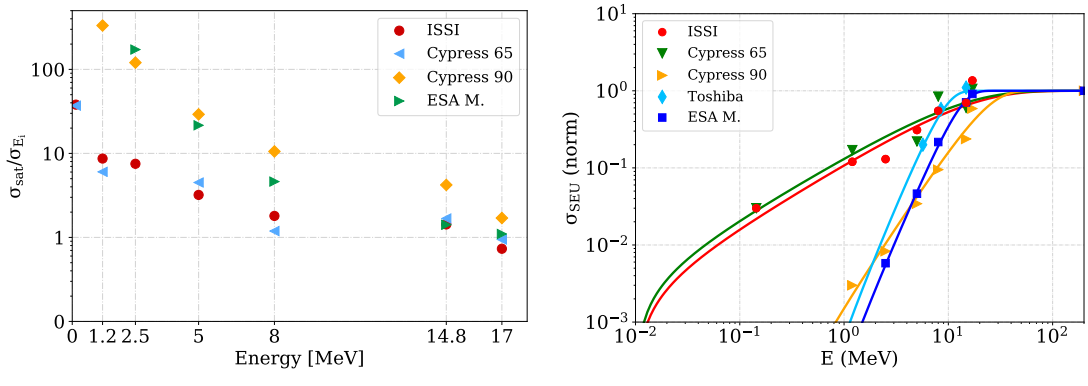

(a) **(b)**

Figure 7.12: (a): Ratio between high energy proton (saturated) and neutron SEU cross sections. The data for the ISSI and both Cypress memories are from the measurements with the package. (b): Weibull functions of the tested memories and experimental SEU cross sections normalized to 1. The Toshiba curve is the standard response so far employed for the HEHeq calculation.

The cross sections of the Cypress 90 and ESA Monitor memories behave according to what was previously assumed, with SEU cross section ratios between high energy and neutrons below 2.5 MeV in the order of several hundred (see Fig. 7.12a). Therefore, the sensitivity of the ISSI 40 nm and Cypress 65 nm memories is still significant at low energies and, as will be shown, this aspect plays a significant role on the contribution to the overall SER of neutrons

below 10 MeV.

Furthermore, for the Cypress 65 and ISSI SRAMs, the 17 MeV neutron cross section (from Table 7.4) is higher than that measured with high energy protons, by 6% and 36%, respectively. In addition, the 17 MeV SEU cross sections are almost a factor of 2 higher than those at 14.8 MeV, and the energy points are solely 2.2 MeV apart. For these memories, the SEU cross section has already reached the saturation for energy as low as 8 MeV.

Table 7.5: Weibull fit parameters of the tested memories and those of the Toshiba reference (from [10]) for the HEHeq calculation.

Memory	σ_{sat} [cm^2/bit]	E_{th} [MeV]	W [MeV]	s
ISSI 40 nm	$1.40{\cdot}10^{-14}$	0.01	14.05	0.82
Cypress 65 nm	$7.73{\cdot}10^{-14}$	0.01	11.57	0.80
Cypress 90 nm	$2.16{\cdot}10^{-13}$	0.1	24.22	1.98
ESA M. 250 nm	$2.60{\cdot}10^{-14}$	0.2	13.08	2.99
Toshiba 400 nm	$6.60{\cdot}10^{-14}$	0.2	9.25	3.02

A Weibull function is adopted to fit the experimental data of each memory and the corresponding parameters are reported in Table 7.5. According to the cross section shape, the threshold energy is set to be 0.01 MeV for the ISSI and Cypress 65 memories, 0.1 MeV for Cypress 90 memory and 0.2 MeV for the ESA Monitor. Even if some memories showed a higher cross section at 17 MeV than with higher proton energies, the latter is kept as saturation cross section. In the Weibull calculation, the neutron measurements and the saturated proton cross section were considered, excluding the 17 MeV data when higher than the saturated value. As shown in the following, this choice is supported by measurements performed with a neutron spectrum up to 11 MeV, produced by the americium-beryllium source at CERN, as well as by SEU cross section simulations. Fig. 7.12b shows the experimental SEU cross sections and the respective Weibull fits normalized to 1. In addition, the Weibull response of the Toshiba memory, employed as a reference SRAM for computing the HEHeq fluence, is added on the plot for comparison from [10].

7.3.4 Additional neutron measurements with the Am-Be source

Aiming at further quantifying the sensitivity of the SRAM components to intermediate-energy neutrons, the americium-beryllium (Am-Be) source described in Section 5.6 was employed. Hence, a continuous spectrum of neutrons is used to perform cross section measurements.

As introduced, the HEHeq fluence depends on the memory response, which is described through a Weibull function, as can be seen in Table 7.6 (values reported in terms of flux for a direct comparison). The expected upset rate in [SEU/Mbit/day] is computed by weighting the differential fluence of the Am-Be source with the memory's Weibull response (from Table 7.5) and compared to that experimentally measured. The results are reported in Table 7.6, showing

Table 7.6: Am-Be SEU measurements vs SEU estimation from the Weibull responses of the memories. The HEHeq fluxes are referred to the tests performed at 5 cm from the centre of the source. For comparison, the HEHeq flux of the Toshiba reference is $1.84 \cdot 10^4$ cm^{-2}/s.

Memory	HEHeq flux [cm^{-2}/s]	$N_{measured}$ [SEU/Mbit/day]	$N_{calculated}$ [SEU/Mbit/day]	$\frac{N_{measured}}{N_{calculated}}$
ISSI 40 nm	$4.0 \cdot 10^4$	39	42	0.93
Cypress 65 nm	$4.6 \cdot 10^4$	209	322	0.65
ESA Monitor	$9.8 \cdot 10^3$	21	22	0.95

an excellent agreement regarding the ISSI and ESA Monitor data. For the Cypress 65 this assessment is less accurate, with an expected upset rate higher by roughly 50% than the measured one, and this difference can mainly be attributed to deviations between the Weibull fit and the actual response function. The agreement was worse when the 17 MeV neutron cross sections were used to calculate the Weibull functions, hence this supports the choice of using the proton SEU cross sections in saturation instead of the 17 MeV ones.

Table 7.7: SEU cross sections of the memories with package and delidded, measured with the Am-Be neutron source.

Memory	$\sigma_{package}$ [cm^2/bit]	$\sigma_{delidded}$ [cm^2/bit]	$\frac{\sigma_{package}}{\sigma_{delidded}}$
ISSI 40 nm	$1.33 \cdot 10^{-14}$	$1.36 \cdot 10^{-14}$	0.97
Cypress 65 nm	$5.01 \cdot 10^{-14}$	$4.79 \cdot 10^{-14}$	1.05
Cypress 90 nm	$1.64 \cdot 10^{-13}$	$1.64 \cdot 10^{-13}$	1.00

In addition, the memories were measured with the package and delidded. However, as shown in Table 7.7 (data from Section 6.6), there is not a significant difference between the resulting SEU cross sections, which are calculated by applying to the Am-Be spectrum the corresponding Weibull function of each memory to retrieve the HEHeq fluence.

7.3.5 SER induced by neutrons below 10 MeV

The SER of the SRAM devices, due to neutrons in the 0.1-10 MeV energy range, is evaluated in atmospheric and accelerator environments that were described in Section 7.1.

As already shown, the SER is calculated integrating the differential spectrum of the considered environment folded with the Weibull response of each memory. Therefore, SEUs are counted starting from the threshold energy of the Weibull functions (of Table 7.5), which is different between memories. For ease of notation, this lower energy limit will be referred to as 0.1 MeV. The present analysis aims to compare intermediate to high energy neutrons, while the effects of thermal neutrons in these memories was studied in Section 7.2. Fig. 7.13 shows the fraction of upsets (in percentage) induced by neutrons with energy between 0.1-10 MeV on the overall rate, for the SRAM memories and different environments. The Cypress 90 nm SEU results are analogous to those of the ESA Monitor, hence they are represented by the

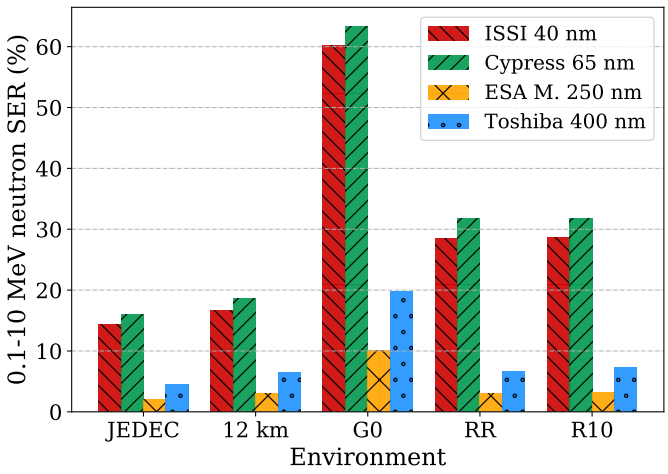

Figure 7.13: SER induced by the fraction of neutrons between 0.1-10 MeV (in percentage) on the total upset rate, for the different technological nodes of SRAM memories and in the ground level, avionic and accelerator environments.

latter. As expected from the neutron SEU cross section response, the Cypress 65 nm has the highest relative upset rate in all the environments. In ground level applications, the SEU rate due to neutrons below 10 MeV is up to 16% of the total, whereas it can be larger for avionic applications at 12 km of altitude, up to 19%. In accelerator environments the contribution is more critical, reaching up to 63% of the failure rate with a soft spectrum such as G0 and 32% with the more energetic environments in R10 and the RR alcove. The ISSI 40 nm memory has also a similar SER to that of the Cypress 65 nm, while the older technologies, 250 nm ESA Monitor, 400 nm Toshiba and 90 nm Cypress memories show a negligible impact for most of the applications, and in any case not exceeding 20%. Despite the very large Cypress 65 and ISSI cross sections at 1.2 MeV, the neutron flux in that region at ground level is not high enough to yield a considerable SEU contribution, although their relative upset rate is 3 times higher than that with older technologies. Conversely, in some accelerator environments, the flux below 10 MeV is considerably higher than that at higher energies (see Fig. 7.2) and the large Cypress 65 cross section at low energy provides a non-negligible contribution to the SER.

The same analysis is performed for neutrons in the 0.1-3 MeV range and the relative SER is depicted in Fig. 7.14. Surprisingly, this range of neutrons, which were considered negligible even for accelerator environments in the first study (Section 7.3.1), can yield a considerable failure rate in the two most sensitive SRAMs. Up to 44% of upsets are induced in the Cypress 65 memory with a soft accelerator spectrum (G0) and 22% with a harder one (RR). At 12 km of altitude, up to 10% of SEUs can be induced. Comparing these results to the SER below 10 MeV, it can be noticed that neutrons between 0.1-3 MeV can have a stronger contribution than neutrons between 3-10 MeV. This occurs because the sensitivity of the memories to low energy neutrons is very high, and the environment fluxes are larger at lower energies. This aspect is well depicted in Fig. 7.14, where the less sensitive memories (ESA Monitor and Toshiba) exhibit a totally negligible contribution.

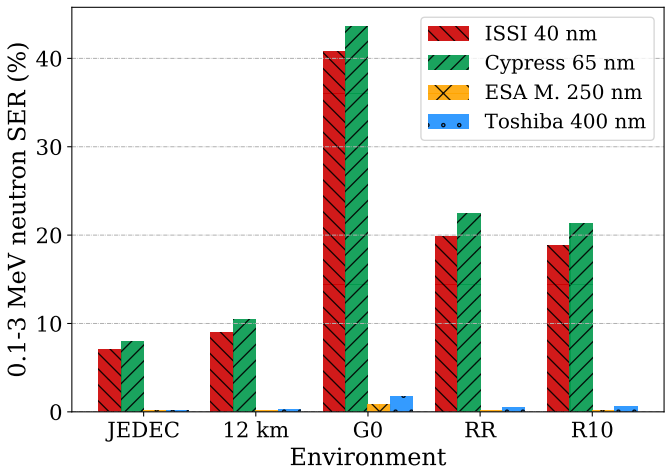

Figure 7.14: SER induced by the fraction of neutrons between 0.1-3 MeV (in percentage) on the total upset rate, for the different technological nodes of SRAM memories and in the ground level, avionic and accelerator environments.

Extending the analysis below 1 MeV for the Cypress 65 memory, the contribution is negligible in atmospheric environments (<5%) and provides an SER of 21% and 13% in G0 and RR, respectively. The failure rate is about 1% for energies below 0.1 MeV (without considering thermal neutrons).

In addition, the fact of assuming the lower threshold energy for the HEHeq fluence calculation of 0.2 MeV (see Eq. 2.8 and 2.6), instead of 0.01 MeV, yields a worst-case SER underestimation of 3.4%. Hence, the 0.2 MeV limit can still be considered in general valid, as the contribution of neutrons below this threshold is negligible.

To summarize, in some accelerator locations, neutrons below 10 MeV can induce more than 60% of the total SEUs and 44% derive from neutrons below 3 MeV. Regarding terrestrial and avionic applications, the relative failure rate below 10 MeV is 16% and 18%, respectively. It can typically be neglected for non-critical devices, but the technology scaling and increasing of sensitivity to low energy neutrons pose some threats also in these environments.

7.3.6 HEHeq fluence underestimation and RHA implications

As a consequence of the previous analysis, the 400 nm Toshiba response employed as reference in the HEHeq calculation (and implemented in FLUKA) can no longer be considered the worst-case response, and the 65 nm Cypress memory shows a greater relative contribution from intermediate-energy neutrons. The underestimation of the Toshiba reference with respect to the Cypress 65 nm memory is quantified by calculating the ratio between the respective HEHeq fluences from Eq. 2.6, and the results are shown in Table 7.8. The HEHeq fluences are calculated considering the G0 and RR spectra for energies from 0.1 MeV until 10, 20 MeV and the full spectrum.

As can be seen, the underestimation in the 0.1-10 MeV range is a factor larger than 6 for

Table 7.8: Ratio between HEHeq fluences calculated through the Cypress 65 and Toshiba memory responses in G0 and RR, considering the fluence of the environment until 10, 20 MeV and the full spectrum.

Spectrum	$\frac{HEHeq(Cypress65)}{HEHeq(Toshiba)}$		
	<10 MeV	<20 MeV	Full
G0	6.22	3.02	1.95
RR	6.21	2.50	1.29

both the soft spectrum (G0) and the harder environment (RR). Furthermore, considering the complete intermediate-energy range between 0.1-20 MeV and the full environment spectrum, the previous underestimation is up to a factor of 3 and 2, respectively. The latter value is more meaningful as the operational environment is composed of the full energy spectrum, but the other ratios provide an estimation for potential LHC environments with softer spectra than G0. It is to be noted that the underestimation of the HEHeq fluence will be directly reflected on the SER.

Consequently, these aspects have important Radiation Hardness Assurance (RHA) implications, and three solutions are presented:

1) The HEHeq fluence can be calculated with the current Toshiba reference response of the RadMon and a safety margin of two can be applied to the HEHeq fluence. However, this approach can be valid for those accelerator environments presenting a harder spectrum than that in G0, from which the fluence underestimation is calculated. Otherwise, the safety margin must be larger, as seen in the examples of Table 7.8.

2) For a worst-case scenario, the Cypress 65 memory should be employed instead of the Toshiba reference in the HEHeq fluence calculation. This approach is more accurate than Solution i) and would work with softer spectra than that of G0. However, it relies on the knowledge of the neutron spectrum in the area of interest, which is not always the case.

3) Both Solutions i) and ii) may lead to an overestimation of the estimated SER for cases in which the memory concerned is not particularly sensitive to intermediate-energy neutrons. The ideal solution would be to fully characterize the component with several intermediate neutron energies, as performed for the present work, but owing to different factors (time constraints, facility availability, costs, etc.) this is not always practically possible. To overcome this difficulty, a more realistic possibility is to qualify the device with 2.5 MeV neutrons, in addition to the high energy protons, whose energy is available in several facilities and is low enough to assess the sensibility of the memory at low energies. In fact, as seen in Section 7.3.3, the SEU cross section measured at 14 MeV (and even at 8 MeV) is still comparable to its value in saturation. From the ratio between the high-energy proton and 2.5 MeV neutron SEU cross sections is instead evident whether the memory is very sensitive to low energy neutrons or not. As shown in Fig. 7.12a,

if this ratio is above 100 the memory will not be particularly sensitive to low energies, hence the SER estimation can be performed by using the Toshiba response. Differently, when the ratio is around 10, the memory will be considerably sensitive to low energy neutrons and the Cypress 65 memory response can be employed instead. For intermediate values of the ratio the relation for estimating the SER is not straightforward, but a possible solution would be to vary the Weibull function of a reference memory (for instance the Cypress 65), until matching with the 2.5 MeV cross section of the new device (normalized to the reference). This action can be performed by varying the s and E_{th} parameters of the Weibull fit, which determine most of the horizontal shift of the function.

7.3.7 Neutron and proton SEU simulations

With the aim of better understanding the behaviour of the Cypress 65 and ISSI memories that, as opposed to previous technologies, show a large sensitivity to low neutron energies, the respective SEU cross sections were calculated through Monte Carlo simulations. In addition, simulations can confirm that, at such low energies (0.144, 1.2 MeV), neutrons can elastically interact with atoms and indirectly deposit the required energy to trigger an SEU. The simulations have been performed using FLUKA and the G4SEE application based on the Geant4 toolkit. Both tools have been developed at CERN and a brief description to set up the simulation for the calculation of the energy deposition is reported in appendix A. A preliminary benchmark was carried out comparing the GEANT4 and FLUKA simulated proton cross sections to the experimental data from KVI and TOP-IMPLART.

Furthermore, the SEU cross sections of neutrons and protons above 50 MeV are considered to be identical in the JEDEC standard [12], above 30 MeV in [13], and assumed the to be the same above 20 MeV in the HEH approximation (See Section 2.3.1). For this reason, proton data are included in the study for comparison to the SEU neutron cross sections.

The Cypress 65 and ISSI memories were modelled with a simple geometry, consisting of a SiO_2 Back End Of Line (BEOL) and a Si bulk, containing the rectangular parallelepiped (RPP) sensitive volume (SV), as will be detailed hereafter. Note that this simplified representation of the BEOL is regarded as an important source of uncertainty for intermediate-energy neutron simulations, in which the specific material composition can have a significant impact on the energy deposition distribution. The critical charge of these memories was chosen to best fit the broad range of experimental data for a given memory model and in accordance with typical values of the technology. Although the critical charge tends to decrease with technology scaling, a single feature size can assume a wide range of critical charges (order of a few fC) [97, 101, 102]. Moreover, the critical charge depends on the node capacitance and internal voltages of the memory, which are not typically known, thus TCAD simulations are normally performed to estimate its value [101]. This approach can hence be referred to as semi-empirical.

The ISSI memory was modelled in FLUKA and the G4SEE tool, with a cubic RPP of 250 nm

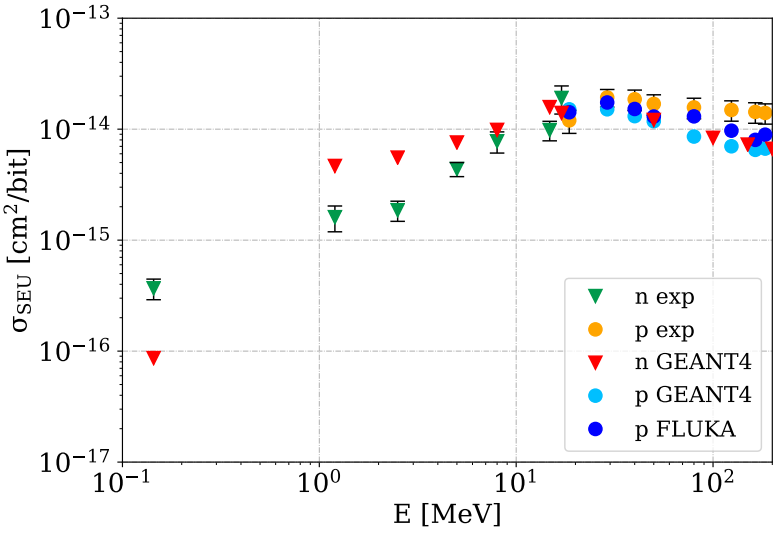

Figure 7.15: ISSI 40 nm proton (p) and neutron (n) cross section simulations and experimental data comparison. Proton simulations derive from FLUKA and GEANT4 tools, while the neutron ones from the latter.

sides and a SiO_2 BEOL thickness of 6 μm. In the former, 100 RPPs were disposed (to reduce the simulation time) in a matrix 10x10 inside a bulk structure of 24.5x24.5x0.35 μm^3, while in G4SEE a single RPP was employed with the same bulk dimensions. The beam dimensions were covering the whole surface of 24.5x24.5 μm^2. The SEU cross section is consequently retrieved through the collected charge inside the sensitive volume, considering a critical charge Q_c of 0.72 fC, to be coherent with the FLUKA model of the same memory from [16]. The deposited energy to critical charge conversion is performed considering the factor of 22.5 MeV/pC. The simulated FLUKA and G4SEE proton SEU cross sections are calculated and shown in Fig. 7.15, together with the proton experimental data. In the same graph, the neutron measurements and G4SEE simulations are reported, also for comparing the data above 30 MeV with the proton SEU cross sections. In addition, the G4SEE simulated neutron SEU cross sections at 50, 100, 150, 200 MeV are included.

Regarding protons, the G4SEE cross sections are compatible within the uncertainty to the experimental data from 18.6 to 50 MeV. At higher energies the agreement is less satisfactory up to 54% of underestimation by the simulation at 184 MeV. Also, the FLUKA model underestimates the proton cross section at high energy up to 44% and has a good agreement below 80 MeV. The difference between the two Monte Carlo tools may be attributed to the implemented physical models.

For neutrons, instead, G4SEE overestimates in general the experimental data, by up to 70% between 17 and 5 MeV. The overestimation is a factor of 3 at low energies (2.5 and 1.2 MeV), while the simulation underestimates the experimental value by 70% at 0.144 MeV. The ISSI neutron cross section simulated at 17 MeV is $1.4{\cdot}10^{-14}$ cm^2/bit, compatible with the high energy proton saturation value rather than with the 17 MeV measurement. The proton SEU cross sections measured and simulated at 18.6 MeV are also compatible with the

neutron cross sections at 14 and 17 MeV, showing that proton and neutron cross sections at intermediate-energies are still very similar.

Similarly, the Cypress 65 memory was modelled with a cubic RPP of 510 nm side, BEOL thickness of 10 µm and Q_c of 0.64 fC. These parameters and dimensions were defined on the basis of the ISSI memory model, which exhibits a similar response, and as the technological node of the Cypress is larger, the RPP is also assumed to be larger. As can be noticed, the critical charge of the Cypress 65 nm memory resulted slightly lower than that of the ISSI 40 nm memory, but as anticipated a single feature size can assume a range of critical charges.

The proton and neutron G4SEE simulations are shown in Fig. 7.16, along with the experimental data. Again, at high proton energies the simulations underestimate the measurements up to 50%. The agreement with neutrons is very good (within 10%) between 8 and 17 MeV. The 5-1.2 MeV are overestimated by the simulations almost a factor of three and the 0.144 MeV cross section underestimated by 72%.

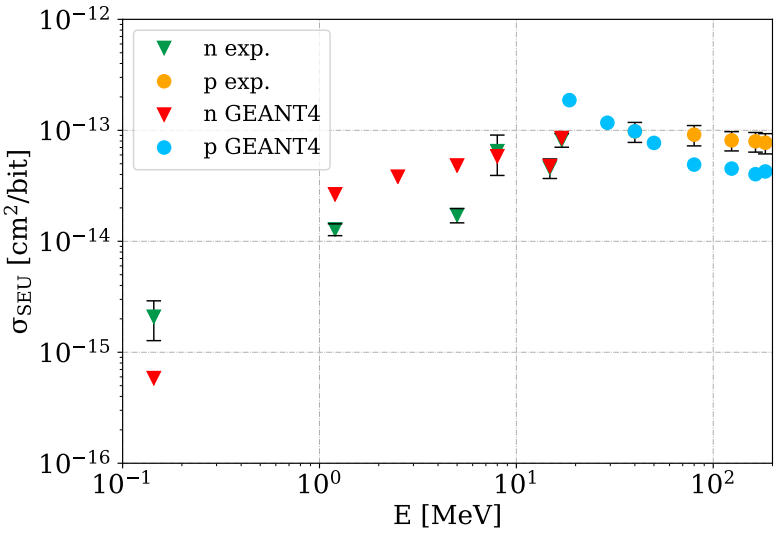

Figure 7.16: Cypress 65 nm proton (p) and neutron (n) cross section simulations and experimental data comparison. Proton and neutron simulations derive from GEANT4.

Considering the measurement uncertainties (around 20% or higher), the simplified model of the memory and the energy range of several orders of magnitude in which the RPP model is evaluated, the agreement can be considered as satisfactory. To note that these simulations were not intended to perfectly fit the experimental data, as the main objective was to verify the possibility of inducing SEUs with low energy neutrons. In fact, even considering the memory only composed of Si and SiO_2, without taking into account materials of metal layers, plugs and other insulators, neutrons are shown to be capable of indirectly depositing enough energy to trigger SEUs. This observation supports that the measured SEU cross sections below 2.5 MeV are actually due to neutron interactions. As a conclusion, simulations show compatible results to the experimental data, as well as the difficulty in having a single model capable of reproducing the SEU cross sections for the broad range of energies and particle species.

Moreover, it is worth noting that the systematic overestimation of both RPP models of

a factor 2-3 with respect to the data in the 1.2-5 MeV neutron range could be attributed to an over-representation of the oxygen content in the BEOL, considered as pure SiO_2. Indeed, being a relatively light atom with respect to other BEOL constituents (Si, Al, Cu) larger energy can be transferred to oxygen in elastic interactions.

While the lowest threshold energy for inelastic interactions of neutrons and ^{28}Si is 2.75 MeV (see Chapter 4), the deposited energy at lower energies is mainly due to elastic scattering, and the two contributions in G4SEE can be disentangled. The elastic and inelastic contributions to the SEU cross section (absolute values) are shown in Fig. 7.17a for the Cypress 65 nm memory, calculated through GEANT4 at varying neutron energy. It is remarkable to observe how inelastic reactions increase with increasing neutron energy, while elastic processes increase with decreasing neutron energy from 17 to 2.5 MeV. For lower energies the collected charge to trigger an SEU is only provided by elastic collisions. Moreover, until 5 MeV SEUs are mainly due to elastic collisions, while with higher energies the inelastic interactions are more effective.

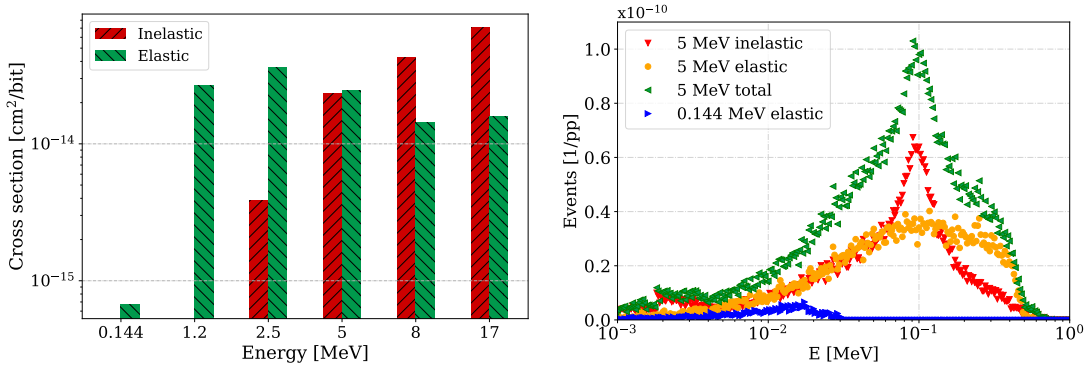

(a) **(b)**

Figure 7.17: (a): Elastic and inelastic contributions on the SEU cross section in the Cypress 65 nm memory at varying neutron energy (from GEANT4 simulations). (b): Example of event energy deposition of elastic and inelastic reactions in silicon for 144 keV and 5 MeV energy neutrons.

As the simplified geometry of the simulation consists of silicon and oxygen, the energy can be transferred only to these atoms. The maximum energy transferred from a neutron during an elastic collision is given by Eq. 7.2.

$$E_{max} = E_n \cdot \frac{4A}{(A+1)^2} \tag{7.2}$$

Here, E_n is the energy of the incoming neutron and A is the mass number of the target atom. Hence, the maximum energy transferred to silicon and oxygen is 13.3% and 22.1% of the initial neutron energy, respectively. For instance, the maximum elastic energy transferred by a neutron of 144 keV in silicon (A=28) is 19 keV, while in oxygen (A=16) is 32 keV. Therefore, most of the deposited energy will result from elastic scattering with oxygen, and more in general with the lighter nucleus. The corresponding maximum deposited charge in silicon and oxygen is 0.84 and 1.42 fC, respectively. Both are above the critical charge for the

ISSI and Cypress 65 models, therefore also from a calculation point of view, elastic scattering from 144 keV neutrons is thought to be capable of depositing sufficient charge to trigger an SEU. Note however that the nuclear stopping power for such low energies, which is negligible compared to the electronic stopping power at higher energies, can have a significant impact on the total energy deposition. The GEANT4 simulations include both contributions. An example of energy deposition events from the G4SEE output can be seen in Fig. 7.17b for 144 keV and 5 MeV neutrons.

7.3.8 Conclusions

Neutrons in the 0.1-10 MeV energy range can play a critical role in inducing SEUs in nm technologies. As shown with a 65 nm SRAM, the neutron cross section at 1.2 MeV is only 6 times lower than its value in saturation, while for previously studied components, it is typically of the order of hundreds of times lower. A similar behaviour was observed for a 40 nm memory. The SER induced by neutrons in the 0.1-10 MeV interval can be up to 63% the overall rate in accelerator environments. At ground level the rate is up to 16%, while for avionic applications at 12 km of altitude it can reach up to 19%, therefore representing a possible threat for high-reliability systems. Even neutrons between 0.1-3 MeV, which resulted negligible in previous studies, can yield a significant impact on the SER, up to 44% in accelerator environments. Moreover, though not covered in this work, the higher SEU cross section of integrated technologies in the 0.1-10 MeV range is expected to have a significant impact on the SER in environments with less energetic neutron spectra than the atmospheric or accelerator ones, such as fission/fusion, or medical.

GEANT4 simulations support the experimental response shape of the memories and the possibility of inducing SEEs even with neutrons of 144 keV due to elastic collisions, showing in addition that neutron and proton SEU cross sections are compatible above 20 MeV. However, the choice of the RPP model dimensions and critical charge to describe a memory is not straightforward, especially when the model has to reproduce both the neutron and proton SEU cross sections ranging several orders of magnitude. Moreover, the package of the memory does not significantly impact the neutron SEU cross section, as experimentally measured. An Am-Be source was used to further validate the intermediate neutron response shape of the devices and the effects of the package.

Moreover, it is shown that the HEHeq standard response used at CERN to estimate the SER of electronics can result in underestimations of up to a factor 2. This underestimation would be larger for accelerator environments with softer spectra than that considered in the analysis. Consequently, three possible RHA solutions are presented.

Finally, SEUs can still be induced even below the so far considered threshold of 0.2 MeV in the HEHEeq fluence calculation, although their contribution to the overall rate is below 4%.

7.4 Impact of Energy Dependence on Ground Level and Avionic SEE Rate Prediction When Applying Standard Test Procedures

SEEs in ground level and avionic applications are mainly induced by neutrons and protons, whose relative contribution of the latter is larger with increasing altitude. At an altitude of 12 km, neutrons are the dominant particle inducing 70% of SEEs, while at 30 km their proportion with respect to other particles is less than 50%. This is because above 18.3 km the contribution from heavy ions begins to be relevant [37]. Moreover, low-energy protons (i.e., in the several MeV range), although not treated in this work, are capable of inducing soft errors through direct ionization and negative muon capture in 90 nm technology and below [103]. Similarly, muons, though not capable of inducing SEEs through indirect ionization due to their leptonic nature, are also capable of inducing SEUs through direct ionization in highly integrated technologies [104].

Currently, there are two main applicable standards, JEDEC JESD89A for ground level and IEC 62396 for avionics, that address the procedure for testing and qualifying electronics for these environments. These test procedures (methods) were summarized in Section 5.1, showing their advantages, disadvantages and limitations which may lead to an underestimation of the SEE rate. M1 consists in characterizing the device with a spallation neutron source, M2 with monoenergetic beams up to 200 MeV, and M3 extends M2 through simulations up to a few GeV.

The atmospheric environment overview was given in Section 3.3, showing the differences in neutron/proton spectra at varying altitude, with data extracted through MAIRE, an online tool based on FLUKA simulations. With these spectra, the SEE rate (SEU and SEL) in three SRAMs is calculated in the following, by applying the different test procedures. These memories present a strong SEE response dependence with energy for both neutrons and protons, which do not saturate after 200 MeV, but still increase up to several GeV. This is due to the presence of tungsten inside their structure, a fissile material when interacting with high energy hadrons. Other SEE studies on the impact of high-Z materials have also been carried out in [105, 106]. The proton SEE contribution is compared to that of neutrons, as well as their predictions using different methods to appraise possible underestimations.

7.4.1 SEE induced by atmospheric neutrons and protons

Alliance, Samsung and Renesas memories were selected for the analysis because of their strong cross section dependence with the energy above 200 MeV, which is due to the presence of tungsten near the sensitive volume [40, 58, 107]. Alliance and Samsung are the same memories of Table 6.3, tested against SEL in ChipIr and characterized with monoenergetic beams in [40]. The SEU analysis was performed using the Renesas SRAM R1LV1616R-1328 (150 nm) of 16 Mbit [107], which uses a radiation hardening technique to increase the critical

charge. Indeed, it is worth noting that the impact of tungsten and thus energy dependence is more relevant for components with relatively high LET thresholds (~10 MeV · cm^2/mg and above), and thus more impacted by the high-LET fission fragments from high-Z materials. Contrarily, typical soft errors, with LET thresholds in the range of ~1 MeV · cm^2/mg would be less impacted, as silicon-like fragments would dominate.

Table 7.9 reports the memory characteristics and the Weibull parameters extracted from a standard qualification up to 230 MeV protons from M2 (Weibull MeV) and considering the actual memory response from M3 saturating after a few GeV (Weibull GeV) calculated through simulations. The corresponding SEL and SEU cross section responses are depicted in Figure 7.18 in units of cm^2/device, in addition to the experimental data. It can be noted that the real saturated cross section is about one order of magnitude larger than that at 230 MeV. Furthermore, the three memories are not sensitive to neutrons below 20 MeV (as their technology is above 150 nm, and they have relatively large LET thresholds).

Table 7.9: SEL and SEU Weibull parameters of the SRAM memories considered for the analysis.

Memory	Tech [nm]	Size	SEE	Weibull	σ_{sat} [cm^2/dev]	E_{th} [MeV]	W [MeV]	S
Alliance	200	4 Mbit	SEL	M2	$4.0 \cdot 10^{-10}$	20	156	1.93
				M3	$7.5 \cdot 10^{-9}$	25	2210	1.41
Samsung	180	4 Mbit	SEL	M2	$5.0 \cdot 10^{-10}$	35	157	1.74
				M3	$7.5 \cdot 10^{-9}$	40	2000	1.25
Renesas	150	16 Mbit	SEU	M2	$1.8 \cdot 10^{-10}$	35	100	1.6
				M3	$8.2 \cdot 10^{-9}$	35	2800	1.3

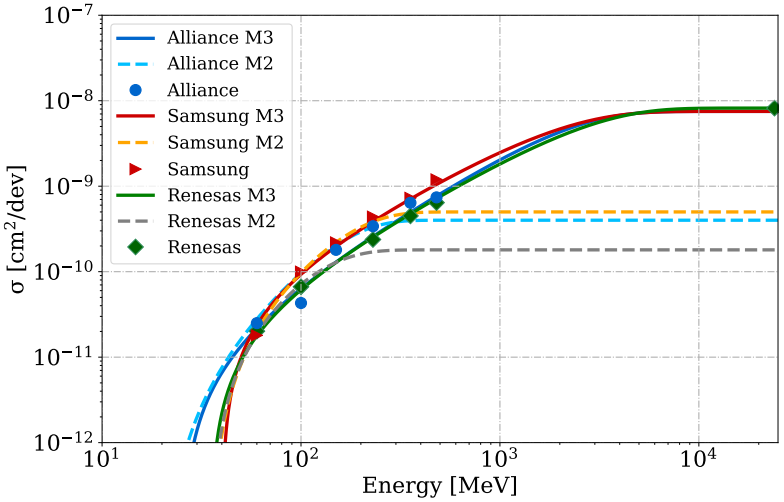

Figure 7.18: SEL and SEU cross sections for the three SRAMs calculated from two different Weibull: standard characterization at 230 MeV (M2) and response up to several GeV (M3) extended through simulations. Experimental data are shown with markers.

The SEE rate for the three memories was calculated by applying M1, M2 and M3 at different altitudes, from the ground level (JEDEC NYC, Geneva) up to 20 km. Thus, the different

methods were applied to the same environment's spectra as a starting point. As far as M1 is concerned, the SEL measurements (Alliance and Samsung) were performed in ChipIr, which provides a spallation neutron spectrum up to 700 MeV. The single memory cross sections were calculated considering the flux above 20 MeV, as these memories are not sensitive to intermediate energy neutrons below 20 MeV. The SEL cross sections resulted in $7.1 \cdot 10^{-11}$ and $6.81 \cdot 10^{-11}$ cm^2/dev for Alliance and Samsung, respectively (from Table 5.14). The cross section value was multiplied by the operational flux (at different altitudes, see Figure 3.7) above 20 MeV to obtain the SEE rate. Indeed, provided there is little difference between the experimental and application neutron spectrum in the 10–20 MeV range, having used 10 MeV as lower limit would hardly have an impact on the results.

Regarding M2 and M3, the SEE rate was computed through the integral of the spectrum folded with the Weibull response from Table 7.9. In the following, the results will be detailed shown for the Alliance memory. They are perfectly representative also for the Samsung, because these memories have a very similar response, as can be deducted from their Weibull functions (Figure 7.18). The conclusions about M2 and M3 are also valid for the Renesas memory and the possible differences will be mentioned.

The SEL results are presented in unit of Failure In Time (FIT) per device, which corresponds to 10^9 working hours. Figure 7.19*a* reports the Alliance SEL rate induced by neutrons and protons, by applying the three methods. Figure 7.19*b* shows the ratio of the Alliance SEL rates between the different methods, which are calculated using the values of Figure 7.19*a*. The ratio M3/M1 will be called A and M3/M2 named B. These ratios represent the SEE underestimation factor when using the standard M1 or M2 compared to the actual response measured with M3. A first observation considering the standard methods is that the FIT rate from M1 underestimates that of M2 by about a factor of 2.

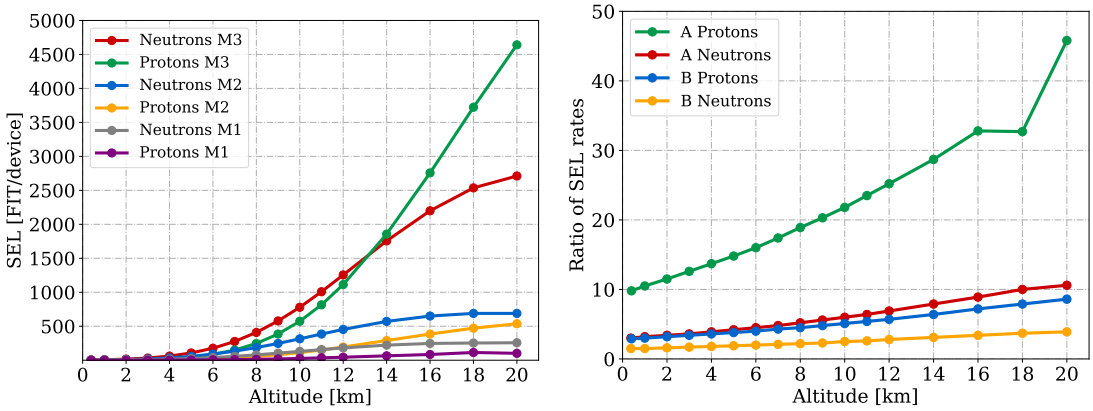

(a) **(b)**

Figure 7.19: (a): SEL Failure in time (FIT)/dev rate for the Alliance memory calculated from M1, M2 and M3 for protons and neutrons. (b) Ratio of the Alliance SEL rates between different methods for neutrons and protons. A = M3/M1, B = M3/M2. The ratio represents the underestimation factor.

Focusing on neutrons (Figure 7.19*b*), M1 and M2 underestimate M3 at ground level by a factor of 3.0 and 1.5, respectively, and the ratios increase with the altitude. At flight altitudes

of 12 km, A and B are 6.9 and 2.8, respectively, and these ratios still increase up to about 11 and 4 at 20 km. The SEU rate calculated for the Renesas shows the rate of B as 4.8 (at 12 km) and 7.0 (at 20 km), which is an underestimation even greater than the SEL one. The SEE [FIT] contribution due to neutrons and protons with energies below and above 230 MeV is shown in Table 7.10 for the three memories at 12 km of altitude. It is clear that the effect of the energy-dependent SEE cross section is relevant. The memory is sensitive to the higher energy fluxes, whose contribution to the SEE was underestimated when considering a SEE cross section saturating at 200 MeV. This phenomenon is visible in Figure 7.19*a* where, using the Weibull fit extracted from 200 MeV (M2) or spallation tests (M1), the SEL [FIT] rates are flatter with the change in altitude compared to those from M3. The trend of M1 in Figure 7.19*a* is, by construction, the same as the integral neutron flux in Figure 3.7. A consequent remark about the standard methods is that M2 is preferable to M1 (although in this case, the conclusion derives from measurements performed at ChipIr, and the results might be different in other spallation facilities).

Table 7.10: SEE [FIT] rate below and above 230 MeV due to neutrons and protons, using the characterization at 230 MeV (M2) and at GeV energies (M3). Calculation at 12 km of altitude.

Memory	SEE [FIT] for E < 230 MeV				SEE [FIT] for E > 230 MeV			
	Neutrons		Protons		Neutrons		Protons	
	M2	M3	M2	M3	M2	M3	M2	M3
Alliance	193	134	34	24	260	1121	161	1090
Samsung	205	169	37	30	321	1273	200	1187
Renesas	121	128	21	23	121	1040	75	1032

Regarding protons, the effect of the three methods is the same as with neutrons (since the proton and neutron memory cross sections are assumed to be equal), but the underestimation is even higher in the ratios A and B, resulting in 10 and 3 at ground level and 25 and 6 at 12 km, respectively. For Renesas, the B ratio is doubled. Moreover, when using M1 or M2 for example (Figure 7.19*a*), the SEE [FIT] rates due to neutrons are always larger than those induced by protons (at 12 km protons induce half of SEE compared to neutrons), whereas with M3, protons cause as many SEE as neutrons at 13 km, and their contribution is larger at higher altitudes (at 12 km, the proton SEE rate is 90% that of neutrons). These neutrons/protons contribution to the SEE [FIT] rate are shown in Fig. 7.20 for the three methods. Therefore, for these types of memories, SEEs from protons are non-negligible compared to those from neutrons already at flight altitudes. In other words, when considering per unit flux, atmospheric protons are more efficient in inducing SEEs than atmospheric neutrons, owing to their larger energies.

In addition, as mentioned in Section 5.1, the IEC standard for avionic proposes a simplified method for calculating the SEE rate at 12 km (M4). It consists of multiplying the spallation cross section by the value of 6000 cm^2/h rounded from 5600 $n/cm^2/h$, which is the integrated flux above 10 MeV, and to scale the flux according to the IEC curve in Figure 3.6*b* for the different altitudes. As shown in the same Figure, the scaling factor is compatible with the curve retrieved from the MAIRE simulations. Calculating the SEE rate at 12 km

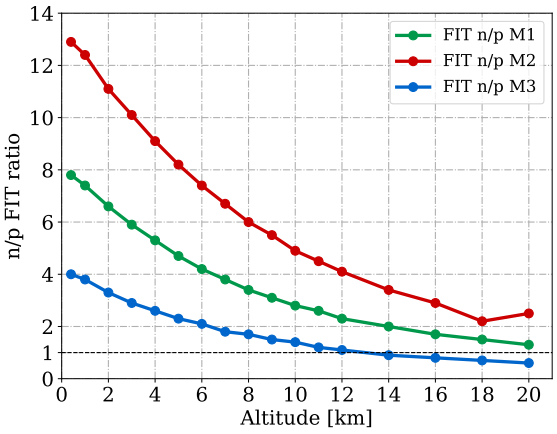

Figure 7.20: Ratio between neutron and proton SEL [FIT] rates for the three methods (Alliance memory).

over Geneva, by applying the aforementioned simplified method for the Alliance memory, it yields 426 FIT/dev. At first glance, this value seems compatible with 453 FIT/dev, calculated considering the neutron contribution from M2 (whereas with M1 the rate is 181 FIT/dev). Therefore, one could conclude that the simplified method is valid for neutrons neglecting the proton contribution. However, the two results are compatible due to compensating effects: the simulated neutron flux above 10 MeV at 12 km is 2834 n/cm^2/h, about half compared to 5600 n/cm^2/h, but the M2 cross section is up to 5 times higher (in saturation at 200 MeV) than that from M1. Furthermore, when comparing the result with M3, the SEL [FIT] rate using the flux of 6000 cm^2/h is 3 times lower, even though it is said to be conservative and incorporate the contribution of protons.

As seen, the SEE underestimation with standard methods is due to two effects: the contribution from high energy particles (neutrons and protons) and the fact that protons are mostly neglected, as in the simplified method that considers only 6.7% of protons in the flux of 6000 cm^2/h at 12 km. The results from Figures 7.19 and 7.20 can be used to quantify these two effects, for example at 12 km of altitude, considering M2 as the standard approach (Alliance memory). From Figure 7.19, the B ratio of neutrons and protons is 2.8 (neutron $SEL_{M3} =$ 1255 FIT, $SEL_{M2} = 453$ FIT) and 5.7 (proton $SEL_{M3} = 1113$ FIT, $SEL_{M2} = 194$ FIT), respectively. These factors quantify the separate underestimations due to protons and neutrons. Employing the avionic simplified method, which neglects part of the protons as shown above, the SEE value is 426 FIT/dev (thus 397 FIT due to neutrons and 29 FIT induced by protons). Therefore, even if the memory was saturating at 200 MeV, the underestimation with the simplified method for neglecting part of the protons is more than a factor of 6 compared to M2. As a summary result, Table 7.11 reports the SEE [FIT] rate at ground level, avionic (12 km) and 20 km of altitude for the three memories, considering the contribution of both neutrons and protons, with their respective A and B ratios.

The SEL and SEU underestimation in ground level applications can be up to a factor of 4. This factor increases with altitude and, at a nominal high of 12 km for commercial flights, the SEE rate can be from 3 to 12 times greater than that predicted by applying the standards.

Table 7.11: Summary SEE [FIT/device] from M1, M2, M3 due to the combined contribution of neutrons and protons, at ground level (Geneva, 375 m), 12 km and 20 km of altitude. A = M3/M1, B = M3/M2.

Memory	SEE	Altitude	M1	M2	M3	A	B
Alliance	SEL	Ground	1.4	3.1	5.1	3.5	1.6
		12	225	647	2368	11	3.7
		20	358	1226	7351	21	6
Samsung	SEL	Ground	1.4	3.6	6.1	4.4	1.7
		12	216	762	2660	12.3	3.5
		20	343	1468	7918	23	5.4
Renesas	SEU	Ground	-	1.8	4.7	-	2.7
		12	-	338	2223	-	6.6
		20	-	618	7075	-	11.4

The ratio is higher at 20 km up to a factor of 23, mainly due to the proton contribution. As a result, the material composition of a new component to test should be assessed, for example by means of a Scanning Electron Microscope (SEM), in order to verify the presence of tungsten or other high-Z materials that can cause the cross section to increase above 200 MeV. The qualification can be carried out accordingly, with the standard methods or through simulations/measurements with facilities providing high energy beams, such as CHARM at CERN. In the absence of such test opportunities, safety margins may need to be incorporated in M1 and M2 in order to account for possible energy dependence.

Moreover, it should be highlighted that whereas this work focuses on the impact of tungsten near the actual sensitive volume of three commercial SRAM components (e.g., metallization and contacts), the effect of other high-Z materials, such as gold packages, has also been investigated in the context of space applications [106]. In addition, it is worth noting that a strong SEE dependence with energy has also been observed for the SEL sensitivity of a commercial analog-to-digital converter ADC device [108], and this underestimation for SEE responses also applies to the accelerator environment [57, 58].

7.4.2 Conclusions

The standard test procedures for the qualification of electronics for ground level and avionic applications make important assumptions that may lead to underestimation of the SEE rate. This occurs with components that present a strong SEE cross section response with energy, which saturates only after several GeV and not around 200 MeV, due to the presence of high-Z materials, such as tungsten, inside the memory structure. For these devices, it was shown that high energy particles (above GeV) in the atmosphere play a fundamental role in inducing SEEs, even though their fluxes are orders of magnitude lower than those at MeV energies. As shown for SEL and SEU rates in SRAMs, two main conclusions can be drawn. The proton contribution to SEEs is non-negligible and comparable to that of neutrons even at flight altitudes (12 km). Moreover, the SEE [FIT] rate, using qualification methods from the

standards, can be underestimated up to a factor of 4 at ground level and up to 12 times in avionic applications. The solution relies on characterizing these components up to a few GeV, through simulations and/or dedicated facilities capable of providing GeV of these energies, through either monoenergetic beams or spallation environments. If such an experimental approach is not feasible, safety margins accounting for possible energy dependence may need to be taken into consideration.

7.5 Summary

The introductory Section 7.1 of this Chapter aimed to compare the spectra of operational environments with those of facilities. The impact of thermal neutrons in accelerator and atmospheric environments was described in Section 7.2. The thermal neutron fluence was compared to the fluence of high energy neutrons, both measured and simulated, showing that their ratio can be up to a factor of 8 and 50 in the LHC tunnel and shielded alcoves, respectively. The SER was estimated for several applications showing it can be up to 95% the total upset rate in SRAMs and FPGAs, with consequent RHA implications.

The effects of intermediate energy neutrons for several energy intervals, which were studied in two subsequent stages in the development of the thesis, were exposed in Section 7.3. The SEU cross sections from Chapter 6 were compared, analysed and used to retrieve the failure rate in operation due to a certain portion of neutrons. It turned out that the SER due to neutrons in the 0.1-10 MeV energy range can be up to 63% the overall rate in accelerator, and even neutrons between 0.1-3 MeV can still yield a significant contribution up to 44%. The study was carried out with monoenergetic neutron measurements and benchmarked with simulations through an RPP model, to demonstrate the possibility of inducing SEUs even with neutron energies as low as 144 keV. It was shown that only elastic scattering contributes to the SEU cross section at these low energies and their comparison to the contribution due to inelastic reaction was evaluated as a function of the energy. Moreover, the results of the intermediate energy neutron sections can be of great interest for fusion and medical applications, although not explicitly treated in this thesis, as they present similar or softer spectra.

In addition from these results, the HEHeq fluence calculation used at CERN was challenged in terms of intermediate energy neutron response and lower threshold energy limit. The analysis showed that the SER can be underestimated up to a factor of 2, which can be larger for environments with softer spectrum than that considered, hence different RHA solutions are proposed. Furthermore, neutrons below the threshold of 0.2 MeV can still induce SEUs, although their contribution resulted lower than 4% of the total rate.

Finally, some studies on SRAM memories carried out for CERN applications can be of interest in other contexts, such as in avionics. To this regard, the SEE rate induced by atmospheric protons and neutrons, in devices with a strong energy dependence, was compared to the predictions from avionics standards, showing important underestimations up to a factor of 4 and 12 in ground level and avionic environments, respectively (Section 7.4).

Chapter 8

Conclusions

8.1 Summary

Neutrons are the main source of SEEs in the LHC accelerator and this thesis aims at describing the SEEs induced by thermal and intermediate energy (0.2 - 20 MeV) neutrons on the overall impact due to the mixed-field environment, besides the effects of highly energetic neutrons (up to a few GeV). The SEE rate for several operational environments of the accelerator is estimated and compared to that in ground level and avionic applications. The qualification approaches for COTS components are derived from the experimental and simulation studies, outlining the guidelines for a Radiation Hardness Assurance (RHA) methodology.

A multitude of irradiation facilities is employed to measure the SEU and SEL cross sections of state-of-the-art SRAMs and other components, from thermal neutrons up to spallation sources and high energy protons, comparing the results and assessing the suitability of the facilities for electronic testing related to accelerator applications. Some of these facilities, such us ILL and ChipIr, have been already employed for other studies and qualifications at CERN, showing the high interest for these studies. To this regard, an approach for calibrating and comparing neutron environments through well-known SEU and SEL based SRAMs is proposed and applied to neutron spallation and mixed-field facilities. The analysis is carried out through measurements and FLUKA simulations, showing that the ChipIr facility can be employed to mimic LHC environments with soft spectra, while CHARM remains the reference for tunnel and other locations with hard spectra.

The inelastic interactions retrieved through a FLUKA driver at the single interaction level (production Monte Carlo) are analyzed in detail to study all the secondary ions generated by the interaction of neutrons in Si, with energies up to 1 GeV. These simulations explain the behaviour as a function of the energy of the SEU cross section experimentally measured, and show qualitatively which ions contribute to the energy deposition in the SV of a device. Si ions are the most effective with primary neutrons of 10 and 14 MeV, while Al ions are expected to give the largest contribution with 20 MeV, through the (n, xn) and (n, xp) reactions, respectively. The $(n, x\alpha)$ reactions are instead important for all energy ranges. When increasing

the incident neutron energy above 20 MeV, the open reaction channels drastically increase and the contribution of heavier secondaries (Si, Mg, Al) is less significant and replaced by the lighter ions (Na, Ne, O and C), especially above 100 MeV. This aspect, along with the fact that the secondary ions produced with primary neutron energies above 100 MeV have similar distributions from Si to F, explains why the SEU cross section is normally saturated above 100 MeV, and testing with higher energies does not significantly impact its value. Indeed, above 100 MeV the heavier ions are less and less produced but their contribution is compensated by that of lighter ions.

Besides, the inelastic interaction analysis along with the RPP FLUKA models used to calculate the SEU and SEL cross sections are combined to explain why the SEL cross section in saturation, differently from that of SEU, is not reproduced with 14 MeV neutron beams. This occurs because an SEL needs a larger quantity of deposited energy compared to an SEU, owing to its larger SV and the typically larger LET_{th} increases the SEL dependence with energy.

Several locations in the tunnel and in shielded alcoves of the accelerator are characterized through measurements and simulations, showing that the fluence of thermal neutrons can be up to 50 times larger than the fluence of HEHeq. Since the related SER can be up to 95% the total upset rate for SRAMs and FPGAs, several RHA solutions are proposed to qualify electronic components and systems to thermal neutrons. For instance, the qualification can be performed at CHARM with a differential measurement by employing a thermal neutron absorber, such as boron carbide.

Some scaled-technology memories exhibited a high sensitivity to intermediate energy neutrons resulting in a relative SER due to neutrons in the 0.1-10 MeV energy range up to 63% the overall rate in the accelerator, and even neutrons between 0.1-3 MeV showed a significant contribution, up to 44%. The study is carried out with monoenergetic neutron measurements and benchmarked with simulations through an RPP model, demonstrating the possibility of inducing SEUs even with neutron energies as low as 144 keV, due to elastic scattering. Therefore, neutrons below the threshold of 0.2 MeV so far assumed in the HEHeq fluence calculation at CERN can still induce SEUs, although their contribution on the overall rate results lower than 4%. In addition, the HEHeq fluence calculation used at CERN can be underestimated up to a factor of 2, which can be larger for environments with softer spectra than that considered, hence, different RHA solutions are outlined.

Moreover, some studies on SRAM memories carried out for CERN applications can be of interest in other contexts, such as in avionics. To this regard, the SEE rate induced by atmospheric protons and neutrons, in devices with a strong SEE cross section energy dependence, is compared to the predictions from avionics standards, showing important underestimations up to a factor of 4 and 12 in ground level and avionic environments, respectively.

In conclusion, from the studies presented in this thesis, it can be derived that thermal and intermediate energy neutrons play a primary role in inducing SEEs in the accelerator, as much as or more than the effect of highly energetic (>20 MeV) particles. These aspects will be taken into account for the qualification of components at CERN and for the SER estimation in future analysis. Indeed, one of the objective of this thesis work has been to pave the way for a

guideline regarding the qualification of accelerator electronics against neutrons, highlighting the significant neutron energies that should be considered. The presented results regarding the accelerator can be applied in other contexts that share similar radiation environments as seen for atmospheric applications, and although not explicitly treated in this work they can be of great interest for fusion and medical applications, as they present similar or softer neutron spectra.

8.2 Outlook on Future Works

Many studies presented in this thesis can be extended for future developments. With the HL-LHC operation planned as of 2025, the radiation levels will consistently increase and therefore SEEs will be even a more serious threat for a successful accelerator operation. The neutron radiation environments of critical locations can be simulated and compared to the present ones, and the corresponding SER can be estimated. Furthermore, a possible future development of the LHC would be the Future Circular Collider (FCC), a more powerful accelerator that would collide particles at 100 TeV of energy, although the project is still in a conceptual and feasibility study. As can be inferred, the high energies involved would imply a high level of radiation, where COTS components may not be suitable anymore, and hence the development of Rad-Hard components could be required.

The analysis of neutron-dominated locations presenting significant levels of thermal and intermediate energy neutrons can be extended to other LHC tunnel and shielded alcove locations of the current LHC machine. For instance, it is likely that some locations will present softer spectra than those analysed and hence the contribution of intermediate energy neutrons would be even greater. In addition, the study could be performed for different electronic components, such as DRAMs, other FPGAs and Flash memories, requiring the design of appropriate test boards.

The RPP models describing the SRAMs can be improved considering the exact dimensions of the involved geometries and other materials that characterize the layers surrounding the sensitive area, for instance through the Scanning Electron Microscope (SEM) analysis. In addition, the information about the amount of boron surrounding the W plugs would be extremely useful to model the device and simulate the thermal neutron cross section. Several attempts to retrieve this information were made through companies providing such as service for the ISSI 40 nm memory, however none of the employed techniques (ToF-SIMS, EDX analysis) could yield the boron content.

The contribution of the nuclear reactions to the SEU cross section can be further analyzed, considering the FLUKA output of the inelastic interactions (from the Preex driver) as an input for the transport Monte Carlo with the geometry of the memory concerned. The implementation of these simulations would require the development of some routines to automatize the process. Otherwise, or in a complementary way to the FLUKA simulations, the secondary contributions to the SEU cross section could also be extracted through the Geant4-based G4SEE

tool that is being currently developed at CERN.

8.3 Publications and Conference Contributions

The work performed at CERN during these three years of PhD, related to the thesis and in support of secondary activities, has led to the publication of several contributions in international journals and conferences:

[1] M. Cecchetto, P. Fernández-Martínez, R. García Alía, R. Ferraro, S. Danzeca, F. Wrobel, C. Cazzaniga and C. D. Frost, "**SEE Flux and Spectral Hardness Calibration of Neutron Spallation and Mixed-Field Facilities**," *in IEEE Transactions on Nuclear Science*, vol. 66, no. 7, pp. 1532-1540, July 2019, doi: 10.1109/TNS.2019.2908067.

[2] M. Cecchetto, R. García Alía, and F. Wrobel, "**Impact of Energy Dependence on Ground Level and Avionic SEE Rate Prediction When Applying Standard Test Procedures**," *Aerospace*, vol. 6, no. 11, Art. no. 11, Nov. 2019, doi: 10.3390/aerospace6110119.

[3] M. Cecchetto, R. García Alía, F. Wrobel, M. Tali, O. Stein, G. Lerner, K. Bilko, L. Esposito, C. B. Castro, Y. Kadi, S. Danzeca, M. Brucoli, C. Cazzaniga, M. Bagatin, S. Gerardin, A. Paccagnella, "**Thermal Neutron-Induced SEUs in the LHC Accelerator Environment**," *in IEEE Transactions on Nuclear Science*, vol. 67, no. 7, pp. 1412-1420, July 2020, doi: 10.1109/TNS.2020.2997992.

[4] M. Cecchetto, R. García Alía, F. Wrobel, A. Coronetti, K. Bilko, D. Lucsanyi, S. Fiore, G. Bazzano, E. Pirovano, R. Nolte, "**0.1-10 MeV Neutron Soft Error Rate in Accelerator and Atmospheric Environments**," *in IEEE Transactions on Nuclear Science*, in phase of publication.

Conferences

[5] M. Cecchetto et Al., "SEE flux and spectral hardness calibration of neutron spallation and mixed field facilities," *18th European Conference on Radiation and Its Effects on Components and Systems (RADECS)*, Gothenburg (Sweden), Sept. 2018, **Poster Contribution**.

[6] M. Cecchetto et Al., "SEU screening using an Am-Be neutron source," *16th International School on the Effects of Radiation on Embedded Systems for Space Applications (SERESSA)*, Noordwijk (The Netherlands), Nov. 2018, **Poster Contribution**.

[7] M. Cecchetto et Al., "Neutron radiation environment in the LHC accelerator at CERN and implications for electronics," *Radiation Testing and Assurance of Space Technologies (RAD-TEST)*, Dubna (Russia), May 2019, **Invited talk**.

[8] M. Cecchetto et Al., “Thermal Neutron-Induced SEUs in the LHC Accelerator Environment,” *19th European Conference on Radiation and Its Effects on Components and Systems (RADECS)*, Montpellier (France), Sept. 2019, **Oral Presentation**.

[9] M. Cecchetto et Al., “0.1-10 MeV Neutron Soft Error Rate in Accelerator and Atmospheric Environments,” *Nuclear And Space Radiation Effects Conference (NSREC)*, Dec. 2020, **Oral Presentation**.

Co-author in publications

[10] R. García Alía, M. Brugger, M. Cecchetto, F. Cerutti, S. Danzeca, M. Delrieux, M. Kastriotou, M. Tali and S. Uznanski "**SEE Testing in the 24-GeV Proton Beam at the CHARM Facility**," *in IEEE Transactions on Nuclear Science*, vol. 65, no. 8, pp. 1750-1758, Aug. 2018, doi: 10.1109/TNS.2018.2829916.

[11] R. García Alía, P. Fernández-Martínez, M. Kastriotou, M. Brugger, J. Bernhard, M. Cecchetto, F. Cerutti et Al., "**Ultraenergetic Heavy-Ion Beams in the CERN Accelerator Complex for Radiation Effects Testing**," *in IEEE Transactions on Nuclear Science*, vol. 66, no. 1, pp. 458-465, Jan. 2019, doi: 10.1109/TNS.2018.2883501.

[12] P. Fernández-Martínez, R. García Alía, M. Cecchetto, M. Kastriotou, N. Kerboub, M. Tali, V. Wyrwoll, M. Brugger et Al., "**SEE Tests With Ultra Energetic Xe Ion Beam in the CHARM Facility at CERN**," *in IEEE Transactions on Nuclear Science*, vol. 66, no. 7, pp. 1523-1531, July 2019, doi: 10.1109/TNS.2019.2907112.

[13] R. García Alía, M. Tali, M. Brugger, M. Cecchetto, F. Cerutti et Al., "**Direct Ionization Impact on Accelerator Mixed-Field Soft-Error Rate**," *in IEEE Transactions on Nuclear Science*, vol. 67, no. 1, pp. 345-352, Jan. 2020, doi: 10.1109/TNS.2019.2951307.

[14] M. Kastriotou, P. Fernández-Martínez, R. García Alía, C. Cazzaniga, M. Cecchetto et al., "**Single Event Effect Testing With Ultrahigh Energy Heavy Ion Beams**," *in IEEE Transactions on Nuclear Science*, vol. 67, no. 1, pp. 63-70, Jan. 2020, doi: 10.1109/TNS.2019.2961801.

[15] V. Wyrwoll, R. García Alía, K. Røed, P. Fernández-Martínez, M. Kastriotou, M. Cecchetto et al., "**Heavy Ion Nuclear Reaction Impact on SEE Testing: From Standard to Ultrahigh Energies**," *in IEEE Transactions on Nuclear Science*, vol. 67, no. 7, pp. 1590-1598, July 2020, doi: 10.1109/TNS.2020.2973591.

[16] C. Cazzaniga, R. García Alía, M. Kastriotou, M. Cecchetto, P. Fernandez-Martinez and C. D. Frost, "**Study of the Deposited Energy Spectra in Silicon by High-Energy Neutron and Mixed Fields**," *in IEEE Transactions on Nuclear Science*, vol. 67, no. 1, pp. 175-180, Jan. 2020, doi: 10.1109/TNS.2019.2944657.

[17] A. Coronetti, R. García Alía, M. Cecchetto, W. Hajdas, D. Söderström, A. Javanainen and F. Saigné, "**The Pion Single-Event Effect Resonance and its Impact in an Accelerator**

Environment," *in IEEE Transactions on Nuclear Science*, vol. 67, no. 7, pp. 1606-1613, July 2020, doi: 10.1109/TNS.2020.2978228.

[18] C. Cazzaniga, M. Rebai, R. García Alía, P. Fernández-Martínez, M. Cecchetto, M. Kastriotou, M. Tardocchi and C. D. Frost, "**Fast Neutron Measurements with Solid State Detectors at Pulsed Spallation Sources**" *in Journal of Neutron Research*, vol. 22, pp. 345–352, Jan. 2020, doi: 10.3233/JNR-190141.

Appendices

Appendix A

Simulations of Event-by-Event Energy Deposition

The SEE cross sections were calculated through FLUKA and G4SEE (Geant4 based), considering the event by event energy deposition in the volume of interest, the latter describing the SRAM sensitive volume. To this regard, as a basis for each simulation, the energy deposition was scored in one or more Rectangular Parallelepipeds (RPPs) embedded in a silicon bulk, and a layer of silicon dioxide (SiO_2) was added to represent the BEOL. The geometrical dimensions and thicknesses of the layers were modelled according to the Scanning Electron Microscopy (SEM) performed on the components. The choice of using more than one RPP in some cases has the only scope of reducing the computation time of the simulation and is not intended to include any other effect (for instance, it does not simulate MBUs, as the spacing between RPPs is not representative of the physical cells).

The workload of both FLUKA and G4SEE simulations is distribute in many CPUs (from 40 to 80) to reduce the simulation time, so that the simulation was carried out within approximately 2 hours. The output file contains the events associated to a certain energy interval (and they are normalized by the total number of primaries only in the FLUKA output).

A typycal example

rgy through the conversion factor of 22.5 MeV/pC and the SEU number for a specific Q_c is calculated by integrating the events with larger energy than the energy associated to the Q_c. Finally, the cross section is calculated by dividing the SEU number by the simulated fluence (reverse of the beam surface).

A.1 Energy deposition in FLUKA

The FLUKA simulations are run with a statistics of $1.8{\cdot}10^9$ primary particles (pp) for each RPP, and therefore, the statistics of the final result considering 100 RPPs is of $1.8{\cdot}10^{11}$ pp for every primary energy. The energy deposition in the FLUKA simulations (version 4.1.0) is per-

formed by adding several cards to the input file and by calling some user-routines, which are FLUKA scripts. The detailed description of these routines is reported in [56] and graphically shown in Figure A.1. A brief description about the required input cards is summarized below:

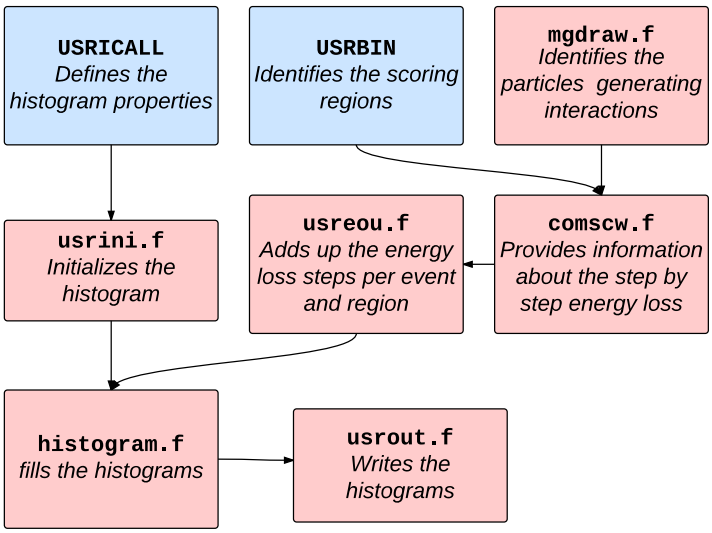

Figure A.1: FLUKA user-routines to perform simulations of event by event energy deposition, from [56].

.

- USERDUMP to enable the access and to call the mgdraw.f user routine.
- USERWEIG to enable the access and to call the mgdraw.f user routine.
- USRBIN to score the energy in the RPPs.
- USRYIELD to score the double differential yield of all particles emerging from inelastic hadronic interactions.
- USRICALL to initialize the user routine, by passing some input information such as the energy binning, deposited energy intervals, etc.
- USROCALL (left blank) to activate the usrout.f user routine.
- LAM-BIAS to enhance the probability of inelastic interaction of primary particles and silicon.

A typical example of SRAM model in FLUKA is depicted in Figure A.2: the BEOL and the silicon layer is visible to the left and a perpendicular cut of the latter is shown to the right with the 100 RPPs. The beam is sent along the z axis with a surface that covers the entire memory area.

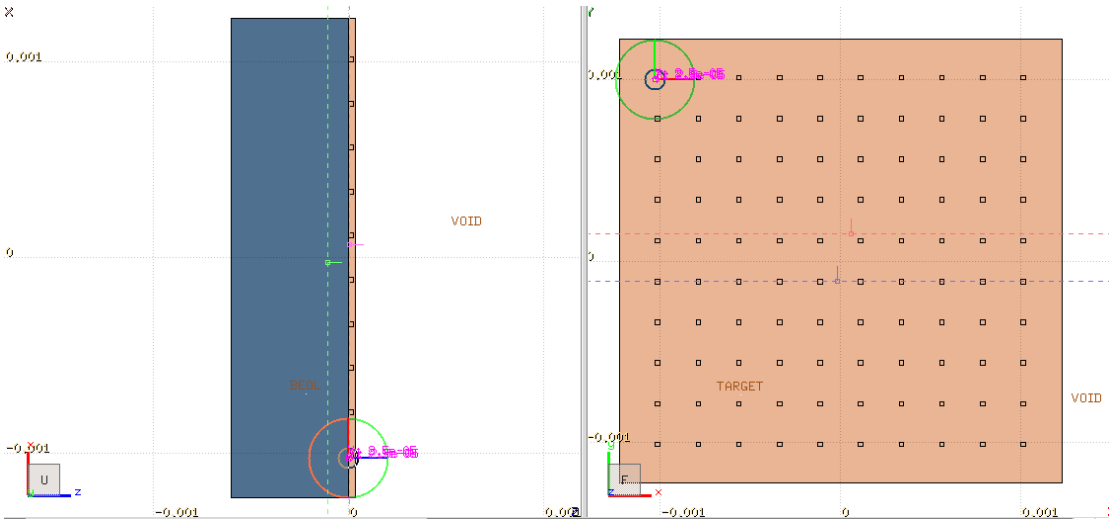

Figure A.2: Example of memory model implemented in FLUKA with 100 RPPs: Side view with the BEOL and Si layers on the left, and perpendicular cut of silicon showing the 10x10 RPPs matrix on the right.

.

A.2 Energy deposition in G4SEE

G4SEE is an application based on the Geant4 toolkit (version 10.6.p01) [109] and has been developed at CERN specifically for studying SEEs. Hence, differently from FLUKA, there is no need to set up specific routines to obtain the event-by-event direct and indirect energy deposition histograms in micro-metric electronic volumes, which is the standard output of G4SEE.

The input parameters are set in a macro file, in which the physics models can also be specified [110], [111]. To this regard, for proton simulations, the $G4HadronElasticPhysics$ hadron elastic models and $FTFP\_BERT$ hadron inelastic models were used. The latter mainly uses the Geant4 Bertini intra-nuclear cascade model at the energies relevant for these studies. One of the main features of geant4 is the possibility of performing transport simulation with neutrons below 20 MeV, and for this, the HP High Precision neutron models and cross sections were used for both elastic and inelastic scattering. G4Em $StandardPhysics\_option4$ was added too, which is the combination of the best and most precise electromagnetic models, needed for the direct energy deposition. The cross section biasing has been also applied for elastic and inelastic interactions of primary protons and neutrons, to enhance the CPU performance of the simulations. Moreover, the application permits to disentangle the energy deposition between inelastic and elastic processes.

The G4SEE version employed for the simulations presented in this thesis was the 0.3.1 and the statistics of each simulation was of at least $1.0{\cdot}10^9$ pp.

Appendix B

Distributions of Secondary Products of Inelastic Interactions

B.1 Energy distribution of single reactions

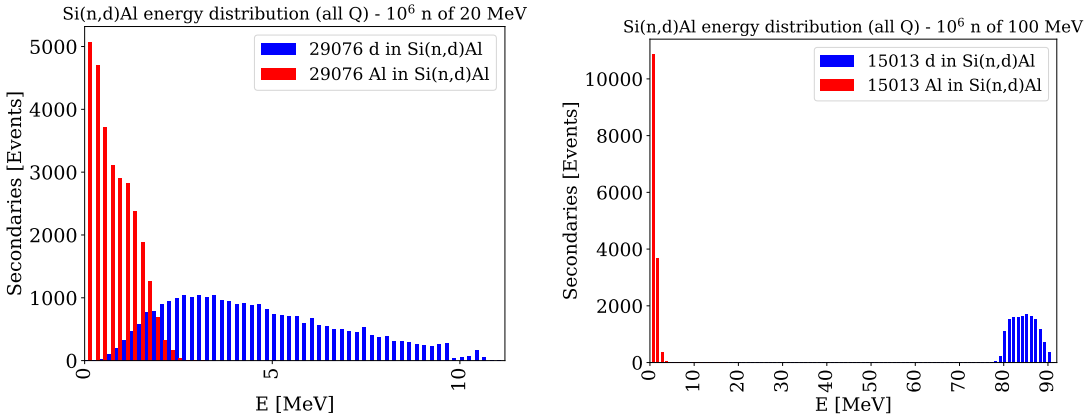

(a) **(b)**

Figure B.1: Energy distribution of $Si(n,d)Al$ secondaries, for incident energies of 20 and 100 MeV.

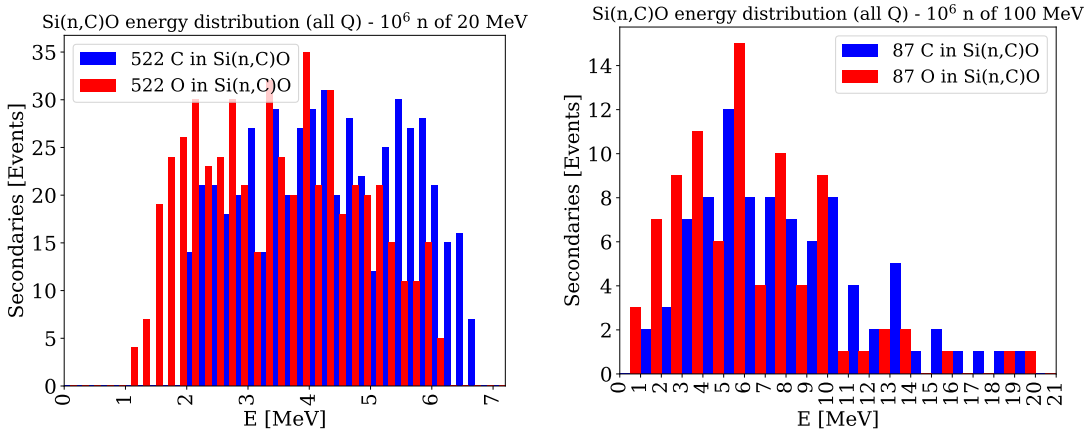

Figure B.2: Energy distribution of $Si(n,C)O$ secondaries, for incident energies of 20 and 100 MeV.

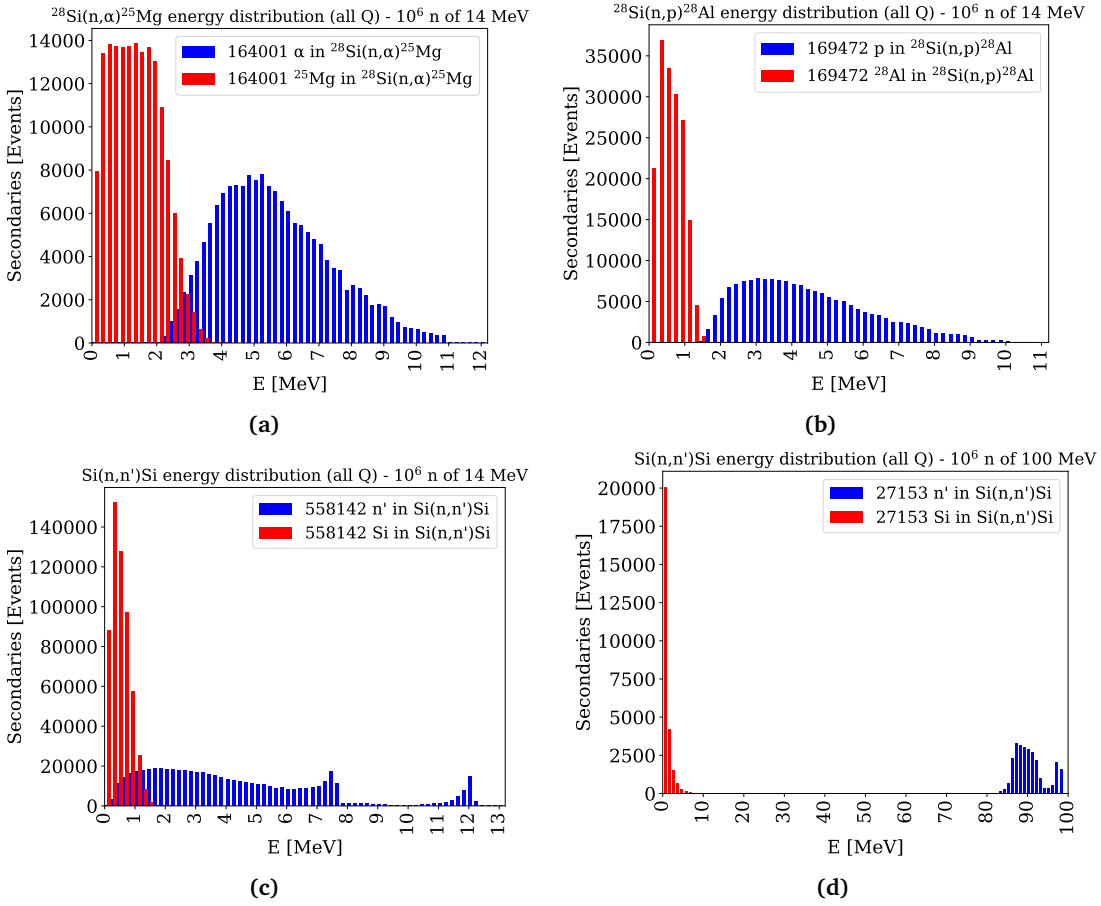

Figure B.3: Energy distribution of the main reactions for incident energies of 14 and 100 MeV, and $Si(n,n')Si$ secondaries at 100 MeV.

B.2 Energy Distributions of Secondaries at Several Incident Energies

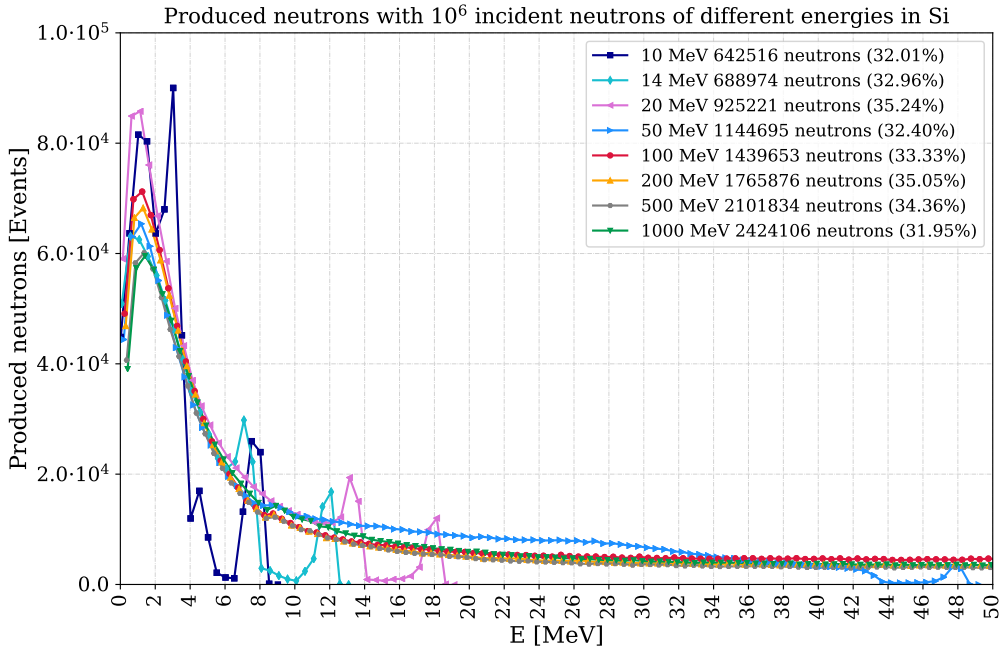

Figure B.4: Neutron energy distribution (spallation) in linear scale, with energy bins of 0.5 MeV.

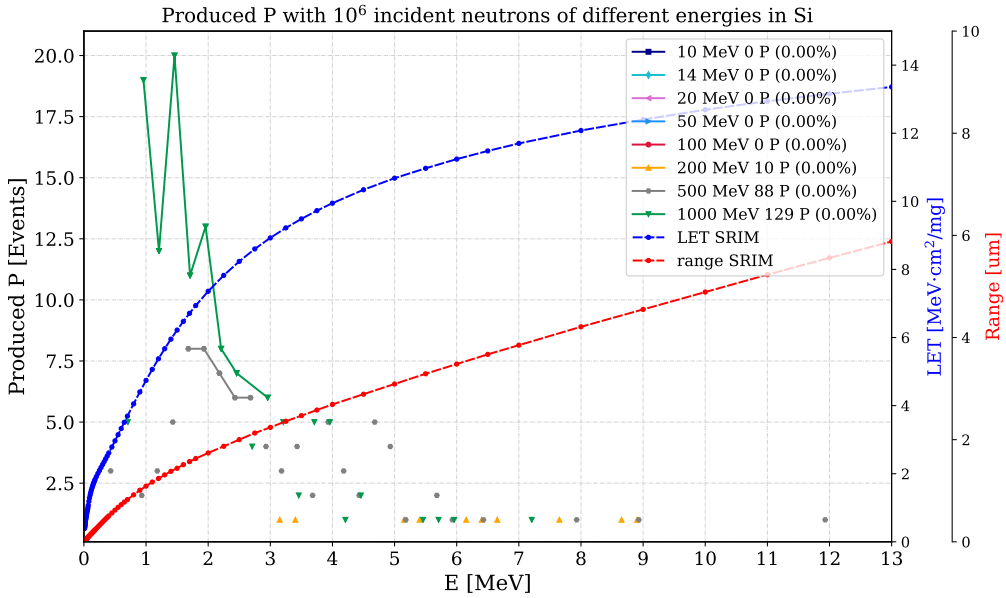

Figure B.5: Energy distribution of P ions in linear scale, with energy bins of 0.25 MeV.

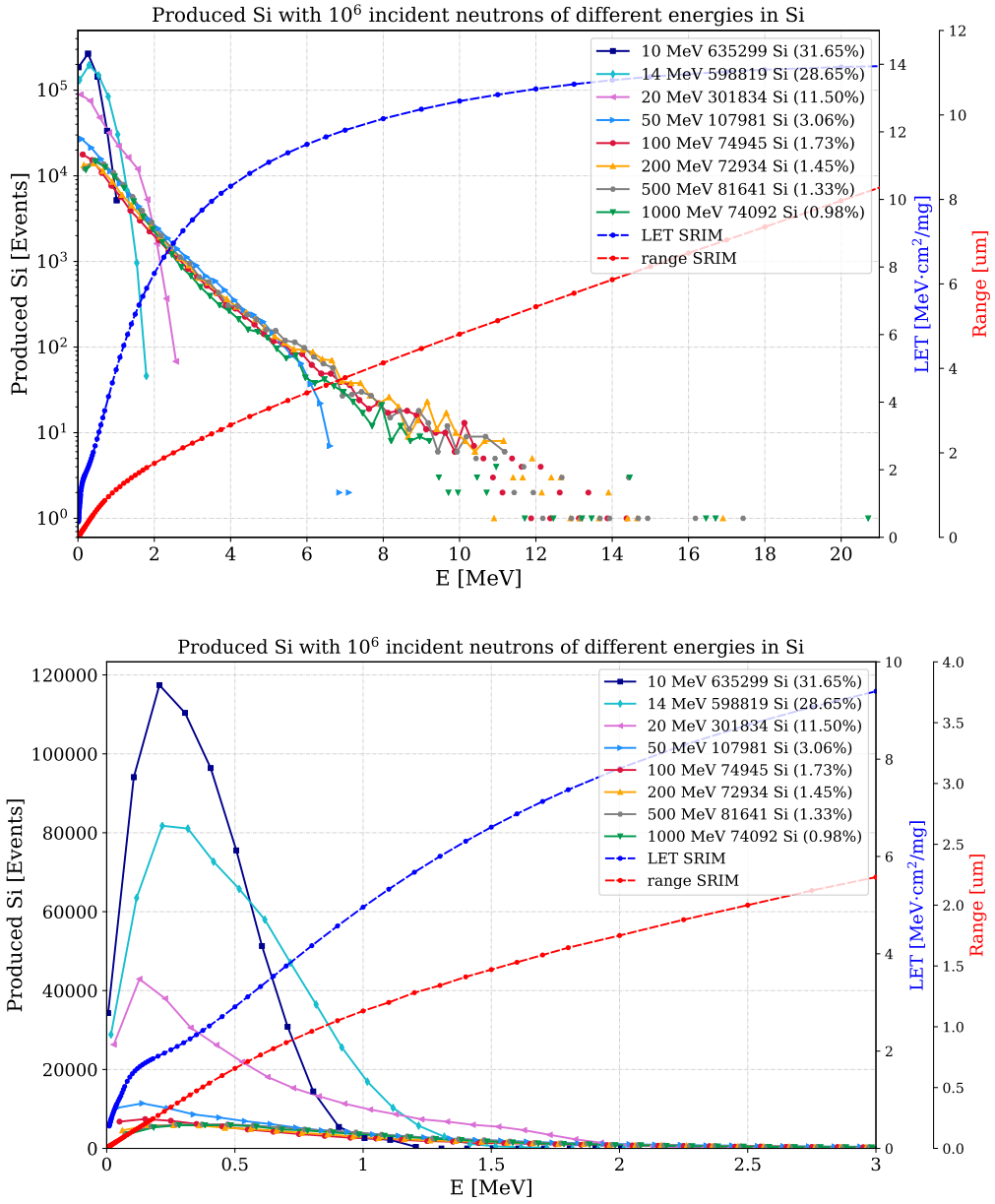

Figure B.6: Energy distribution of Si ions in log and linear scale, with energy bins of 0.25 and 0.1 MeV, respectively.

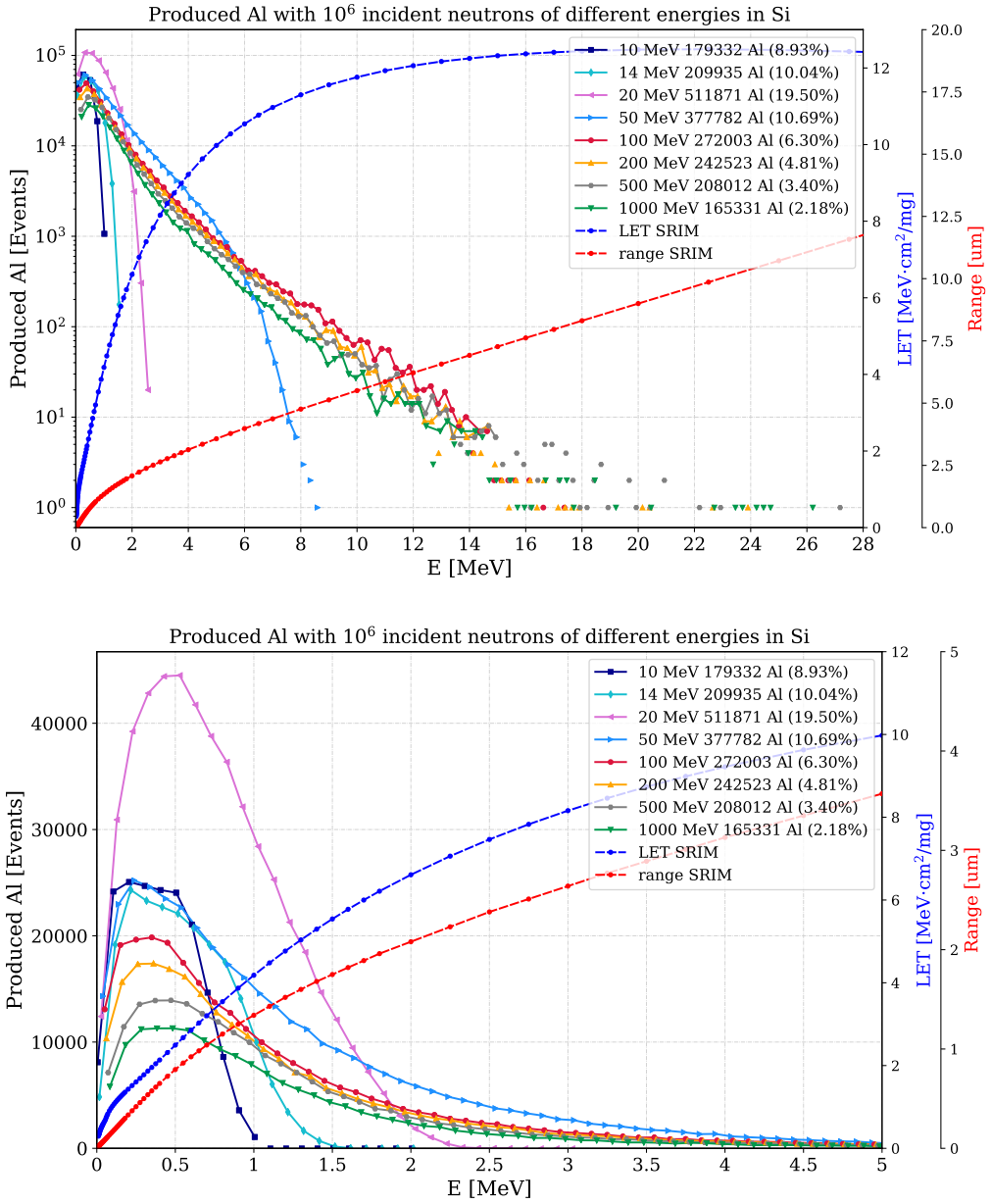

Figure B.7: Energy distribution of Al ions in log and linear scale, with energy bins of 0.25 and 0.1 MeV, respectively.

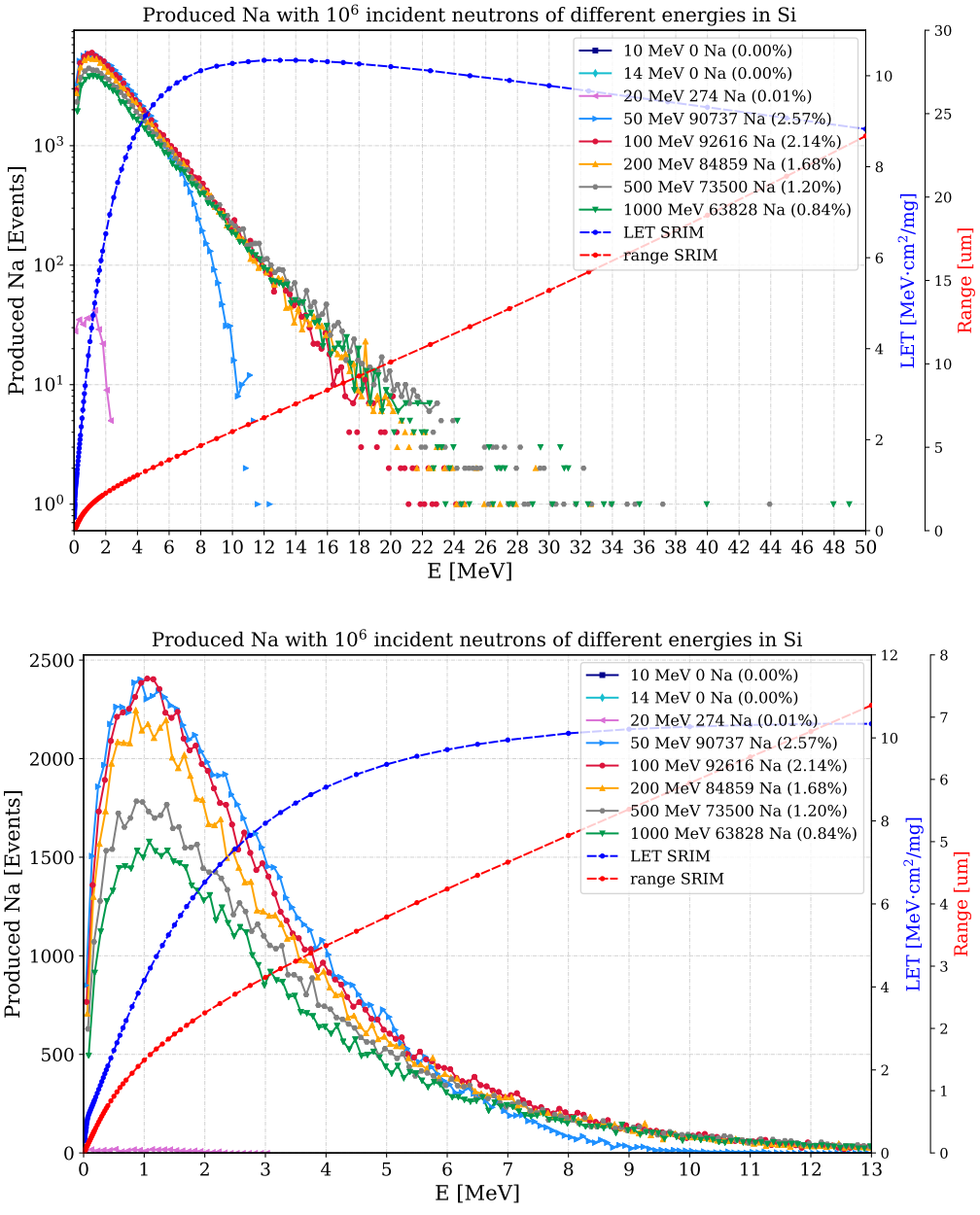

Figure B.8: Energy distribution of Na ions in log and linear scale, with energy bins of 0.25 and 0.1 MeV, respectively.

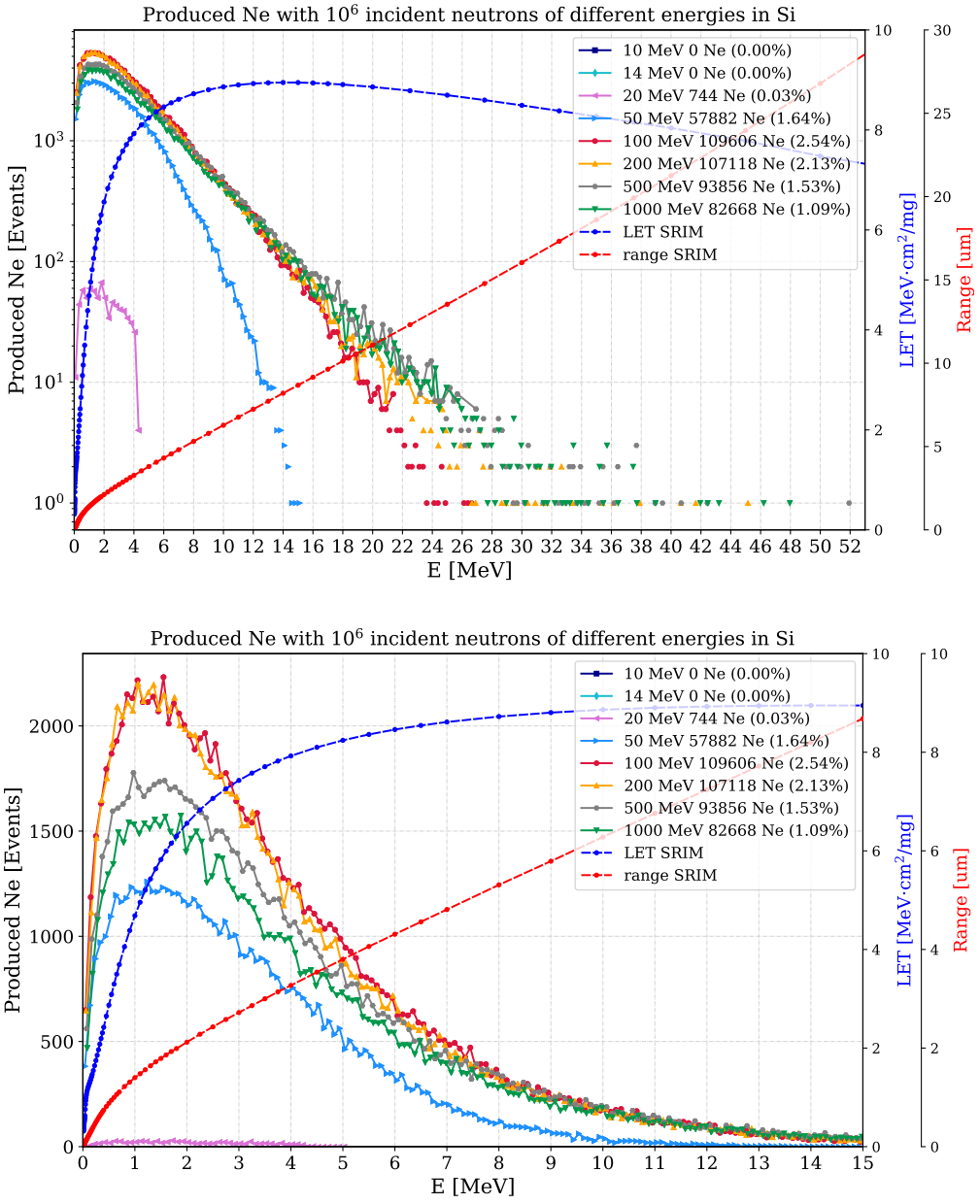

Figure B.9: Energy distribution of Ne ions in log and linear scale, with energy bins of 0.25 and 0.1 MeV, respectively.

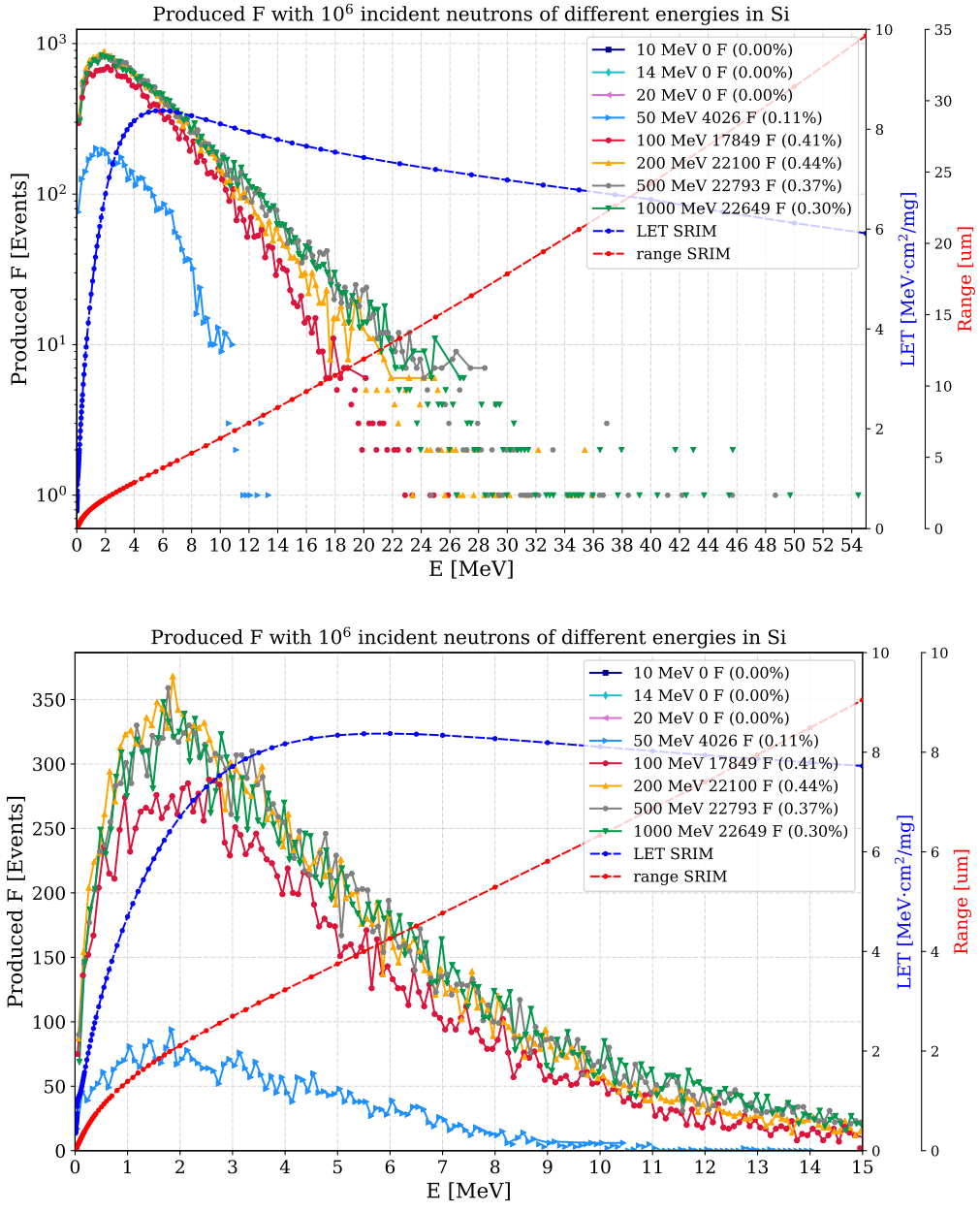

Figure B.10: Energy distribution of F ions in log and linear scale, with energy bins of 0.25 and 0.1 MeV, respectively.

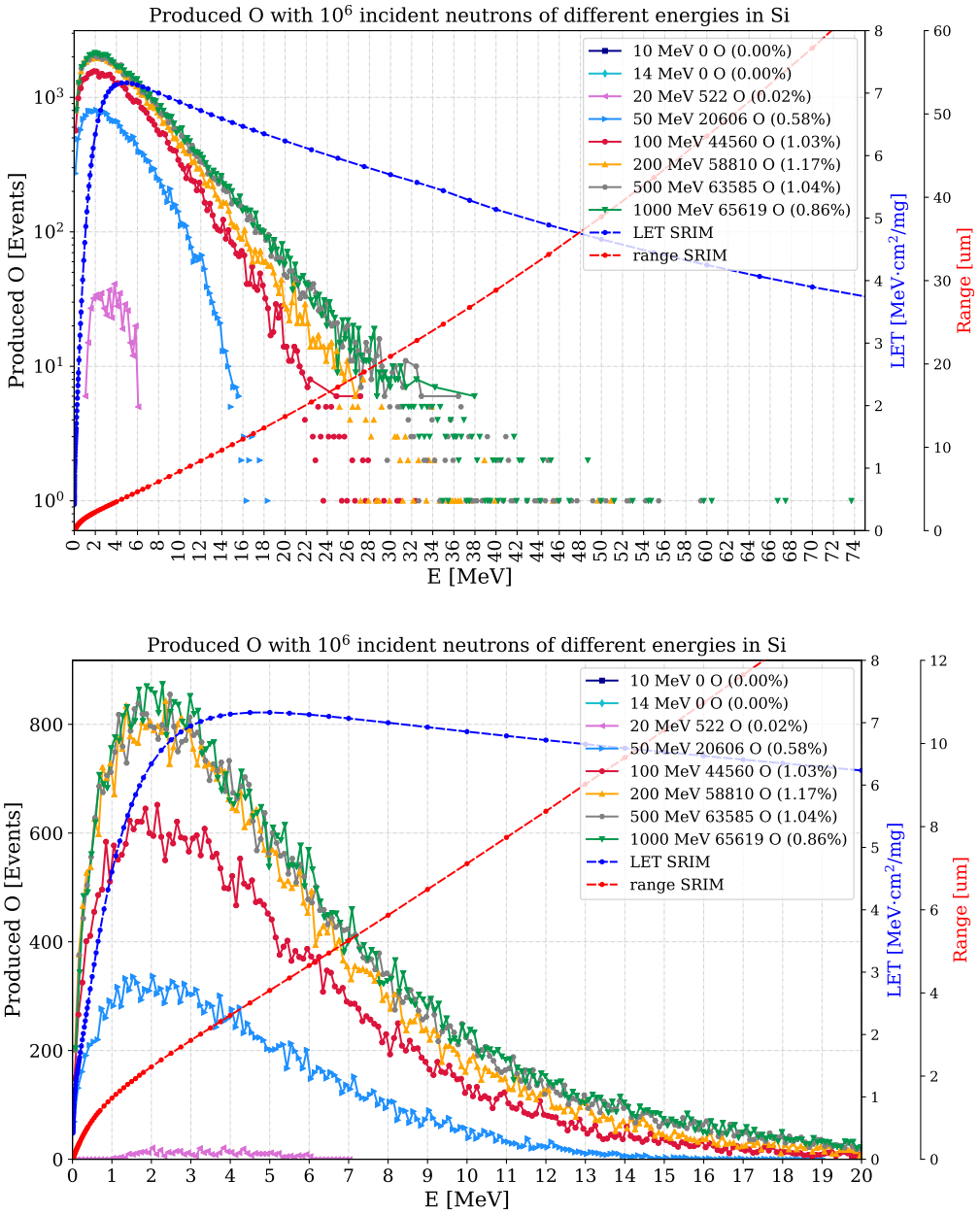

Figure B.11: Energy distribution of O ions in log and linear scale, with energy bins of 0.25 and 0.1 MeV, respectively.

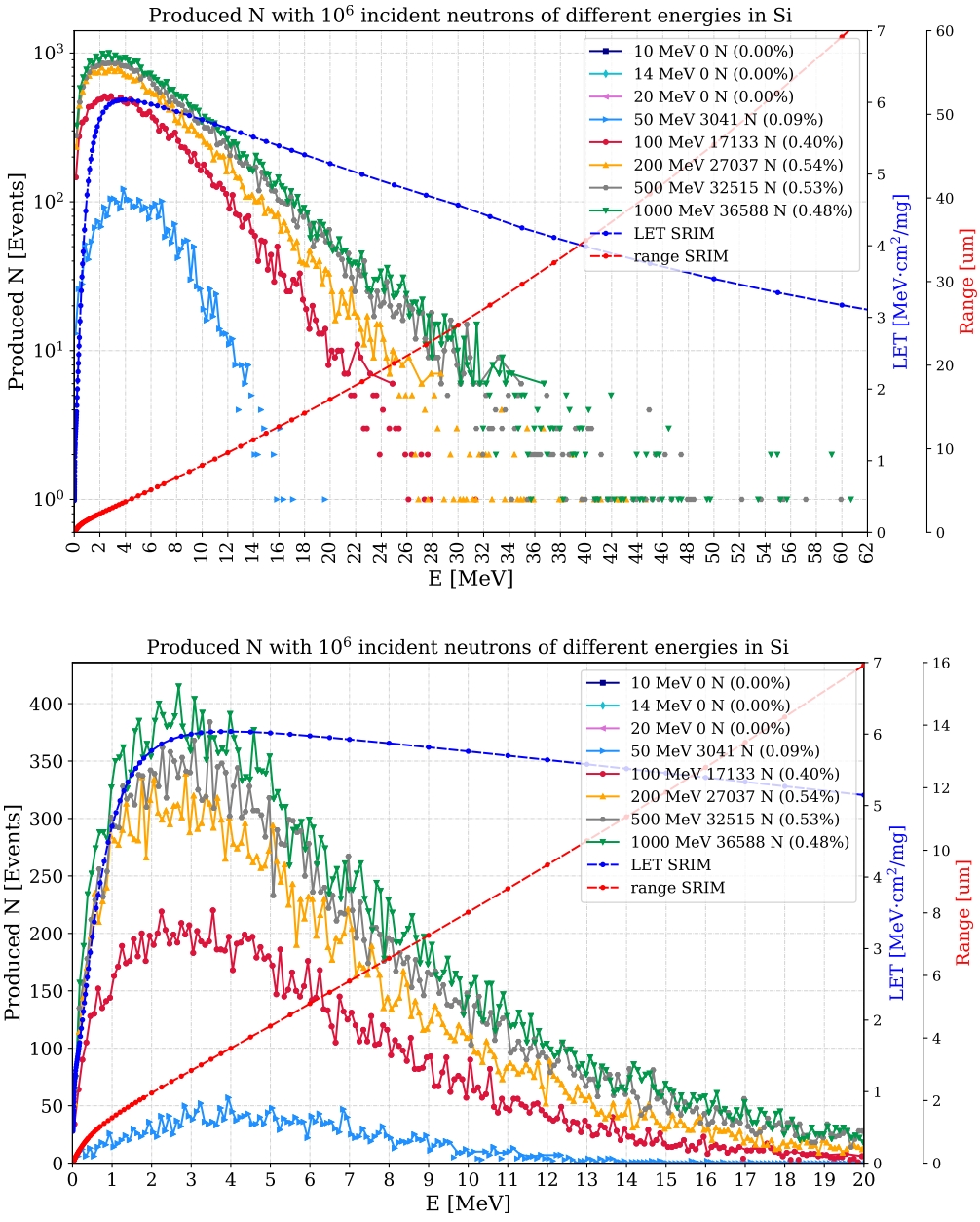

Figure B.12: Energy distribution of N ions in log and linear scale, with energy bins of 0.25 and 0.1 MeV, respectively.

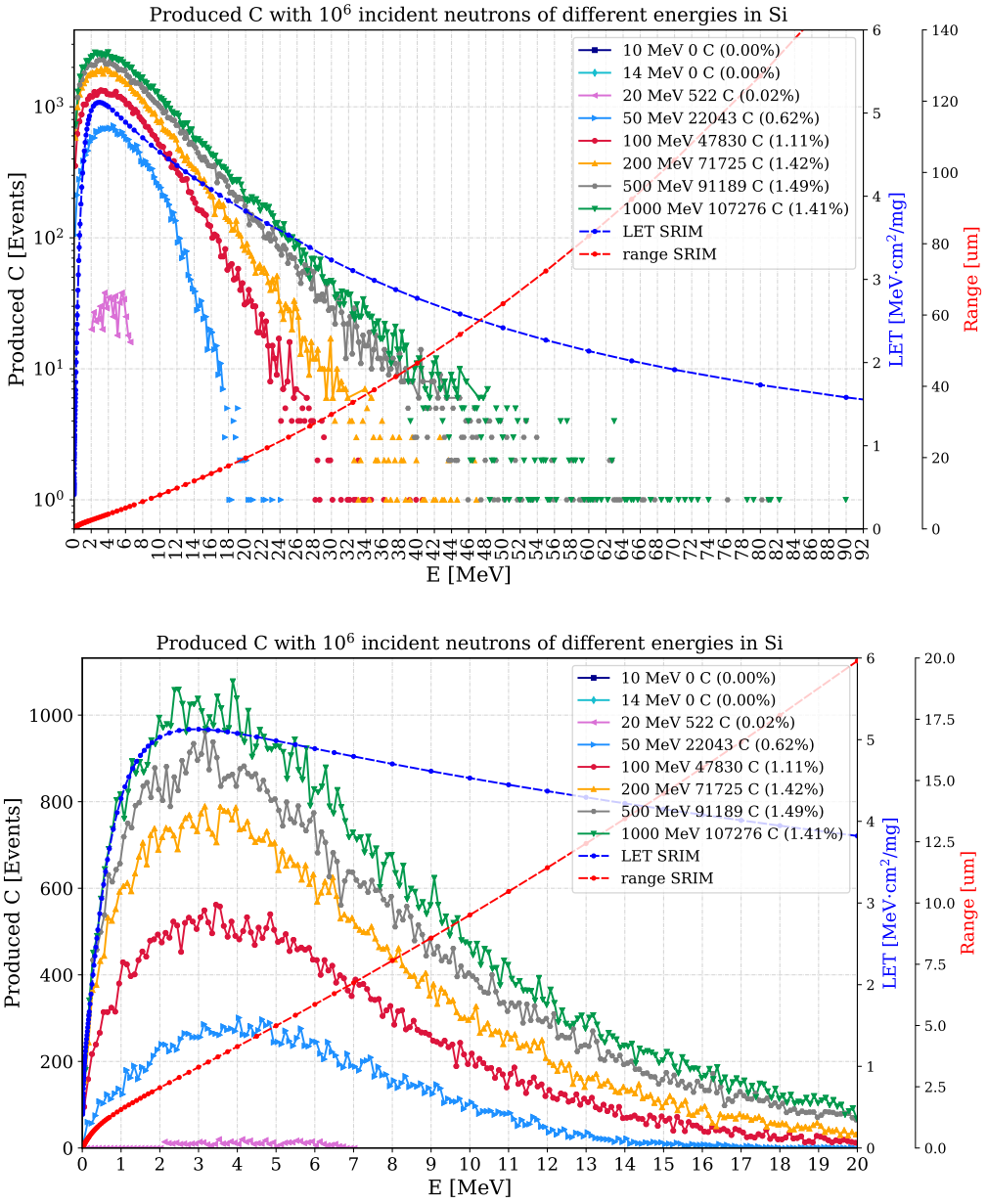

Figure B.13: Energy distribution of C ions in log and linear scale, with energy bins of 0.25 and 0.1 MeV, respectively.

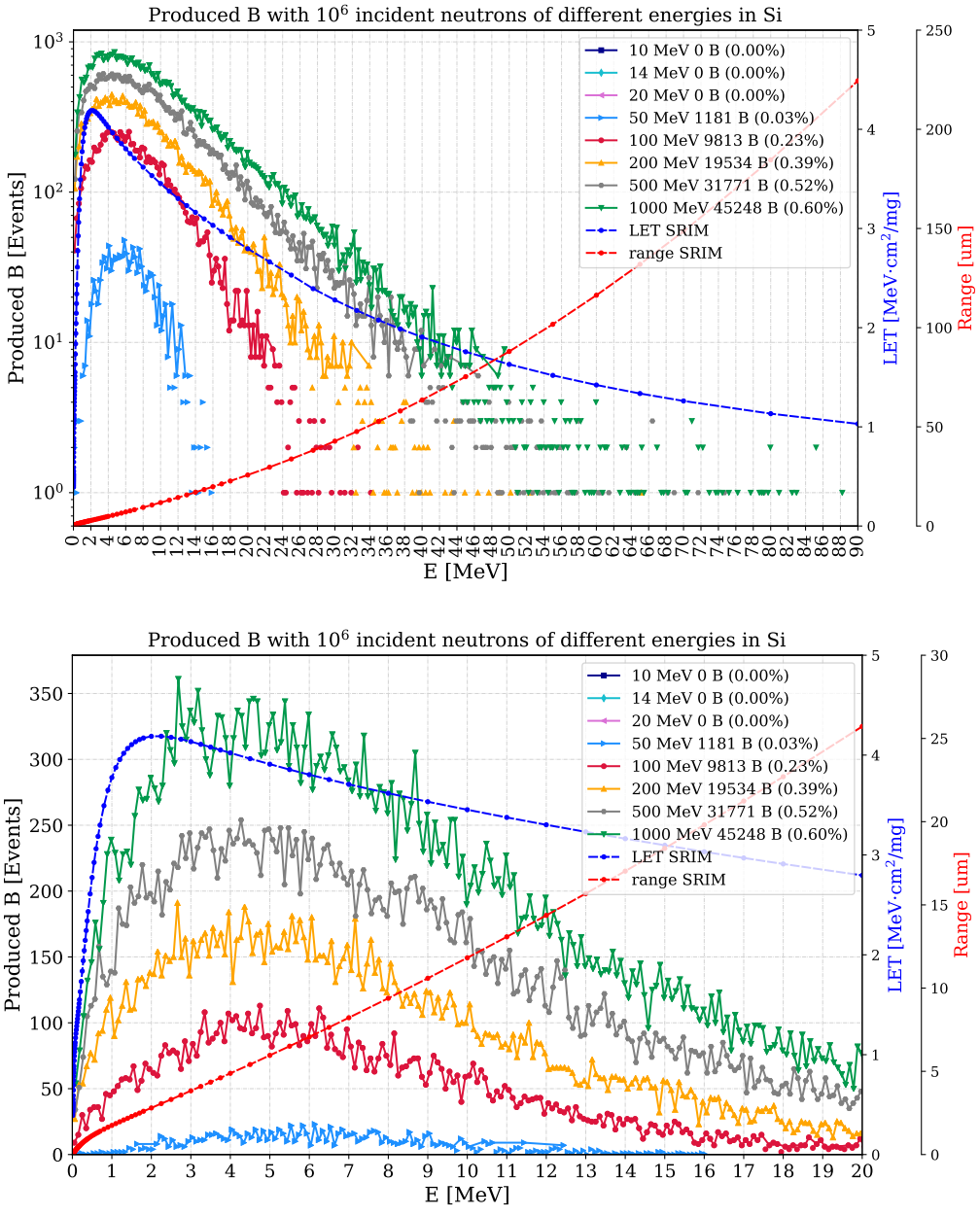

Figure B.14: Energy distribution of B ions in log and linear scale, with energy bins of 0.25 and 0.1 MeV, respectively.

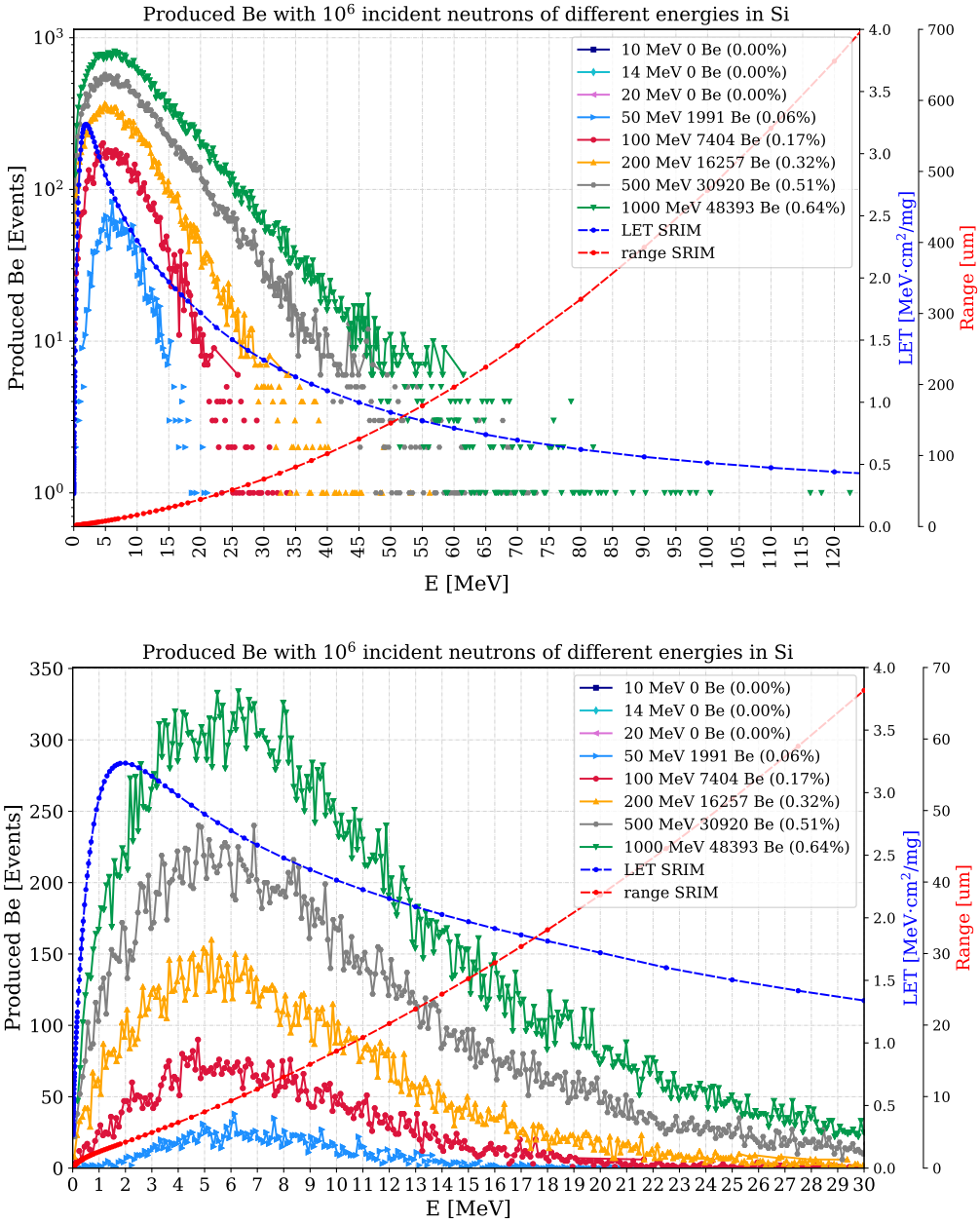

Figure B.15: Energy distribution of Be ions in log and linear scale, with energy bins of 0.25 and 0.1 MeV, respectively.

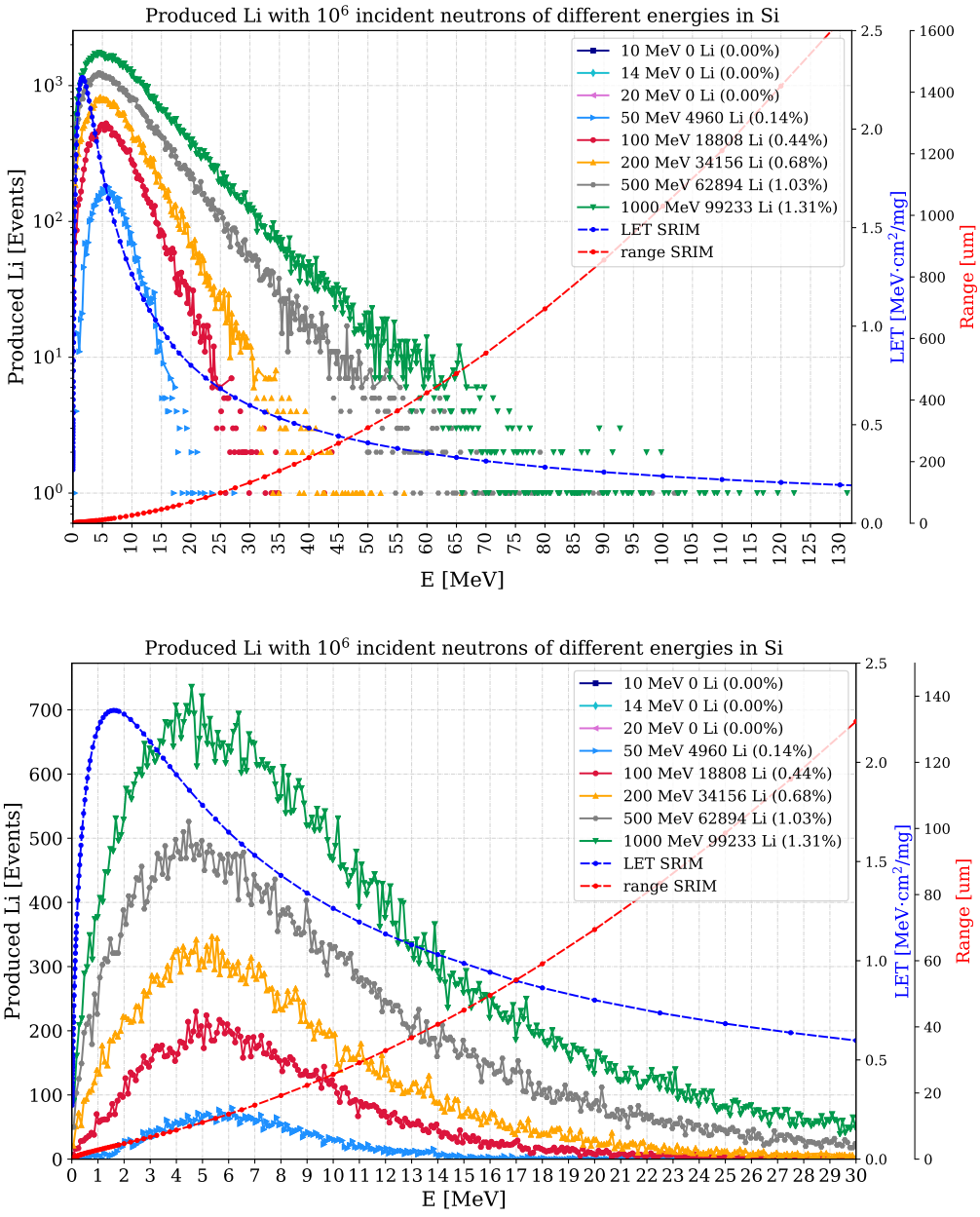

Figure B.16: Energy distribution of Li ions in log and linear scale, with energy bins of 0.25 and 0.1 MeV, respectively.

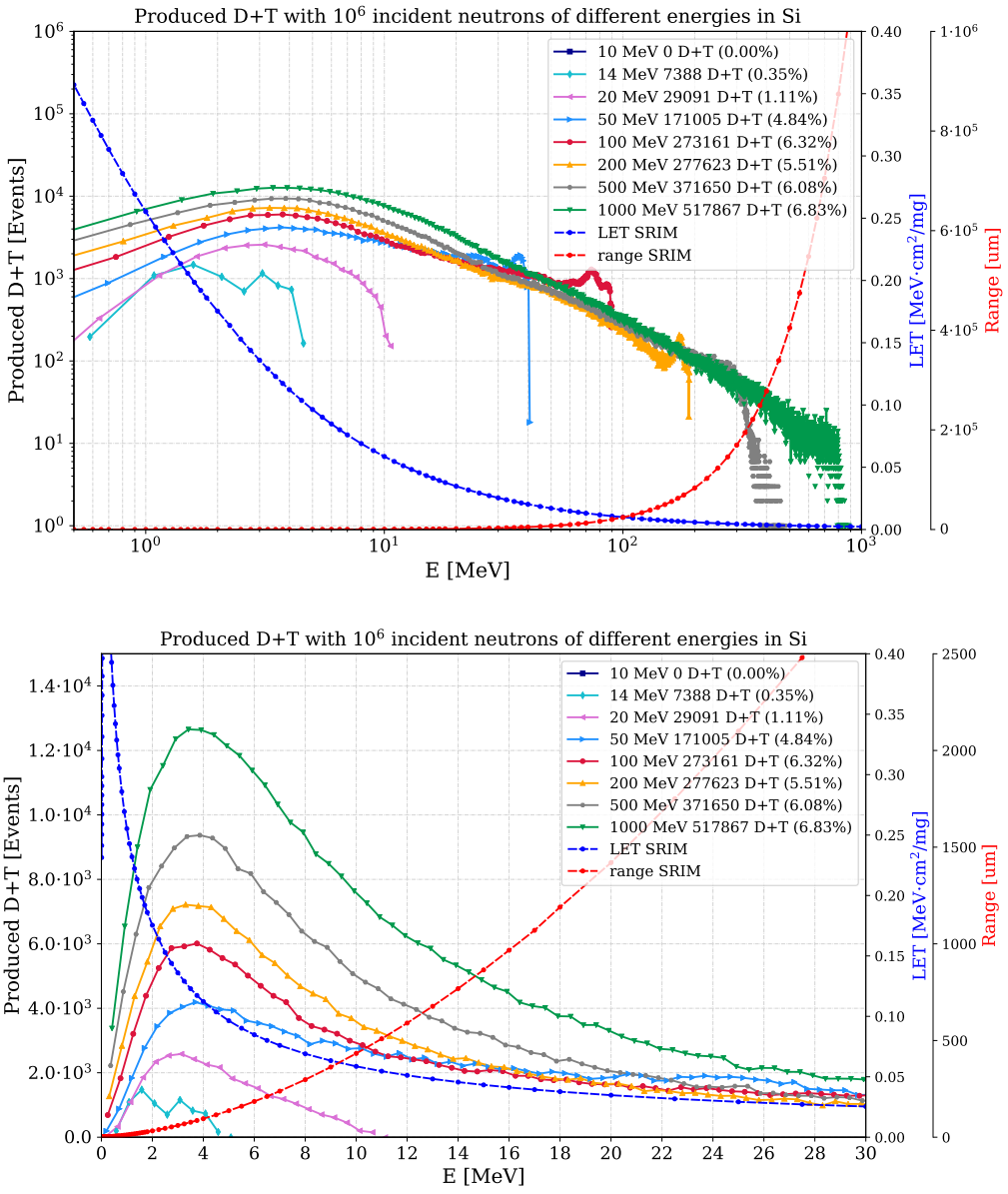

Figure B.17: Energy distribution of D+T ions in log and linear scale, with energy bins of 0.5 MeV. LET and range from SRIM are relative to deuteron.

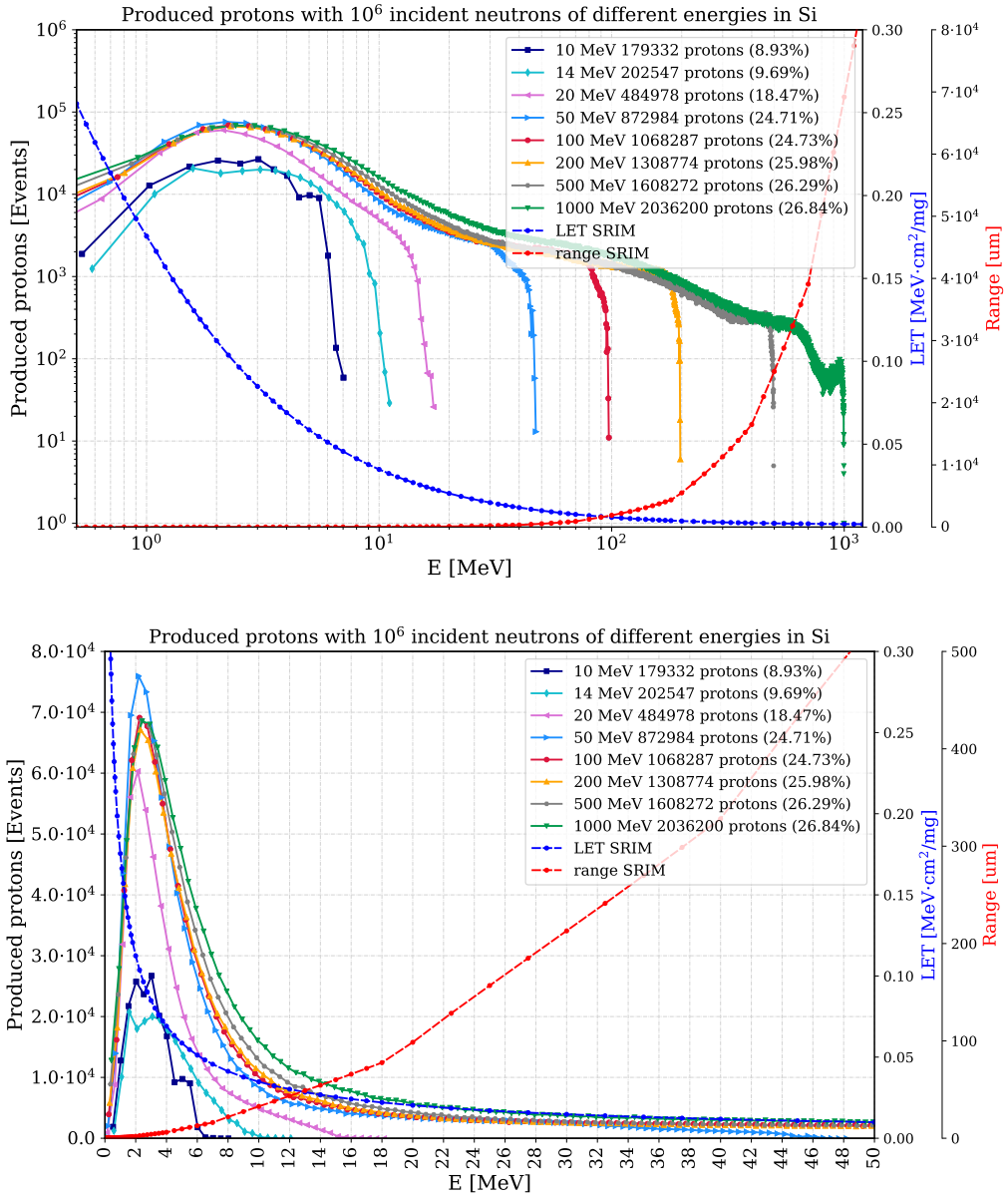

Figure B.18: Proton energy distribution in log and linear scale, with energy bins of 0.5 MeV.

B.3 LET and Energy of Secondary Ions

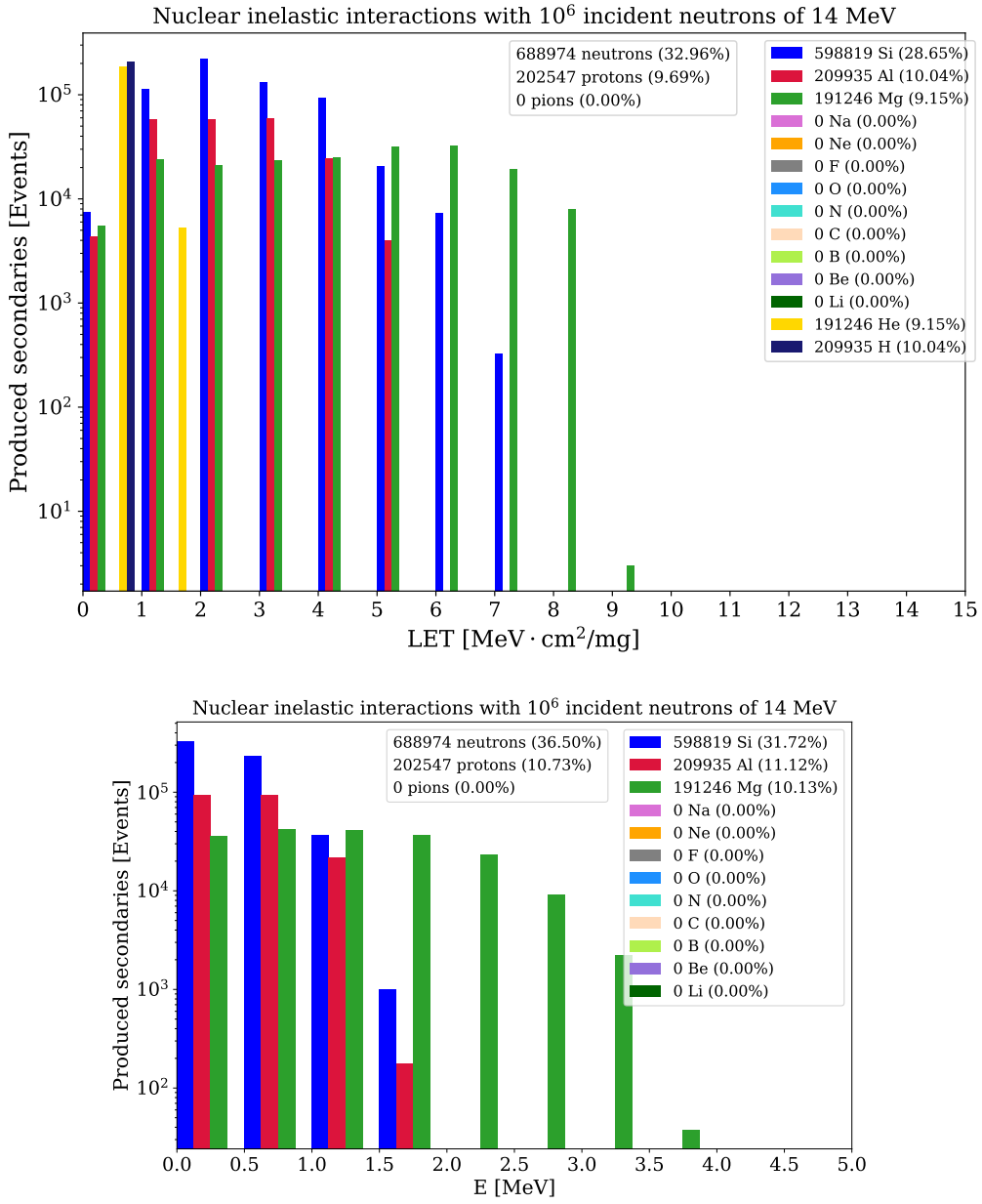

Figure B.19: LET and Energy of secondary ions produced in inelastic interactions of 14 MeV neutrons in Si.

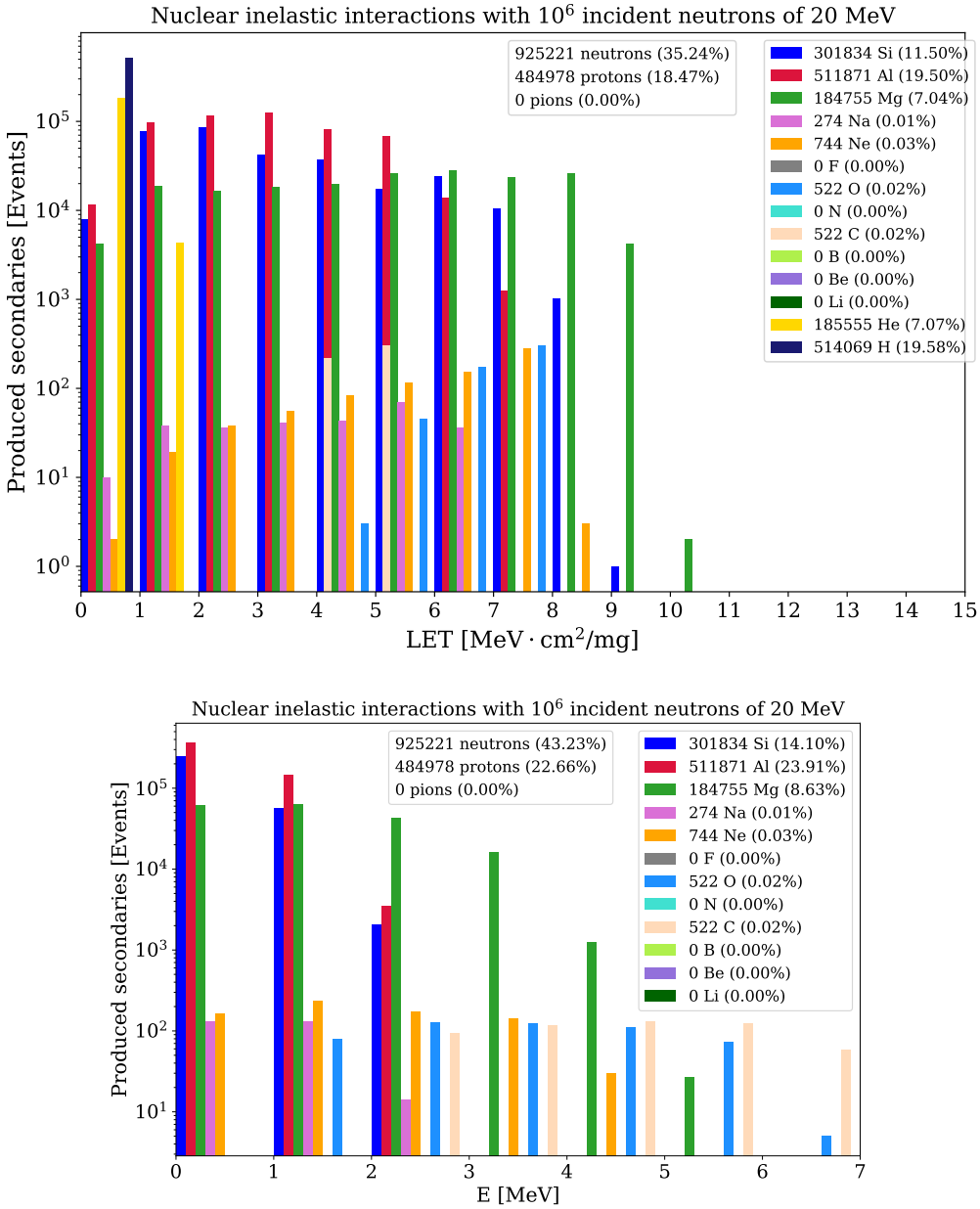

Figure B.20: LET and Energy of secondary ions produced in inelastic interactions of 20 MeV neutrons in Si.

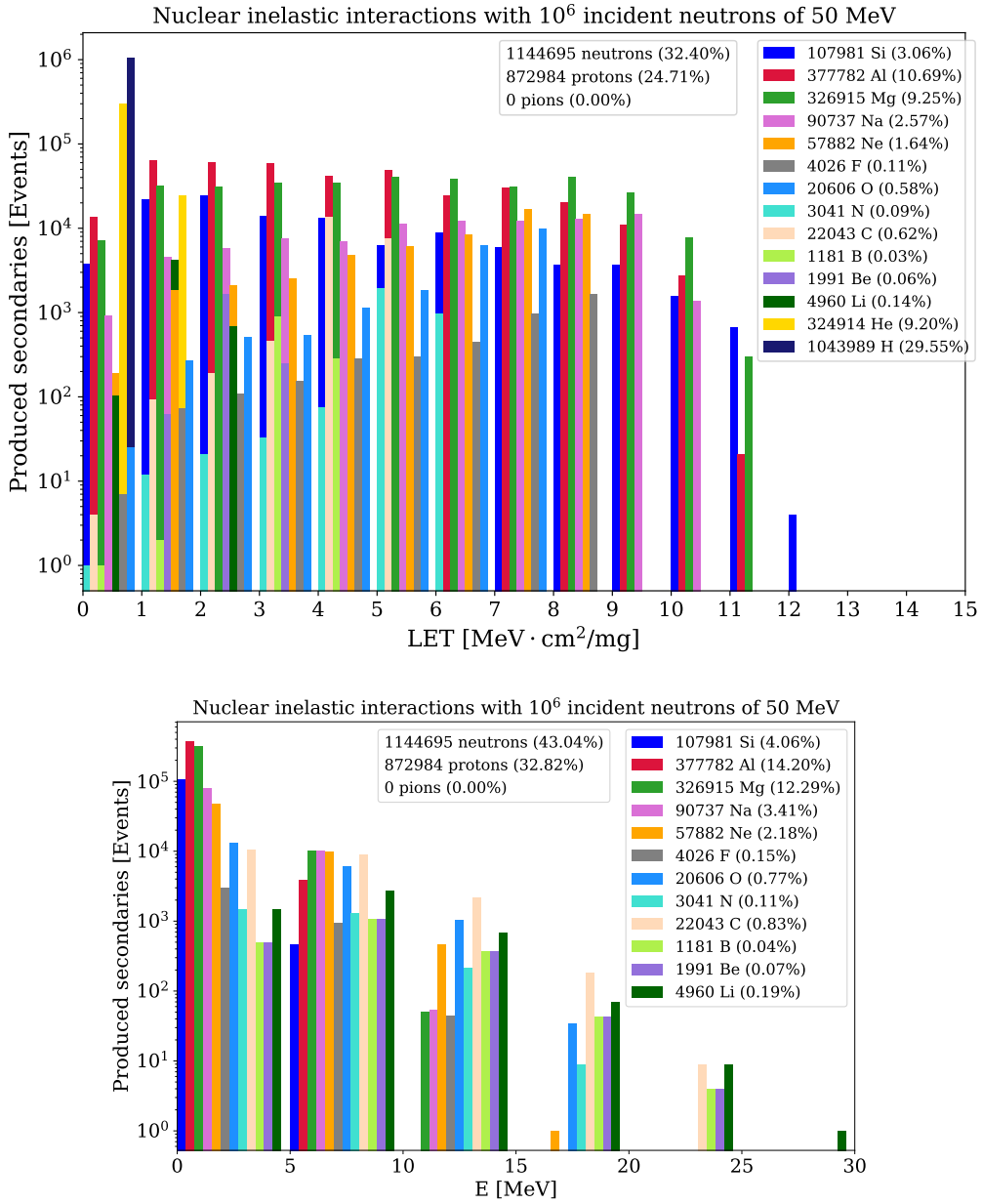

Figure B.21: LET and Energy of secondary ions produced in inelastic interactions of 50 MeV neutrons in Si.

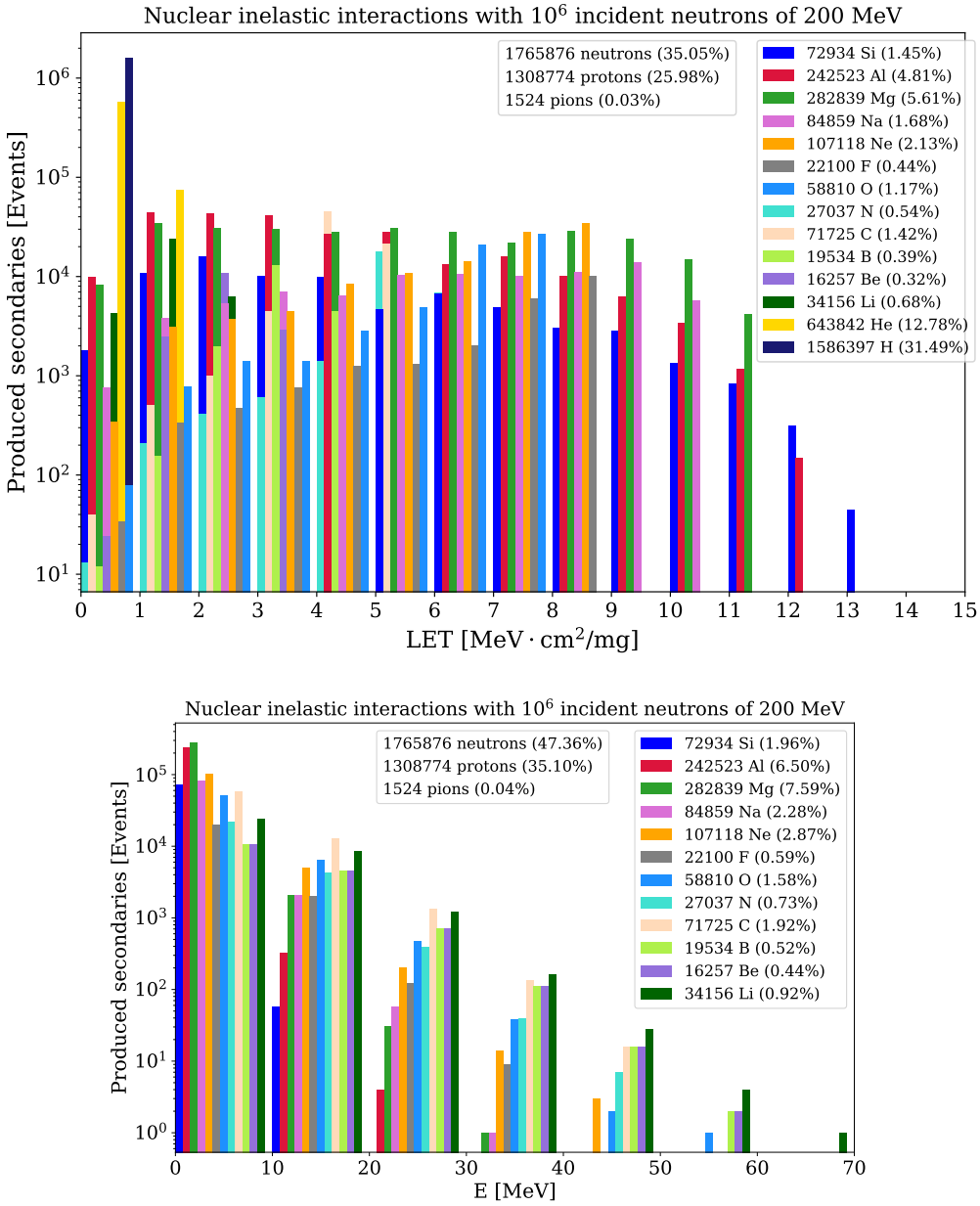

Figure B.22: LET and Energy of secondary ions produced in inelastic interactions of 200 MeV neutrons in Si.

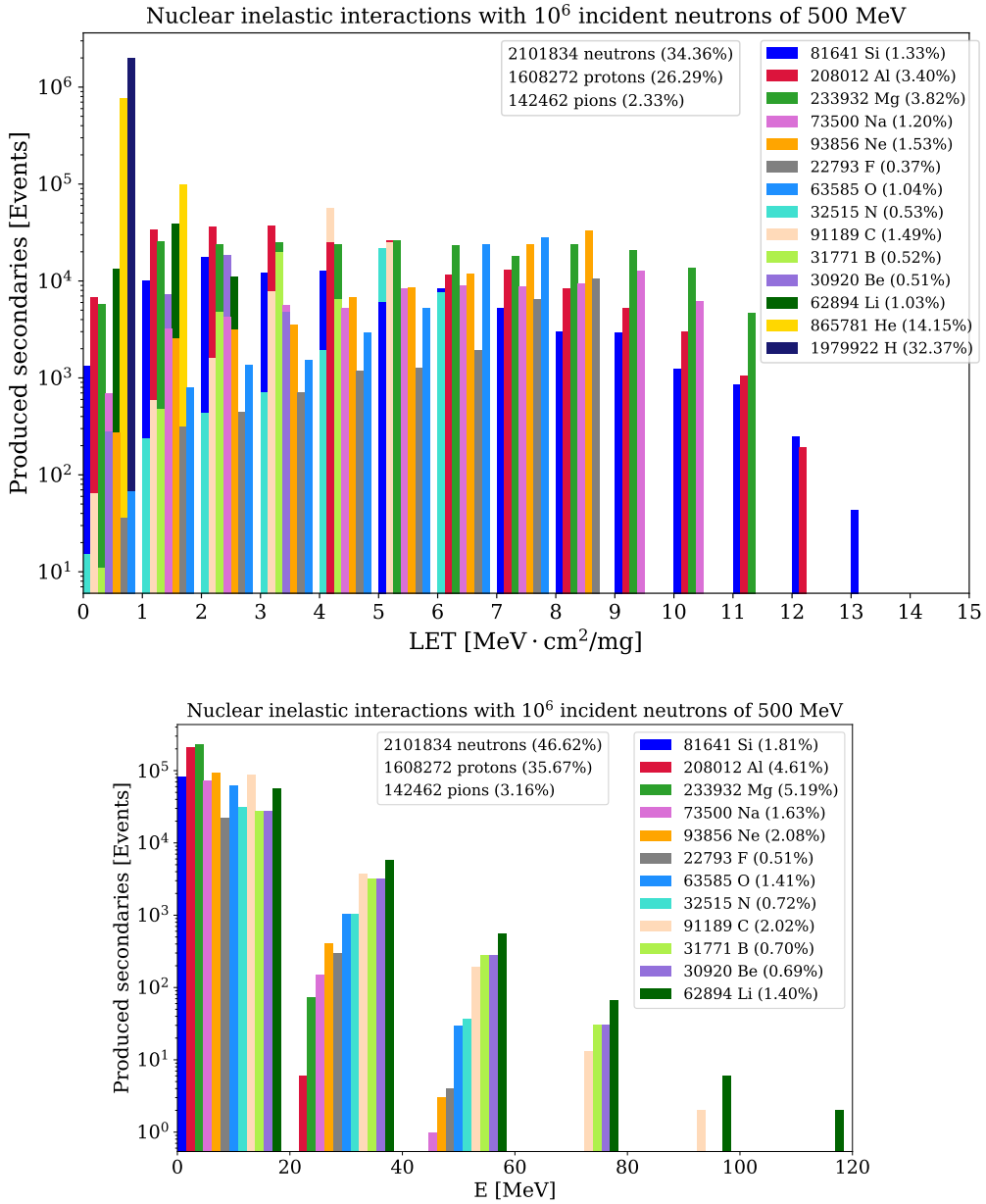

Figure B.23: LET and Energy of secondary ions produced in inelastic interactions of 500 MeV neutrons in Si.

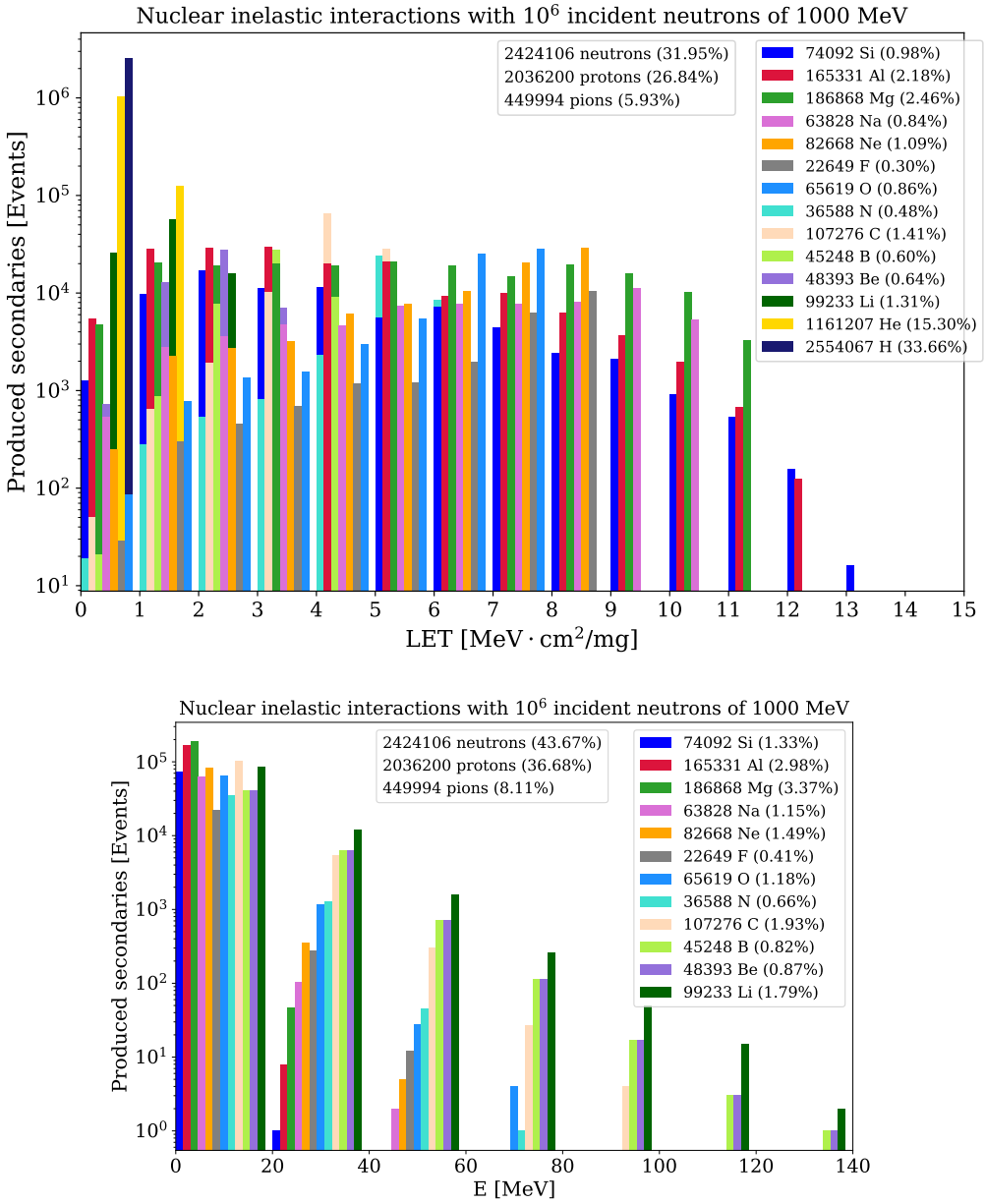

Figure B.24: LET and Energy of secondary ions produced in inelastic interactions of 1000 MeV neutrons in Si.

Appendix C

Experimental Cross Sections and Other Numerical Values

C.1 Poisson Distribution Tables

N	95% Limits lower	upper	N	95% Limits lower	upper	N	95% Limits lower	upper
0	0.0	3.7	17	9.9	27.2	34	23.5	47.5
1	0.1	5.6	18	10.7	28.4	35	24.3	48.7
2	0.2	7.2	19	11.5	29.6	36	25.1	49.8
3	0.6	8.8	20	12.2	30.8	37	26.0	51.0
4	1.0	10.2	21	13.0	32.0	38	26.8	52.2
5	1.6	11.7	22	13.8	33.2	39	27.7	53.3
6	2.2	13.1	23	14.6	34.4	40	28.6	54.5
7	2.8	14.4	24	15.4	35.6	41	29.4	55.6
8	3.4	15.8	25	16.2	36.8	42	30.3	56.8
9	4.0	17.1	26	17.0	38.0	43	31.1	57.9
10	4.7	18.4	27	17.8	39.2	44	32.0	59.0
11	5.4	19.7	28	18.6	40.4	45	32.8	60.2
12	6.2	21.0	29	19.4	41.6	46	33.6	61.3
13	6.9	22.3	30	20.2	42.8	47	34.5	62.5
14	7.7	23.5	31	21.0	44.0	48	35.3	63.6
15	8.4	24.8	32	21.8	45.1	49	36.1	64.8
16	9.4	26.0	33	22.7	46.3	50	37.0	65.9

Table C.1: Margin limits of the Poisson distribution with confidence level of 95%.

C.2 Tabulated SEU Cross Sections and Other Numerical Values

Table C.2: SEU cross sections measured at ChipIr at different incident neutron angles in position C. Tester memories were powered at 3.3 V. It is to be noted that both Cypress memories were tested delidded and with different date codes with respect to other test campaigns.

Device	Date Code	Incidence angle (deg)	σ_{SEU} [cm^2/bit]	$\pm 2\sigma$ (%)
ESA Mon. (2018)	1330	0	$2.28 \cdot 10^{-14}$	11.7
ESA Mon. (2019)	1817	0	$2.10 \cdot 10^{-14}$	10.4
ISSI 40 nm	1650	0	$9.69 \cdot 10^{-15}$	10.4
		30	$1.19 \cdot 10^{-14}$	11.8
		60	$1.38 \cdot 10^{-14}$	11.8
		90	$1.24 \cdot 10^{-14}$	12.3
Cypress 90 nm 8 Mbit delid	1437	0	$5.73 \cdot 10^{-14}$	11.0
		15	$5.48 \cdot 10^{-14}$	11.4
		30	$6.28 \cdot 10^{-14}$	12.0
		60	$6.25 \cdot 10^{-14}$	11.1
		90	$7.49 \cdot 10^{-14}$	11.3
Cypress 90 nm 16 Mbit delid	1525	0	$3.95 \cdot 10^{-14}$	10.2
		30	$4.39 \cdot 10^{-14}$	11.0
		60	$5.12 \cdot 10^{-14}$	11.4
		75	$3.71 \cdot 10^{-14}$	11.6
		90	$3.33 \cdot 10^{-14}$	11.7

Table C.3: Thermal neutron cross sections measured at ILL and test conditions for ISSI 40 nm, Cypress 65 nm and 90 nm (8 Mbit and 16 Mbit). The flux was 10^9 n/cm^2/s. *test performed with 0.5 mm thickness boron carbide placed between the memory and the beam. The tester results with nominal voltage are highlighter in bold.

Memory	Vm [V]	Fluence [n/cm^2]	SEU	MBU	σ_{SEU} [cm^2/bit]	$\pm 1\sigma$ (%)
ESA Monitor (2019)	3.3	$2.7{\cdot}10^{11}$	15354	-	$3.36{\cdot}10^{-15}$	11.8
ESA Monitor (2017)	3.3	$2.5{\cdot}10^{10}$	1392	-	$4.51{\cdot}10^{-15}$	29.0
ISSI 40	0.73	$3.0{\cdot}10^{9}$	1630	0	$1.62{\cdot}10^{-14}$	12.0
	0.83	$3.0{\cdot}10^{9}$	796	0	$7.91{\cdot}10^{-15}$	12.3
	0.92	$2.0{\cdot}10^{9}$	405	0	$6.03{\cdot}10^{-15}$	12.8
	1.02	$2.0{\cdot}10^{9}$	347	0	$5.17{\cdot}10^{-15}$	12.9
	1.11	$2.0{\cdot}10^{9}$	353	0	$5.26{\cdot}10^{-15}$	12.9
	1.20	$2.0{\cdot}10^{9}$	337	0	$5.02{\cdot}10^{-15}$	13.0
	1.29	$2.0{\cdot}10^{9}$	306	0	$4.56{\cdot}10^{-15}$	13.1
	1.39	$2.0{\cdot}10^{9}$	330	0	$4.92{\cdot}10^{-15}$	13.0
	1.48	$2.0{\cdot}10^{9}$	313	0	$4.66{\cdot}10^{-15}$	13.0
	1.57	$2.0{\cdot}10^{9}$	395	0	$5.89{\cdot}10^{-15}$	12.8
	1.66	$5.0{\cdot}10^{9}$	805	0	$4.80{\cdot}10^{-15}$	12.3
	1.76	$5.0{\cdot}10^{9}$	752	0	$4.48{\cdot}10^{-15}$	12.3
	1.85	$2.0{\cdot}10^{9}$	295	0	$4.40{\cdot}10^{-15}$	13.1
	1.94	$4.0{\cdot}10^{9}$	505	0	$3.76{\cdot}10^{-15}$	12.6
	2.03	$4.0{\cdot}10^{9}$	532	0	$3.96{\cdot}10^{-15}$	12.5
	2.12	$4.0{\cdot}10^{9}$	500	0	$3.73{\cdot}10^{-15}$	12.6
	2.22	$4.0{\cdot}10^{9}$	510	0	$3.80{\cdot}10^{-15}$	12.6
	2.41	$4.0{\cdot}10^{9}$	565	0	$4.21{\cdot}10^{-15}$	12.5
	2.60	$4.0{\cdot}10^{9}$	570	0	$4.25{\cdot}10^{-15}$	12.5
	2.80	$4.0{\cdot}10^{9}$	514	0	$3.83{\cdot}10^{-15}$	12.6
	2.99	$4.0{\cdot}10^{9}$	522	0	$3.89{\cdot}10^{-15}$	12.5
	3.30	$\mathbf{3.0{\cdot}10^{11}}$	**31766**	**2**	$\mathbf{3.16{\cdot}10^{-15}}$	**11.8**
	3.59	$4.0{\cdot}10^{9}$	551	0	$4.11{\cdot}10^{-15}$	12.5
Cypress 65	**3.30**	$\mathbf{2.2{\cdot}10^{11}}$	**1827**	**0**	$\mathbf{4.91{\cdot}10^{-16}}$	**12.0**
Cypress 90 nm 16 Mbit	2.20	$1.7{\cdot}10^{11}$	1045	0	$3.75{\cdot}10^{-16}$	12.2
	2.20	$8.8{\cdot}10^{10}$	0*	0*	*	*
	3.30	$\mathbf{1.5{\cdot}10^{11}}$	**983**	**1**	$\mathbf{3.88{\cdot}10^{-16}}$	**12.2**
Cypress 90 nm 8 Mbit	1.55	$6.0{\cdot}10^{10}$	325	0	$6.46{\cdot}10^{-16}$	13.0
	1.60	$1.2{\cdot}10^{11}$	638	0	$6.34{\cdot}10^{-16}$	12.4
	1.65	$6.0{\cdot}10^{10}$	271	0	$5.38{\cdot}10^{-16}$	13.2
	1.70	$6.0{\cdot}10^{10}$	310	0	$6.16{\cdot}10^{-16}$	13.1
	3.30	$\mathbf{2.6{\cdot}10^{11}}$	**1274**	**0**	$\mathbf{5.80{\cdot}10^{-16}}$	**12.1**

Table C.4: 18.6 MeV memory cross sections with package and delidded, tested at the TOP-IMPLART LINAC. The cross sections with package resulted higher than those delidded are highlighted in bold.

Device	E [MeV]	Φ [n/cm^2]	SEU	σ_{SEU} [cm^2/bit]	$\pm 2\sigma$ (%)
ESA Monitor with lid	18.6	$4.39 \cdot 10^{9}$	21	$2.85 \cdot 10^{-16}$	$^{+54}_{-39}$
ESA Monitor no lid	18.6	$2.69 \cdot 10^{10}$	11616	$2.58 \cdot 10^{-14}$	10.2
ISSI 40 nm	18.6	$3.52 \cdot 10^{9}$	1415	$1.20 \cdot 10^{-14}$	11.3
ISSI 40 nm delid	18.6	$5.74 \cdot 10^{9}$	2285	$1.19 \cdot 10^{-14}$	10.8
Cypress 65 nm	18.6	$1.40 \cdot 10^{10}$	389	$1.66 \cdot 10^{-15}$	14.2
Cypress 65 nm delid	18.6	$1.05 \cdot 10^{10}$	553	$3.14 \cdot 10^{-15}$	13.1
Cypress 90 nm 8 Mbit	18.6	$3.50 \cdot 10^{9}$	2601	$\mathbf{8.85} \cdot 10^{-14}$	10.7
Cypress 90 nm 8 Mbit delid	18.6	$3.50 \cdot 10^{9}$	1271	$\mathbf{4.33} \cdot 10^{-14}$	11.5
Cypress 90 nm 16 Mbit	18.6	$3.50 \cdot 10^{9}$	2526	$4.30 \cdot 10^{-14}$	10.8
Cypress 90 nm 16 Mbit delid	18.6	$3.50 \cdot 10^{9}$	5849	$9.95 \cdot 10^{-14}$	10.3

Table C.5: 29 MeV memory cross sections with package and delidded, tested at the TOP-IMPLART LINAC. The cross sections with package resulted higher than those delidded are highlighted in bold.

Device	E [MeV]	Φ [n/cm^2]	SEU	σ_{SEU} [cm^2/bit]	$\pm 2\sigma$ (%)
ESA Monitor with lid	29	$5.36 \cdot 10^{9}$	2090	$2.32 \cdot 10^{-14}$	10.9
ESA Monitor no lid	29	$2.32 \cdot 10^{10}$	10895	$2.80 \cdot 10^{-14}$	10.2
ISSI 40 nm	29	$3.43 \cdot 10^{9}$	2225	$\mathbf{1.93} \cdot 10^{-14}$	11.0
ISSI 40 nm delid	29	$3.42 \cdot 10^{9}$	1829	$\mathbf{1.60} \cdot 10^{-14}$	10.9
Cypress 65 nm	29	$9.80 \cdot 10^{9}$	1182	$\mathbf{7.19} \cdot 10^{-15}$	10.4
Cypress 65 nm delid	29	$8.42 \cdot 10^{9}$	723	$\mathbf{5.12} \cdot 10^{-15}$	10.6
Cypress 90 nm 8 Mbit	29	$3.41 \cdot 10^{9}$	3394	$\mathbf{1.19} \cdot 10^{-13}$	10.2
Cypress 90 nm 8 Mbit delid	29	$9.87 \cdot 10^{9}$	4772	$\mathbf{5.77} \cdot 10^{-14}$	10.3
Cypress 90 nm 16 Mbit	29	$6.76 \cdot 10^{9}$	5755	$5.07 \cdot 10^{-14}$	12.5
Cypress 90 nm 16 Mbit delid	29	$6.70 \cdot 10^{9}$	8357	$7.44 \cdot 10^{-14}$	11.6

Table C.6: SRAM cross sections measured at 5 cm from the AmBe neutron source, calculated considering the HEHeq flux from the Toshiba reference implemented in FLUKA, and the actual response of each memory. Memories tested with package and delidded (ISSI with package was at 5.6 cm from the source) and their cross section ratio.

Device	SEU	$\sigma_{SEU}^{HEHeq-Toshiba}$ [cm^2/bit]	$\sigma_{SEU}^{HEHeq-Memory}$ [cm^2/bit]	$\pm 2\sigma$ (%)	$\frac{\sigma_{SEU}^{pack}}{\sigma_{SEU}^{del}}$
ISSI 40 nm	2150	$2.88 \cdot 10^{-14}$	$1.33 \cdot 10^{-14}$	10.89	0.97
ISSI 40 nm delid	2697	$2.97 \cdot 10^{-14}$	$1.36 \cdot 10^{-14}$	10.72	
Cypress 65 nm	5685	$1.25 \cdot 10^{-13}$	$5.01 \cdot 10^{-14}$	10.35	1.05
Cypress 65 nm delid	4364	$1.20 \cdot 10^{-13}$	$4.79 \cdot 10^{-14}$	10.45	
Cypress 90 nm 8 Mbit	1049	$4.63 \cdot 10^{-14}$	$1.64 \cdot 10^{-13}$	11.75	1.00
Cypress 90 nm 8 Mbit delid	845	$4.63 \cdot 10^{-14}$	$1.64 \cdot 10^{-13}$	12.14	
Cypress 90 nm 16	1859	$5.09 \cdot 10^{-14}$	-	11.02	0.98
Cypress 90 nm 16 delid	1901	$5.21 \cdot 10^{-14}$	-	11.00	

Table C.7: 14.8 MeV neutron SEU cross sections measured at FNG for the RADSAGA v1 SRAM with standard (1), low (2) and high (3) voltage threshold.

V_{PS} [V]	Φ [n/cm^2]	SEU_1	σ_{SEU1} [cm^2/bit]	$\pm 2\sigma$	SEU_2	σ_{SEU2} [cm^2/bit]	$\pm 2\sigma$	SEU_3	σ_{SEU3} [cm^2/bit]	$\pm 2\sigma$
0.3	$2.85 \cdot 10^{11}$	347	$1.53 \cdot 10^{-13}$	11.3	171	$1.49 \cdot 10^{-13}$	12.6	134	$1.19 \cdot 10^{-13}$	13.2
0.6	$1.68 \cdot 10^{11}$	77	$5.74 \cdot 10^{-14}$	15.2	45	$6.67 \cdot 10^{-14}$	18	41	$6.18 \cdot 10^{-14}$	18.5
0.9	$3.72 \cdot 10^{11}$	105	$3.53 \cdot 10^{-14}$	14	66	$4.41 \cdot 10^{-14}$	15.9	29	$1.97 \cdot 10^{-14}$	21.1
1.2	$3.60 \cdot 10^{11}$	64	$2.22 \cdot 10^{-14}$	16	42	$2.9 \cdot 10^{-14}$	18.4	34	$2.38 \cdot 10^{-14}$	19.9

Table C.8: ESA SEU Monitor (1817) cross sections measured at PTB (no lid).

Device	E [MeV]	Φ [n/cm^2]	SEU	σ_{SEU} [cm^2/bit]	$\pm 2\sigma$ (%)
ESA Monitor	5	$1.66 \cdot 10^{9}$	34	$1.20 \cdot 10^{-15}$	$^{+43}_{-32}$
	8	$2.88 \cdot 10^{9}$	276	$5.63 \cdot 10^{-15}$	15.7
	17	$5.09 \cdot 10^{8}$	205	$2.37 \cdot 10^{-14}$	17.2

Table C.9: Cross section measured at PTB with monoenergetic neutrons from 144 keV to 17 MeV. Memories tested with chip package and delidded in some cases. Test performed in parallel (back position) to another tester motherboard is denoted with "*".

Device	E [MeV]	Φ [n/cm^2]	SEU	MBU (2x)	σ_{SEU} [cm^2/bit]	$\pm 2\sigma$ (%)	$\frac{\sigma_{SEU}^{pack}}{\sigma_{SEU}^{del}}$
ISSI 40 nm	0.144	$7.20 \cdot 10^9$	90	0	$3.68 \cdot 10^{-16}$	23.3	1.27
ISSI 40 nm delid	0.144	$2.37 \cdot 10^9$	23	0	$2.89 \cdot 10^{-16}$	$^{+40}_{-45}$	
ISSI 40 nm	1.2	$5.34 \cdot 10^9$	293	0	$1.61 \cdot 10^{-15}$	15.4	1.45
ISSI 40 nm delid	1.2	$3.07 \cdot 10^9$	116	0	$1.11 \cdot 10^{-15}$	21.1	
ISSI 40 nm	2.5	$2.76 \cdot 10^9$	175	0	$1.86 \cdot 10^{-15}$	18.1	1.06
ISSI 40 nm delid	2.5	$6.05 \cdot 10^9$	362	0	$1.76 \cdot 10^{-15}$	14.5	
ISSI 40 nm	5	$1.27 \cdot 10^9$	189	0	$4.37 \cdot 10^{-15}$	17.7	
ISSI 40 nm	8	$5.83 \cdot 10^9$	1540	0	$7.77 \cdot 10^{-15}$	11.2	
ISSI 40 nm	17	$4.97 \cdot 10^8$	323	0	$1.91 \cdot 10^{-14}$	15.0	0.97
ISSI 40 nm delid	17	$3.09 \cdot 10^8$	206	0	$1.96 \cdot 10^{-14}$	17.2	
Cypress 65 nm	0.144	$2.84 \cdot 10^9$	101	0	$2.09 \cdot 10^{-15}$	22.3	1.02
Cypress 65 nm delid	0.144	$2.24 \cdot 10^9$	78	0	$2.04 \cdot 10^{-15}$	24.8	
Cypress 65 nm	1.2	$4.78 \cdot 10^9$	1041	0	$1.28 \cdot 10^{-14}$	11.8	
Cypress 65 nm delid	2.5	$2.12 \cdot 10^9$	429	1	$1.19 \cdot 10^{-14}$	13.9	
Cypress 65 nm	5	$6.27 \cdot 10^8$	183	0	$1.72 \cdot 10^{-14}$	17.8	
Cypress 65 nm	8	$2.09 \cdot 10^9$	1140	0	$6.49 \cdot 10^{-14}$	11.6	
Cypress 65 nm	17	$6.13 \cdot 10^8$	853	0	$8.19 \cdot 10^{-14}$	12.1	1.12
Cypress 65 nm delid	17	$7.31 \cdot 10^7$	91	0	$7.32 \cdot 10^{-14}$*	23.2	
Cypress 90 nm 8	1.2	$5.02 \cdot 10^9$	27	0	$6.40 \cdot 10^{-16}$	$^{+46}_{-36}$	
Cypress 90 nm 8	2.5	$5.78 \cdot 10^9$	86	0	$1.77 \cdot 10^{-15}$	23.8	
Cypress 90 nm 8	5	$1.83 \cdot 10^9$	112	0	$7.30 \cdot 10^{-15}$	21.4	
Cypress 90 nm 8	8	$1.32 \cdot 10^9$	223	1	$2.02 \cdot 10^{-14}$	16.7	
Cypress 90 nm 8	17	$4.49 \cdot 10^8$	472	5	$1.25 \cdot 10^{-13}$	13.6	2.74
Cypress 90 nm 8 delid	17	$5.45 \cdot 10^8$	209	0	$4.56 \cdot 10^{-14}$	17.1	

C.3 SER due to Neutrons of Several Energy Ranges

Table C.10: SEU (%) due to neutrons in the 1-3 MeV energy interval for different environments, from the softer to the harder. Considered spectrum >1 MeV whose portion appertaining to the considered energy range is reported in the Spectrum (%) column.

1-3 MeV	Spectrum (%)	ESA M.	Toshiba	Cypress	FPGA
UJ	19.7	0.1	0.2	0.1	0.9
G0	54.7	1.5	0.7	0.8	5
ChipIr	4.7	0	0.1	0	0.4
JEDEC	21.6	0.1	0.2	0.1	1
RR	33.8	0.2	0.5	0.2	1.9
R10	37.4	0.6	0.2	0.3	2.3

Table C.11: SEU (%) due to neutrons in the 1-10 MeV energy interval for different environments, from the softer to the harder. Considered spectrum >1 MeV whose portion appertaining to the considered energy range is reported in the Spectrum (%) column.

1-10 MeV	Spectrum (%)	ESA M.	Toshiba	Cypress	FPGA
UJ	33.6	2.5	4.5	1.7	10.5
G0	78.1	18.2	10.8	8.2	37.4
ChipIr	12.1	1.5	2.7	1	5.6
JEDEC	36.5	2.7	4.8	1.9	11.6
RR	49.6	6.7	3.7	2.6	15.7
R10	54.2	7.2	4	2.8	17.3

Table C.12: SEU (%) due to neutrons in the 1-20 MeV energy interval for different environments, from the softer to the harder. Considered spectrum >1 MeV whose portion appertaining to the considered energy range is reported in the Spectrum (%) column.

1-20 MeV	Spectrum (%)	ESA M.	Toshiba	Cypress	FPGA
UJ	39.4	9.6	12.3	7.1	18.4
G0	84.1	39.2	31	24.1	54.4
ChipIr	19.8	8.9	10.9	6.7	13.9
JEDEC	43.4	11.4	14.5	8.5	21.1
RR	56	17.8	13.5	9.9	26.5
R10	60.5	19.2	15.1	11.7	28.5

Table C.13: SEU (%) due to neutrons in the 1-100 MeV energy interval for different environments, from the softer to the harder. Considered spectrum >1 MeV whose portion appertaining to the considered energy range is reported in the Spectrum (%) column.

1-100 MeV	Spectrum (%)	ESA M.	Toshiba	Cypress	FPGA
UJ	79.1	69.8	68.9	67.9	71.9
G0	95.3	82.1	79.6	77.6	86.6
ChipIr	61.4	56.1	57.1	55	58.6
JEDEC	59.8	60.4	59	57.5	63.5
RR	75.7	54.5	52.1	50.1	59.3
R10	75	48.8	46.3	44.1	54.7

Bibliography

[1] "CERN Document Server." https://cds.cern.ch/record/2684277.

[2] J. F. Ziegler, M. Ziegler, and J. Biersack, "SRIM – The stopping and range of ions in matter (2010)," *Nuclear Instruments and Methods in Physics Research Section B: Beam Interactions with Materials and Atoms*, vol. 268, no. 11, pp. 1818 – 1823, 2010. 19th International Conference on Ion Beam Analysis.

[3] B. Robert and K. Kirby, *Radiation Handbook for Electronics*. 2019.

[4] "TENDL Library." https://tendl.web.psi.ch/tendl_2019/tendl2019.html. Accessed: 2020.

[5] H. H. K. Tang, "Nuclear physics of cosmic ray interaction with semiconductor materials: Particle-induced soft errors from a physicist's perspective," *IBM Journal of Research and Development*, vol. 40, no. 1, pp. 91–108, 1996.

[6] S. Gerardin, "Corso di Qualità e Affidabilità in Elettronica: Single Event Effects." 2015/2016.

[7] C. Detcheverry, C. Dachs, E. Lorfevre et al., "SEU critical charge and sensitive area in a submicron CMOS technology," *IEEE Transactions on Nuclear Science*, vol. 44, no. 6, pp. 2266–2273, 1997.

[8] R. García Alía, M. Brugger, S. Danzeca et al., "Single event effects in high-energy accelerators," *Semiconductor Science and Technology*, vol. 32, p. 034003, feb 2017.

[9] S. Danzeca, G. Spiezia, M. Brugger et al., "Qualification and Characterization of SRAM Memories Used as Radiation Sensors in the LHC," *IEEE Transactions on Nuclear Science*, vol. 61, no. 6, pp. 3458–3465, 2014.

[10] K. Roeed, M. Brugger, D. Kramer et al., "Method for Measuring Mixed Field Radiation Levels Relevant for SEEs at the LHC," *IEEE Transactions on Nuclear Science*, vol. 59, no. 4, pp. 1040–1047, 2012.

[11] M. Cecchetto, R. García Alía, S. Gerardin, M. Brugger et al., "Impact of Thermal and Intermediate Energy Neutrons on SRAM SEE Rates in the LHC Accelerator," *IEEE Transactions on Nuclear Science*, vol. 65, no. 8, pp. 1800–1806, 2018.

[12] "Measurement and Reporting of Alpha Particle and Terrestrial Cosmic Ray-Induced Soft Errors in Semiconductor Devices. JEDEC Standard 89A (JESD89A)." https://www.jedec.org/standards-documents/docs/jesd. Accessed: October 2019.

[13] D. Lambert, F. Desnoyers and D. Thouvenot, "Investigation of neutron and proton SEU cross-sections on SRAMs between a few MeV and 50 MeV," in *2009 European Conference on Radiation and Its Effects on Components and Systems*, pp. 148–154, 2009.

[14] K. Roed, V. Boccone, M. Brugger et al., "FLUKA Simulations for SEE Studies of Critical LHC Underground Areas," *IEEE Transactions on Nuclear Science*, vol. 58, no. 3, pp. 932–938, 2011.

[15] B. D. Sierawski, K. M. Warren, R. A. Reed et al., "Contribution of low-energy (< 10 MeV) neutrons to upset rate in a 65 nm SRAM," in *2010 IEEE International Reliability Physics Symposium*, pp. 395–399, 2010.

[16] R. G. Alía, M. Tali, M. Brugger, M. Cecchetto et al., "Direct Ionization Impact on Accelerator Mixed-Field Soft-Error Rate," *IEEE Transactions on Nuclear Science*, vol. 67, no. 1, pp. 345–352, 2020.

[17] E. Petersen, *Single Event Effects in Aerospace*. 01 2011.

[18] M. Brugger, R. Garcia Alia, S. Danzeca et al., "Radiation Effects, Calculation Methods and Radiation Test Challenges in Accelerator Mixed Particle and Energy Environments."

[19] C. Weulersse, S. Houssany, N. Guibbaud et al., "Contribution of Thermal Neutrons to Soft Error Rate," *IEEE Transactions on Nuclear Science*, vol. 65, no. 8, pp. 1851–1857, 2018.

[20] R. C. Baumann and E. B. Smith, "Neutron-induced 10B fission as a major source of soft errors in high density SRAMs," *Microelectronics Reliability*, vol. 41, no. 2, pp. 211 – 218, 2001.

[21] A. Hands, P. Morris, K. Ryden et al., "Single Event Effects in Power MOSFETs Due to Atmospheric and Thermal Neutrons," *IEEE Transactions on Nuclear Science*, vol. 58, no. 6, pp. 2687–2694, 2011.

[22] Y. Fang and A. S. Oates, "Thermal Neutron-Induced Soft Errors in Advanced Memory and Logic Devices," *IEEE Transactions on Device and Materials Reliability*, vol. 14, no. 1, pp. 583–586, 2014.

[23] Takashi Y., Takashi K., Taiki U., Hideya M. et al., "Origin analysis of thermal neutron soft error rate at nanometer scale," *Journal of Vacuum Science & Tech.*, vol. 33, no. 2, p. 020604, 2015.

[24] J. L. Autran, S. Serre, S. Semikh et al., "Soft-Error Rate Induced by Thermal and Low Energy Neutrons in 40 nm SRAMs," *IEEE Transactions on Nuclear Science*, vol. 59, no. 6, pp. 2658–2665, 2012.

[25] C.H. Kim, I.-C. Rho, S.H. Kim et al., "Improvement of Adhesion Performances of CVD-W Films Deposited on B[sub 2]H[sub 6]-Based ALD-W Nucleation Layer," *Electrochemical and Solid-State Letters*, vol. 12, no. 3, p. H80, 2009.

[26] R. Alía García, M. Brugger, S. Danzeca et al., "SEE cross section calibration and application to quasi-monoenergetic and spallation facilities," *EPJ Web Conf.*, vol. 153, p. 08015, 2017.

[27] G. Spiezia, P. Peronnard, A. Masi et al., "A New RadMon Version for the LHC and its Injection Lines," *IEEE Transactions on Nuclear Science*, vol. 61, no. 6, pp. 3424–3431, 2014.

[28] D. Kramer, M. Brugger, V. Klupak et al., "LHC RadMon SRAM Detectors Used at Different Voltages to Determine the Thermal Neutron to High Energy Hadron Fluence Ratio," *IEEE Transactions on Nuclear Science*, vol. 58, no. 3, pp. 1117–1122, 2011.

[29] F. Wrobel, J. M. Palau, M. C. Calvet et al., "Incidence of multi-particle events on soft error rates caused by n-Si nuclear reactions," *IEEE Transactions on Nuclear Science*, vol. 47, no. 6, pp. 2580–2585, 2000.

[30] G. Battistoni, F. Cerutti, A. Fasso et al., "The FLUKA code: Description and benchmarking," *AIP Conf. Proc.*, vol. 896, no. 1, pp. 31–49, 2007.

[31] G. Battistoni, T. Boehlen, F. Cerutti et al., "Overview of the FLUKA code," *Annals Nucl. Energy*, vol. 82, pp. 10–18, 2015.

[32] T.T. Böhlen, F. Cerutti, M.P.W Chin et al., "The FLUKA Code: Developments and Challenges for High Energy and Medical Applications," *Nucl. Data Sheets*, vol. 120, pp. 211–214, 2014.

[33] V. Vlachoudis, "FLAIR: A Powerful But User Friendly Graphical Interface For FLUKA," in *Int. Conf. on Mathematics, Computational Methods & Reactor Physics (M&C 2009), Saratoga Springs, New York,*, 2009.

[34] R. García Alía, M. Brugger, F. Cerutti et al., "LHC and HL-LHC: Present and Future Radiation Environment in the High-Luminosity Collision Points and RHA Implications," *IEEE Transactions on Nuclear Science*, vol. 65, no. 1, pp. 448–456, 2018.

[35] A. Esposito, R. Bedogni, L. Lembo, and M. Morelli, "Determination of the neutron spectra around an 18 MV medical LINAC with a passive Bonner sphere spectrometer based on gold foils and TLD pairs," *Radiation Measurements*, vol. 43, no. 2, pp. 1038 – 1043, 2008. Proceedings of the 15th Solid State Dosimetry (SSD15).

[36] Ota S., Kobayashi S., Sihver L. et al., "Neutron production in the lunar subsurface from alpha particles in galactic cosmic rays," *Earth Planet Sp*, vol. 63, p. 25–35, 2011.

[37] ISO Central Secretary, "Process management for avionics—Atmospheric radiation effects. Guidelines for single event effects testing for avionics systems.," Standard IEC Standard 62396-1, International Electrotechnical Commission, Geneva, CH, 2016.

[38] ISO Central Secretary, "Process management for avionics—Atmospheric radiation effects. Accommodation of atmospheric radiation effects via single event effects within avionics electronic equipment.," Standard IEC Standard 62396-2, International Electrotechnical Commission, Geneva, CH, 2017.

[39] "MAIRE, RadMod Research." https://www.radmod.co.uk/maire. Accessed: August 2019.

[40] R. García Alía, M. Brugger, S. Danzeca et al., "SEL Hardness Assurance in a Mixed Radiation Field," *IEEE Transactions on Nuclear Science*, vol. 62, no. 6, pp. 2555–2562, 2015.

[41] M. Cecchetto, P. Fernández-Martínez, R. G. Alía et al., "SEE Flux and Spectral Hardness Calibration of Neutron Spallation and Mixed-Field Facilities," *IEEE Transactions on Nuclear Science*, vol. 66, no. 7, pp. 1532–1540, 2019.

[42] ISO Central Secretary, "Process management for avionics - Atmospheric radiation effects. Assessment of thermal neutron fluxes and single event effects in avionics systems.," Standard IEC Standard 62396-5, International Electrotechnical Commission, Geneva, CH, 2014.

[43] A. Ferrari and P. Sala, "Treating High Energy Showers," in *Training Course on the Use of MCNP in Radiation Protection and Dosimetry*, pp. 1–34, 1996.

[44] P. Sala and G. Battistoni, "The physics of the FLUKA code: hadronic models, FLUKA course," 2006.

[45] K. S. Krane and D. Halliday, *Introductory nuclear physics*. New York: Wiley, 1987.

[46] J. Baggio, D. Lambert, V. Ferlet-Cavrois et al., "Single Event Upsets Induced by 1–10 MeV Neutrons in Static-RAMs Using Mono-Energetic Neutron Sources," *IEEE Transactions on Nuclear Science*, vol. 54, no. 6, pp. 2149–2155, 2007.

[47] S. Abe and Y. Watanabe, "Analysis of Charge Deposition and Collection Caused by Low Energy Neutrons in a 25-nm Bulk CMOS Technology," *IEEE Transactions on Nuclear Science*, vol. 61, no. 6, pp. 3519–3526, 2014.

[48] F. Wrobel, J. M. Palau, M. C. Calvet and P. Iacconi, "Contribution of SiO_2 in neutron-induced SEU in SRAMs," *IEEE Transactions on Nuclear Science*, vol. 50, no. 6, pp. 2055–2059, 2003.

[49] G. Gasiot, V. Ferlet-Cavrois, J. Baggio et al., "SEU sensitivity of bulk and SOI technologies to 14-MeV neutrons," *IEEE Transactions on Nuclear Science*, vol. 49, no. 6, pp. 3032–3037, 2002.

[50] F. Miller, C. Weulersse, T. Carrière et al., "Investigation of 14 MeV Neutron Capabilities for SEU Hardness Evaluation," *IEEE Transactions on Nuclear Science*, vol. 60, no. 4, pp. 2789–2796, 2013.

[51] "ENDF database." http://www-nds.ciae.ac.cn/exfor/endf.htm. Accessed: 2020-05.

[52] F. H. Ruddy, A. R. Dulloo, J. G. Seidel et al., "The fast neutron response of 4H silicon carbide semiconductor radiation detectors," *IEEE Transactions on Nuclear Science*, vol. 53, no. 3, pp. 1666–1670, 2006.

[53] "^{25}Mg level scheme structure." https://www.nndc.bnl.gov/nudat2/NuDatBandPlotServlet?nucleus=25MG&unc=nds. Accessed: 2020-07-24.

[54] C. Cazzaniga et al., "CERN AmBe RADSAGA CAMPAIGN." https://edms.cern.ch/document/2172247/2. EDMS 2172247/1.

[55] C. Cazzaniga et Al., "A diamond based neutron spectrometer for diagnostics of deuterium-tritium fusion plasmas," *Review of Scientific Instruments*, vol. 85, 2014.

[56] R. Garcia Alia, *Radiation Fields in High Energy Accelerators and their impact on Single Event Effects*. PhD dissertation, Dep. Information I2S, Montpellier Univ., Dec. 2014.

[57] R. G. Alía, E. W. Blackmore, M. Brugger et al., "SEL Cross Section Energy Dependence Impact on the High Energy Accelerator Failure Rate," *IEEE Transactions on Nuclear Science*, vol. 61, no. 6, pp. 2936–2944, 2014.

[58] R. García Alía, M. Brugger, S. Danzeca et al., "Energy Dependence of Tungsten-Dominated SEL Cross Sections," *IEEE Transactions on Nuclear Science*, vol. 61, no. 5, pp. 2718–2726, 2014.

[59] Alía, Rubén García and Brugger, Markus and Danzeca, Salvatore et al., "Single event effects in high-energy accelerators," *Semiconductor Science and Technology*, vol. 32, p. 034003, Feb. 2017. Publisher: IOP Publishing.

[60] D. Lambert, J. Baggio, G. Hubert et al., "Analysis of Quasi-Monoenergetic Neutron and Proton SEU Cross Sections for Terrestrial Applications," *IEEE Transactions on Nuclear Science*, vol. 53, no. 4, pp. 1890–1896, 2006.

[61] "ILL - Institut Laue Langevin - Rapport transparence et sécurité nucléaire – Institut Laue Langevin." https://www.ill.eu/fileadmin/user_upload/ILL/5_Reactor_and_safety/High-flux_reactor/TSN/Annuel-TSN-2019.pdf. Grenoble, 2019.

[62] J. Beaucour, J. Segura-Ruiz, B. Giroud et al., "Grenoble Large Scale Facilities for Advanced Characterisation of Microelectronics Devices," in *2015 15th European Conference on Radiation and Its Effects on Components and Systems (RADECS)*, pp. 1–4, 2015.

[63] M. Cecchetto et al., "SEU and SEL measurements using 14-MeV and thermal neutron beams." https://cds.cern.ch/record/2649007?ln=en. CERN-ACC-NOTE-2018-0047.

[64] M. Cecchetto, A. Coronetti and R. Garcia Alia, "ILL Thermal Neutron Test Campaign." https://edms.cern.ch/ui/file/2304699/1/RADSAGA_Test_Report_10_v1.2_ILL_docx_cpdf.pdf. Version no. 1.2 – EDMS 2304699 v.1 03/03/2020.

[65] M. Cecchetto, *Impact of thermal and intermediate energy neutrons on the semiconductor memories for the CERN high-energy accelerators*. Master Thesis dissertation, Department of Information Engineering, University of Padova (IT), July 2017.

[66] G. Bazzano et al., "Dosimetric characterization of an irradiation set-up for electronic components testing at the TOP-IMPLART proton linear accelerator," in *19th European Conference on Radiation and Its Effects on Components and Systems (RADECS)*, pp. 1–4, 2019.

[67] Picardi, L. and Ampollini, A. and Bazzano et al., "Beam commissioning of the 35 MeV section in an intensity modulated proton linear accelerator for proton therapy," *Phys. Rev. Accel. Beams*, vol. 23, p. 020102, Feb 2020.

[68] C. De Angelis, A. Ampollini, G. Bazzano et al., "THE TOP-IMPLART PROTON LINEAR ACCELERATOR: INTERIM CHARACTERISTICS OF THE 35 MEV BEAM," *Radiation Protection Dosimetry*, vol. 186, pp. 113–118, 05 2019.

[69] S. Fiore, M. Angelone, S. Loreti et al., "The Frascati Neutron Generator FNG: a Fast Neutron Facility for Irradiation Experiments," in *2018 18th European Conference on Radiation and Its Effects on Components and Systems (RADECS)*, pp. 1–3, 2018.

[70] F. Chiarelli, *Full Monte Carlo simulation of the Frascati Neutron Generator with the FLUKA package for radioprotection studies*. Master Thesis dissertation, Tor Vergata, University of Rome (IT), 2018.

[71] R. Nolte and D. J. Thomas, "Monoenergetic fast neutron reference fields: I. Neutron production," *Metrologia*, vol. 48, pp. S263–S273, oct 2011.

[72] R. Nolte and D. J. Thomas, "Monoenergetic fast neutron reference fields: II. Field characterization," *Metrologia*, vol. 48, pp. S274–S291, oct 2011.

[73] H.J. Brede and M. Cosack and G. Dietze et al., "The Braunschweig accelerator facility for fast neutron research: 1: Building design and accelerators," *Nuclear Instruments and Methods*, vol. 169, no. 3, pp. 349 – 358, 1980.

[74] R. Nolte, S. Nolte, S. Röttger et al., *PTB Contribution to the Key Comparison CCRE (III)-K11: Comparison of Neutron Fluence Measurements for Neutron Energies of 27 KeV, 565 KeV, 2.5 MeV and 17 MeV*. PTB-Bericht / N: Neutronenphysik, Fachverlag NW in der Carl Schünemann Verlag GmbH, 2018.

[75] F. Pozzi, *CERN Radiation Protection (RP) calibration facilities*. PhD dissertation, Fac. Mechanical Engineering, Technical Univ. of Munich., Sept. 2015.

[76] D. Chiesa, M. Nastasi, C. Cazzaniga et al., "Measurement of the neutron flux at spallation sources using multi-foil activation," *Nuclear Instruments and Methods in Physics Research Section A: Accelerators, Spectrometers, Detectors and Associated Equipment*, vol. 902, pp. 14 – 24, 2018.

[77] C. Cazzaniga and C. D. Frost, "Progress of the Scientific Commissioning of a fast neutron beamline for Chip Irradiation," *Journal of Physics: Conference Series*, vol. 1021, p. 012037, may 2018.

[78] J. Mekki, M. Brugger, R. Garcia Alia et al., "CHARM: A Mixed Field Facility at CERN for Radiation Tests in Ground, Atmospheric, Space and Accelerator Representative Environments," *IEEE Transactions on Nuclear Science*, vol. 63, no. 4, pp. 2106–2114, 2016.

[79] A. Infantino, "FLUKA Monte Carlo Modelling of the CHARM Facility's Test Area: Update of the Radiation Field Assessment." CERN-ACC-NOTE-2017-0059.

[80] J. Mekki, "CHARM Secondary Emission Chamber." CERN EDMS 1553668/1.

[81] "Beam intensity monitoring at the IRRAD proton facility." CERN EDMS 1554165, 2015.

[82] D. M. Hiemstra and E. W. Blackmore, "LET spectra of proton energy levels from 50 to 500 MeV and their effectiveness for single event effects characterization of microelectronics," *IEEE Transactions on Nuclear Science*, vol. 50, no. 6, pp. 2245–2250, 2003.

[83] Dickens, Scouting, and Oz, "SEE Testing Lessons." Jet Propulsion Laboratory, California Institute of Technology.

[84] W. E. Ricker, "The Concept of Confidence or Fiducial Limits Applied to the Poisson Frequency Distribution," *Journal of the American Statistical Association*, vol. 32, no. 198, pp. 349–356, 1937.

[85] R. Harboe-Sorensen, C. Poivey, F. X. Guerre et al., "From the Reference SEU Monitor to the Technology Demonstration Module On-Board PROBA-II," *IEEE Transactions on Nuclear Science*, vol. 55, no. 6, pp. 3082–3087, 2008.

[86] M. Cecchetto, R. Garcia Alia and M. Tali, "ESA SEU Monitor calibration." https://edms.cern.ch/document/2059465/1. CERN-EDMS-NOTE-2059465.

[87] S. Abe, T. Sato, J. Kuroda et al., "Impact of Hydrided and Non-Hydrided Materials Near Transistors on Neutron-Induced Single Event Upsets," in *2020 IEEE International Reliability Physics Symposium (IRPS)*, pp. 1–7, 2020.

[88] D. Oliveira, F. F. dos Santos, G. Piscoya Dávila et al., "High-Energy Versus Thermal Neutron Contribution to Processor and Memory Error Rates," *IEEE Transactions on Nuclear Science*, vol. 67, no. 6, pp. 1161–1168, 2020.

[89] M. Bagatin, S. Gerardin, A. Paccagnella and V. Ferlet-Cavrois, "Single and Multiple Cell Upsets in 25-nm NAND Flash Memories," *IEEE Transactions on Nuclear Science*, vol. 60, no. 4, pp. 2675–2681, 2013.

[90] M. Bagatin, S. Gerardin, and A. Paccagnella, "Space and terrestrial radiation effects in flash memories," *Semiconductor Science and Technology*, vol. 32, p. 033003, feb 2017.

[91] S. Gerardin, M. Bagatin, A. Paccagnella et al., "Neutron and Alpha Single Event Upsets in Advanced NAND Flash Memories," *IEEE Transactions on Nuclear Science*, vol. 61, no. 4, pp. 1799–1805, 2014.

[92] S. Gerardin, M. Bagatin, A. Ferrario et al., "Neutron-Induced Upsets in NAND Floating Gate Memories," *IEEE Transactions on Device and Materials Reliability*, vol. 12, no. 2, pp. 437–444, 2012.

[93] G. Tsiligiannis, S. Danzeca, R. García Alía et al., "Radiation Effects on Deep Submicrometer SRAM-Based FPGAs Under the CERN Mixed-Field Radiation Environment," *IEEE Transactions on Nuclear Science*, vol. 65, no. 8, pp. 1511–1518, 2018.

[94] M. Tali, *Single-event radiation effects in hardened and state-of-the-art components for space and high-energy accelerator applications*. PhD dissertation, Univ. Jyväskylä, Jyväskylä, Finland, 2019.

[95] D. Lambert, F. Desnoyers, D. Thouvenot et al., "Single Event Upsets Induced by a few MeV Neutrons in SRAMs and FPGAs," in *2017 IEEE Radiation Effects Data Workshop (REDW)*, pp. 1–5, 2017.

[96] H. Quinn, A. Watkins, L. Dominik and C. Slayman, "The Effect of 1–10-MeV Neutrons on the JESD89 Test Standard," *IEEE Transactions on Nuclear Science*, vol. 66, no. 1, pp. 140–147, 2019.

[97] G. Hubert and L. Artola, "Experimental Evidence of Ground Albedo Neutron Impact on Soft Error Rate for Nanoscale Devices," *IEEE Transactions on Nuclear Science*, vol. 66, no. 1, pp. 262–269, 2019.

[98] G. Hubert and L. Artola, "Study of Secondary Scattering/Albedo Neutron Fields and Their Impacts on SER as Function of Scene Topologies," *IEEE Transactions on Nuclear Science*, vol. 67, no. 1, pp. 201–209, 2020.

[99] E. R. van der Graaf, R. W. Ostendorf, M. van Goethem et al., "AGORFIRM, the AGOR facility for irradiations of materials," in *2009 European Conference on Radiation and Its Effects on Components and Systems*, pp. 451–454, 2009.

[100] R. Secondo et al., "Cypress CY62157EV30 Radiation Test Report at PSI." https://edms.cern.ch/document/1569090/1. CERN-EDMS-NOTE-2059465.

[101] R. Naseer, Y. Boulghassoul, J. Draper et al., "Critical Charge Characterization for Soft Error Rate Modeling in 90nm SRAM," in *2007 IEEE International Symposium on Circuits and Systems*, pp. 1879–1882, 2007.

[102] S. Abe and Y. Watanabe, "Analysis of Charge Deposition and Collection Caused by Low Energy Neutrons in a 25-nm Bulk CMOS Technology," *IEEE Transactions on Nuclear Science*, vol. 61, no. 6, pp. 3519–3526, 2014.

[103] B. D. Sierawski, J. A. Pellish, R. A. Reed et al., "Impact of Low-Energy Proton Induced Upsets on Test Methods and Rate Predictions," *IEEE Transactions on Nuclear Science*, vol. 56, no. 6, pp. 3085–3092, 2009.

[104] B. D. Sierawski, M. H. Mendenhall, R. A. Reed et al., "Muon-Induced Single Event Upsets in Deep-Submicron Technology," *IEEE Transactions on Nuclear Science*, vol. 57, no. 6, pp. 3273–3278, 2010.

[105] J. R. Schwank, M. R. Shaneyfelt, J. Baggio et al., "Effects of particle energy on proton-induced single-event latchup," *IEEE Transactions on Nuclear Science*, vol. 52, no. 6, pp. 2622–2629, 2005.

[106] T. L. Turflinger, D. A. Clymer, L. W. Mason et al., "RHA Implications of Proton on Gold-Plated Package Structures in SEE Evaluations," *IEEE Transactions on Nuclear Science*, vol. 62, no. 6, pp. 2468–2475, 2015.

[107] S. Uznanski, R. G. Alia, E. Blackmore et al., "The Effect of Proton Energy on SEU Cross Section of a 16 Mbit TFT PMOS SRAM with DRAM Capacitors," *IEEE Transactions on Nuclear Science*, vol. 61, no. 6, pp. 3074–3079, 2014.

[108] R. García Alía, M. Brugger, M. Cecchetto et al., "SEE Testing in the 24-GeV Proton Beam at the CHARM Facility," *IEEE Transactions on Nuclear Science*, vol. 65, no. 8, pp. 1750–1758, 2018.

[109] J. Allison, K. Amako, and J. A. et al., "Recent developments in Geant4," *Nuclear Instruments and Methods in Physics Research Section A: Accelerators, Spectrometers, Detectors and Associated Equipment*, vol. 835, pp. 186 – 225, 2016.

[110] G. Collaboration, "Geant4 Guide For Physics Lists." http://cern.ch/geant4-userdoc/UsersGuides/PhysicsListGuide/BackupVersions/V10.6/fo/PhysicsListGuide.pdf. Release 10.6, Rev4.0, December 2019.

[111] G. Collaboration, "Geant4 Physics Reference Manual." http://cern.ch/geant4-userdoc/UsersGuides/PhysicsReferenceManual/BackupVersions/V10.6/fo/PhysicsReferenceManual.pdf. Release 10.6, Rev4.0, December 2019.